1990

An analysis of an eddy-resolving global ocean model in the tropical Indian Ocean

Long, Erik Christopher

Monterey, California. Naval Postgraduate School

NPS-68-90-008

NAVAL POSTGRADUATE SCHOOL

Monterey, California

THESIS

ANALYSIS OF AN EDDY-RESOLVING
GLOBAL OCEAN MODEL
IN THE TROPICAL INDIAN OCEAN

by

Erik Christopher Long

September 1990

Thesis Advisor: Albert J. Semtner, Jr.

Prepared for:
National Science Foundation
1800 G Street N. W.
Washington, DC 20550

NAVAL POSTGRADUATE SCHOOL
Monterey, CA 93943

Rear Admiral Ralph W. West, Jr.
Superintendent

Harrison Shull
Provost

This project was funded by the National Science Foundation, 1800 G Street N. W., Washington, DC 20550.

Released By:

[redacted]

Dean of Faculty and Graduate Studies

Unclassified

Security Classification of this page

REPORT DOCUMENTATION PAGE

1a Report Security Classification: Unclassified	1b Restrictive Markings
2a Security Classification Authority	3 Distribution Availability of Report: Approved for public release; distribution is unlimited.
2b Declassification/Downgrading Schedule	
4 Performing Organization Report Number(s): NPS-68-90-008	5 Monitoring Organization Report Number(s)
6a Name of Performing Organization: Naval Postgraduate School; 6b Office Symbol (*If Applicable*): OC	7a Name of Monitoring Organization: Naval Postgraduate School
6c Address (*city, state, and ZIP code*): Monterey, CA 93943-5000	7b Address (*city, state, and ZIP code*): Monterey, CA 93943-5000
8a Name of Funding/Sponsoring Organization: National Science Foundation; 8b Office Symbol (*If Applicable*)	9 Procurement Instrument Identification Number: NSF Grant No. ATM-8705980
8c Address (*city, state, and ZIP code*)	10 Source of Funding Numbers: Program Element Number / Project No / Task No / Work Unit Accession No

11 Title (*Include Security Classification*): ANALYSIS OF AN EDDY-RESOLVING GLOBAL OCEAN MODEL IN THE TROPICAL INDIAN OCEAN

12 Personal Author(s): Long, Erik Christopher

13a Type of Report	13b Time Covered	14 Date of Report (*year, month,day*)	15 Page Count
Master's Thesis	From To	September 1990	158

16 Supplementary Notation: The views expressed in this thesis are those of the author and do not reflect the official policy or position of the Department of Defense or the U.S. Government.

17 Cosati Codes			18 Subject Terms (*continue on reverse if necessary and identify by block number*)
Field	Group	Subgroup	Oceanographic Numerical Modeling, Indian Ocean, Ocean General Circulation Model, Eddy-Resolving, Somali Current, Tropical, Equatorial

19 Abstract (continue on reverse if necessary and identify by block number)

This paper examines the Semtner and Chervin global ocean model in the tropical Indian Ocean. The primitive equation, eddy-resolving model covers a domain from 75°S to 65°N at a horizontal resolution of 1/2°, with 20 vertical levels. In a new phase of an ongoing simulation, the wind stress has been changed from annual mean wind forcing to seasonal forcing, using the Hellerman and Rosenstein (1983) wind stress. The model is shown to reproduce the seasonal features of the Indian Ocean circulation. The seasonally-reversing Somali Current is simulated by the model, and includes seasonal undercurrents and a two-gyre system during the southwest monsoon. Westward flow occurs beneath the Southwest Monsoon Current during June and July. The major equatorial currents of the two monsoon regimes are well-represented, including semiannual Wyrtki jets and the Equatorial Undercurrent. The seasonal features of the marginally-resolved Leeuwin Current are present in the model. Monthly mass transports ha - been calculated for the major equatorial currents, as well as the Pacific-Indonesian throughflow, and are consistent with observations. The structure of deep equatorial jets in the model is highly baroclinic, an upward tilt in the jets from west to east accounts for simultaneous westward and upward phase propagation of the zonal velocity.

20 Distribution/Availability of Abstract	21 Abstract Security Classification
[X] unclassified/unlimited [ ] same as report [ ] DTIC users	Unclassified
22a Name of Responsible Individual: Albert J. Semtner, Jr	22b Telephone (*Include Area code*): (408) 646-3267; 22c Office Symbol: OC/Se

DD FORM 1473, 84 MAR — 83 APR edition may be used until exhausted; All other editions are obsolete — security classification of this page: Unclassified

19 Abstract (continued)

The Haney (1971) method of prescribing surface heat flux, adapted to the Levitus (1982) data base, is analyzed by comparing the model surface heat flux and monthly temperature fields with existing climatologies. The model is shown to exhibit an inherent interannual variability, despite the interannual invariance of the wind stress. The small amount of interannual variability is superimposed on a strong seasonal cycle. Near-surface currents in the model are in good agreement with existing studies of drifting surface buoys.

Approved for public release; distribution is unlimited.

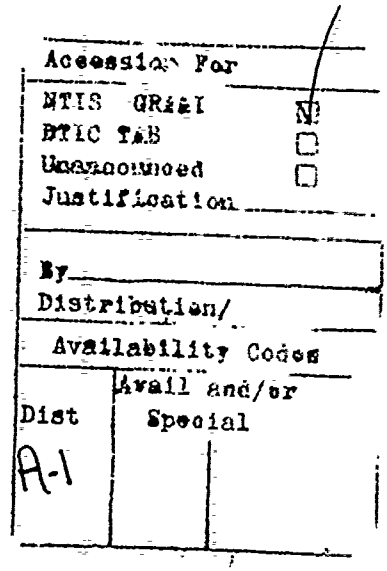

Analysis of an Eddy-Resolving Global Ocean Model in the Tropical Indian Ocean

by

Erik Christopher Long
Lieutenant Commander, United States Navy
B.A., Oberlin College, 1979
B.S.E.E., Washington University, 1979

Submitted in partial fulfillment of the requirements for the degree of

MASTER OF SCIENCE IN METEOROLOGY AND PHYSICAL OCEANOGRAPHY

from the

NAVAL POSTGRADUATE SCHOOL
September, 1990

Author: [redacted]
Erik Christopher Long

Approved by: [redacted]
Albert J. Semtner, Jr., Thesis Advisor

[redacted]
Mary L. Batteen, Second Reader

[redacted]
Curtis A. Collins, Chairman,
Department of Oceanography

ABSTRACT

This paper examines the Semtner and Chervin global ocean model in the tropical Indian Ocean. The primitive equation, eddy-resolving model covers a domain from 75°S to 65°N at a horizontal resolution of 1/2°, with 20 vertical levels. In a new phase of an ongoing simulation, the wind stress has been changed from annual mean wind forcing to seasonal forcing, using the Hellerman and Rosenstein (1983) wind stress. The model is shown to reproduce the seasonal features of the Indian Ocean circulation. The seasonally-reversing Somali Current is simulated by the model, and includes seasonal undercurrents and a two-gyre system during the southwest monsoon. Westward flow occurs beneath the Southwest Monsoon Current during June and July. The major equatorial currents of the two monsoon regimes are well-represented, including semiannual Wyrtki jets and the Equatorial Undercurrent. The seasonal features of the marginally-resolved Leeuwin Current are present in the model. Monthly mass transports have been calculated for the major equatorial currents, as well as the Pacific-Indonesian throughflow, and are consistent with observations. The structure of deep equatorial jets in the model is highly baroclinic; an upward tilt in the jets from west to east accounts for simultaneous westward and upward phase propagation of the zonal velocity.

The Haney (1971) method of prescribing surface heat flux, adapted to the Levitus (1982) data base, is analyzed by comparing the model surface heat flux and monthly temperature fields with existing climatologies. The model is shown to exhibit an inherent interannual variability, despite the interannual invariance of the wind stress. The small amount of interannual variability is superimposed on a strong seasonal cycle. Near-surface currents in the model are in good agreement with existing studies of drifting surface buoys.

TABLE OF CONTENTS

ACKNOWLEDGMENT

This work is supported by grants ATM-8705980 and OCE-8812472 from the National Science Foundation. Computing resources were provided by the Scientific Computing Division of the National Center for Atmospheric Research. NCAR is sponsored by the National Science Foundation.

The good Lord provided us with each other as our most valuable resource, and that has not changed in this world of microprocessors to supercomputers. Mike McCann provided tremendous support involving the model and the Ocean Processor, customization of programs to provide analysis products, and the animation of the model output. This project would not have been possible without his assistance. Animation was developed using software tools supplied by the National Center for Supercomputer Applications. Fritz Schott, Jim O'Brien, and Stuart Godfrey gave me the benefit of their tremendous experience in providing comments on the interpretation of the results. Bob Chervin steadfastly ran the model on the Cray X-MP, providing a steady flow of output for me to analyze. Curt Collins graciously allowed the use of his Macintosh for preparing graphics, and gave me the encouragement to show the model results at the TOGA conference. Tom Bettge's Ocean Processor and supporting documentation enabled the straightforward anlysis of the archived data, and his timely responses to questions simplified many problems. My colleagues, Larry Gordon and Tom Murphree, provided mutual support and valuable feedback in the model output analysis. Mary Batteen was a tremendous resource in the comparison of the model output with observations and thesis preparation. My fiancee, Whitney Fay, made me very happy by distracting me from working on my thesis, until I needed to finish it, when she understandingly left me alone. Mike VanWoert was my role model in becoming an oceanographer without getting wet.

Finally, Bert Semtner gave me the freedom to be Chief Oceanographer of the model Indian Ocean, gave me guidance when I needed it, patiently answered my questions as I gained understanding of ocean modeling, and made the project an enjoyable educational experience.

I. INTRODUCTION

The Semtner and Chervin (1988) study of global ocean circulation reported the results of an eddy-resolving global ocean model forced by mean annual climatological winds. The purpose of this paper is to report on the follow-on experiment, which forces the ocean model with mean monthly wind stress. Due to the intense seasonal cycle of the tropical monsoon, the change to seasonal forcing in the model was expected to have its greatest impact in the tropics. This study examines the seasonal cycle of the tropical Indian Ocean in the model.

A. BACKGROUND

The worldwide industrial growth of the 20th century has caused environmental changes which man is only beginning to understand. The advent of global remote sensing systems has recently given us the ability to monitor the effect that man has on the world climate, yet we still know very little about the time scales of naturally-occurring climatic variability. We now recognize that there are important feedback mechanisms between the atmosphere and the oceans, which must be understood if we are to be able to predict climatic change. Computer simulation is the most promising tool for projecting the results of increased atmospheric emissions by industrial activity, and it may help predict the environmental impact of pollution of the seas. The trends in increasing computer power indicate that we may soon have sufficient computing resources available to conduct studies of climatic change, using coupled air-ocean simulations with realistic physics. The recent development of eddy-resolving global ocean models is a very important step in the development of global climate modeling.

Simulations of the ocean circulation require approximately 1,000 times as much computer power as atmospheric simulations, because of the smaller space scales and longer time scales of motion in the sea. Hence, researchers involved with general circulation ocean modeling have always been limited in the scope of their studies by the available computer power. Although simulations of the global ocean circulation have been performed for more than 20 years, the understanding of the important role of mesoscale and sub-mesoscale features in the ocean requires that an ocean model must resolve mesoscale eddies if it is to accurately portray the energetics and variability of the ocean. While some global modeling strategies have attained mesoscale eddy-resolving resolution, limitations in computer power have required some limitation in the model physics, such as quasi-geostrophic or layered models. The Semtner and Chervin model (Semtner and Chervin (1988), Chervin and Semtner (1988)), hereafter referred to as SCM, is the first attempt at a primitive equation, eddy-resolving global circulation simulation.

As physical limitations in semiconductor technology are reached, computational power has continued to increase through the use of supercomputer architecture employing multiple, parallel processors. The SCM code was designed to be able to exploit rapid increases in computing power expected in the 1990's by being easily reconfigured to run on new models of Cray supercomputers, employing up to 64 processors. Although the use of multitasking may afford significant speed increases, any bottlenecks in the program (*i. e.*, steps which must be run on only one processor) severely restrict the speedup gained by adding additional processors. This relationship is described in Amdahl's Law:

$$S = \frac{N}{1 + s\,(N - 1)} \qquad (1)$$

where the speedup (S) to be gained by going from 1 processor to N processors is strongly dependent upon N and s, the sequential fraction of program which must be performed on one processor. As the number of processors becomes greater, the requirement for

efficiency increases. The SCM code results in a sequential fraction of 0.0036, allowing it to achieve a speedup factor of 3.96 when run on a four processor machine, 7.80 on eight processors, 15.18 on a 16-processor machine, and 52.17 on a 64-processor machine. Ocean models will have to become extraordinarily efficient to take maximum advantage of parallel processing. The SCM, when run at 1/2° horizontal resolution (as in Semtner and Chervin (1988) and this study), is only marginally eddy-resolving, but is fully capable of greater resolution when run on more powerful machines.

B. THE INDIAN OCEAN

The surface currents in the Indian Ocean are divided into two seasonal regimes, associated with the northeast and southwest monsoons. As shown in Figure 1.1(a), the northeast monsoon regime consists of a system of zonal currents, defined from south to north by the Antarctic Circumpolar Current, the South Equatorial Current, the Equatorial Countercurrent, and the North Equatorial Current. The southwest monsoon season (Figure 1.1(b)) creates the powerful northeastward-flowing Somali Current, and a two-gyre system defined by the the Antarctic Circumpolar Current, the South Equatorial Current, and the Southwest Monsoon Current.

Oceanographic observations in the Indian Ocean have lagged those of the Atlantic and Pacific Oceans, due to the limited number of shipping lanes, long transit times and great cost of sending oceanographic ships to the area from North American and European ports, as well as limited financial and naval interests in the area by major oceanographic countries. Figure 1.2(a) (from Levitus, 1982) shows the density of Indian Ocean surface and subsurface temperature measurements, and Figure 1.2(b) shows the distribution of surface observations in the Indian Ocean from the Hanstenrath and Lamb (1979) atlas. The coverage is very sparse outside of the shipping lanes.

This paucity of observations is quite significant, because the Indian Ocean has many unique and seasonal features, which have no analog in the Atlantic and Pacific Oceans. The basin is closed to the north, and the presence of the Asian continent causes several of the unique Indian Ocean features. First, the monsoon cycle in the Indian Ocean is much stronger than in the other oceans, due to such key elements as heating of the Himalayan massif, and intensification of winds along the African coast. Unlike the Atlantic and Pacific Oceans, the Indian Ocean has no communication with northern polar or subpolar waters. Furthermore, as described in Brekhovskikh *et al.*, (1986), the presence of the Indian subcontinent causes a significant east/west basin difference in moisture patterns. The monsoon brings seasonal reversals of surface currents at several points in the Indian Ocean, including the Somali Current, zonal surface currents at the Equator, the Leeuwin Current, which flows into the prevailing wind, and the Equatorial Undercurrent.

Although equatorial undercurrents are known to exist in the Atlantic, Pacific, and Indian Oceans, the monsoon seasonal cycle causes the equatorial undercurrent in the Indian Ocean to be quite unique. The Equatorial Undercurrent (Cromwell Current in the Pacific, Lomonosov Current in the Atlantic) is a thin, equatorially-trapped subsurface eastward jet which traverses the entire basin beneath a strong, westward surface flow. It is a persistent feature in the Atlantic and Pacific Oceans, but has been observed only in the boreal spring in the Indian Ocean. However, like many other phenomena in the tropical Indian Ocean, the data is sparse. Observations have reported westward subsurface currents during the southwest monsoon, and a highly baroclinic structure, but the seasonal cycle of the subsurface structure is not well understood.

The goal of this study is to describe the seasonal cycle of the tropical Indian Ocean in the SCM, and to compare the model with observations. There are two significant results which may come out of such an analysis. The first is to demonstrate the credibility of the

model (and to determine weaknesses which need to be improved in further studies). The second result is that the ocean may be studied systematically, gaining insight into processes at work which have escaped limited observational resources.

II. THE MODEL

The progress of numerical modeling, like so many other technologies, has been largely evolutionary, with small improvements added to refine existing model codes, in between major revolutionary steps associated with new computer architectures. This study falls into the former category; the difference between this study and the model described by Semtner and Chervin (1988) is that monthly wind forcing is incorporated, instead of an annual mean forcing. The SCM code is a primitive equation, robust-diagnostic global ocean circulation model with 20 vertical levels and 1/2° by 1/2° degree horizontal resolution, covering a domain from 75°S to 65°N. The model is based on the Bryan-Cox model code (Bryan and Cox,1968), revised to allow arbitrary bathymetry and coastlines (Bryan, 1969), updated for vector processing (Semtner, 1974) and for supercomputers employing parallel processors (Semtner and Chervin, 1988). Figure 2.1 illustrates the major general ocean circulation development efforts which led up to this model. Further details of the historical progression of global ocean modeling are given in Semtner (1986a).

TABLE 2.1. EXPERIMENTAL SEQUENCE , AFTER SEMTNER AND CHERVIN (1988).

				Restoring Time Constant	
Phase	Integration Period, years	Wind Forcing	Horizontal Mixing	25-710 m	Deep Ocean
1	0-4	Annual mean	Laplacian	1 year	1 year
2	4-10	Annual mean	Laplacian	3 years	3 years
3	10-18	Annual mean	Laplacian	none	3 years
4	18-22.5	Annual mean	biharmonic	none	3 years
5	22.5-32.5	Monthly	biharmonic	none	3 years

This study is part of a 32.5-year simulation of the global ocean circulation. The paper deals with the results of Phase 5 of the experiment, as listed in Table 2.1. Phases 1-4 were reported by Semtner and Chervin (1988). Since this paper is dealing with the monthly

wind forcing, the year numbers referred to in this paper will apply only to Phase 5 (Year 1 is the first year of simulated monthly forcing).

The wind stress used in the model comes from the Hellerman and Rosenstein (1983) global data set. These wind stress values, defined on a grid with 2° spacing, have been interpolated to the 1/2° surface velocity grid points of the model. While Phases 1 through 4 used annual mean Hellerman and Rosenstein wind stress, in Phase 5, the data base was partitioned into mean monthly values. A smooth curve was fit to these monthly values, and divided into daily increments. During the integration, the wind stress is held constant over a three day period, at the end of which model results are archived, and a new value of wind stress is selected. Over a three-year period, each daily wind stress value is used once, and applied for three days. While the wind stress in Phase 5 has seasonal variability, it has no interannual variability. It will be shown that this lack of interannual variablity leads to some features in the model climatology which deviate from observational climatology. However, the non-linear characteristics of the model give it an inherent (but small) interannual variability.

Temperature and salinity fluxes at the surface have been parameterized by forcing the surface grid points to monthly mean Levitus (1982) values on a monthly time scale, after the method of Haney (1971). In Phase 5, the heat and salt budgets are unconstrained between 25 and 710 m, while the deep layers are restored to Levitus values on a 3-year time scale. The only Levitus forcing that occurs within the thermocline is from 55°-65°N, and from 65°-75°S, where T and S are restored to Levitus (1982) on a 3-year time scale. In this robust-diagnostic, free-thermocline strategy (Sarmiento and Bryan, 1982) , the top layer is forced with wind stress on the momentum grid points and with Levitus forcing on the T,S points, while the seasonal thermocline is completely free over most of the domain.

Since the 30 years of this study is short compared with the millenium time scale of the deep ocean, the deep layers are weakly restored to Levitus values to constrain any drift.

The 20 vertical levels in the model are stacked downward, with the local bathymetry defined by the number of boxes. The levels are unevenly spaced, with 10 levels in the upper 710 m to resolve the thermocline. Figure 2.2 illustrates the vertical arrangement of levels in the model. The spatial averaging of bathymetry required by the grid size and some simplifications in geometry have resulted in an idealized model ocean (Figure 2.3). The Red Sea, the Gulf of Aden, the Persian Gulf, the Gulf of Oman, the Andaman Sea, and the Great Bight of Australia have been filled in. In order to simplify calculations of the mass transport streamfunction (Semtner, 1986b), some major islands have been connected to continental land masses: Madagascar has been connected to Africa by filling in the Mozambique Channel. Sumatra, Java, and Borneo have been incorporated into a larger, simplified southeast Asian peninsula, and the islands of New Guinea and Tasmania have been connected to Australia. Other islands, such as Ceylon, Socotra, and the Seychelles, have been shoaled to a depth of 100 m (then subjected to nine-point smoothing), which allows their major bathymetric features to remain in place, yet eliminates the numerical need to perform a line integration around these islands (Semtner, 1986b). The bathymetry of the model is shown in Figure 2.4. While performing line integrations around every island is possible, it was considered to be too inefficient to include every island in this global circulation study. The incorporation of the free-surface effect by Killworth *et al.* (1990) requires no such line integration, and the use of an arbitrary number of islands without such computational penalty is now possible.

Although the geography has been simplified, the Indian Ocean is not constrained by any regional boundary conditions. It is free to exchange momentum, heat, and salt with the other parts of the world ocean, which are being simulated simultaneously. The transport of

warm water from the western Pacific Ocean through the Indonesian Archipelago, across the Indian Ocean, and into the Atlantic Ocean via Agulhas rings has been described for the annual forcing phases of the simulation by Semtner and Chervin (1988).

Other features of the model include a Richardson Number-dependent parameterization of vertical mixing after the method of Pacanowski and Philander (1981), and biharmonic parameterization of frictional and diffusive properties. The explicit treatment of eddies allows the amount of mixing carried out by parameterization of sub-grid scale processes to be minimized. The eddies perform the bulk of the work of mixing momentum, salt, and heat, leading to a fairly realistic representation of the global circulation.

III. WIND STRESS

It is important to understand the dynamics of the Indian Ocean in terms of seasonal variation in the wind stress; this section will review the annual cycle of Hellerman and Rosenstein (1983) wind stress in the tropical Indian Ocean of the global model. The monthly mean wind stress, which was used to force Phase 5 of the experiment, is shown in Figures 3.1-3.6. The predominant feature is the wind stress due to the southeasterly trade winds. The SE trades are very constant in azimuth throughout the year, with significant variation only in magnitude and latitudinal extent. The other major feature of the mean forcing is the southwesterly winds in the western Arabian Sea and the Bay of Bengal. These areas, however, have a large seasonal variability in both azimuth and magnitude, and it is this monsoon which is associated with the major ocean circulation changes in the Indian Ocean.

In January (Figure 3.1 (a)), northeasterly flow is prevalent in the Indian Ocean and Arabian Sea in the Northern Hemisphere, known as the Northeast Monsoon. The northeasterly flow extends to approximately 10°S in the western Indian Ocean near Madagascar. South of 10°S, the winds are from ESE in the western Indian Ocean, becoming southeasterly in the eastern Indian Ocean. These are the southeasterly trade winds. From 63°E to the eastern part of the Indian Ocean, there is a band of westerlies with a latitudinal extent of 5°, located slightly south of the equator. This band of westerlies and the southeasterly trades converge to form the Intertropical Convergence Zone (ITCZ) at 10°S. The maximum wind stress is approximately 1.3 dyn cm^{-2}, located off of the Somali Coast. In February (Figure 3.1(b)) the flow is virtually identical to January, with flow weakening in the eastern Indian Ocean.

In March, the flow is weakened in the western Indian Ocean, with the wind stress having decreased to less than 1 dyn cm^{-2}, as illustrated in Figure 3.2(a). The highest wind stresses are due to the SE trades in the eastern Indian Ocean. In the western Arabian Sea, the winds have veered, blowing towards the Gulf of Aden (toward the western boundary in the model), while the flow is northerly in the central Arabian Sea as part of a large anticyclonic flow. The climatology shows an anticyclone centered at 15°N, 87°E in the Bay of Bengal.

By April (Figure 3.2(b)) the SE trades have become stronger, penetrating as far north as the Equator in the Western Indian Ocean. The maximum wind stress is approximately 1.5 dyn cm^{-2}, and the SE trades extend further to the east. There is a southeasterly onshore flow over the Kenya/Somali coast, and the wind stress is very weak in the western Arabian Sea. A weak anticyclone is present in the central Arabian Sea, resulting in northwesterly winds alongshore at the Indian coast. The anticyclonic circulation in the Bay of Bengal has resulted in a reversal of the direction of the wind stress since January. The ITCZ (not shown) has shifted north, and the band of equatorial westerlies has also shifted north, with its direction changing from WNW to WSW. The band of westerly winds has also increased its latitudinal width to 10° (*i.e.*, between 10°S and the equator).

May is a transition month from the NE to SW monsoon regime. Figure 3.3(a) shows that the cross-equatorial flow is much stronger. The SE trades extend to the equator, then become southwesterly. The southerly onshore flow at the Kenyan coast has increased in magnitude. The weak anticyclonic flows of April in the Arabian Sea and Bay of Bengal have been replaced by a strong westerly anticyclonic flow in the Arabian Sea, and a strong westerly cyclonic flow in the Bay of Bengal. The wind stress in the western Arabian Sea has completed a 180° shift since March and increased its amplitude to a maximum of 1.3

dyn cm^{-2}. The winds in the western Indian Ocean have attained the basic pattern that they will retain throughout the oncoming SW monsoon season.

In June, the circulation pattern established in May picks up tremendous strength with the onset of the SW Monsoon, as depicted in Figure 3.3(b). Wind stresses in the western Indian Ocean have increased 2-3 dyn cm^{-2}. The onshore flow in India and southeast Asia has become much stronger. The wind stress in the western Indian Ocean approaches 4 dyn cm^{-2}. The SE trades turn and become SW at the equator in the western Indian Ocean, and at 2°S in the eastern Indian Ocean.

July (Figure 3.4(a)) is the month of the largest wind stress values of the SW Monsoon. Hellerman and Rosenstein (1983) reported that the highest wind stress in the 106-year global data set occurs in the western Indian Ocean. The wind stress at 10°N/53°E is 4.9 dyn cm^{-2}. The great intensity of the winds in this region is due to the Finlater Jet (Finlater, 1969), which causes intensification of the southerly wind flowing onshore over Kenya and Somalia. The wind stress in the western Indian Ocean has a typical increase of 1 dyn cm^{-2} from June to July.

The SE trades in the western Indian Ocean continue to increase in magnitude during August (Figure 3.4(b)), creating wind stresses of nearly 2 dyn cm^{-2}. In contrast, the southwesterly monsoon winds in the northwest Indian Ocean decrease, reducing wind stresses there by 0.5-1 dyn cm^{-2}.

September (Figure 3.5(a)) brings further weakening of the SW Monsoon, with wind stress levels decreasing by 1-2 dyn cm^{-2}. The climatological wind stress magnitudes in September are only 0.5-1 dyn cm^{2} greater than the levels in May, indicating that the SW Monsoon season is nearly over.

The October wind stress plot (Figure 3.5(b)), shows a pattern of weak wind stress in the northern Indian Ocean, indicative of transition to the NE monsoon season. While the

Arabian Sea experienced a large scale anticyclonic circulation in September, the anticyclonic flow is now weak in the western Arabian Sea, while the flow in the eastern Arabian Sea is cyclonic. Although the Bay of Bengal wind stress pattern indicates that cyclonic winds remain, the magnitude is small and there is no Burmese onshore flow as seen in September. The SE trades have typical values of 1.5 dyn cm^{-2}, weakening from the September values.

The November climatological wind stress plot (Figure 3.6(a)) illustrates that the transition to the NE Monsoon regime is complete. Northeasterly flow dominates the Bay of Bengal and the Arabian Sea, resulting in wind stresses less than 1 dyn cm^{-2}. The weakening SE trades have shifted to the east and the equatorial westerly pattern is weaker.

The December plot of wind stress (Figure 3.6(b)) is very similar to the pattern of January. There is an increase in wind stress strength to 1 dyn cm^{-2}, and the belt of westerlies has shifted south of the Equator.

IV. RESULTS

A. NEAR-SURFACE CURRENTS

1. The Seasonal Cycle

In this section, plots of the monthly mean current vectors will be discussed. The monthly mean currents are chosen to illustrate the seasonal cycle of the SCM in the Indian Ocean, forced by the Hellerman and Rosenstein (1983) winds. Before the monthly mean currents are reviewed, several points should be emphasized. First, the lack of interannual variability in the wind stress causes the monthly mean currents (and many other mean fields) to be very similar from year to year. However, the eddy fields do vary considerably from year to year, as illustrated by Figure 4.1. Figure 4.1 (a) shows the instantaneous vector field at 37.5 m in the western Indian Ocean on January 15 of Year 4, and Figure 4.1 (b) shows the same field on January 16 of Year 5 (January 15 was not archived that year). The eddy activity of the model is the most striking feature of these plots, and there is considerable variation in the eddy fields between the two years shown. In the monthly mean vector plots (January of Year 4 is shown in Figure 4.2; Year 5 is not shown) , the averaging of the eddies creates a "patchiness", and the geostrophic currents are the dominant feature. While differences can be seen in the monthly mean vector plots from year to year, the changes are minor, and the Year 4 monthly mean plots presented below are considered to be a representative sample of the multiple year simulation. Figure 4.1 also illustrates that, as expected, the instantaneous currents throughout the basin are more vigorous than the mean flows depicted below.

The monthly mean near-surface (37.5 m depth) geostrophic currents in the Indian Ocean basin of Year 4 of the simulation are shown in Figures 4.2-4.13. (Since the

upper grid boxes are 25 m thick each, the Ekman effects are largely confined to the top layer (not shown)). In January, Figure 4.2 shows the South Equatorial Current (SEC) flowing westward at approximately 15°S in response to the forcing of the SE trades. It turns south at the east coast of Africa to feed the Agulhas Current, and north to feed the Equatorial Countercurrent (ECC). The NE Monsoon forces the westward-flowing North Equatorial Current (NEC) from 2°S to 8°N. It turns south at the African coast to join the SEC, becoming source waters for the ECC. The NE Monsoon turns at the equator to form a band of equatorial westerlies, which provide the continued forcing for the ECC as it transits the entire basin between 3°S and 7°S.

In February (Figure 4.3), the NEC attains its greatest strength, achieving westward velocities as high as 68 cm s^{-1}. By March (Figure 4.4), with the reduced wind stress from the waning NE Monsoon, velocities are reduced throughout the NEC, the reduced wind stress in the eastern Indian Ocean causes the NEC to retreat to the west. As the NEC weakens, the ECC becomes more concentrated as its southern bound moves from 7°S to 5°S in response to the south equatorial westerly trades shifting farther to the north.

In April (Figure 4.5), although westward wind stress is no longer available to drive the NEC, the NEC continues to exist as a weak westward countercurrent south of India throughout the SW monsoon. The ECC in April becomes a meandering flow between 5°S and the equator in the western Indian Ocean, splitting into two jets at 75°E. One jet remains at the equator, in the region of eastward wind stress where the Wyrtki jet forms in May, and the other at 5°S, in the region of the doldrums between the SE trades and the equatorial westerlies. This branching of the eastward flow south of the equator persists throughout the southwest monsoon period until the ECC is re-established in December. The eastward flow at 5°S, characterized as the ECC during the NE monsoon, remains a distinct jet during the SW monsoon, however, during the SW monsoon period it

is no longer a countercurrent, and is considered part of the SW Monsoon Current. The southwesterly flow along the Somali coast has minimal velocities in April, as expected in a region of weak wind stress.

The rapid onset of the SW Monsoon in late May causes the climatological monthly mean wind stress in May to be northeastward along the Somali coast, resulting in a reversal of the Somali Current (Figure 4.6). The eastward flow has formed an equatorial surface jet (Wyrtki jet), and is confined between 3°N and 3°S. The core of the jet attains an eastward velocity in excess of 1 m/s between 60°E and 80°E. A weak eastward circulation remains in the equatorial trough at 5°S.

By June, the eastward-flowing SW Monsoon Current (SMC) is established at 5°N (Figure 4.7). Increased solar insolation in the Northern Hemisphere causes the ITCZ to move northward in the summer hemisphere, and the equatorial trough in the winter hemisphere moves equatorward. As a result, the region of maximum eastward wind stress migrates northward, and the doldrums move closer to the equator. Although the eastward component of wind stress at the equator has increased to the west of 60°E, it decreases between 60°E and 80°E, as shown in Figure 3.3. This results in a weakening of the equatorial jet, which reached a maximum in May, and the subsequent intensification of the SMC. The Somali Current has strengthened under the increased wind stress, forming a western boundary current which extends as a strong jet to 8°N, where it recirculates southward to feed the SMC and the equatorial surface jet. The current recirculates southward in several sections, with branching at 4°, 6°, and 8°N. The branch at 4°N forms part of an anticyclonic gyre, extending to the Equator, known as the Southern Gyre.

In July (Figure 4.8) there is continued weakening of the equatorial surface jet, and strengthening of the SMC. The former equatorial surface jet has moved south into the doldrums, while a westward countercurrent has developed at 2°N, between the two

eastward currents. The appearance of the countercurrent is due to surfacing of a westward deep level current (the deeper currents will be discussed separately in sections B and C of this chapter). Under the influence of continued strengthening zonal wind stress, the SMC no longer branches off from the equatorial jet, but is fed from the Somali Current recirculation, and becomes visible as a distinct jet at approximately 70°E. Its greatest strength occurs at 82°E, where the core of the jet attains a velocity of 80 cm s^{-1}. In the month of the highest wind stress in the western Indian Ocean, the Somali Current also reaches its highest velocity of 201 cm s^{-1}. The Somali Current continues to be a one-gyre system, with the Southern Gyre centered at approximately 3°N. The broad offshore branching of the Somali Current extends from 4°N to 12°N. Despite the strong wind stress throughout the Arabian Sea and the Bay of Bengal, the circulation in these basins remains generally weak.

By August (Figure 4.9) the broad northern segment of the Somali Current offshore flow has developed into a second gyre. This northern gyre, known as the Great Whirl, is centered at 10°N, while the Southern Gyre remains centered at 3°N. The former equatorial surface jet may again be referred to as the Equatorial Countercurrent, since it is again flowing eastward, at 3°S, in an opposite direction to the zonal wind stress throughout most of the basin. The SMC has weakened in its peak intensity in response to the reduced wind stress during August, yet it becomes organized into a coherent jet slightly farther to the west, at 65°E. The transitory westward countercurrent which appeared in July at 2°N is no longer visible at the 37.5 m level.

Increased equatorial zonal wind stress in the eastern Indian Ocean in September results in a southern branching of the SMC, forming a jet just to the north of the equator (Figure 4.10). This jet peaks at 76 cm s^{-1} at a longitude of 87°E. As the equatorial trough moves southward, this jet will reform the Wyrtki surface equatorial jet. The ECC is

present in the doldrums at 4°S, extending across most of the ocean basin. In the Somali Current region, the Great Whirl has moved northward to 12°N, while the Southern Gyre has developed into two anticyclonic circulations. One of these gyres is centered at 3°N, at the August position of the Southern Gyre, and the other one has formed at 6°N from the broad offshore flow of the Southern Gyre. An anticyclonic gyre has formed to the northeast of the Great Whirl, at 13°N/58°E. This gyre is the model analog of the Socotra Eddy.

In October (Figure 4.11), with alongshore transport by the Somali Current greatly diminished, the zonal currents in the western Indian Ocean are more clearly organized. October, like May, is a month of relative maximum wind stress at the equator The Wyrtki jet no longer appears as a southern branching of the SW Monsoon Current, but is a continuous zonal jet from the Somali Current region to the eastern end of the basin. It attains a maximum velocity of 81 cm s^{-1} at 84°E, with the core of the jet at 1°N. This corresponds to the region of highest zonal wind stress. The Great Whirl is located at 12°N, while the two gyres to the south are located at 4°N and 7°N. These southern gyres are substantially weaker than they were in September.

In November (Figure 4.12), there are two anticyclonic gyres visible at 10°N and 14°N, which are remnants of the Great Whirl and the Socotra Eddy. The zonal current at the equator attains a semiannual maximum in November, as the Wyrtki jet is centered on the equator. It attains a maximum velocity of 75 cm s^{-1} at 83°E.

During December (Figure 4.13) the Great Whirl continues to diminish, the surface equatorial jet loses strength, and the ECC reorganizes. As a result, the model Indian Ocean circulation returns to the basic pattern it had in January (Figure 4.2).

2. The Wyrtki Jet

As first described by Wyrtki (1973), a semiannual surface equatorial jet appears in the Indian Ocean during periods of maximum zonal wind stress. This relationship can be clearly seen in the longitude-time plots of Figure 4.14. Figure 4.14 (a) shows relative maxima in the magnitude and zonal extent of the zonal wind stress in the months of May and October, related to the seasonal migration of the ITCZ. (Another zonal maximum is visible in the western Indian Ocean in June and July, related to the Finlater Jet.) Figure 4.14 (b) shows the vertical integral of the zonal current at the equator in the top two levels of the model (12.5 and 37.5 m). It shows eastward currents with maxima in May and November, in response to the periods of maximum zonal wind stress.

Figure 4.15 (Reverdin (1987), after Cutler and Swallow (1984)) shows that observations of zonal equatorial currents, derived from ship drift reports in the Indian Ocean, show equal strengths of the two Wyrtki Jets (the time scale is reversed from that presented in Figure 4.14), whereas the SCM has the May jet (113 cm s^{-1}) stronger than the November jet (72 cm s^{-1}). Similar results have been obtained in the Geopyhysical Fluid Dynamics Laboratory (GFDL) of Princeton University regional simulation of the Indian Ocean, which also uses Hellerman and Rosenstein (1983) winds. (F. Schott, personal communication). (Figure 4.15 also shows the good agreement of the strength of the model NEC (68 cm s^{-1}) with the ship drift reports (>60 cm s^{-1}). Overall, as shown in Figures 4.14 and 4.15, there is good agreement in the timing and strength of the SCM surface equatorial currents with observations.)

B. THE EQUATORIAL UNDERCURRENT

The subsurface velocity structure in the tropical Indian Ocean has not been well-sampled spatially or temporally. Studies of the area have shown a great deal of variability and a high degree of baroclinicity in the subsurface flow. Due to the variability of the

monsoon forcing, the Equatorial Undercurrent (EUC) in the Indian Ocean displays much more variability than its counterparts, the Cromwell Current and the Lomonosov Current in the Pacific and Atlantic oceans, respectively. The "equatorial undercurrents" are described as thin, equatorially-trapped eastward jets, which are located beneath strong, westward-flowing equatorial surface flows. The eastward-flowing EUC has been observed to exist in the Indian Ocean during January through April, extending from 50°E to 90°E. Khanaichenko (1974) cites mass transports ranging from 11 to 40 Sv, with a mean of 26 Sv.

The SCM Year 4 zonal current velocity at the equator was averaged between 117.5 and 160 m depth, and its longitude-time dependence is shown in Figure 4.16. The eastward EUC is visible from January to April, attaining a peak zonal velocity of 62 cm s^{-1} at 80°E during March. Kort (1977) reported that observations of the EUC at 64.5°E revealed a peak velocity of 64 cm s^{-1} at 100 m depth on 18 March, 1974, while the SCM output on the tape archived at 19 March of Year 4 shows a peak at 57 cm s^{-1} at a depth of 117 m. Mass transports of the EUC at 80°E in Year 4 range from 19-31 Sv. Leetmaa and Stommel (1980) took measurements of the EUC at 55.5°E, and found that at the end of the northeast monsoon, the EUC shifts southward to merge with the ECC; in contrast, the SCM shows that the EUC moves upward and merges with the northward-migrating ECC.

A period of westward velocities is seen in Figure 4.16 during the months of June through August. Several authors have reported westward velocities at this level during the southwest monsoon, including the studies of Knox (1976), Luyten and Swallow(1976), Luyten (1981,1982), Polonskiy and Shapiro (1983), Ponte and Luyten (1990). Knox (1976) reported that the westward undercurrent was observed following the semiannual eastward Wyrtki jets, as a possible relaxation of water "piled up" in the eastern basin by the Wyrtki jets. The SCM shows a westward undercurrent following only the May Wyrtki Jet.

One possible reason that the model shows only one period of the westward undercurrent is because the SCM Wyrtki jet in November is much weaker than the May jet (Figure 4.14) while the ship drift observations (Figure 4.15) indicate Wyrtki jets of equal strength.

The seasonal cycle of the vertical structure of the zonal currents at the equator during Year 4 is shown in Figures 4.17-4.28. Figures 4.17-4.22 show the zonal current velocity along the equator from 0-610 m, while Figures 4.23-4.28 illustrate the zonal currents in a cross section at 80°E, from 20°S-20°N. The time sequence of Figures 4.17-4.22 shows the eastward EUC beneath the NEC during the SE Monsoon, and merging of the EUC with the Wyrtki jet in April (Figure 4.18 (b)) and May (Figure 4.19(a)). The westward undercurrent is shown during the boreal summer, and the semiannual Wyrtki jet is visible again in October (Figure 4.21 (b)). Figures 4.23-4.28 illustrate the same features of the seasonal cycle, yet show off-equatorial features as well. The appearance of the westward countercurrent at 3°N in July (Figure 4.26 (a)) is shown to be a surfacing of the westward undercurrent. The synoptic structure throughout the basin can be seen in Figures 4.29 and 4.30, which show meridional sections at 60°E, 70°E, 80°E, and 90°E for the months of February and July in Year 4. Leetmaa and Stommel (1980) studied the EUC at 55.5°E, and found that at the end of the northeast monsoon, the EUC shifts southward to merge with the ECC, but the SCM shows the EUC moves upward and merges with the Wyrtki jet (see Page 20 also). Figure 4.31 is a vector plot of the instantaneous currents at 117.5 m, archived on March 10 of Year 4. It clearly shows the EUC spanning the entire basin, and the eddy-resolving nature of the model is apparent. The eastward flow of the ECC can be seen to the south of the EUC.

C. DEEP CURRENTS

The seasonal variability of the EUC and baroclinic structure of the equatorial Indian Ocean, along with a sparse set of observations, have made it very difficult for

oceanographers to come up with a comprehensive picture of the flow in even the shallowest subsurface layers. The model exhibits the same type of complex vertical structure that the observations (Knox (1976), Luyten and Swallow(1976), Luyten (1981,1982), Polonskiy and Shapiro (1983), Ponte and Luyten (1990)) suggest, as shown in Figure 4.32, a cross section from 3°S to 3°N. Taken in March, when the EUC is at its peak strength, the plot indicates cores of westward flow near the surface and at 435 m depth, while separate eastward cores are visible at 117 m, 1160 m, and 3575 m depth. Analysis of time sequences of zonal current plots indicate that an upward phase propagation of the zonal currents takes place in the equatorial region. However, O'Neill and Luyten (1984) reported that acoustic dropsonde observations of the equatorial Indian Ocean at 53°E do not yield evidence of vertical phase propagation of the zonal currents. McCreary (1987) reported model results which suggested that the interaction between deep mean currents and near-resonant Kelvin waves can account for much of the observed deep jet structure without vertical phase propagation. However, the theory of deep jet dynamics remains incomplete; McCreary (1987) reported that while the model reproduced the deep current structure well, the near-surface flux field was unrealistic. Further observational and theoretical work is required to suggest changes to the SCM which would more accurately represent the dynamics of the deep jet structure.

The currents at 4125 m during June of Year 4 are illustrated in Figure 4.33. The model domain at this level shows the various deep basins in the Indian Ocean: the Arabian Basin, the Somali/Mascarene Basin, and the Madagascar Basin in the western Indian Ocean, and the Mid-Indian Basin and Wharton Basin, separated by the Ninety East Ridge. A series of deep eddies are visible, as is the tendency of the currents to form western boundary currents. A series of strong, anomalous currents is seen at approximately 123°E, in the Celebes Sea, where anomalous data in the Levitus (1982) data base was revealed by

the model. The temperatures at this depth are 5-10°C too high, causing the model to respond to the anomalous gradients by creating currents which are too strong. (This example of the model revealing bad data in the Levitus data base suggests that the model may be able to point out more subtle deficiencies in the global observational data bases.)

The complexity of the subsurface currents in the Indian Ocean is further demonstrated in Figure 4.34, illustrating the longitude-time dependence of the zonal velocity at 435 m depth. This figure shows a pattern of convergence and divergence, which travels westward at approximately 25-35 cm s^{-1}. This pattern of convergence and divergence is visible also in Figure 4.35, a plot of monthly mean current vectors at the 435 m level during March of Year 4. The westward movement suggests another interpretation to the upward phase propagation of the zonal velocity in the model. Figures 4.17-4.22 show that the zonal jets tilt upward from west to east; westward propagation of such a tilted feature would also create an upward phase propagation at a fixed point on the equator. The source of the tilt of the jets in the model is unclear; it is not visible in the deep thermal structure, which suggests that the distribution of vertical velocity may play a role.

D. THE LEEUWIN CURRENT

The western coast of Australia is another unique region of the Indian Ocean. While most eastern boundary surface currents are the equatorward portions of the subtropical gyres, the Leeuwin Current is a poleward-flowing (southward) eastern boundary current. The poleward Leeuwin Current forms in the austral autumn and winter, flowing along the edge of the continental shelf, eventually extending around the Great Australian Bight. The Leeuwin Current has only recently been documented, in part because it is a very narrow current, sometimes less than 30 km wide. The Leeuwin Current is also quite notable for moving at significant speeds (maximum approximately 1.8 m s^{-1}), in opposition to the prevailing wind stress. Recent observational, modeling, and theoretical studies of the

Leeuwin Current have been summarized in Church *et al.* (1989) and Weaver and Middleton (1989). The prevailing theory, as espoused by Thompson (1984) and Godfrey and Ridgway (1985), is that the Leeuwin Current is driven by large alongshore steric height gradients. Weaver and Middleton (1989) and Batteen and Rutherford (1990) demonstrated that the Leeuwin Current could be modeled by primitive equation models, using climatological winds, and without resolution of the continental shelf. Since these modeling studies employed much finer horizontal grid resolution than the SCM, the ability of the model to resolve Leeuwin Current features was a matter of some interest. Although the SCM cannot resolve the Leeuwin Current to the level of the observations and local modeling studies, it does demonstrate many of the seasonal features of the Leeuwin Current. However, the current is marginally resolved, and suggests that operation of the model at 1/4° horizontal resolution will result in a more accurate representation of the structure of the Leeuwin Current.

The monthly (Year 4 data) averaged vector and temperature plots of Figures 4.36 through 4.47 illustrate the seasonal cycle of the Leeuwin Current. The vector plots show eastward geostrophic currents, turning poleward at the Australian continental shelf. During the austral summer, the eastward flow turns poleward when it meets the shelf at 29°-31°S. Church *et al.* (1989) describes it as a northeastward flow, turning poleward near the shelf at 29°-31°S. The Leeuwin Current is visible in austral fall and winter, as the eastward flow turns poleward over a wider range of latitudes, and is augmented by strong flow from the northwest shelf. Figures 4.37-4.40 show the development of this southwest flow on the northwest shelf from February to June. During the same period, the Leeuwin Current progresses further around Cape Leeuwin each month, creating an eastward flow along the southern Australian coast . The series of plots shows an eastward flow along the northwest shelf from July through December, as well as re-establishment of westward flow

along the southern coast of Australia. The plots of the temperature field also show features described by Church *et al.*: high temperature (>25°C) waters spread south of 20°S in austral autumn and winter, and the Leeuwin Current holds the SST at 32°S above 22°C until after June. However, the plots do not show 20°-22°C water carried north to 25°S in summer as described by Church *et al.*, they show 22°-23°C water at this latitude in December, January, and February. Plots of the salinity field (not shown) also depict features described by Church *et al.*: low salinity (<35 psu) waters spreading south of 20°S in autumn and winter. However, there were differences in the salinity fields as well. The salinity at 32°S in the model in June was 35.6; Church *et al.* describes winter salinity at this latitude as 32.2-32.4.

Additionally, cross sections were plotted to simulate the Leeuwin Current Interdisciplinary Experiment (LUCIE) sections depicted in the study of Church *et al.* (1989). Sample comparisons are shown in Figure 4.48 for the Dongara (30°S) LUCIE sections. Figure 4.41 (a) shows the LUCIE September 1986-February 1987 mean alongshore currents for the Dongara section, and Figure 4.48 (b) shows the corresponding model section of v velocity during January, Year 4. The LUCIE current section depicts mean southward flow (20 cm s^{-1}) at the 300 m isobath, and mean northward flow of 15 cm s^{-1} at 500 m. The model shows upper level southward flow of 5 cm s^{-1}, and a northward flow of 9 cm s^{-1} at 310 m. The temperature fields of June are compared in Figures 4.48 (c) and (d). The model section shows downward bending of the isotherms at the coast, but less intense than the LUCIE section. The 20°C isotherm matches well; however, the 21°C isotherm does not.

E. SURFACE HEAT FLUX

One of the difficulties in designing a global ocean circulation model is that the investigator must prescribe the heat flux consistently throughout the domain, in a manner

which is consistent with climatology. Unfortunately, there are no suitable global climatologies of heat flux. The method used to parameterize surface heat flux in the SCM (Semtner and Chervin (1988)) is adapted after the method of Haney (1971). Rather than explicitly prescribing either the sea surface temperature or the surface heat flux, a suitable climatological temperature (in this case the Levitus (1982) monthly mean temperature at 12.5 m for a given grid point) is used as a set point in a negative feedback loop control system. At each time step of the integration, if the model temperature is colder (warmer) than climatology at a given point, then it is warmed (cooled) at a prescribed rate. The Levitus (1982) data base was the only climatology suitable for this approach, because it is global in scope, available at multiple levels , and seasonal. The model incorporates a forcing term which applies this virtual heat flux toward the Levitus (1982) values on a monthly time scale. The form of the term, applied to the top temperature grid point (12.5 m) at every time step, is approximately

$$\frac{\partial T}{\partial t} = \ldots + \frac{T_{Levitus} - T_{Model}}{30 \text{ days}} \qquad (1)$$

The parameterization of the complex heat budget by such a simplified approach warrants some investigation. Comparison of the Levitus surface thermal forcing with the available regional climatologies of heat fluxes demonstrates that the Haney method parameterizes the surface heat fluxes adequately in the Indian Ocean basin. Figure 4.49 illustrates the surface heat fluxes calculated from the Cooperative Ocean-Atmosphere Data Set (COADS) by Rao et. al. (1989) for the months of January, April, July, and October. Figure 4.50 shows the fluxes calculated in the Hastenrath and Lamb (1979) atlas for the same months, and the model's surface heat flux due to Levitus temperature forcing in Year 7 is portrayed in Figure 4.51. The model matches the Hastenrath and Lamb (1979) climatology better than the Rao climatology. This may be due to the much longer time

spans of the Levitus (1982) data base (1900-1978) and the National Climatic Center data (1911-1970) from which the Hastenrath and Lamb (1979) flux calculations were derived, compared with the COADS data (1950-1979) that Rao *et al.* (1989) used.

In general, the SCM heats and cools the Indian Ocean in the proper regions, although the magnitudes of the heat flux show some variation from the climatology. The model heats the Arabian Sea and Bay of Bengal in April much less than the heating of the ocean depicted by the climatologies. The model consistently shows strong heating just south of Madagascar. One other area where the model shows much stronger forcing than in the climatology is along the African coast in July. The model has a maximum heating of the ocean of over 450 w m^{-2}, while the climatologies (with heavy spatial averaging and sparse sampling) only show up to 160 w m^{-2} in this area. The mean monthly plots of Figure 4.51 show the contrast between the complex heat flux allowed by the model during a given month and the temporally/spatially-smoothed climatologies. The Levitus forcing also illustrates the freedom that the top level of the model has to depart from the climatology.

The Levitus forcing (Figure 4.52), when compared with plots of vertical velocity (Figure 4.52), allows us to qualitatively assess the effects of upwelling and thermal advection on the Levitus forcing. As an example, areas of strong heat flux into the ocean are visible in the Somali Current region in July, while strong upwelling is confined to a smaller region along the Somali Coast. The advection of the cold, upwelled water accounts for the remaining area of strong heat flux into the Arabian Sea. During the months of December through April, the maximum intensity of surface thermal forcing in the model is at the southern coast of Madagascar; this "cold spot" is a numerical artifact due to divergence, and illustrates that the heat flux maps, combined with upwelling and advection assessments, may be used to help identify such anomalies in the model.

F. THE SOMALI CURRENT SYSTEM

The Somali Current forms a two-gyre system in the model, as described previously. A series of instantaneous plots of the Somali Current at 37.5 m is shown in Figure 4.53. This series, covering the period from June 2 through August 16 of Year 4, shows how the Southern Gyre is formed at approximately 2-3°N, and remains there, while the Great Whirl is centered at 8°N on July 14, and has moved north to 10° by August 16. The Great Whirl continues to move northward, but moves farther northward than shown by observations, because of the bathymetric simplifications of the model (J. O'Brien, personal communication). The island of Socotra has been shoaled, and the Gulf of Aden filled in, which both play an important role by the time the Great Whirl passes Cape Guardafui at the tip of Somalia. Figure 4.54 illustrates the classical connection between the wind stress along the Somali coast, surface currents turning offshore, upwelling, and associated cold temperatures. The upwelled temperatures are as cold as 14°C in the mean monthly plots.

The lack of interannual variability in the Hellerman and Rosenstein (1983) wind stress creates a Somali Current gyre system which forms in a consistent manner throughout the simulation, while observations have noted considerable variation in the development and propagation of the two-gyre system, due to variability in the winds from year to year. The lack of interannual variability in the wind forcing in the model leads to a lack of temporal and spatial variability in the upwelling regions along the Somali coast. Hence, along the east African coast during the summer, the model climatology has colder temperatures than indicated in the climatological fields. Furthermore, as reported by Jensen (1989), the forcing of the Somali Current by Hellerman and Rosenstein (1983) wind stress results in the less-common situation where the Southern Gyre does not move northward and coalesce with the Great Whirl. Simulations of the more common situation where the two gyres coalesce have been performed by Luther and O'Brien (1985), using seasonal wind stress

derived from the National Climate Center Global Marine Sums (TD-9757) data set, which has climatological winds on a 1° grid, instead of the 2° grid of the Hellerman and Rosenstein (1983) wind stress used by the Semtner and Chervin model. Luther and O'Brien's (1989) continuous interannual simulation of the Indian Ocean, which used Cadet and Diehl's (1984) 23-year series of observed winds, was divided into 14 years where the two gyres coalesced, 7 years where the Southern Gyre did not move to the north, and 2 years without a two-gyre system. The output of the Semtner and Chervin model forced by Hellerman and Rosenstein (1983) wind stress in the tropical Indian Ocean is encouraging, and indicates that the model climatology may be made more realistic (particularly in the Somali Current region) by incorporating interannual variability into the wind stress. Unfortunately, a suitable global set of multiyear observations is not yet available.

The Somali Current in the model attains velocities as high as 2 m s^{-1}, which are lower than the highest observed currents of approximately 3.5 m s^{-1}, although this should be expected due to the climatological wind stress and the horizontal resolution of the current. One of the difficulties in analyzing the Somali Current of the SCM is that the software tools do not allow sections to be taken perpendicular to the coast; only zonal or meridional cross-sections may be used to assess the Somali Current. It is common practice for the observations to be taken in an alongshore/offshore plane, so direct comparison is difficult. Quadfasel and Schott (1983) presented historical surface current data at 5°N along the Somali Coast (Figure 4.55); accompanying SCM values of mean monthly v velocity are presented for comparison. Cross-sections of v were taken at 5°N/48°E-52°E, and maximum values of the prevailing current tabulated for the monthly mean tapes of Year 4. These values show strong similarity in the development of the strength of the Somali Current in the model with averaged observations.

The Somali Current is known to extend barotropically to great depths during the SW monsoon, yet a southward-flowing undercurrent has been documented during the spring transition and in the late summer.(Leetmaa (1982), Schott and Quadfasel (1982), Quadfasel and Schott (1983), Schott (1983)). During the northeast monsoon, there is no southward under(counter)current, since the flow is southwestward at the surface and at deeper levels. Cross-sections of v velocity at 5°N and vector plots at various levels have been used to analyze whether the SCM represents these subsurface flows correctly along the step-like model continental outline. Leetmaa *et al.*(1982) presented cross-sections of alongshore flow at 5°N, as shown in Figure 4.56 (a) for 16-17 May 1979. A cross section of v velocity (5°N/48°-53°E) from the SCM monthly mean tape of May, Year 4 is presented for comparison in Figure 4.56 (b). Although the monthly mean currents in the model are weaker, the structure is similar, and the southward-flowing undercurrent is present at the proper depth with the core at the proper level. Plots similar to Figure 4.56 (b) indicate that the SCM has southward flow at the surface during the months of November through February, and northward flow with deep southward undercurrents during March, April, and May. The SCM deep northward-flowing Somali Current has no undercurrent from June through August, but in September and October a deep undercurrent is present. Vector plots give additional insight into the behavior of the undercurrent in the model. Year 4 instantaneous vector plots at 37.5 m, 222.5 m, and 435.0 m along the African coast are presented in Figures 4.57, 4.58, and 4.59, depicting the flow on May 15, July 14, and October 15, respectively. Observations have reported that the undercurrent tends to turn offshore between 3-5°N, while the undercurrents in the SCM show more complicated flow patterns.

G. THROUGHFLOW IN THE INDONESIAN ARCHIPELAGO

A key test of any global ocean model is its ability to accurately simulate the interaction between ocean basins. Although the SCM has some limitations in this respect, such as the lack of interaction with the Arctic Ocean, it does allow flow between the Pacific and Indian Oceans. The model domain includes a channel between the Asian continent and Australia/New Guinea (Fig. 2.4). The SCM has submerged some islands, and incorporated others into the Asian landmass, but the Java Trench and adjacent continental shelves do allow significant transport. A net transport from the Pacific Ocean into the Indian Ocean is known to occur through the Indonesian archipelago.

As Semtner and Chervin (1988) described, the flow of warm Pacific waters into the Indian Ocean through the Indonesian archipelago is vital to the heat transport across the Indian Ocean and into the Atlantic. The mass transport into the Indian Ocean may play a part in the flow of the SEC, West Australian Current, and in the Leeuwin Current (Godfrey and Golding (1981), Godfrey and Ridgway(1985),Kundu and McCreary (1986), Weaver and Middleton (1989)). Interannual variability in the flow from the Pacific into the Indian Ocean may be associated with the El Niño Southern Oscillation (White *et al.* (1985), Nicholls (1984)).

Despite the importance of the flow between the Pacific and Indian Oceans, the throughflow and its interannual variability have not been well-observed. Estimates inferred from observations include 5 Sv by Fine (1985) and 8.5 Sv by Gordon (1986). Estimates from numerical modeling studies range from 7 Sv, by Kindle *et al.* (1987), to Godfrey's (1989) estimate of 16±4 Sv. Godfrey (1989) argued that the actual throughflow must be closer to 16 Sv than to 0 Sv by modeling Indian Ocean steric heights with no throughflow, and showing that the resulting steric height gradients show a much poorer match to observations than the model output with 16 Sv throughflow. Semtner and Chervin (1988)

reported a throughflow into the Indian Ocean of 15-18 Sv. The throughflow in the SCM agrees well with the results of the annual forcing phase of the experiment. Mean monthly mass transport calculations at 117.5°E from 5 years of the seasonal forcing are presented in Table 4.1 . The mean annual westward throughflow is 17.74 Sv.

TABLE 4.1. MEAN WESTWARD MASS TRANSPORT IN THE INDONESIAN ARCHIPELAGO.

Month	Net Westward Transport (Sv)	Standard Deviation (Sv)
January	15.96	.94
February	18.74	.70
March	20.66	.80
April	21.28	.38
May	18.20	1.02
June	18.64	.29
July	17.72	.72
August	16.08	.79
September	16.72	.51
October	16.94	.32
November	16.22	.55
December	15.70	.88

These results are illustrated in Figures 4.60 and 4.61. Figure 4.60 shows the monthly mean westward, eastward, and net westward transport for the five-year time series. The eastward and westward transports are highly correlated because strengthening of the westward-flowing Pacific North Equatorial Current, which turns south at the western boundary of the basin, results in strengthening of eastward-flowing countercurrents. Furthermore, any eddies in the section will contribute equally to an increase in eastward and westward flows. Figure 4.61 shows the five years of monthly net westward transport overlaid on the mean net westward transport. The interannual variability of the monthly mean mass transports in the presence of interannually-invariant wind forcing is shown, and the seasonal cycle of mass transport is well-defined. Figure 4.62 shows the bathymetry and typical zonal transport across the sections at 117.5°E.

V. DISCUSSION AND CONCLUSIONS

A. MODEL TEMPERATURE VS. CLIMATOLOGY

If the goal of a model is to simulate the ocean as accurately as possible, then the model should exhibit a realistic climatology. In the case of the SCM, the question is whether the inputs of the Levitus (T,S) and Hellerman and Rosenstein (wind stress) climatologies result in a model which reproduces the Levitus (1982) climatology. For a complete analysis of the SCM climatology, averages of individual months over multiple years are necessary, but these products have not yet been compiled. However, the amount of inherent interannual variability of the SCM is small, and the fields contoured from January of one year look very similar to January of any year, due to the lack of interannual variability in the Hellerman and Rosenstein wind stress. As described previously, the eddy fields are unique for each year, mixing heat, momentum, and salt, yet the mean monthly results are quite similar from year to year Significant comparisons can be made between the SCM mean monthly temperature plots and climatology. Comparisons of monthly mean 12.5 m T in Year 7 are shown with the Hastenrath and Lamb (1979) sea surface temperatures in Figures 5.1-5.12.

Overall, the robust-diagnostic, free-thermocline strategy does not constrain the Semtner and Chervin (1988) model so severely that it must diagnostically reproduce the Levitus (1982) climatology of T (or S), but allows a prognostic solution in accordance with the applied wind stress, where advection, upwelling, and the mixing effects of eddies may dominate the solution at any given grid point. The primitive equation global ocean model responds to the seasonal forcing with a realistic simulation of the circulation, and produces

a model climatology which is in good agreement with the historical data bases of observations in the tropical Indian Ocean.

There are differences between the observed and model climatologies which illustrate deficiencies not only in the model, but also in the climatological data base, both of which must be overcome to enable long-term studies of climatic trends. The observations of the Somali Current are inadequate, and result in temporal and spatial averaging of the climatological data in the region which is inadequate for the intensity and interannual variability of the current. The lack of interannual variability in the Hellerman and Rosenstein (1983) wind stress creates deviations from climatology in the Somali Current region, due to the formation of upwelling zones in the same place every year, and no northward movement of the Southern Gyre. Figure 5.7 shows that along the Somali coast in July, the temperatures get as low as 13°C, yet the climatology shows isotherms only as low as 22°C. While multiyear averages would smooth some of the isotherms, there would still remain a strong packing of the isotherms along the Somali coast in the model that would be significantly cooler than the 22° isotherm. There are some further improvements to the model climatology available from increased resolution, such as correction of the packing of isotherms into the "stairstep" shelf contours along the Somali coast.

B. COMPARISON WITH CURRENT DRIFTER STUDIES

The SCM produces a vast amount of archived data, and the vector plots generated from this data reveal the synoptic picture of the currents in the Indian Ocean as the seasonal cycle progresses. The realistic circulation of the SCM is strikingly apparent when compared with studies of drifting surface buoys in the Indian Ocean. Molinari *et al.* (1990) described the current distributions derived from surface buoy trajectories in the tropical Indian Ocean, analyzing buoys deployed between 1975 and 1987. Qualitative comparisons were made of the figures and descriptions of Molinari *et al.* (1990) with the

SCM output. Although a direct comparison of the data sets to generate difference plots could prove informative, it was beyond the scope of this study, and must be considered for future work. The SCM results matched the descriptions of the surface circulation patterns by Molinari *et al.* quite closely, and monthly average current vectors derived from the buoys are shown as Figures 5.13 -5.16, for comparison with the 37.5 m vector plots of Figures 4.1-4.6. During the boreal winter, the SCM does not have the strong eastern boundary current shown by buoy trajectories along Indonesia, between 5°S and 10°S. In the Bay of Bengal, the model shows a separation of the western boundary current during boreal winter at approximately 17°N, approximating the separation at 19°N described by the buoy trajectories. The buoy average velocities in March show a meandering of the ECC in the western Indian Ocean at 5°S, a feature that is closely duplicated in the model vector plot of Figure 4.4.

C. MASS TRANSPORTS

Monthly mean zonal mass transports for the major equatorial currents have been calculated for Year 4 at four longitudes: 60°,70°,80°, and 90°E. In taking on such a task in the Indian Ocean, there were several arbitrary definitions made. Undercurrents with closed subsurface isotachs were segregated from the mass transport calculations of the surface currents as much as possible, and surface currents were calculated only as deep as 610m. The EUC was considered to be the eastward flowing undercurrent during the months when it could be distinguished from the ECC. In May, it had surfaced to be included with the ECC. Although an eastward current occurs throughout the year at approximately 5°S, it was not calculated as an explicit current. The eastward-flowing ECC was defined to exist at a given longitude from the time when it could be distinguished from the waning SMC and Wyrtki jet in December or January, through the end of May, when it was included with the SMC (as it could no longer be considered a countercurrent). The SEC was defined

throughout the year, and was, with few exceptions, the equatorial current with the greatest mass transport. Surprisingly, the NEC and the westward flow which remained to the south of India during the SW monsoon could be calculated as a current throughout the year. The results of these arbitrary definitions and calculations are shown in Figures 5.17-5.22.

The zonal mass transports are illustrated in Figures 5.17-5.20, while the variation of mass transport with longitude is shown for the months of February (Figure 5.21) and July (Figure 5.22). Several trends are evident from these figures. First, the EUC achieved its highest mass transport at 70°E, and weakest at 90°E. It peaked in March, except at 90°E, where the maximum zonal mass transport occurred in February. The inclusion of the surfaced EUC with ECC calculations in May, combined with the Wyrtki jet, resulted in a peak in the ECC in May, except at 90°E, where it peaked in April. June was the strongest month for the SMC because the Wyrtki jet was included, thereafter showing a general decline as a result of the waning of the Wyrtki jet, and increased northward mass transport by the Somali Current. The SMC reached a secondary peak in October/November, with the second Wyrtki jet. Figures 5.22 and 5.23 illustrate the significant variation in the zonal mass transports with longitude, showing greater variation in February than July.

D. OBSERVATIONS FROM ANIMATION STUDIES

In the late stages of this project, some data analysis and animation tools became available, which brought new insight into the model output. Monthly mean tapes were analyzed for the global ocean for four years of the seasonal cycle. The temperature fields were displayed as raster images, using various color schemes for enhancement of details. The prominent feature of animation of the global images was the strong, regular seasonal cycle in the model, which was much more significant than any interannual variability.

The animation of the Indian Ocean data set was even more revealing. A time series of 122 three-day instantaneous archive tapes were analyzed for the variables u, v, and T, encompassing year 4 of the study in the Indian Ocean. The richness of wave activity is striking, and shows the eddies at work in the model, transporting and diffusing heat. The animation of three-day intervals is very smooth, with jitter only at the end of the year where the loop goes back to the beginning of Year 4. Figure 5.23 was generated prior to the animation. It illustrates the standard deviation of sea surface slope for both the annual (Figure 5.23 (a)) and monthly (Figure 5.23 (b)) wind forcing phases of the model. The strong eddy activity implied in Figure 5.23 (b) is quite prominent in the animation. The eddies appear to be lee waves in the zonal flow past the tip of India. Animation also shows the northward movement of the cold temperature pattern associated with upwelling, as the Great Whirl separates from the Somali coast. The deep effects of the Somali Current and associated gyres can be seen, where temperature patterns similar to the surface patterns are visible at multiple levels. The meandering of the ECC in the western basin in March shows up strongly in the temperature fields.

Animation of the 160 m level in the ocean is quite striking, illustrating the westward transport of heat by the SEC and NEC in January and February, while the equatorial eastward transport of heat by the EUC becomes evident by March. This eastward transport of heat at the 160 m level is strongly enhanced in May and June, as the Wyrtki Jet and the EUC merge. The warm pool of water transported in the eastern end of the basin circulates cyclonically in the Bay of Bengal as a coastally-trapped Kelvin wave, and propagates around the tip of India into the Arabian Sea. This pool of warm water serves as an excellent tracer for the eddies formed at the southwest tip of India. Animation of the temperature fields supports the theory that the westward equatorial undercurrent is due to relaxation of water piled up by the Wyrtki jet. When the surge of warm water transported

eastward by the Wyrtki Jet reaches the coast, it appears to reflect back to the west during June and July. The animation dramatically illustrates the role of the SEC in transporting heat across the Indian Ocean and into the Agulhas Current, as described in Semtner and Chervin (1988). Not only does the SEC transport warm water from the Pacific, but concurrently with the northward-travelling wave in the Bay of Bengal, a southward-travelling Kelvin wave brings warm water into the Indonesian-Australian passage, where warm eddies are shed into the SEC for transport across to the Atlantic.

Various sections of zonal velocity were animated to investigate the issue of upward phase propagation discussed in Chapter IV.C. Animation of meridional sections shows an upward phase propagation of u velocity throughout the seasonal cycle. The hypothesis that this upward phase propagation is due to westward propagation of a feature with some vertical tilt is supported by animation of a zonal section of u velocity, taken along the equator. This animation shows very definite westward phase propagation to be taking place, and suggests that further investigation into this phenomenon is warranted.

E. CONCLUSIONS

While further improvements may be gained by improving the horizontal and vertical resolution of the model, the continued improvement of global ocean models clearly calls for better climatologies of wind stress, incorporating greater resolution and interannual variability. Improved bathymetry in the model is desirable as the resolution is improved, accompanied by a more realistic representation of islands. The study of Killworth *et al.* (1990) indicates that the calculations involving islands may be tractable with a free-surface effect. The use of such large models generates massive data sets, requiring new visualization tools for analysis. The animation tools explored in the course of this study were tremendously helpful in understanding the features of the circulation. While other improvements are also desirable, including the addition of the Arctic Ocean and improved

modeling of the mixed layer, any major changes must be tested carefully before embarking on a task as extensive as this. The parameterization of surface heat flux according to climatology of temperature, while less desirable than explicitly prescribing the heat flux, remains the best option, as suitable climatologies of heat flux are unavailable, and heat fluxes remain an object of extensive investigation and discussion.

The Semtner-Chervin eddy-resolving global ocean model accurately simulates many of the features of the seasonal cycle of the tropical Indian Ocean. Model output shows that this global model captures details of circulation previously available only through regional simulations. The model simulates the development of the tropical circulation in the two monsoon regimes, including the South Equatorial Current, North Equatorial Current, Equatorial Countercurrent, SW Monsoon Current, Equatorial Undercurrent, and seasonal Wyrtki jets The seasonally reversing Somali Current develops a Southern Gyre and the Great Whirl, and seasonal undercurrents The model clearly indicates a seasonal, poleward-flowing circulation off the western Australian coast, simulating the Leeuwin Current. Mass transports of the zonal equatorial currents display considerable variability across the basin, and the throughflow from the Pacific displays a strong seasonal cycle with small interannual variability. The model monthly mean temperature fields show a good agreement with climatology of sea surface temperature, and the current vector plots are in agreement with surface drifting buoy studies. The analysis of the SCM output in the tropical Indian Ocean suggests that the model is capable of producing even better results given better resolution, and improved wind stress, incorporating interannual variability.

APPENDIX

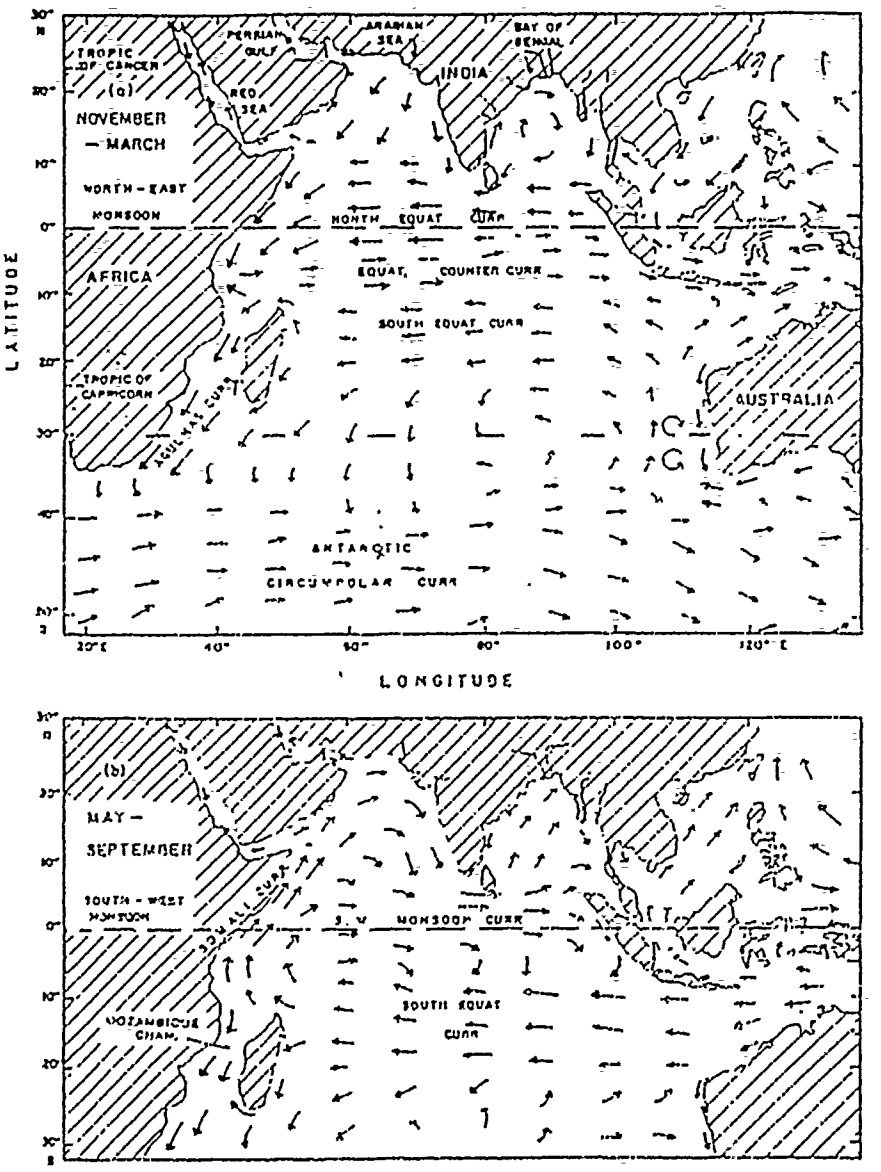

Figure 1.1 Surface Circulation of the Indian Ocean (Pickard and Emery, 1982). (a) Northeast monsoon, and (b) Southwest monsoon.

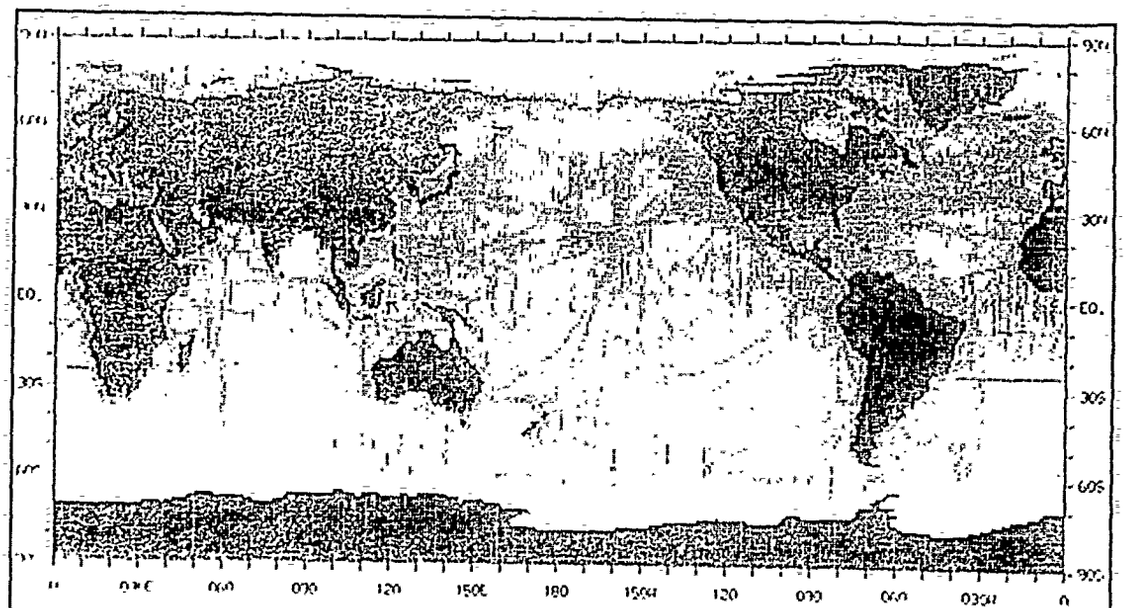

Figure 7.—Sea surface distribution of one-degree squares containing temperature observations from the merged-temperature data set (*SD*+*MBT*+*XBT*) for Northern Hemisphere summer (August, September, October). A small dot indicates a one-degree square containing 1-4 observations, a large dot indicates 5 or more observations.

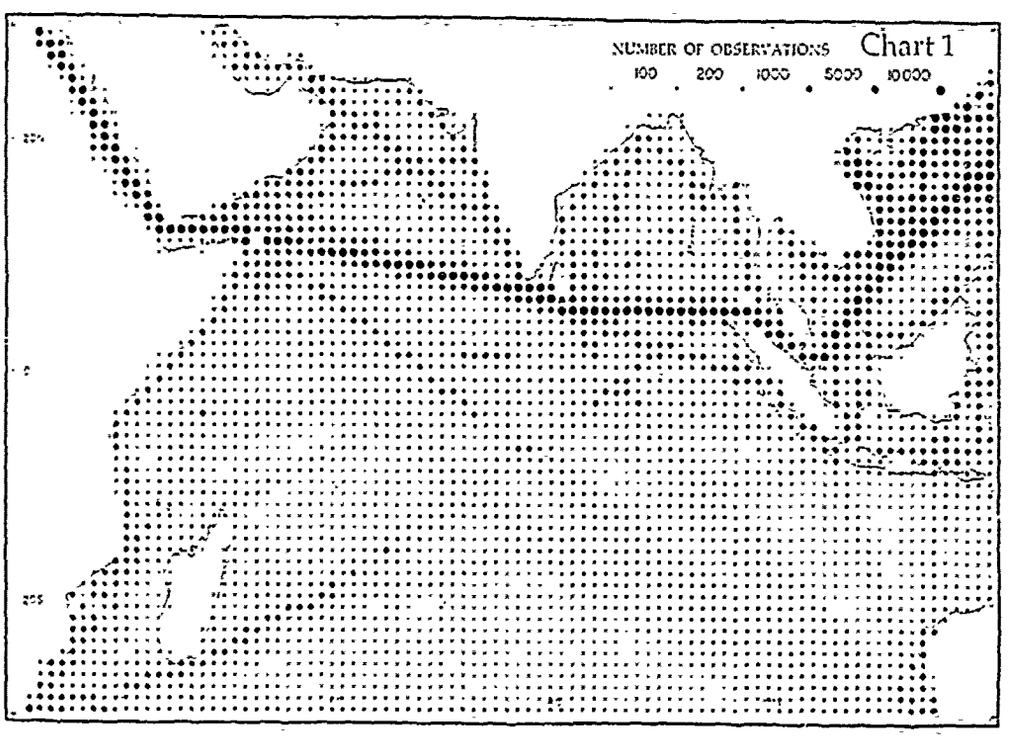

Figure 1.2 **Density and distribution of Indian Ocean observations.** (a) Surface and subsuface observations from Levitus (1982) (b) Surface observations from Hastenrath and Lamb (1979).

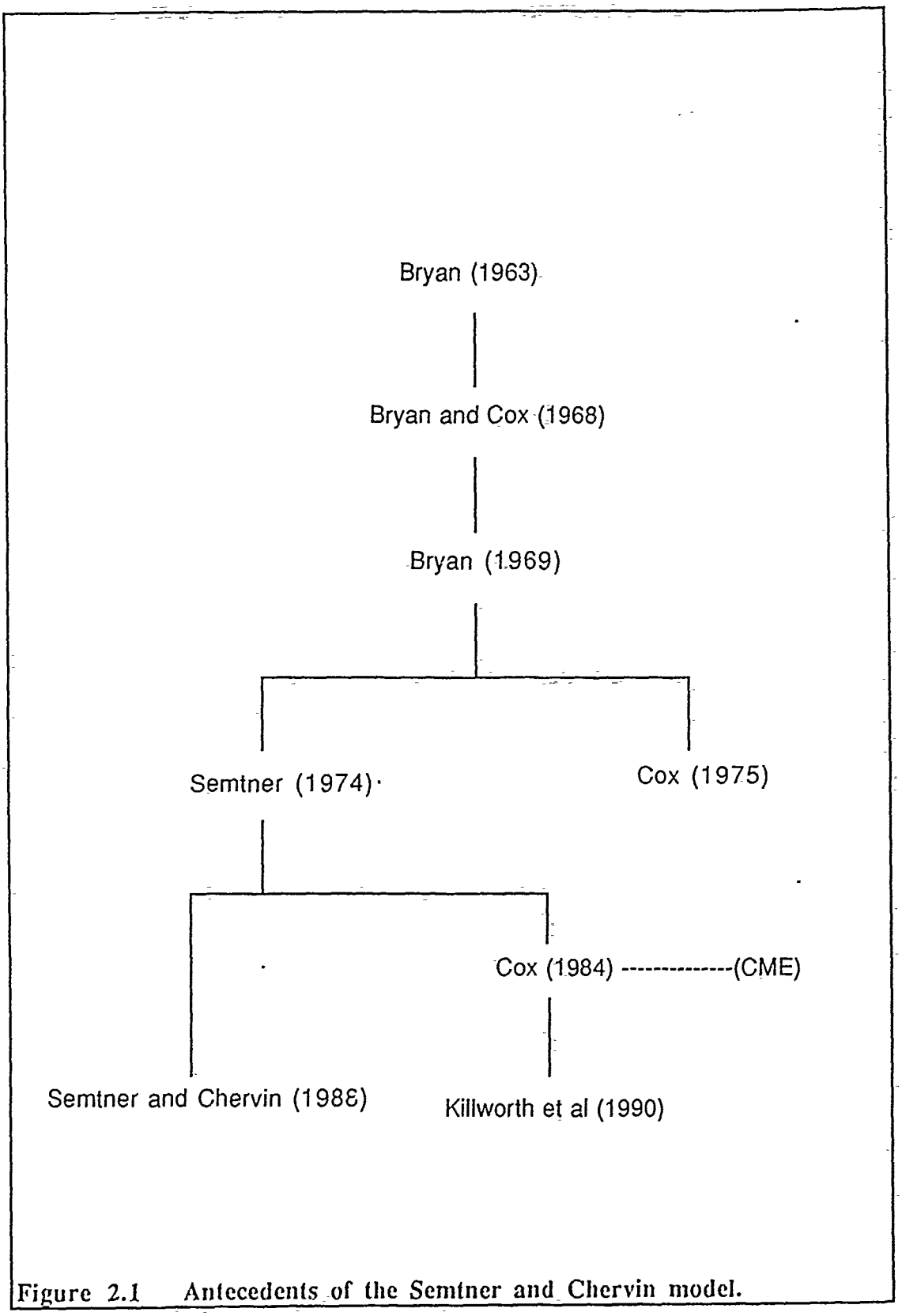

Figure 2.1 Antecedents of the Semtner and Chervin model.

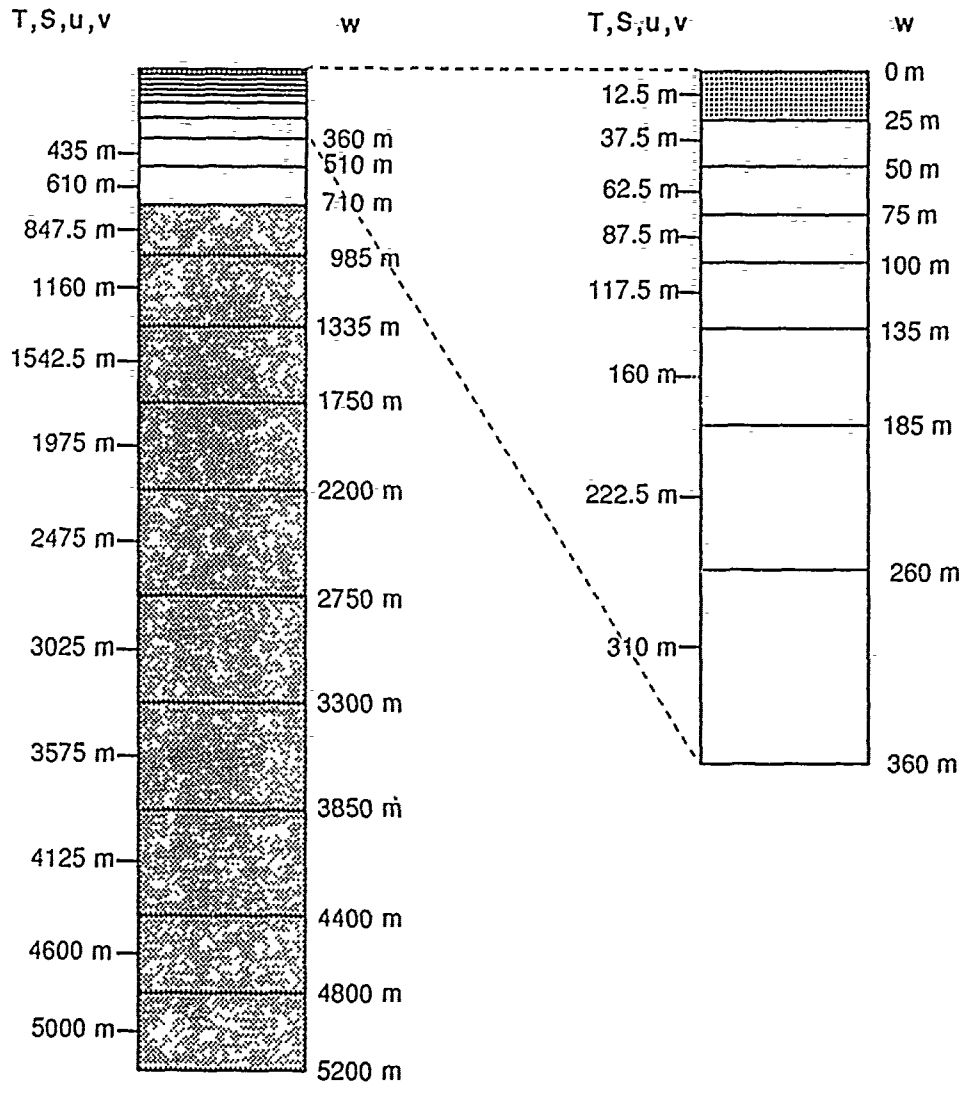

Figure 2.2 Vertical levels in the model. The vertical velocity is defined at the interface between boxes. T, S, u, and v are all defined at the same vertical level. Temperature and salinity are defined at the center of the boxes, while u and v are defined at the midpoint of the vertical edges of the boxes. The top box is restored to Levitus (1982) values on a 30-day time scale, while boxes below 710m are restored on a 3-year time scale.

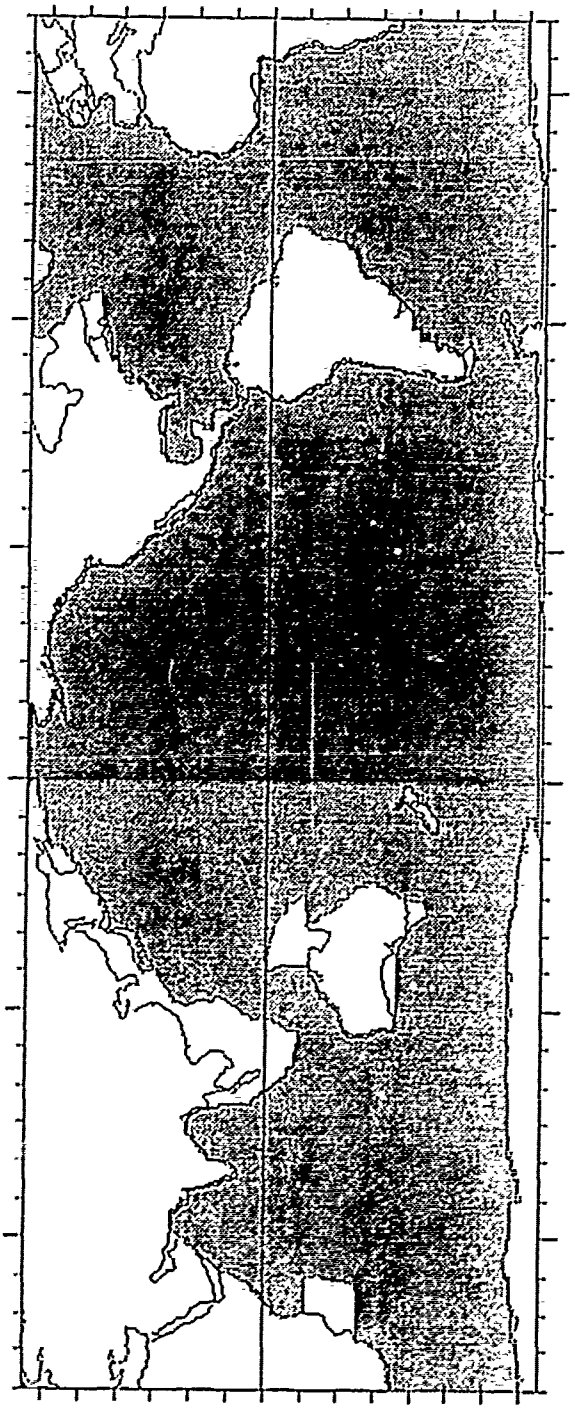

Figure 2.3 The global ocean model domain at 12.5 m. The only islands are Australia/New Guinea, New Zealand, Antarctica. Other islands have been shoaled or attached to continental land masses, and marginal seas have been filled in.

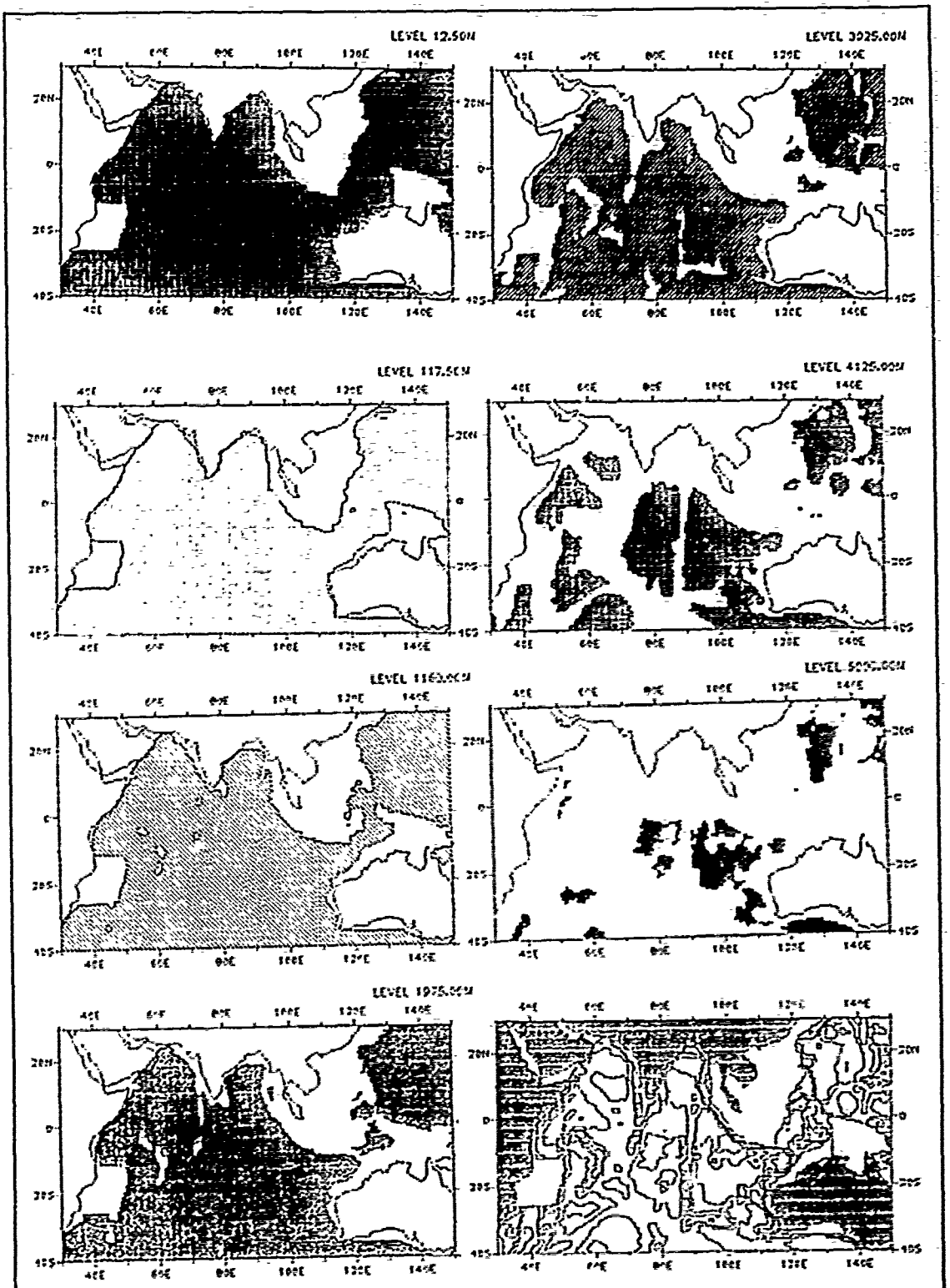

Figure 2.4 The Indian Ocean bathymetry of the global ocean model. (a) 12.5 m, (b) 117.5 m, (c) 1160m, (d) 1975 m, (e) 3025 m, (f) 4125 m, (g) 5000 m, and (h) composite.

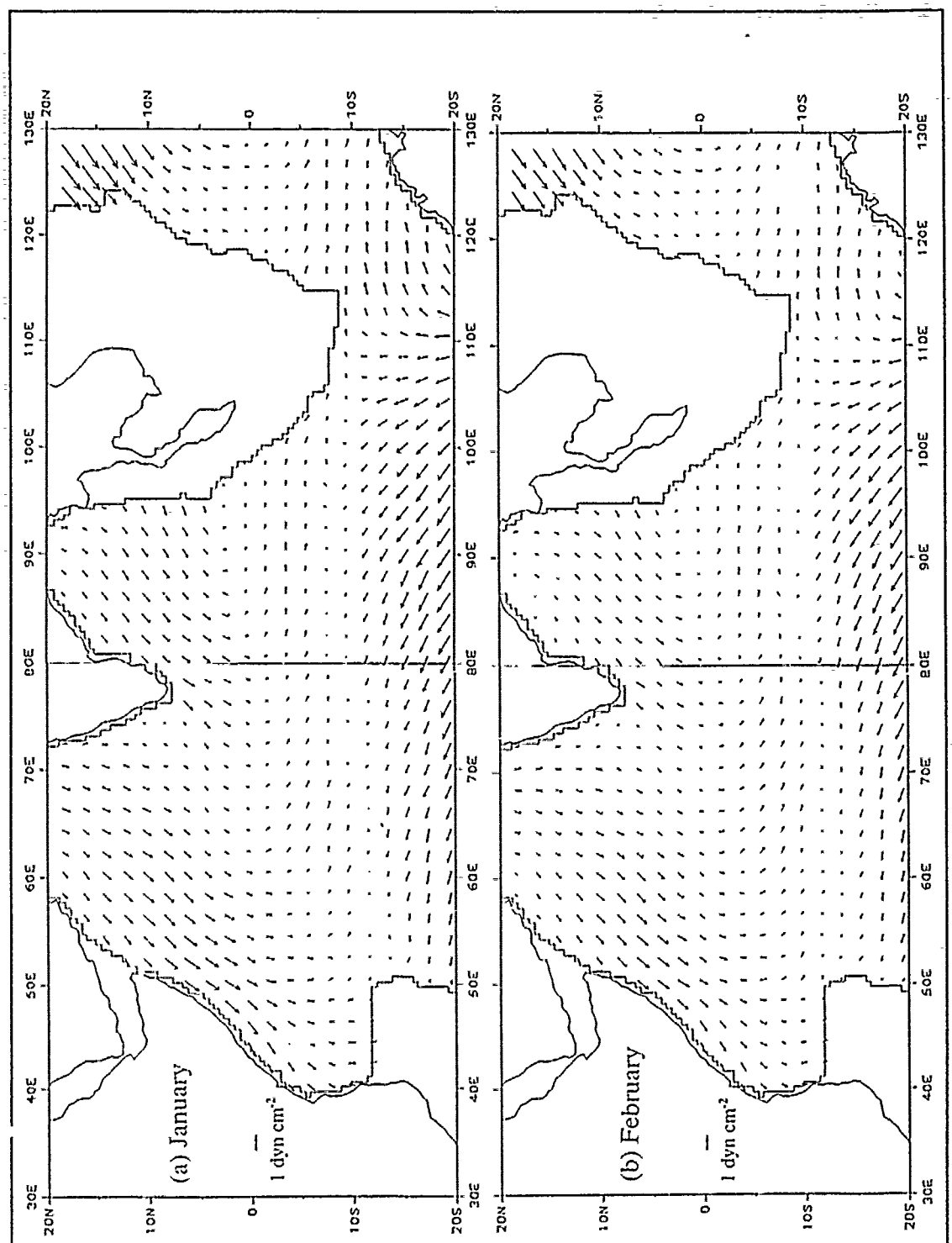

Figure 3.1 Monthly mean Hellerman and Rosenstein (1983) wind stress during Year 4. (a) January and (b) February.

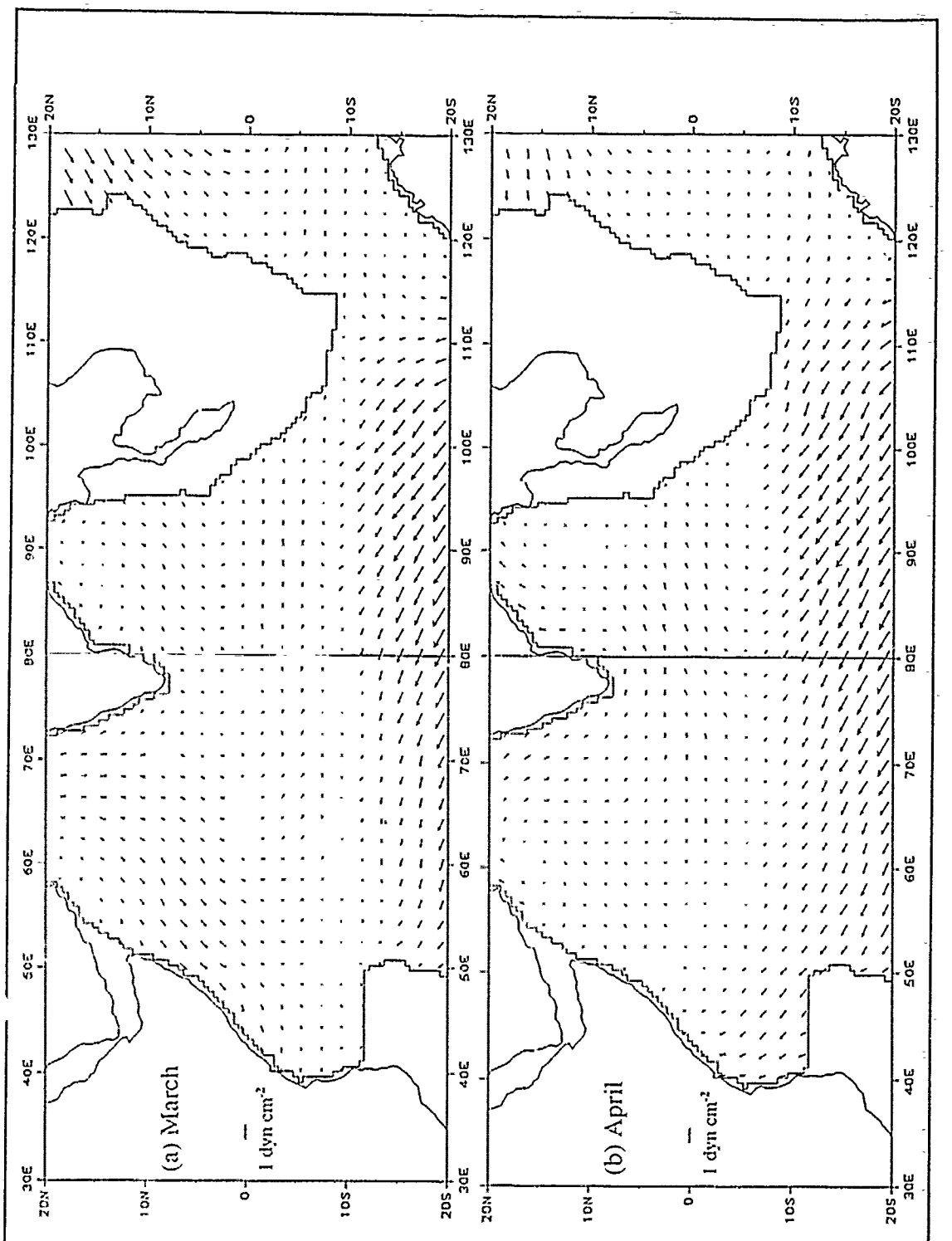

Figure 3.2 Monthly mean Hellerman and Rosenstein (1983) wind stress during Year 4. (a) March and (b) April.

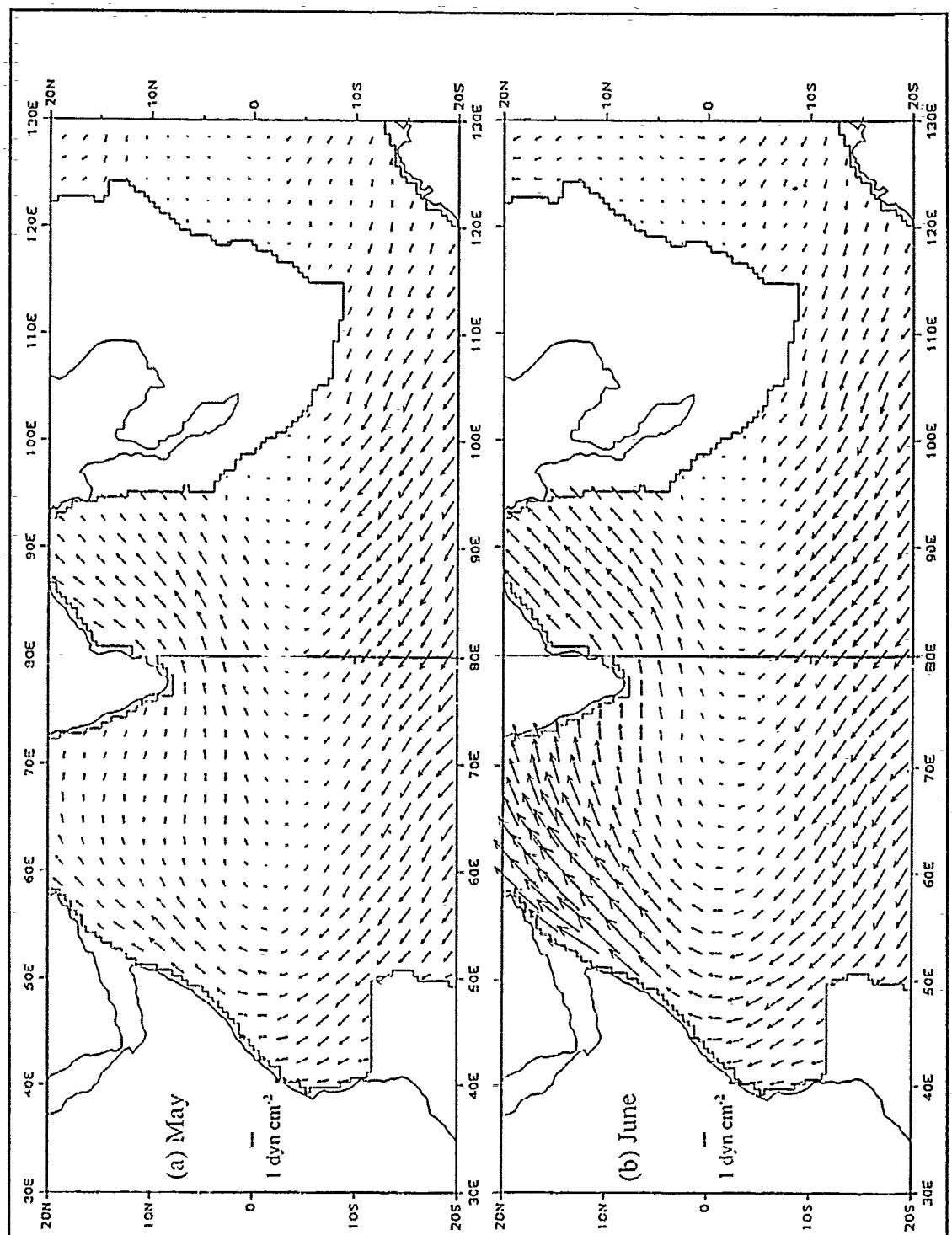

Figure 3.3 Monthly mean Hellerman and Rosenstein (1983) wind stress during Year 4. (a) May and (b) June.

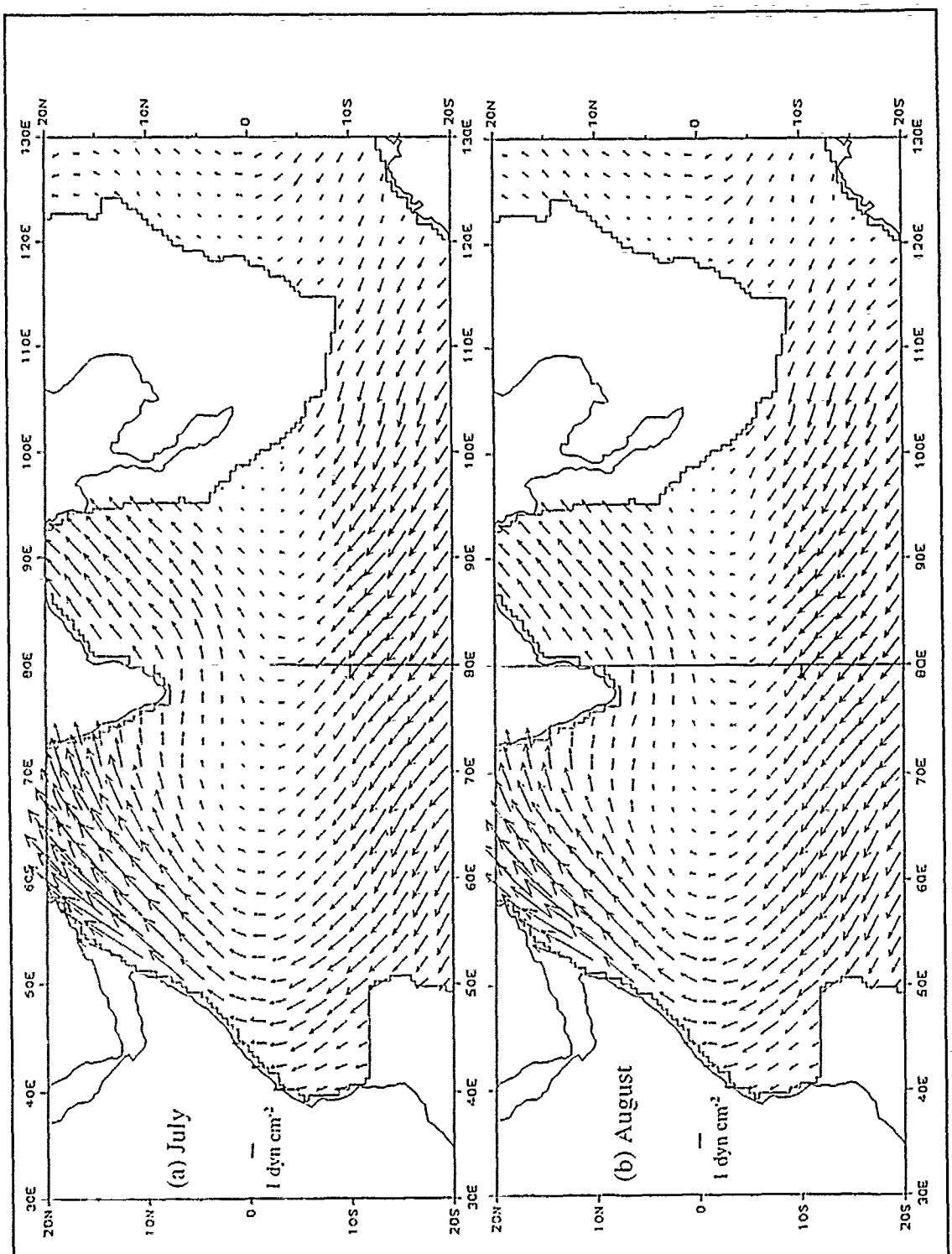

Figure 3.4 Monthly mean Hellerman and Rosenstein (1983) wind stress during Year 4. (a) July and (b) August.

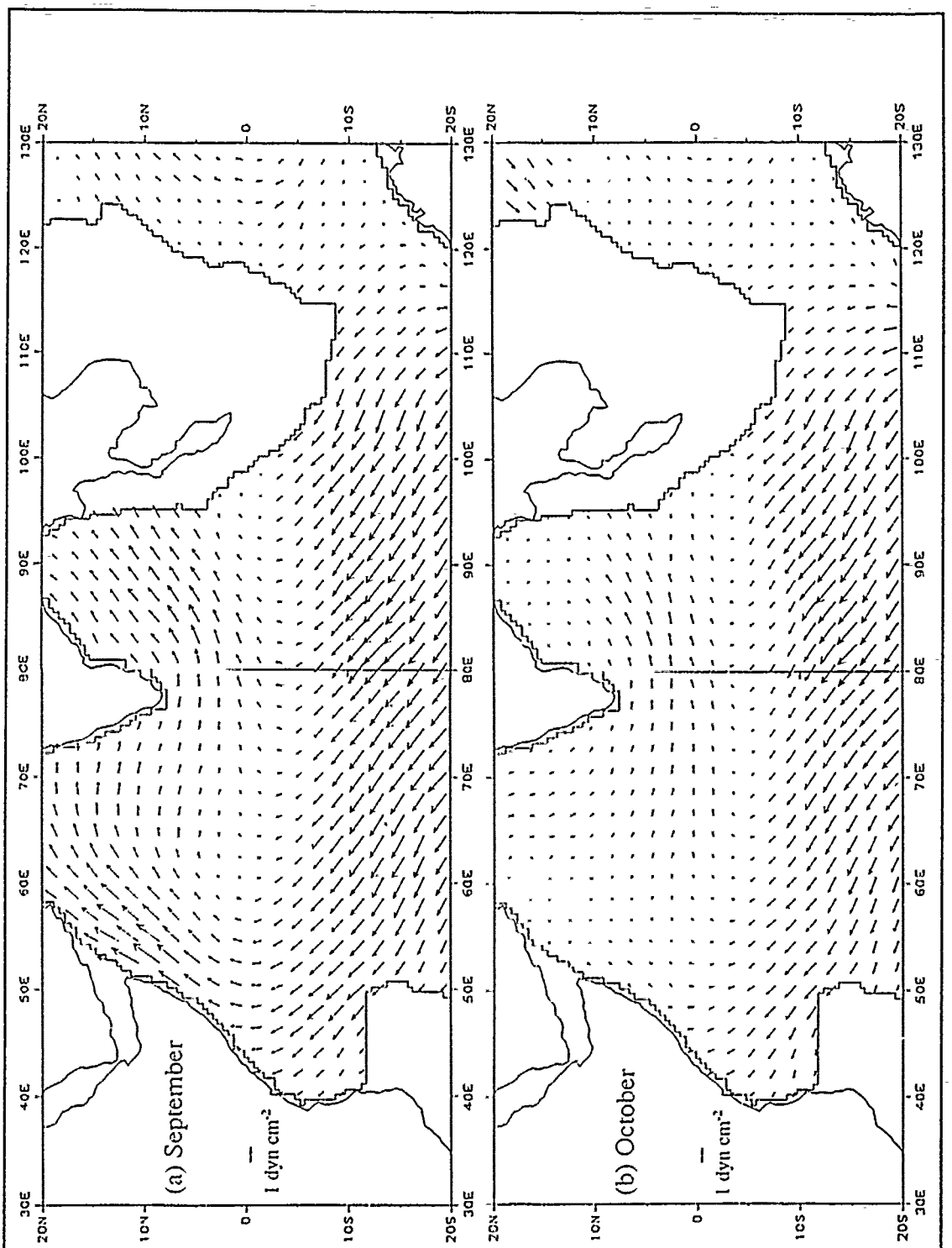

Figure 3.5 Monthly mean Hellerman and Rosenstein (1983) wind stress during Year 4. (a) September and (b) October.

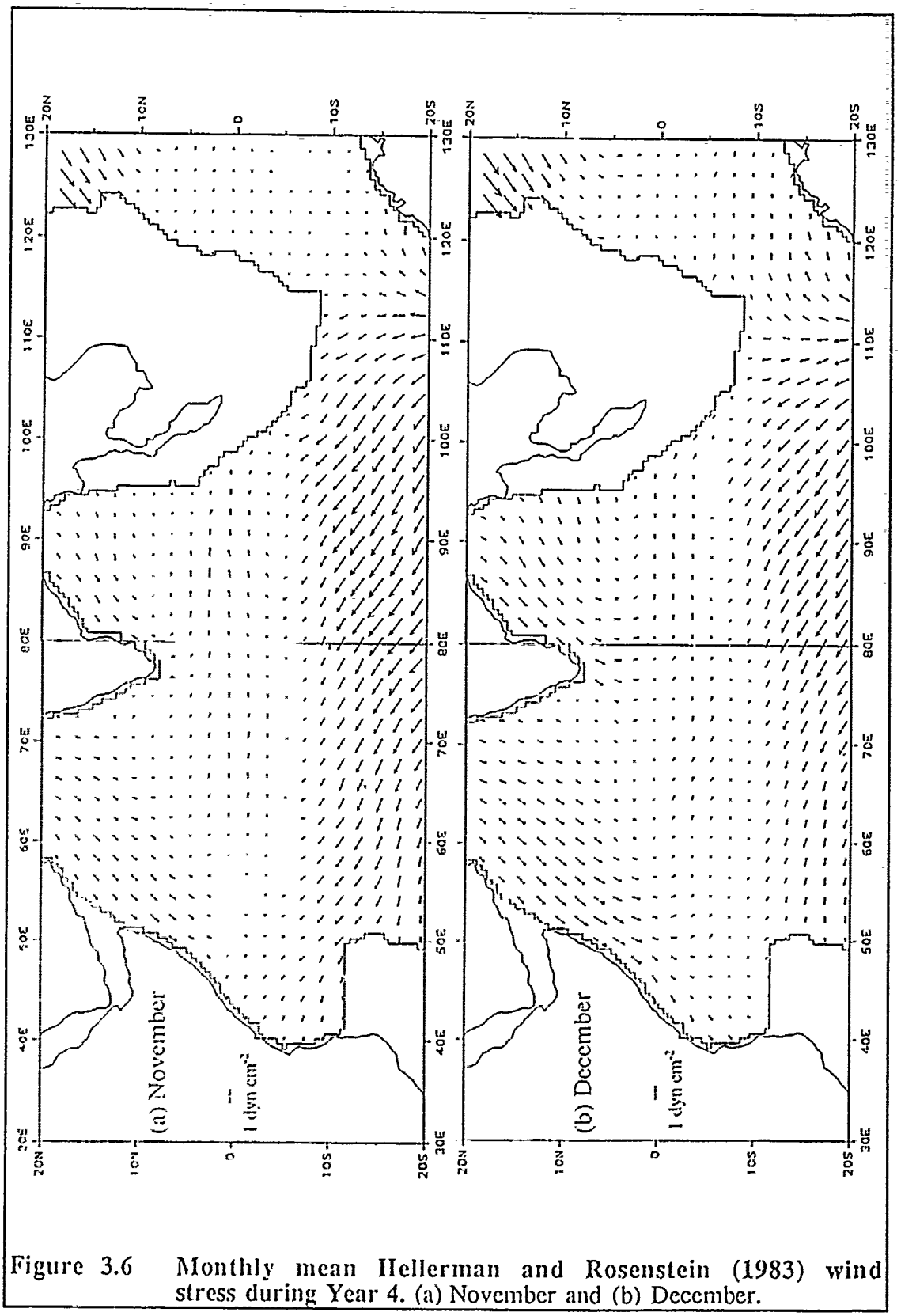

Figure 3.6 Monthly mean Hellerman and Rosenstein (1983) wind stress during Year 4. (a) November and (b) December.

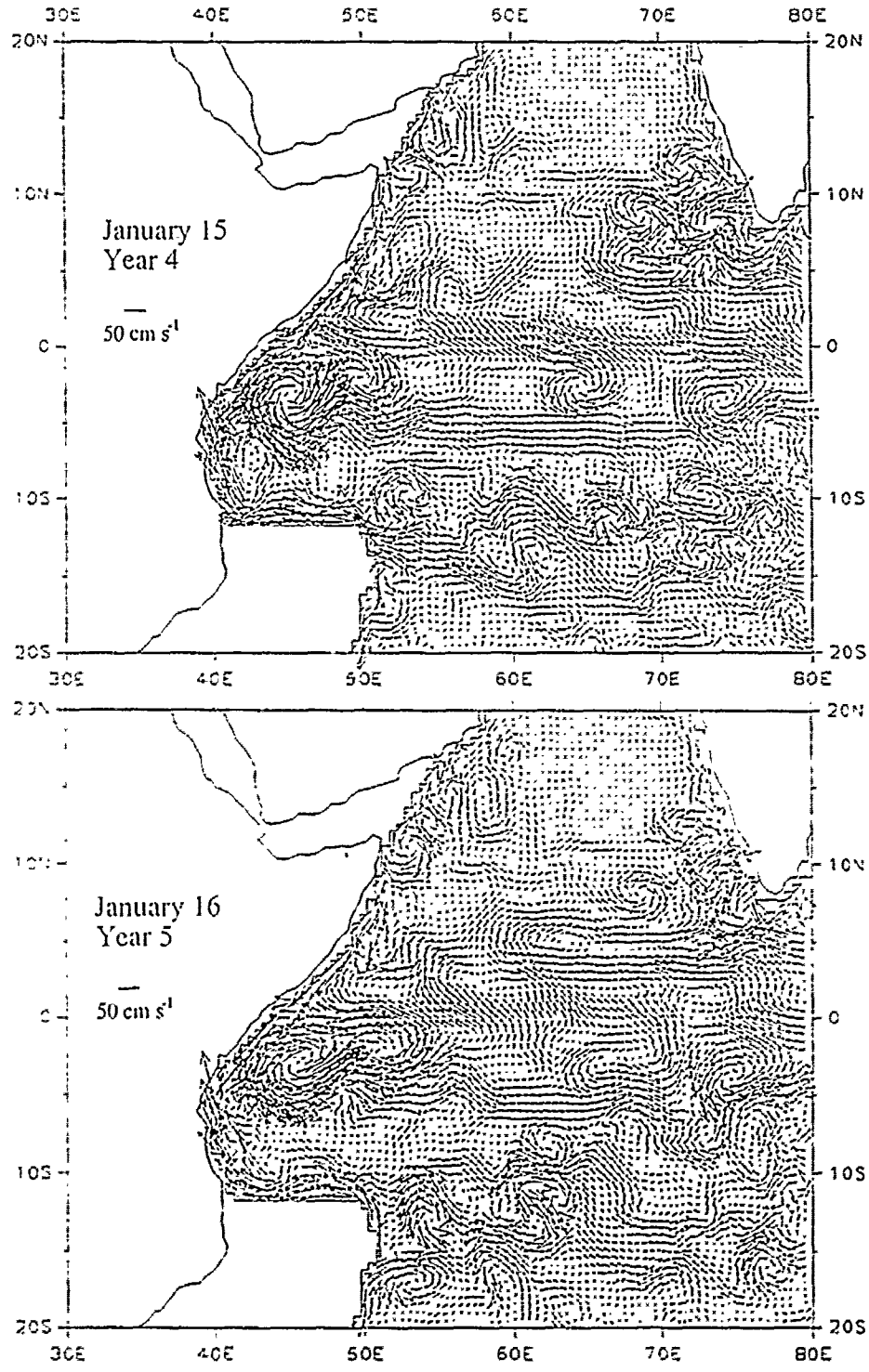

Figure 4.1 Instantaneous current vectors at 37.5 m.. (a) January 15, Year 4, and (b) January 16, Year 5, illustrating interannual variability of the eddy fields in the model.

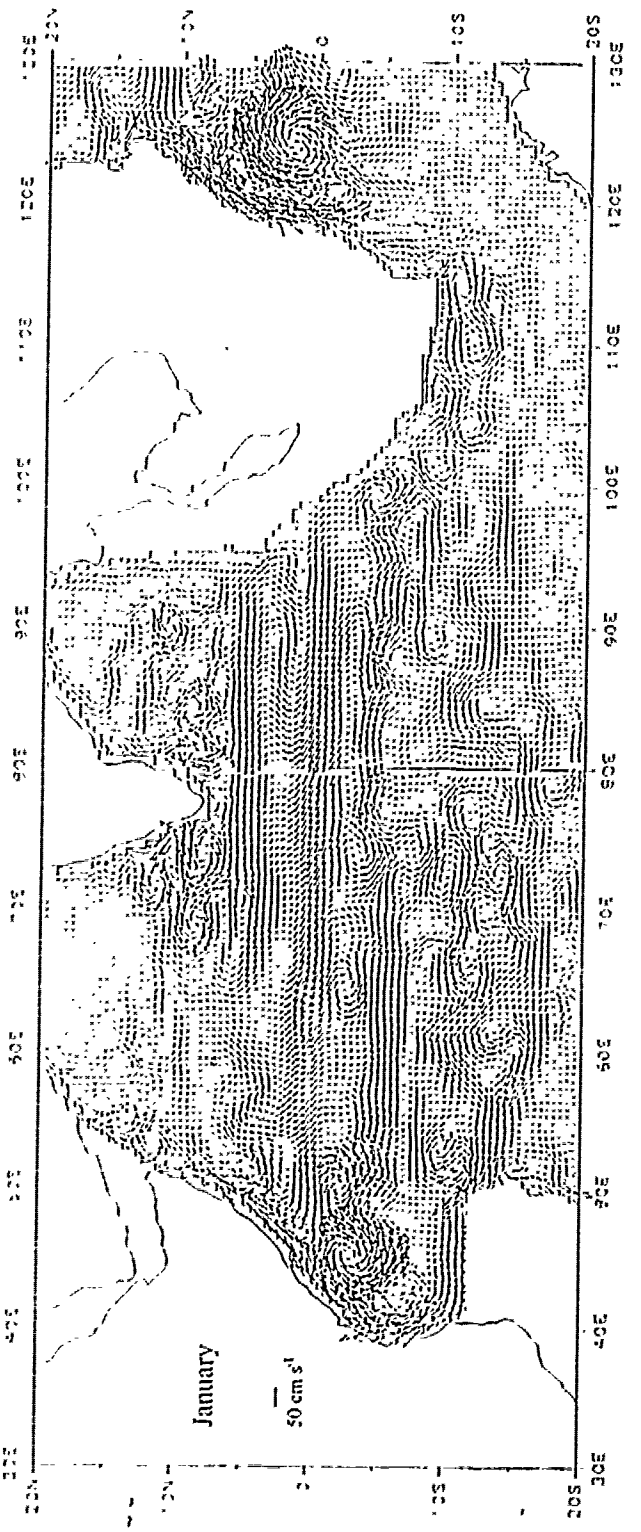

Figure 4.2 Monthly mean current vectors at 37 m during January of Year 4.

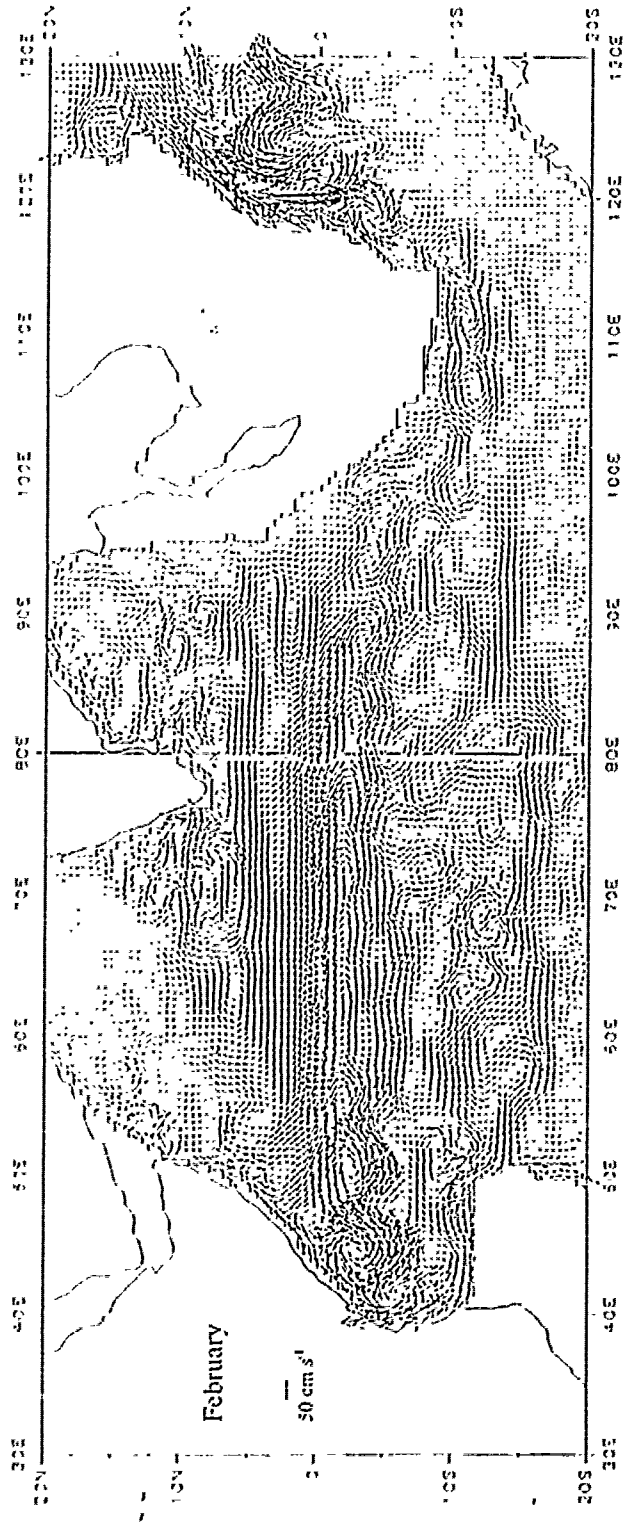

Figure 4.3 Monthly mean current vectors at 37 m during February of Year 4.

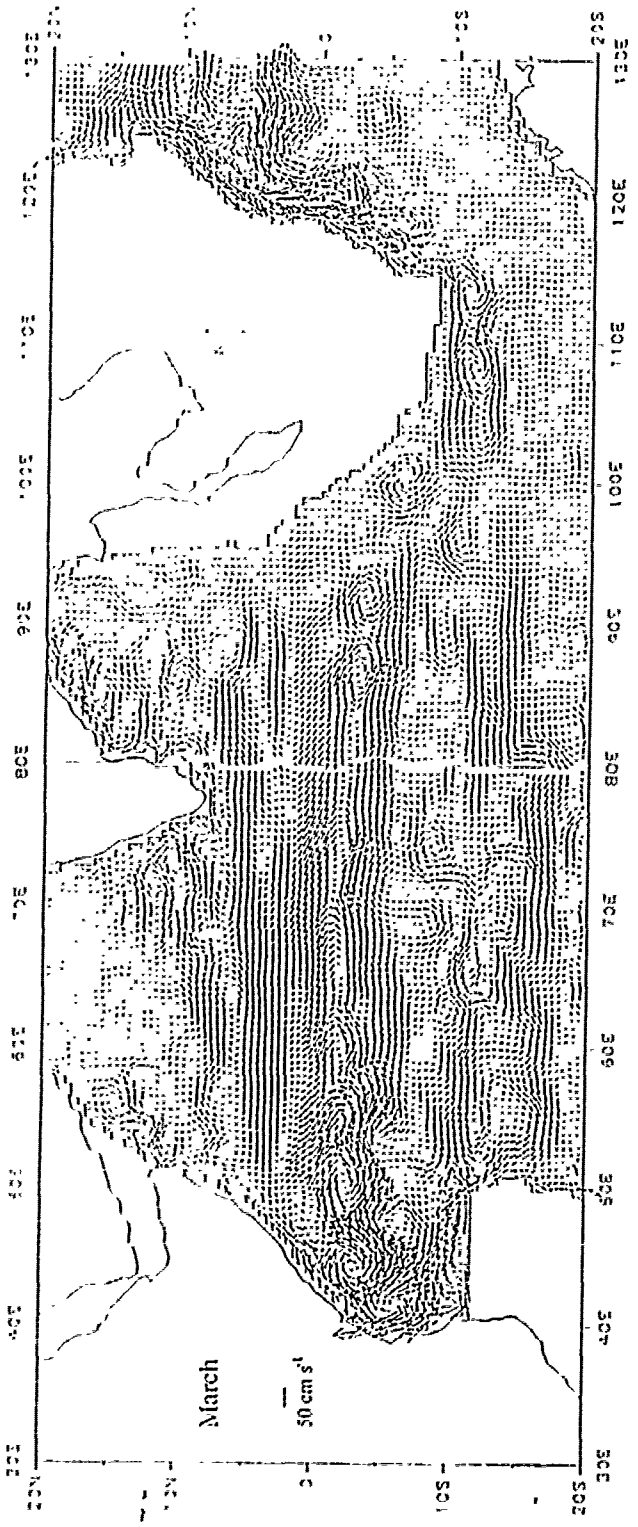

Figure 4.4 Monthly mean current vectors at 37 m during March of Year 4.

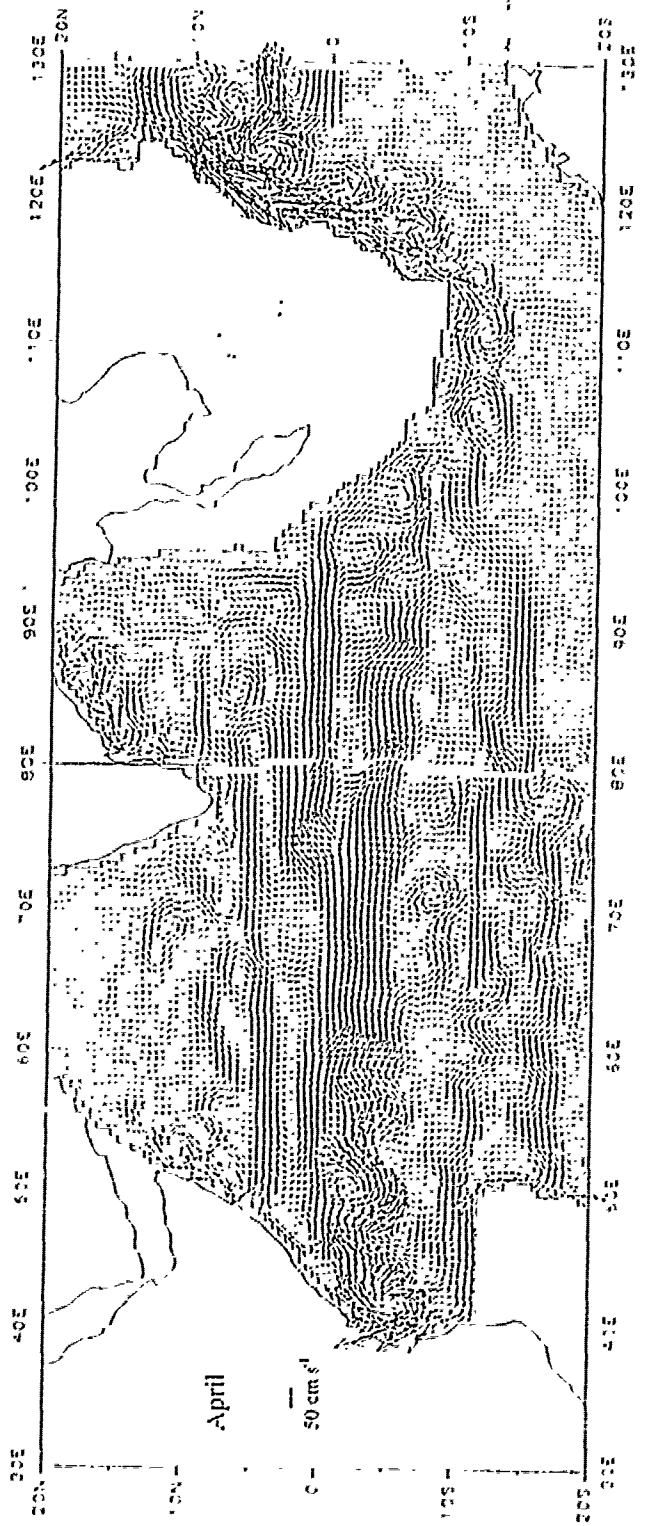

Figure 4.5 Monthly mean current vectors at 37 m during April of Year 4.

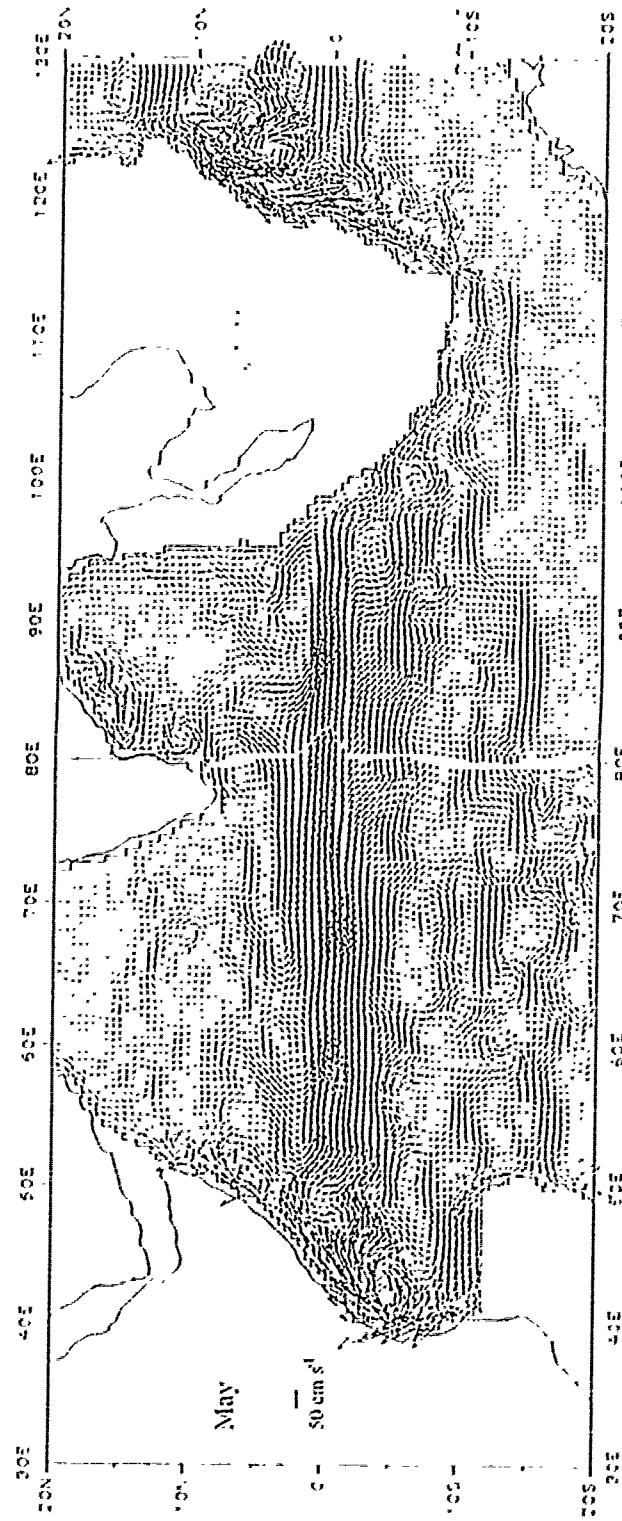

Figure 4.6 Monthly mean current vectors at 37 m during May of Year 4.

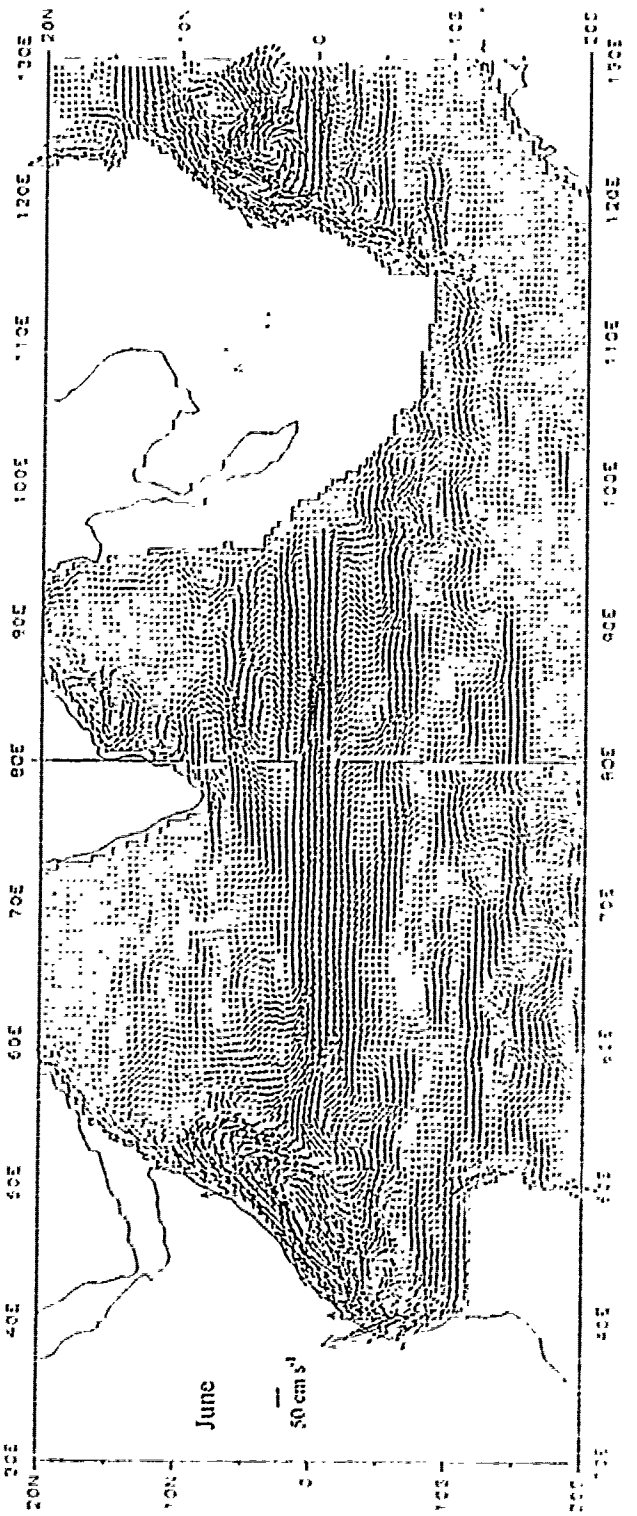

Figure 4.7 Monthly mean current vectors at 37 m during June of Year 4.

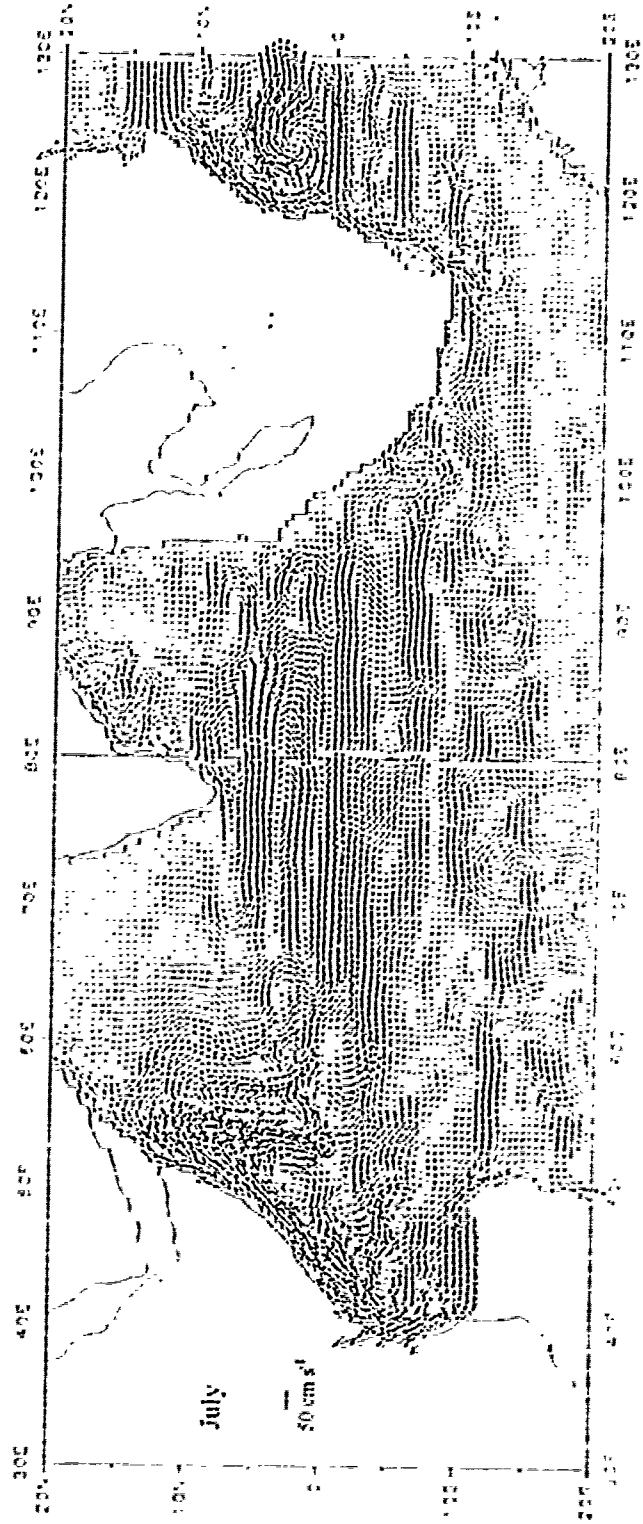

Figure 4.8 Monthly mean current vectors at 37 m during July of Year 4.

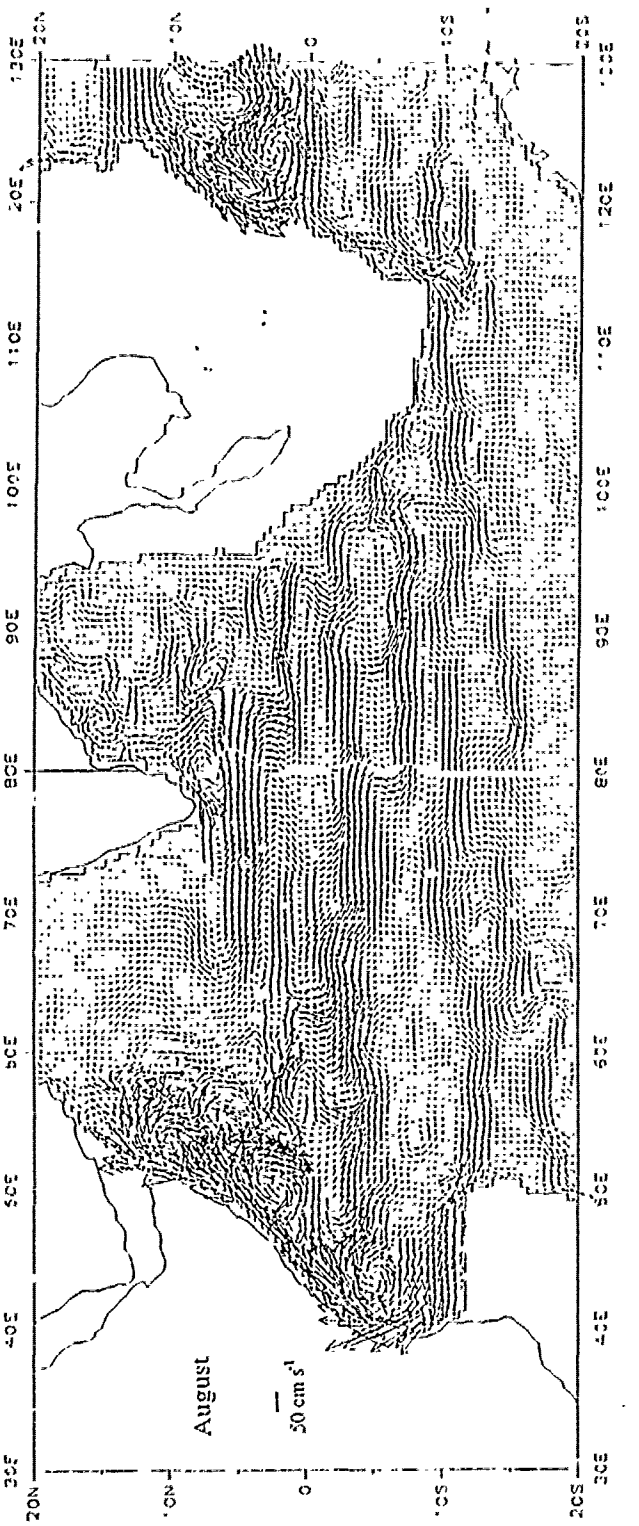

Figure 4.9 Monthly mean current vectors at 37 m during August of Year 4.

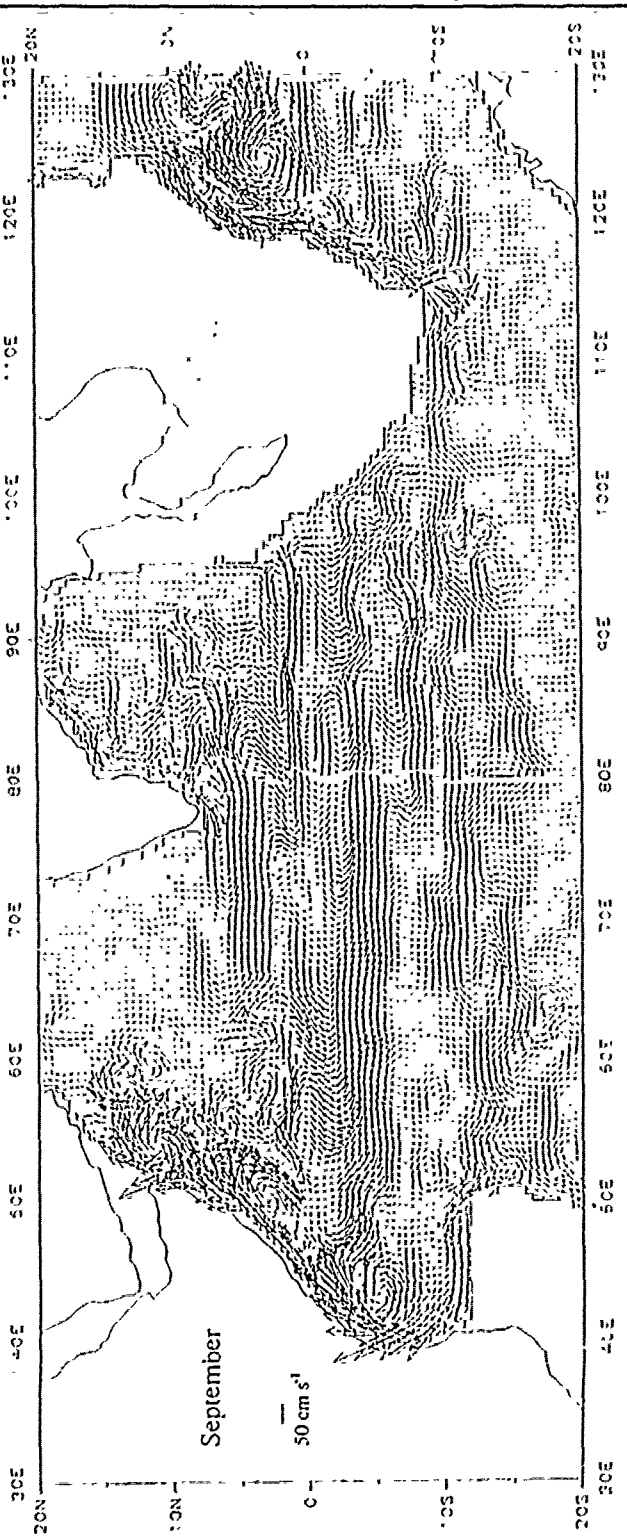

Figure 4.10 Monthly mean current vectors at 37 m during September of Year 4.

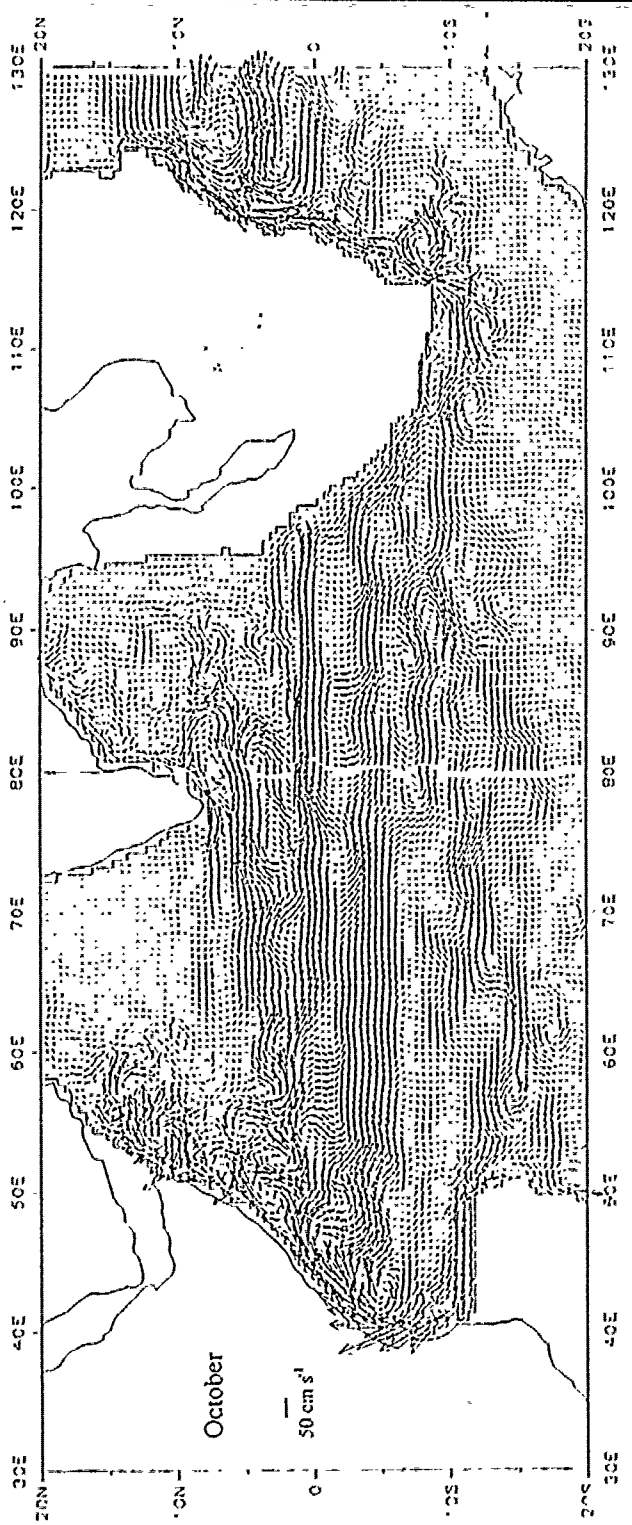

Figure 4.11 Monthly mean current vectors at 37 m during October of Year 4.

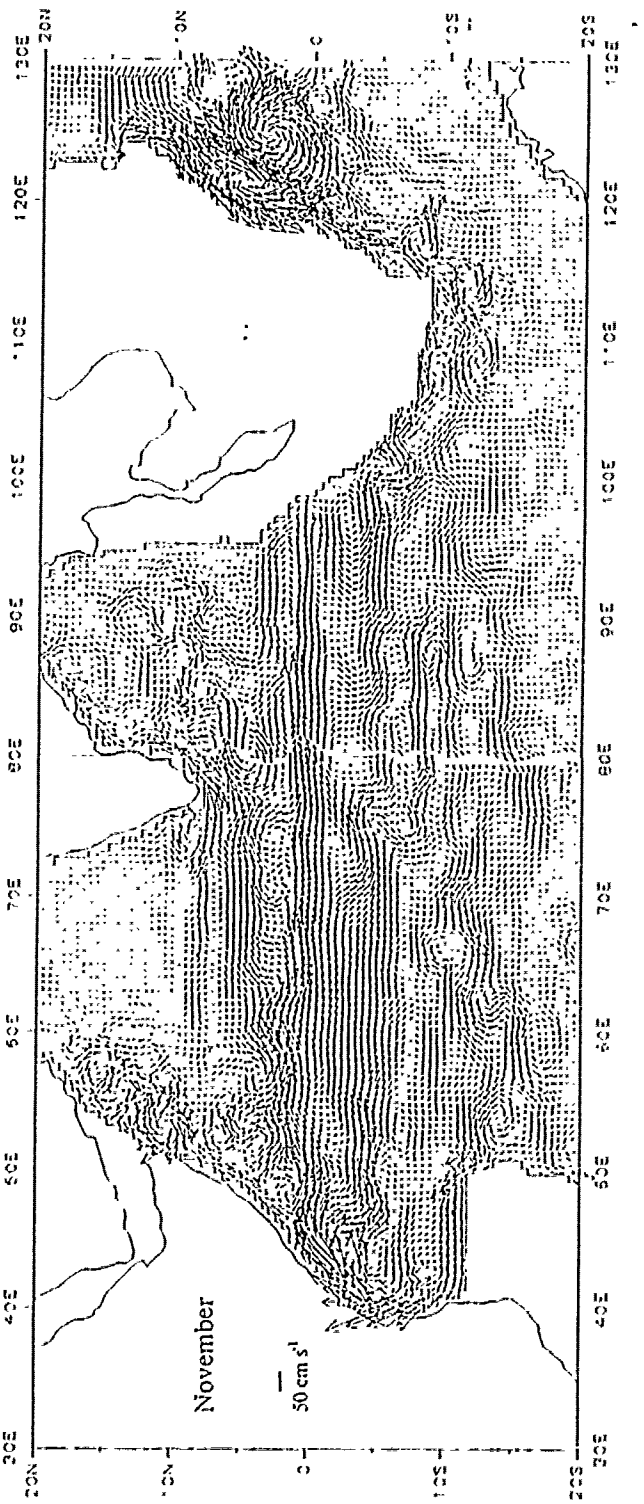

Figure 4.12 Monthly mean current vectors at 37 m during November of Year 4.

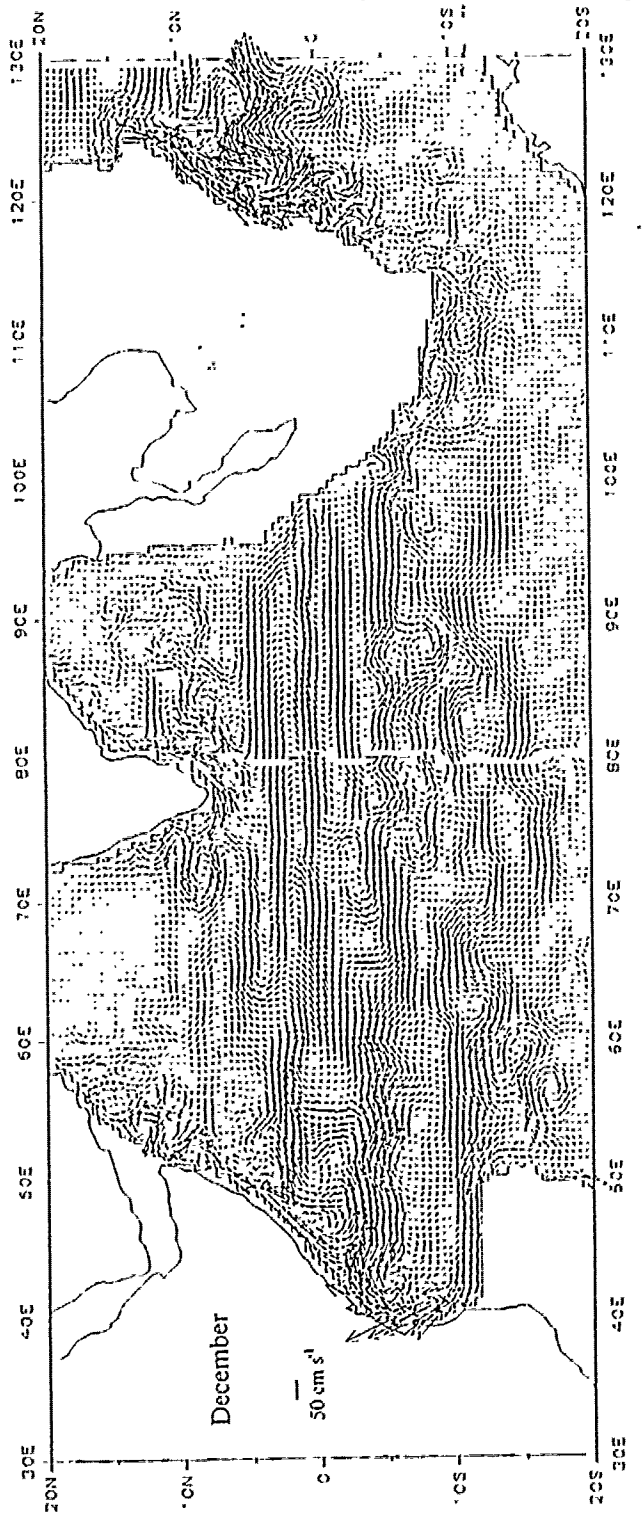

Figure 4.13 Monthly mean current vectors at 37 m during December of Year 4.

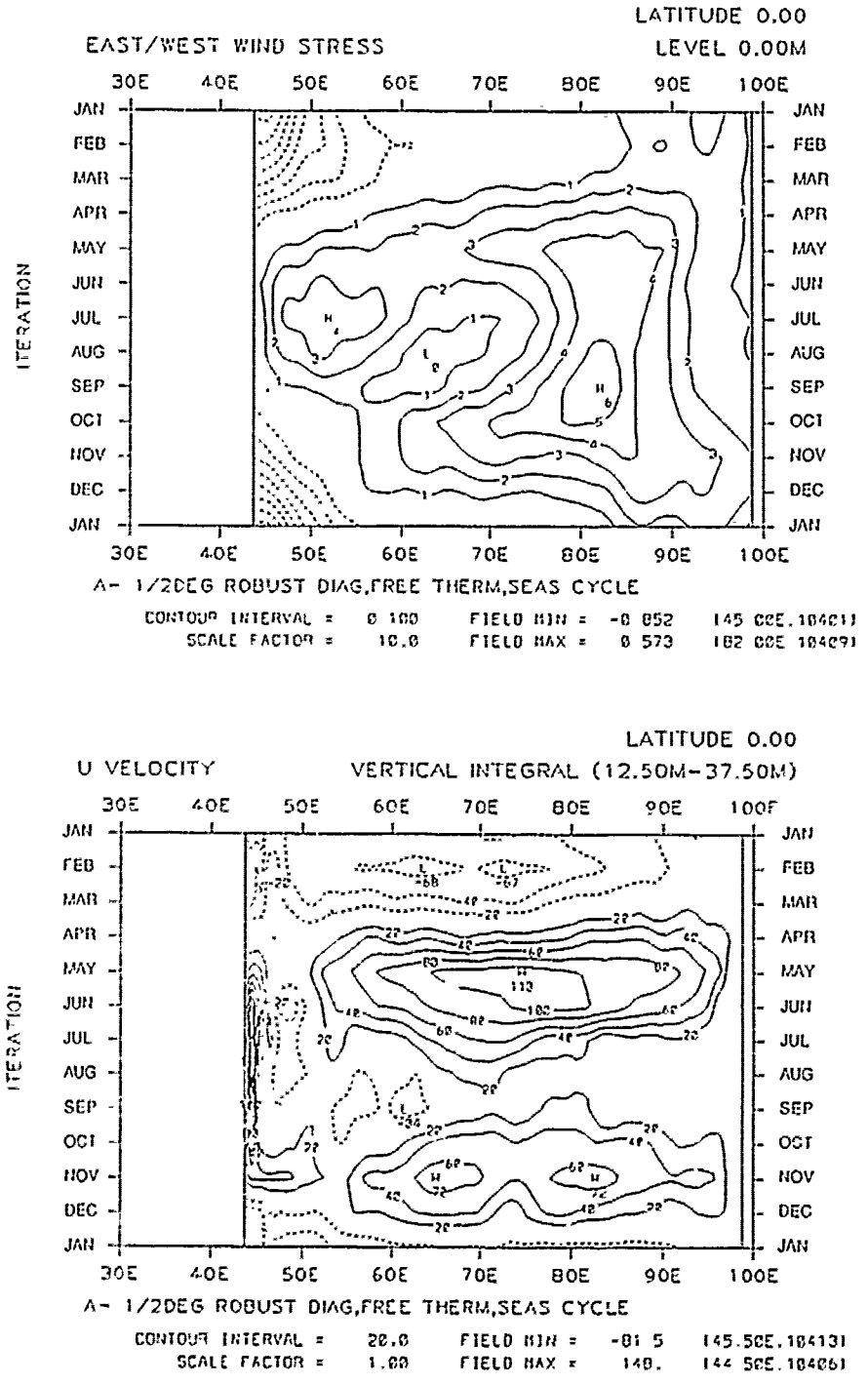

Figure 4.14 Dependence of the Wyrtki Jet on seasonal wind stress in Year 4. Longitude-time plots of a) Zonal wind stress and (b) 12.5-37.5m zonal currents.

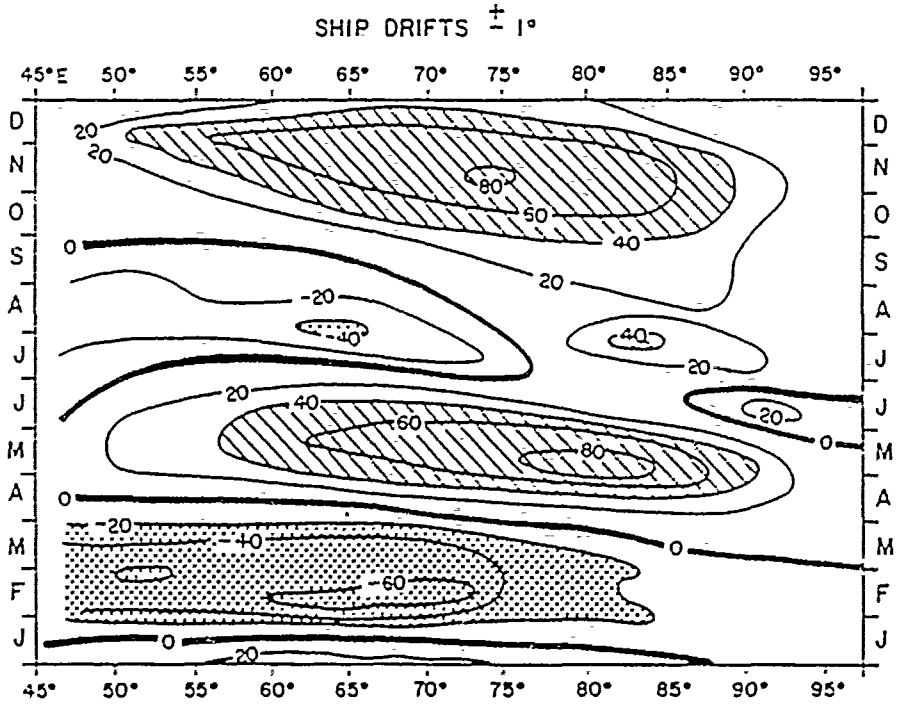

Figure 4.15 Equatorial zonal current estimates from ship drift reports. (Reverdin (1987) after Cutler and Swallow (1984) 1°S-1°N. The time scale is reversed relative to Figure 4.14.

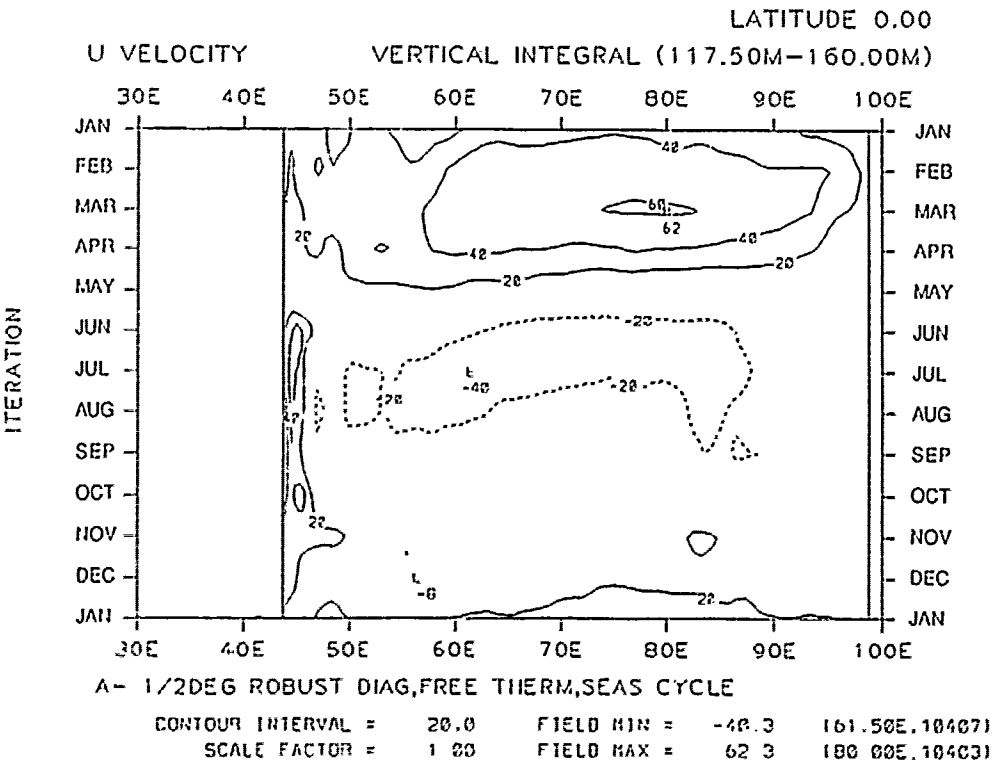

Figure 4.16 Longitude-time plot of the EUC during Year 4. Zonal currents integrated between 117.5 and 160 m.

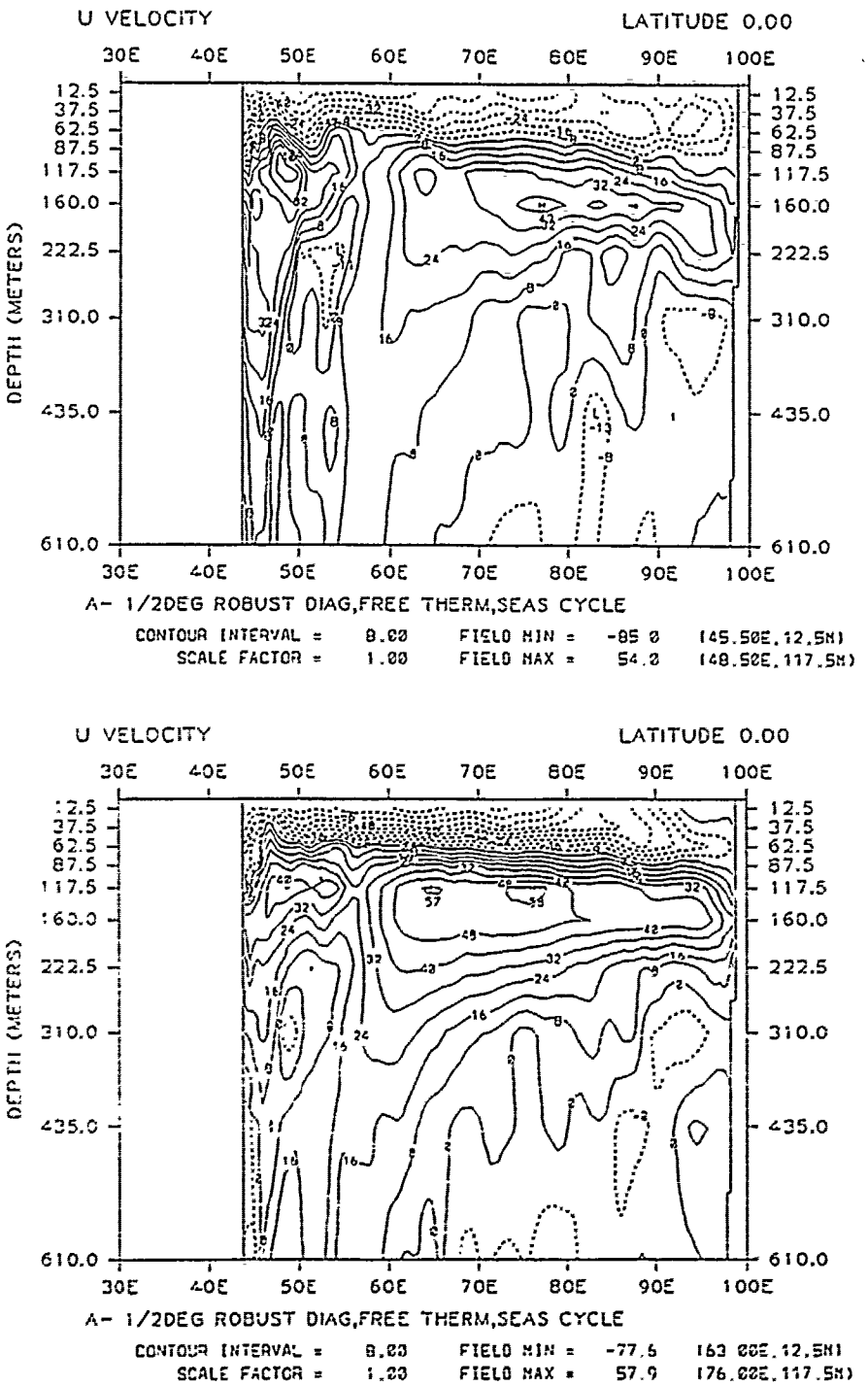

Figure 4.17 Monthly mean zonal currents at the equator during Year 4. (a) January and (b) February.

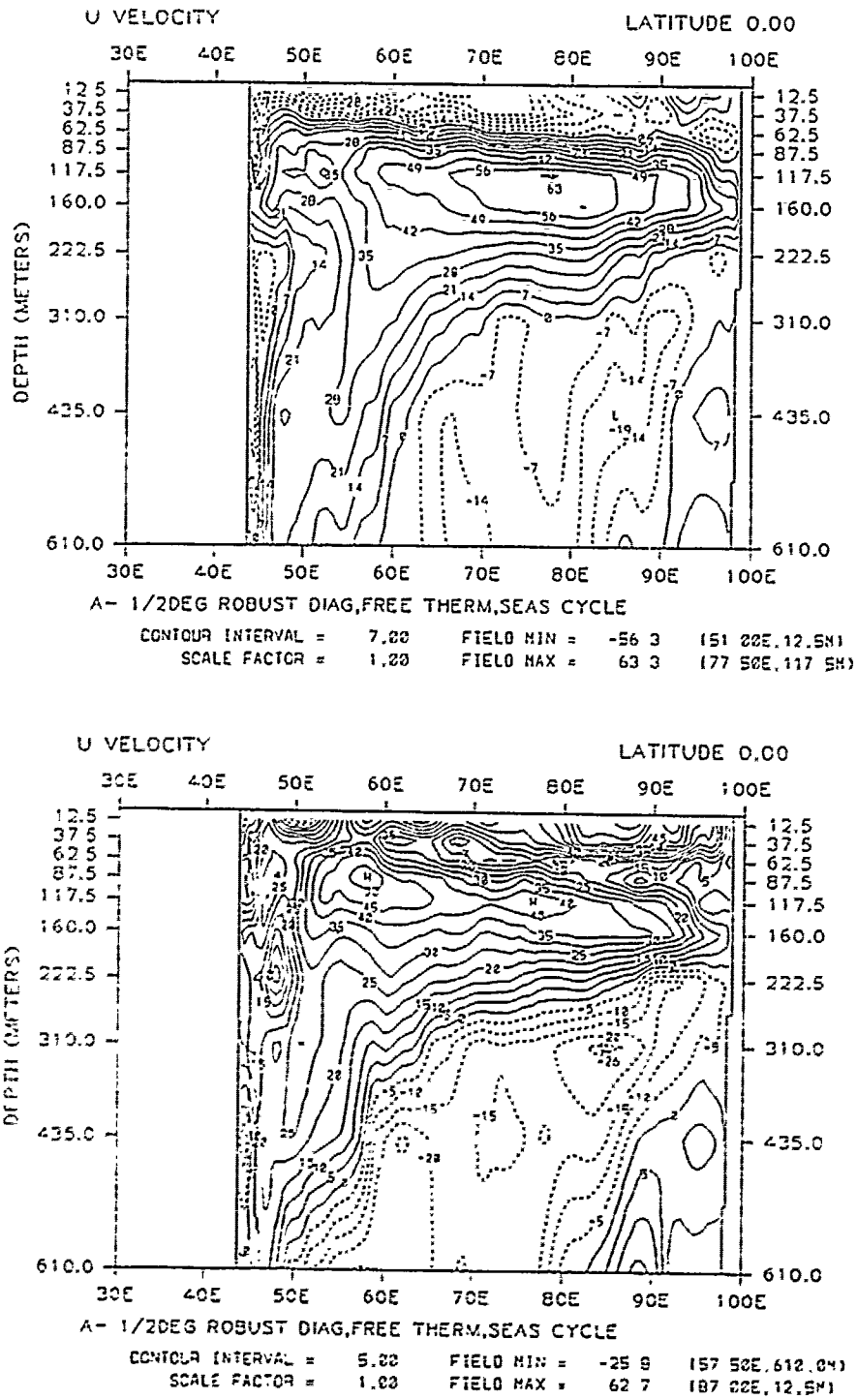

Figure 4.18 Monthly mean zonal currents at the equator during Year 4. (a) March and (b) April.

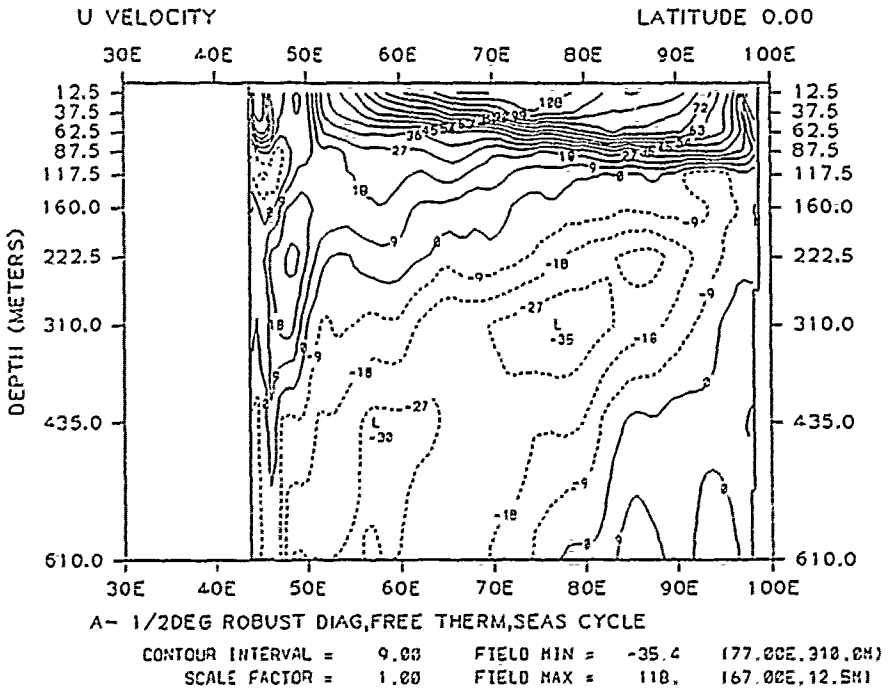

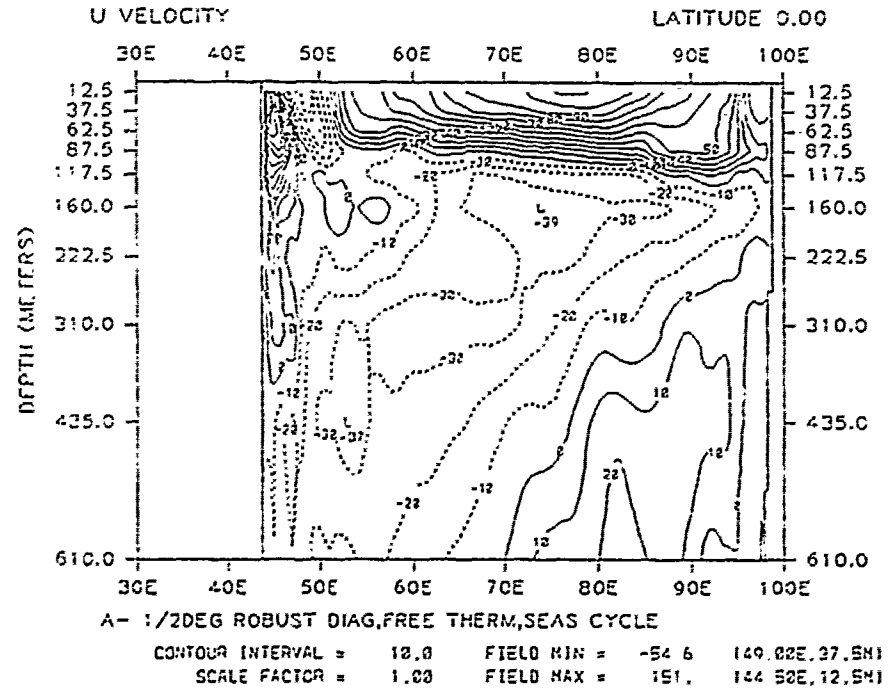

Figure 4.19 Monthly mean zonal currents at the equator during Year 4. (a) May and (b) June.

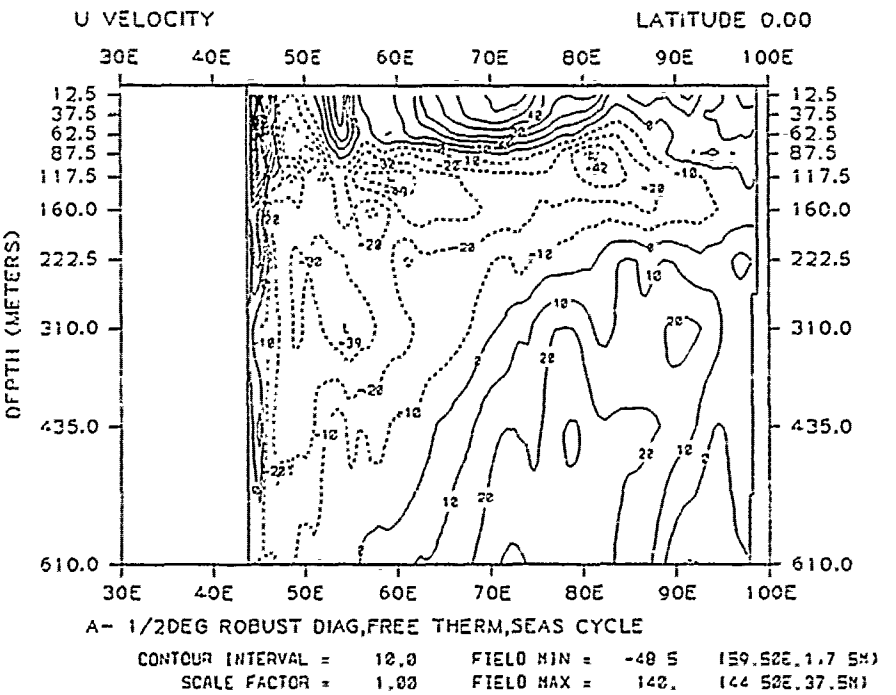

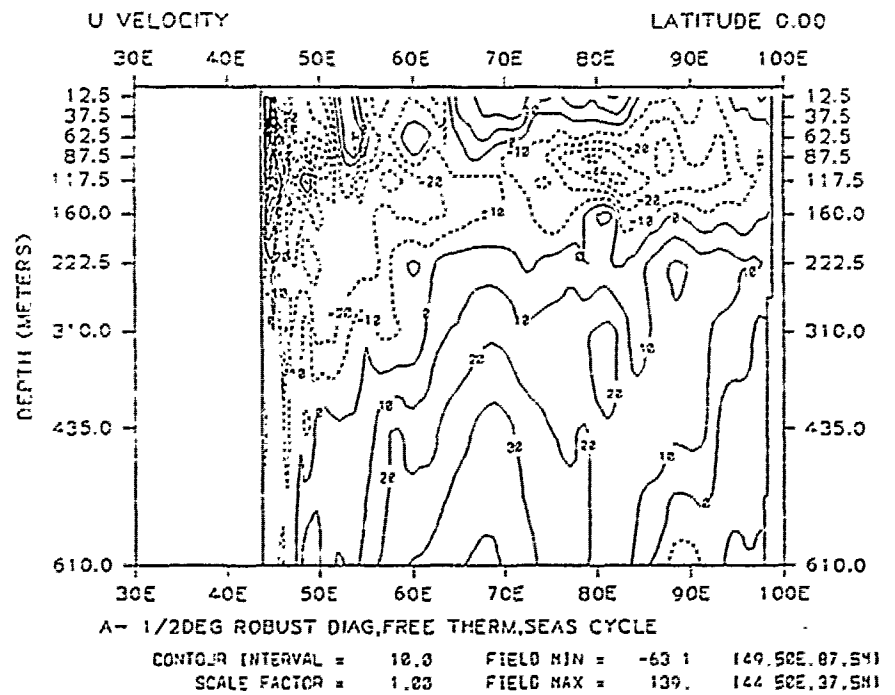

Figure 4.20 Monthly mean zonal currents at the equator during Year 4. (a) July and (b) August.

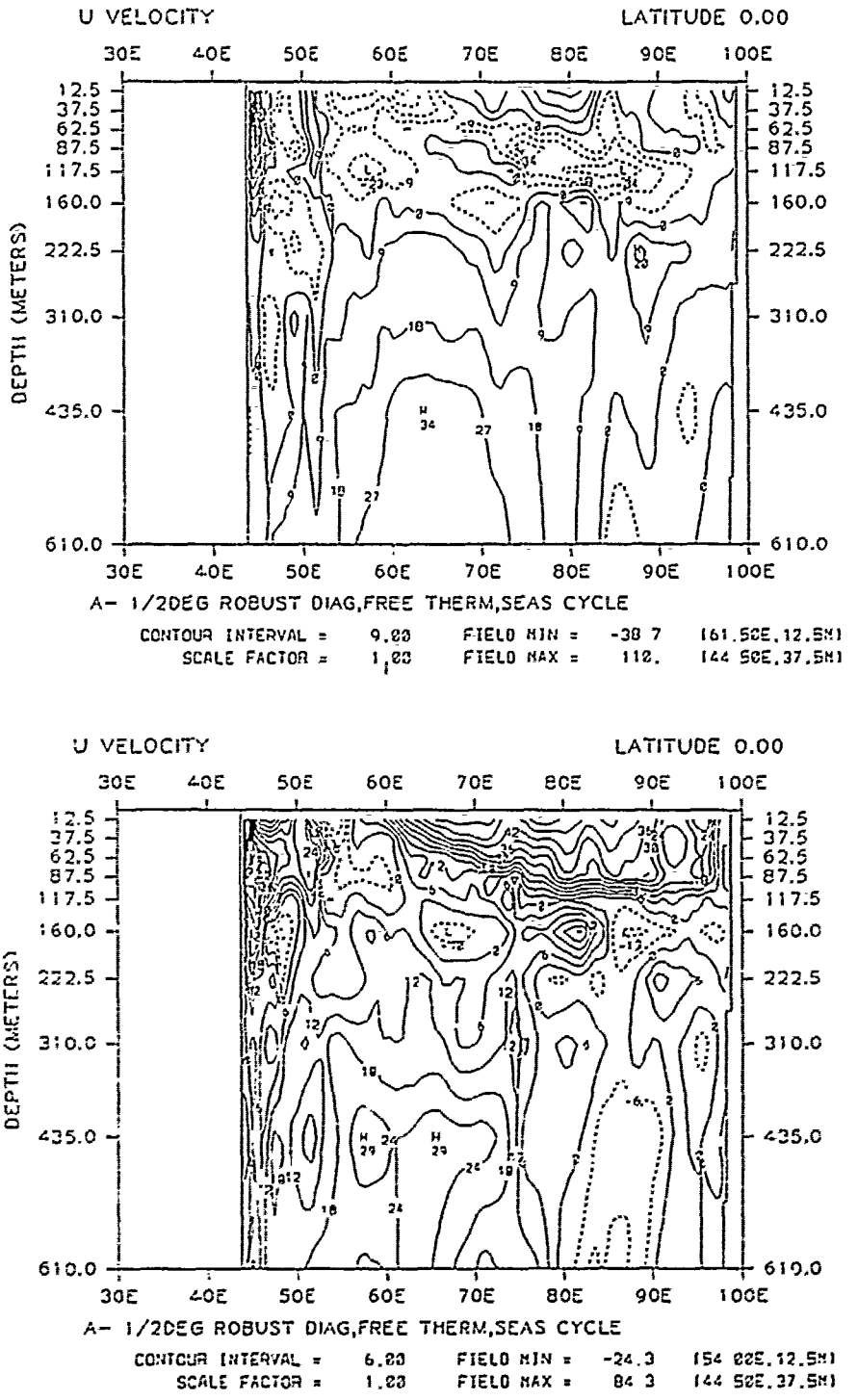

Figure 4.21 Monthly mean zonal currents at the equator during Year 4. (a) September and (b) October.

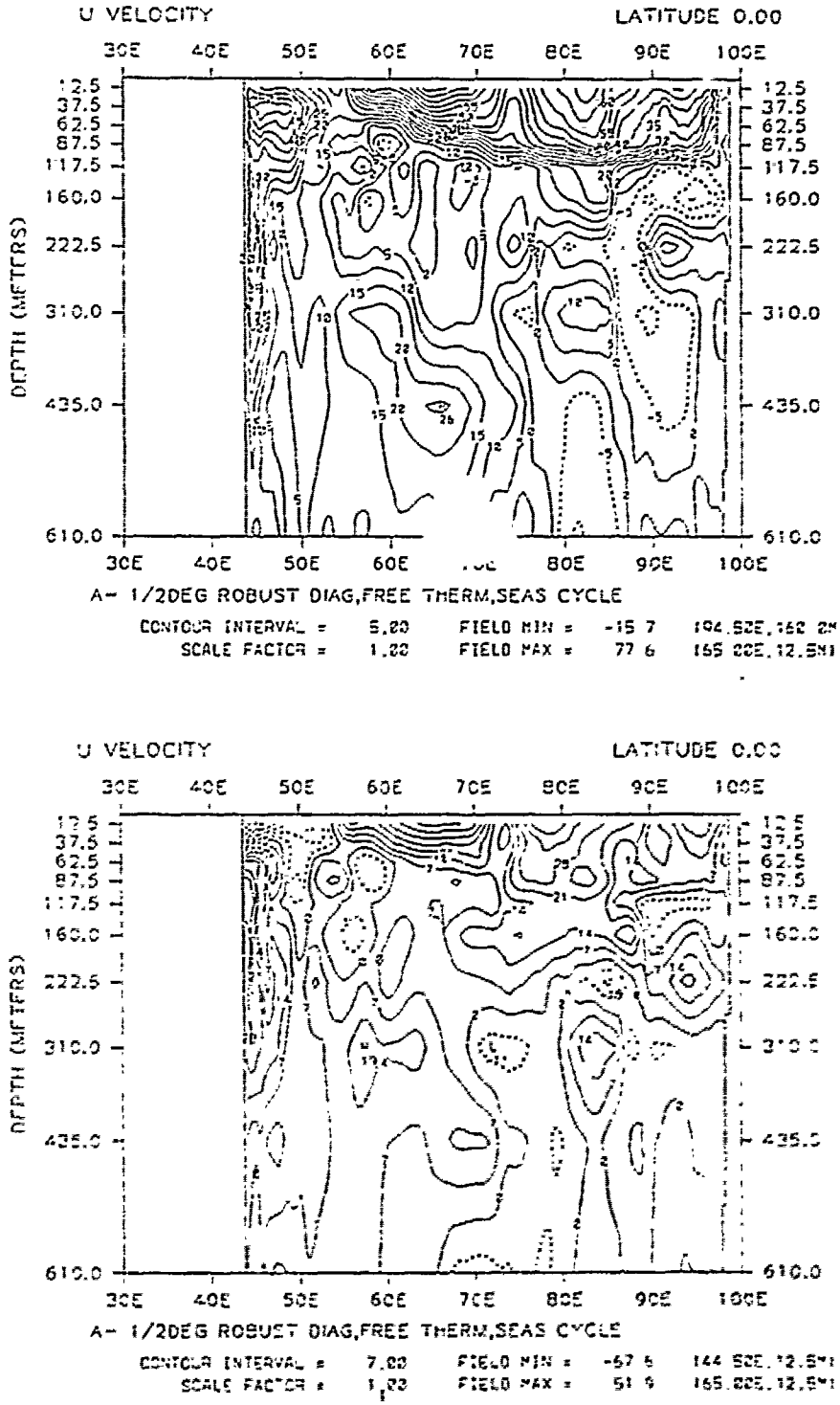

Figure 4.22 Monthly mean zonal currents at the equator during Year 4. (a) November and (b) December.

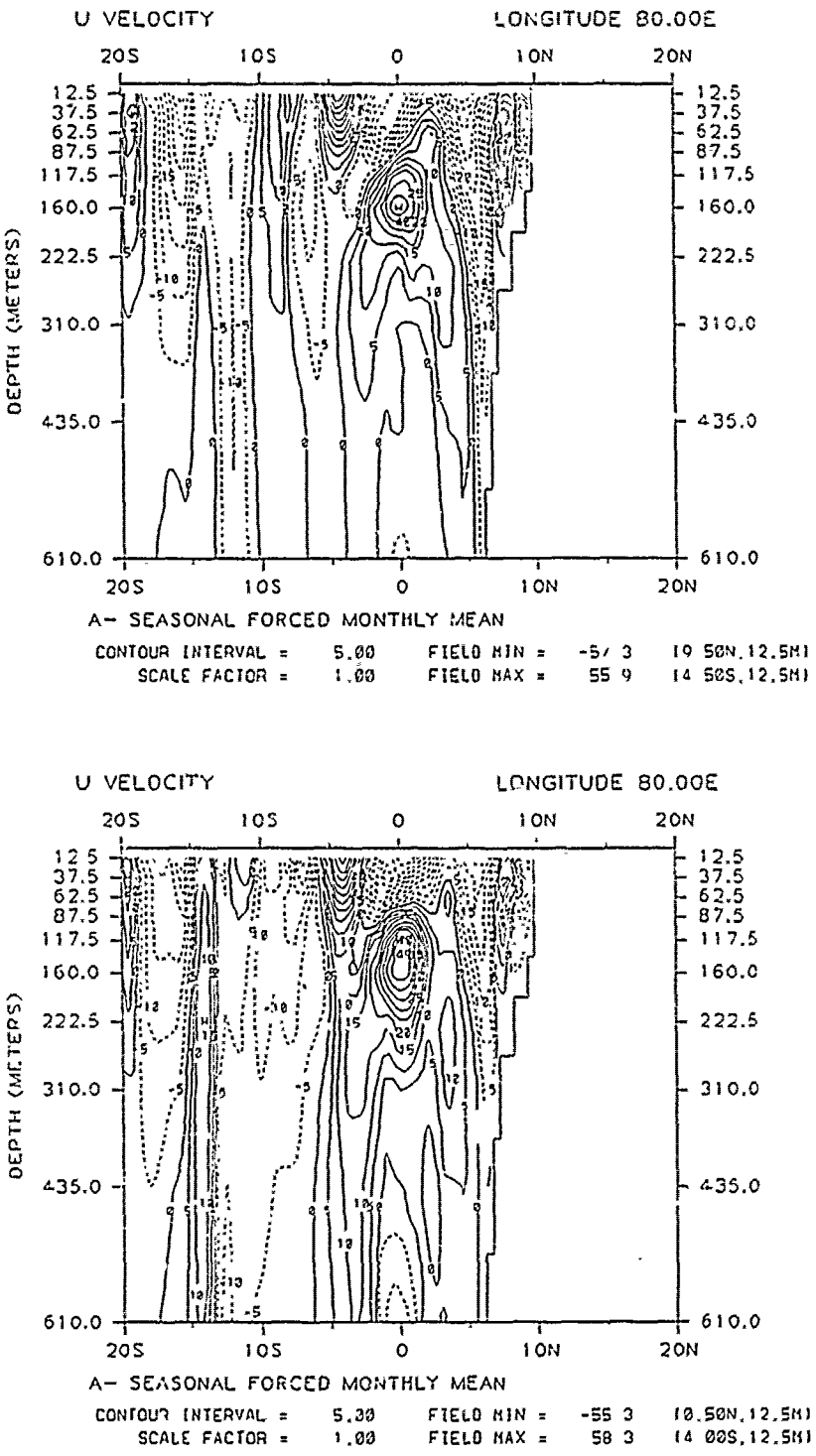

Figure 4.23 Monthly mean zonal currents at 80°E during Year 4. (a) January and (b) February.

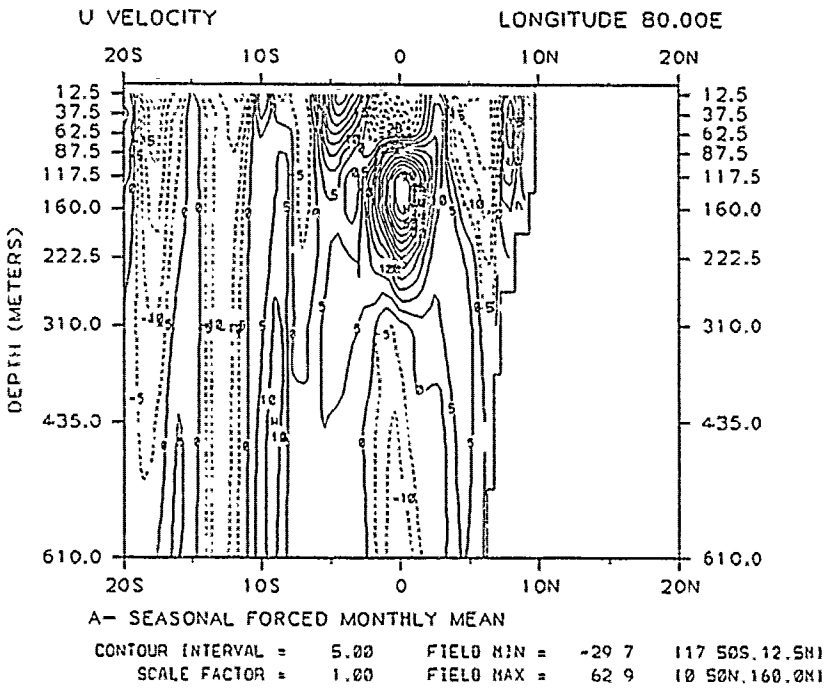

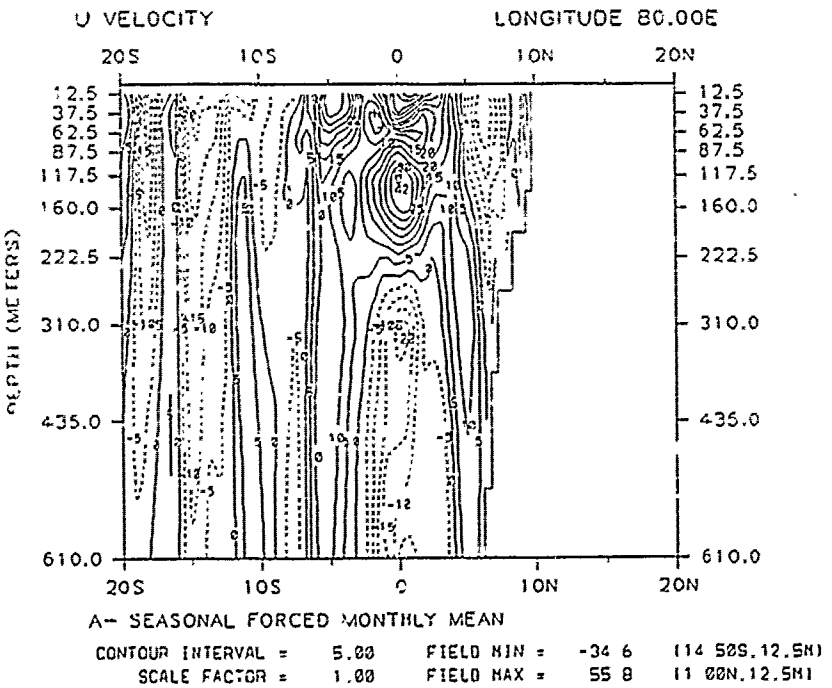

Figure 4.24 Monthly mean zonal currents at 80°E during Year 4. (a) March and (b) April.

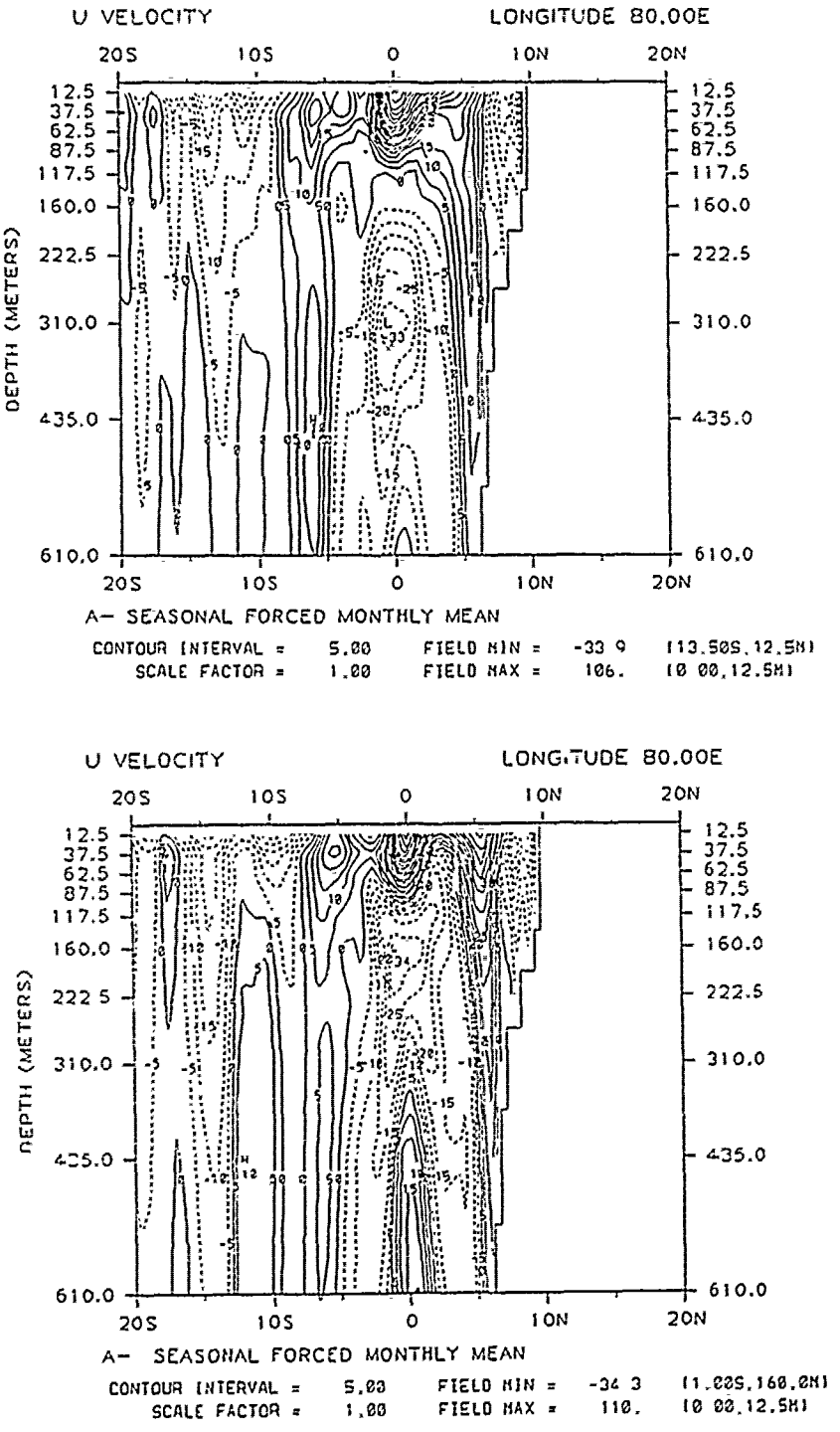

Figure 4.25 Monthly mean zonal currents at 80°E during Year 4. (a) May and (b) June.

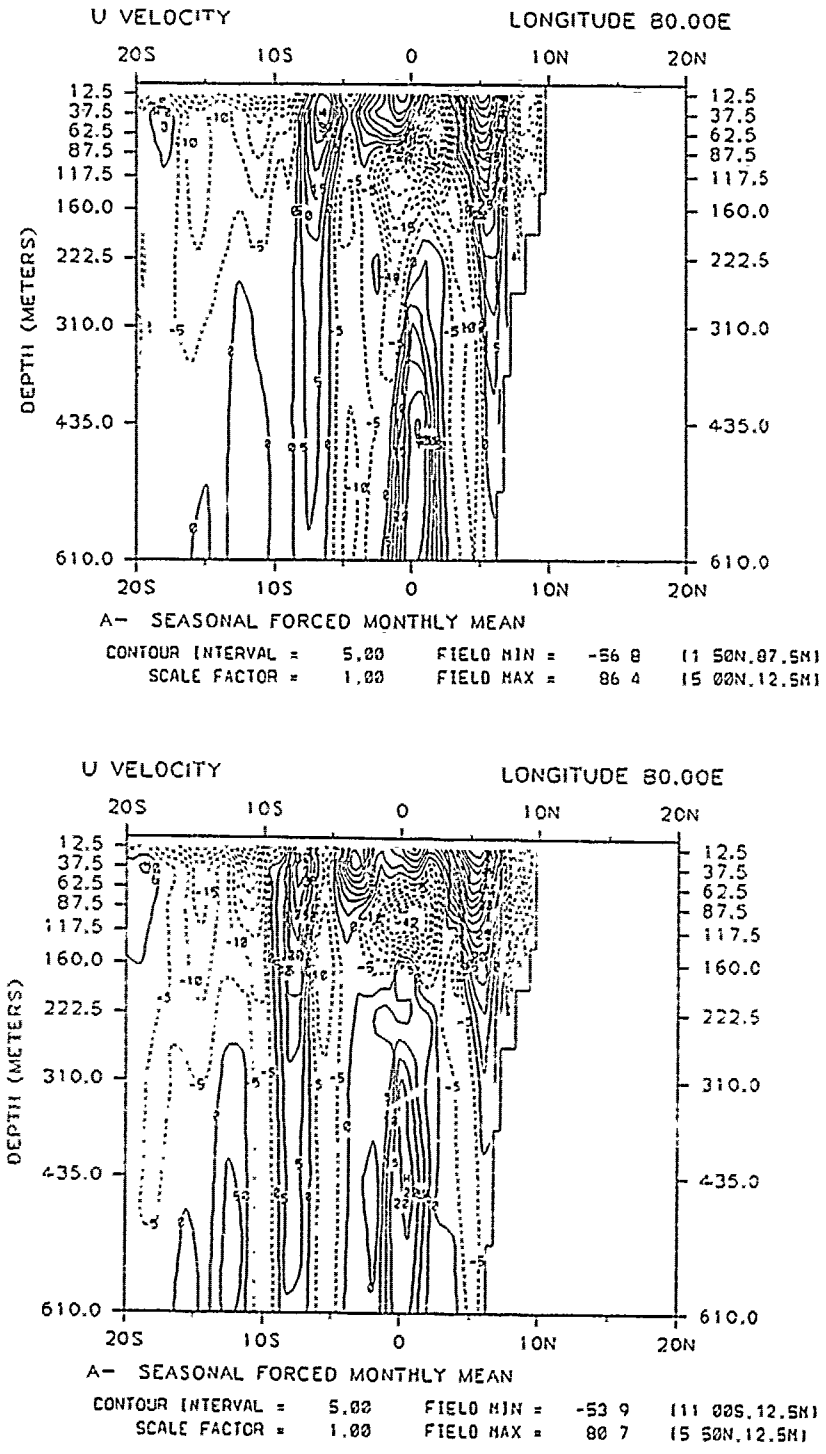

Figure 4.26 Monthly mean zonal currents at 80°E during Year 4. (a) July and (b) August.

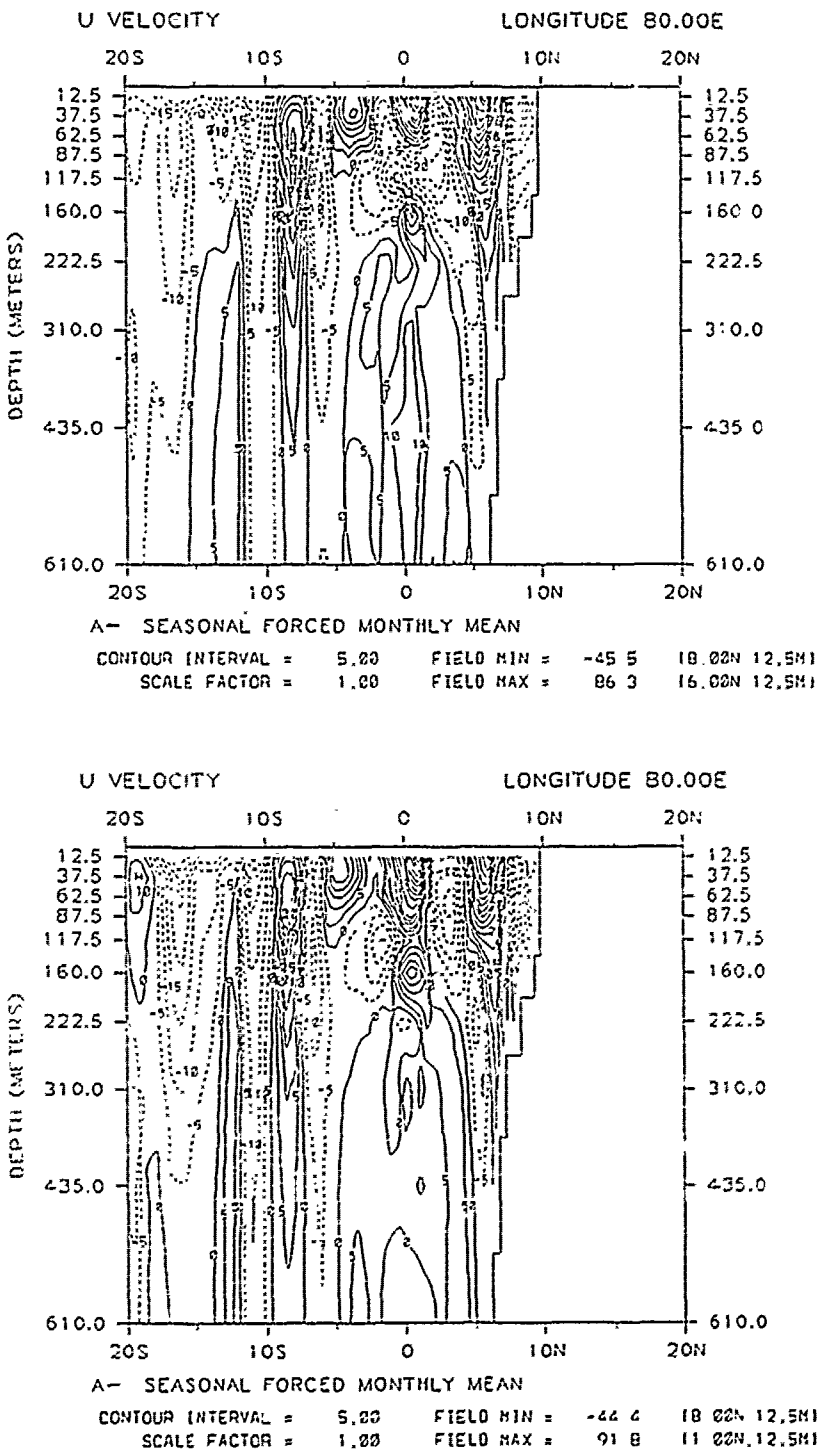

Figure 4.27 Monthly mean zonal currents at 80°E during Year 4. (a) September and (b) October.

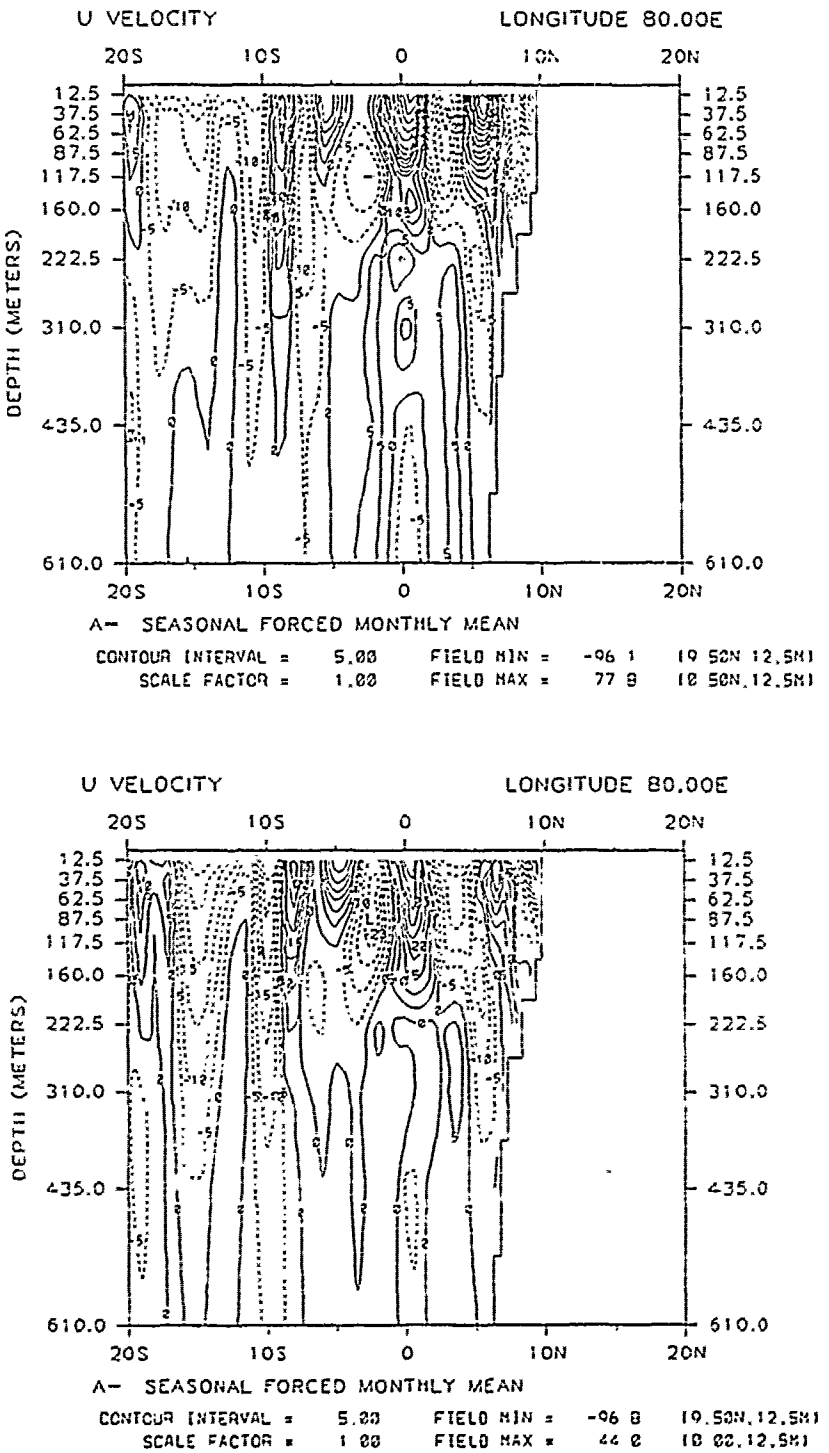

Figure 4.28 Monthly mean zonal currents at 80°E during Year 4. (a) November and (b) December.

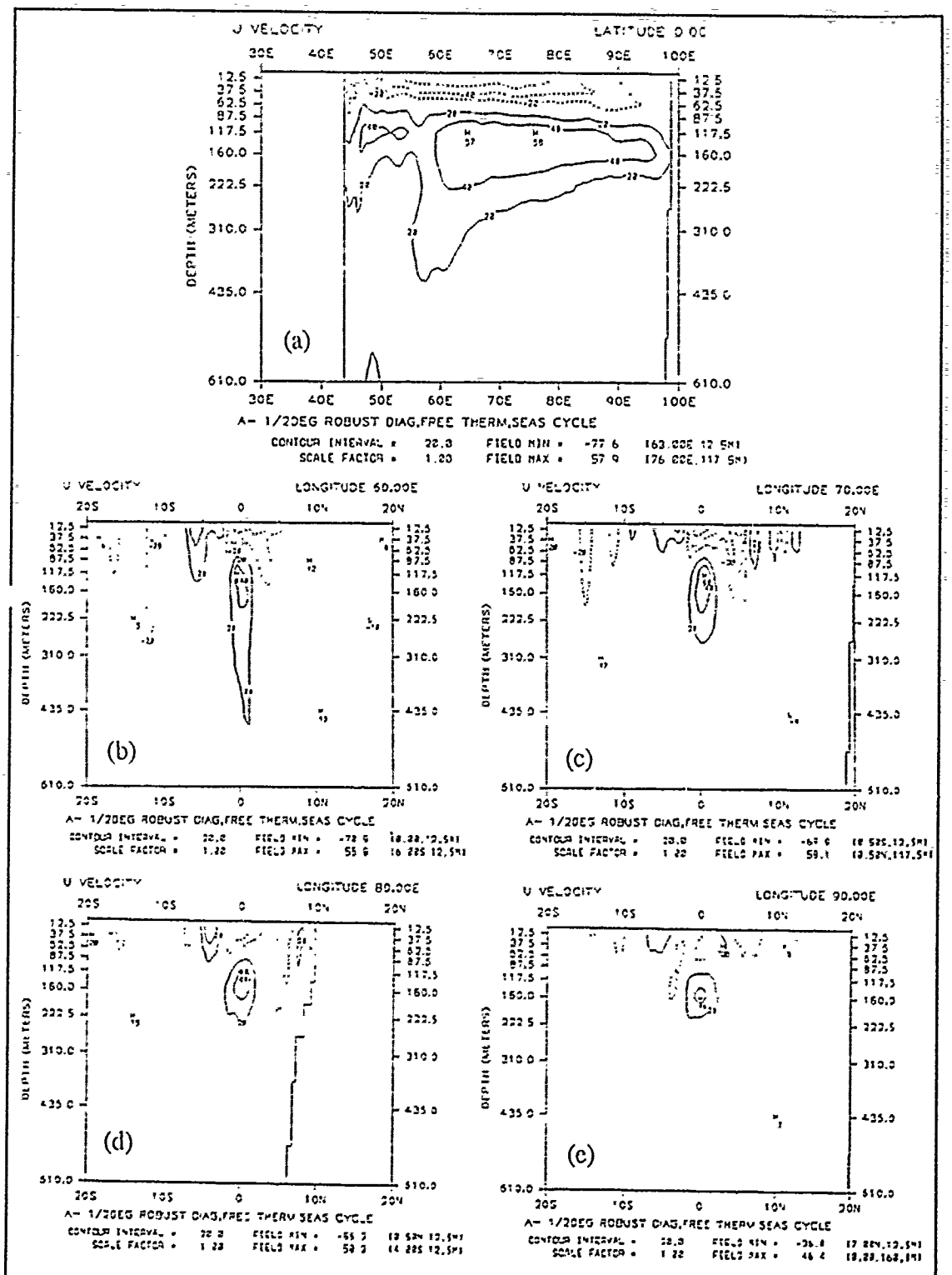

Figure 4.29 Mean monthly zonal currents in February of Year 4. (a) Meridional section at 0°, (b) 60°E, (c) 70°E, (d) 80°E, (e) 90°E.

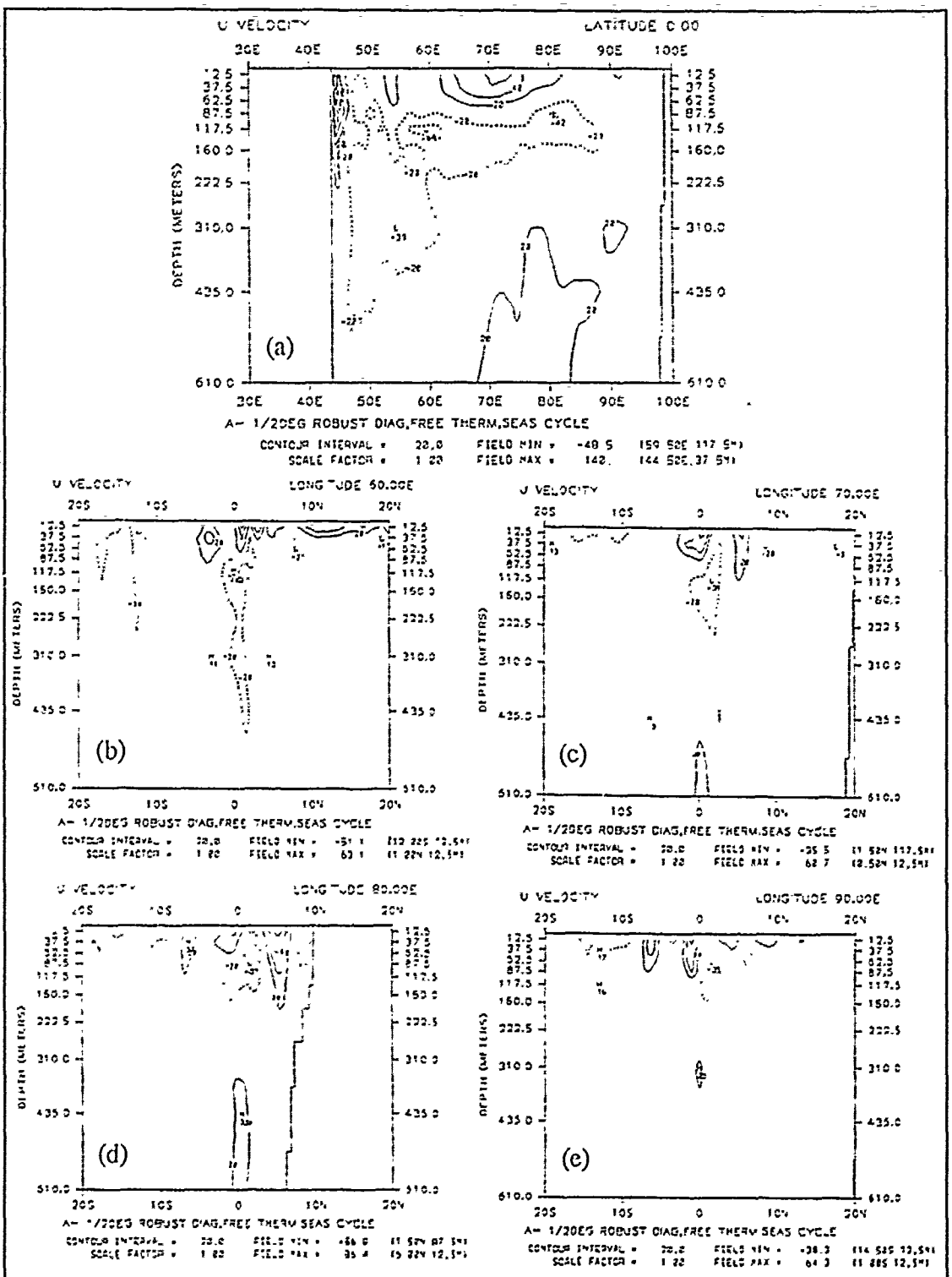

Figure 4.30 Mean monthly zonal currents in July of Year 4. (a) Meridional section at 0°, (b) 60°E, (c) 70°E, (d) 80°E, (e) 90°E.

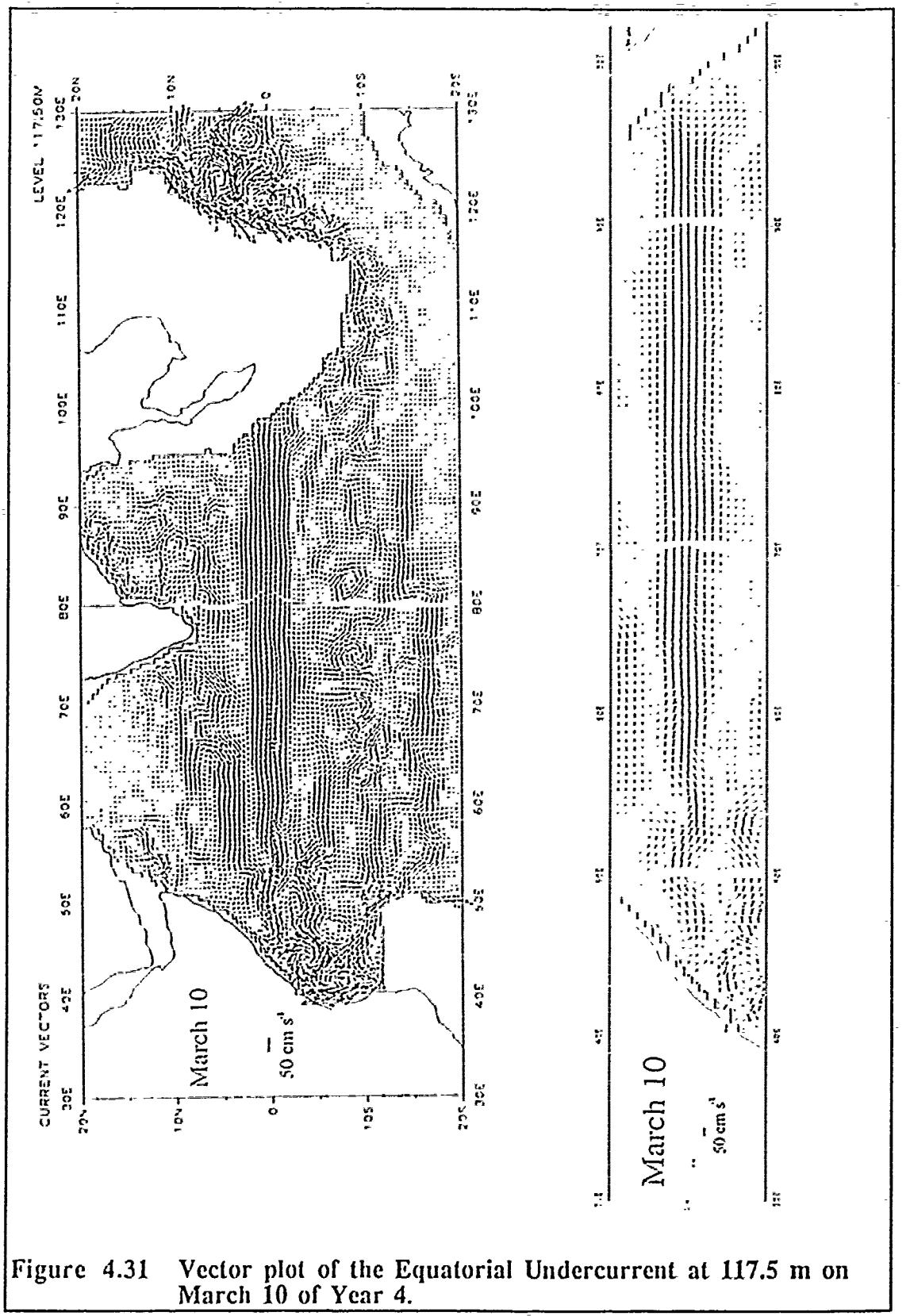

Figure 4.31 Vector plot of the Equatorial Undercurrent at 117.5 m on March 10 of Year 4.

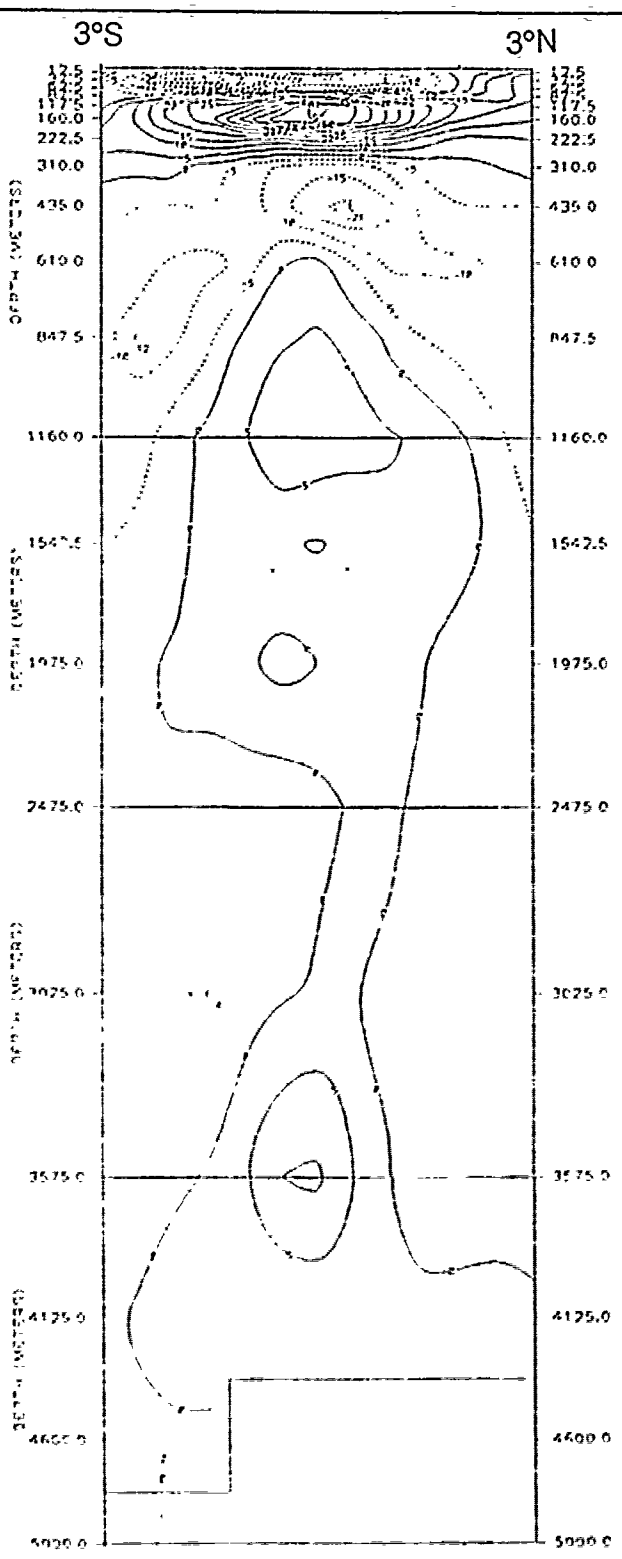

Figure 4.32 **Deep current structure in the equatorial Indian Ocean.** This plot of zonal velocity (cm s^{-1})at 85°E on 19 March of Year 4 illustrates the complex deep current structure in the equatorial region.

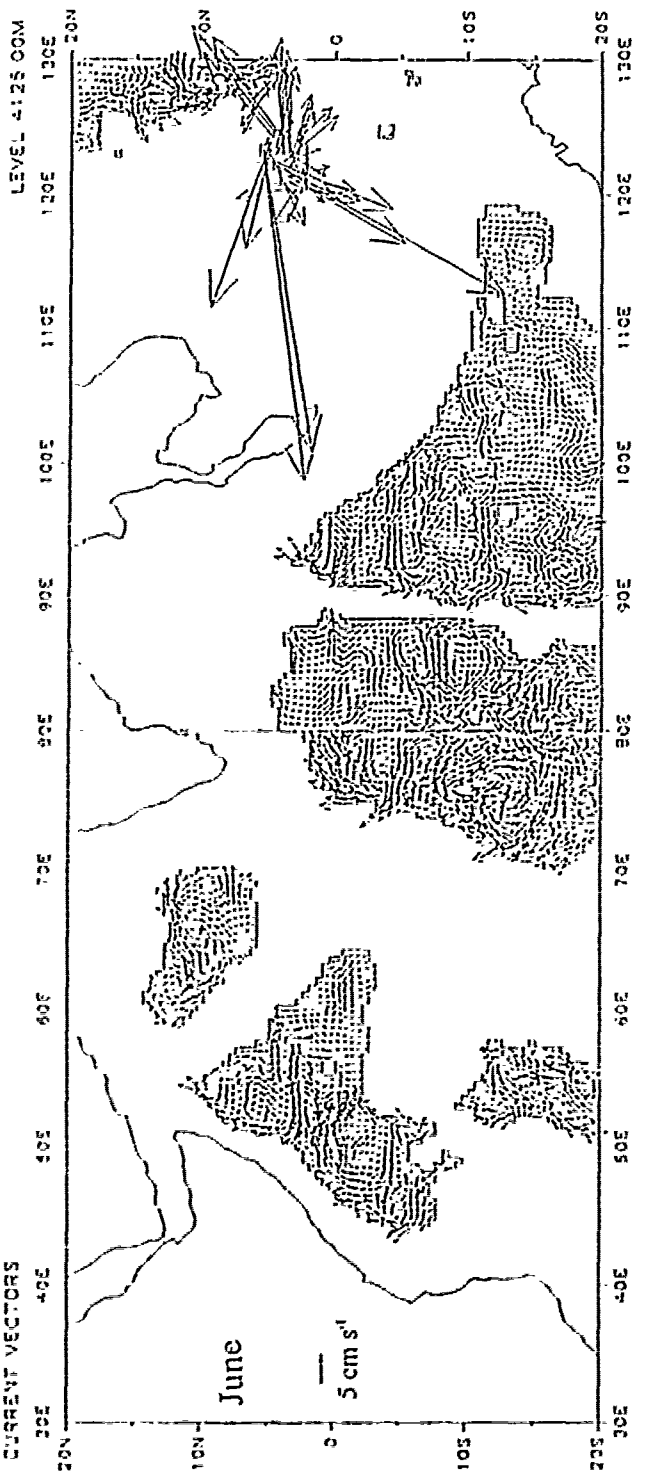

Figure 4.33 **Mean monthly current at 4125 m during of Year 4.** The anomalous currents in the Celebes Sea are due to bad data discovered in the Hellerman and Rosenstein data set during the model run.

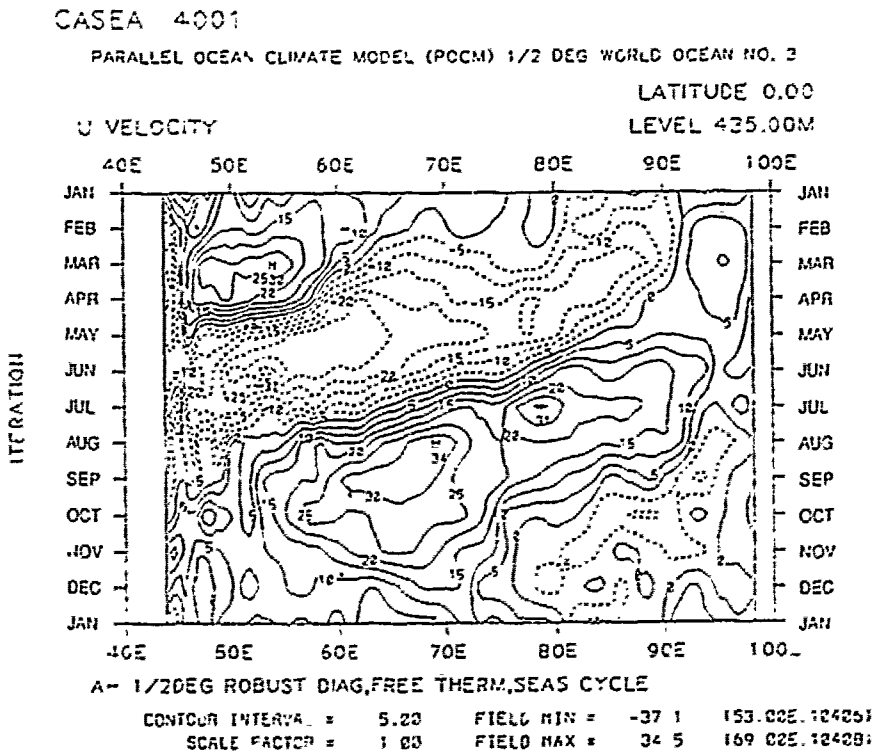

Figure 4.34 Longitude-time plot of Year 4 zonal velocity at the equator at 435 m. A system of westward-moving regions of convergence and divergence is visible.

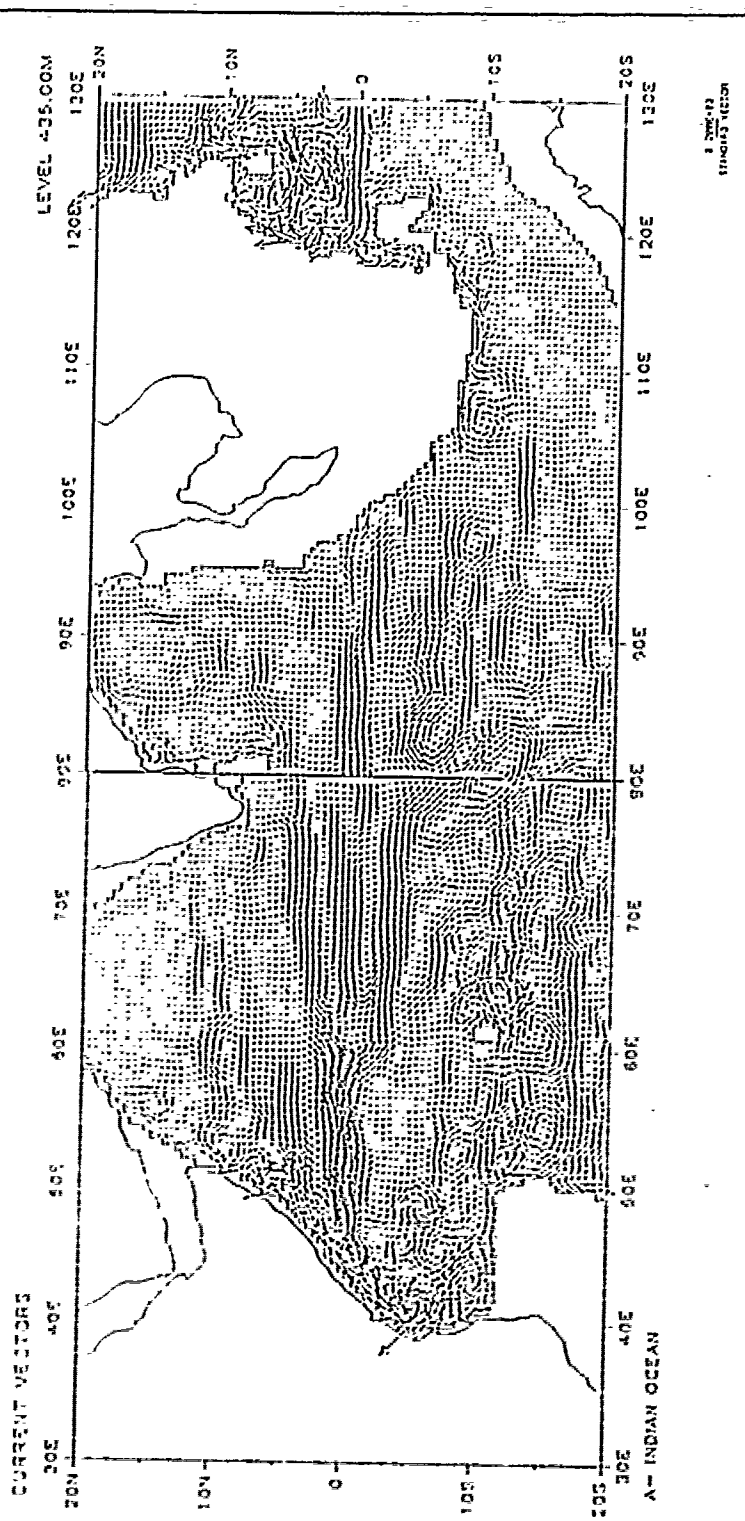

Figure 4.35 Currents at 435 m during March of Year 4.

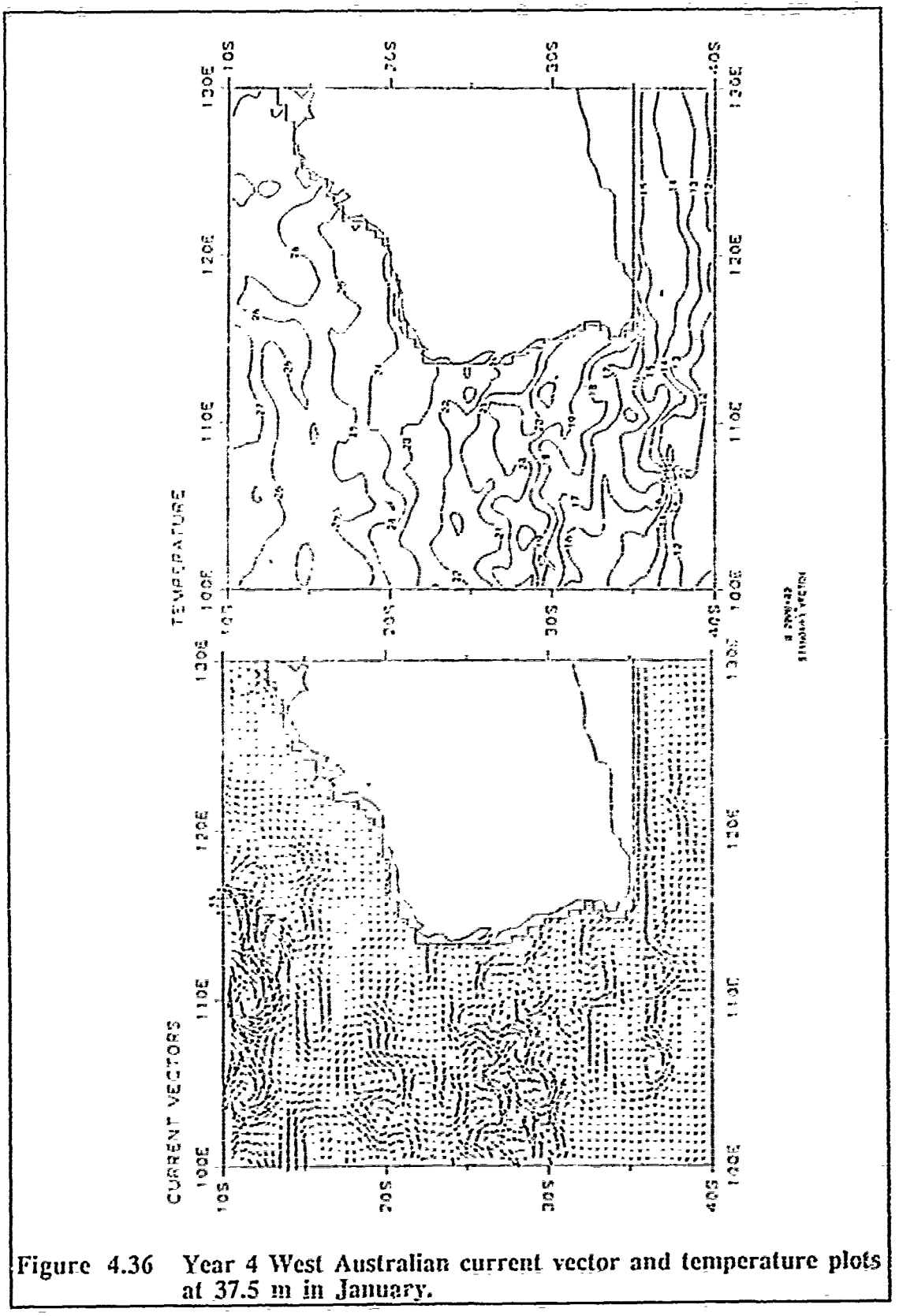

Figure 4.36 Year 4 West Australian current vector and temperature plots at 37.5 m in January.

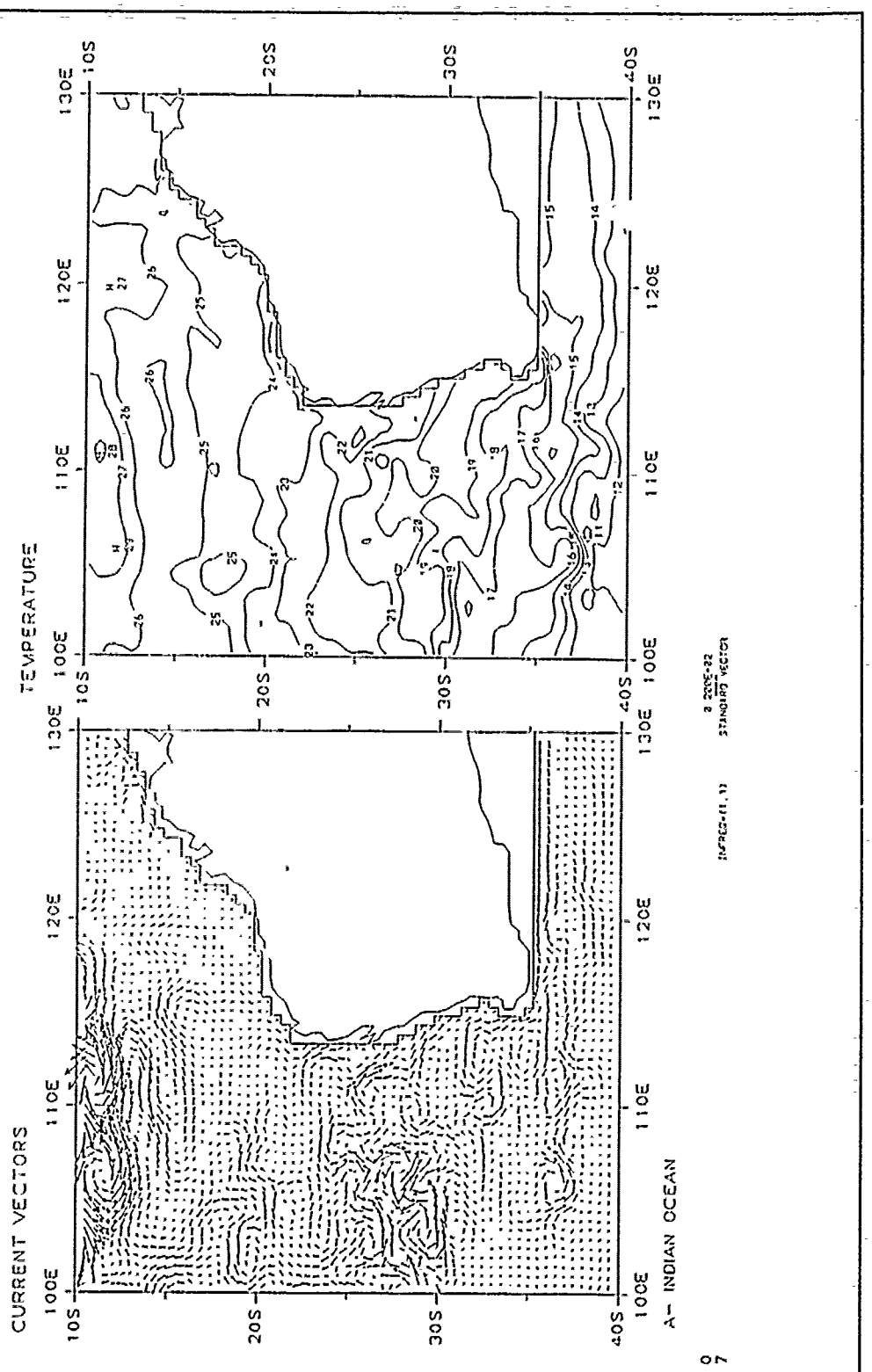

Figure 4.37 Year 4 West Australian current vector and temperature plots at 37.5 m in February.

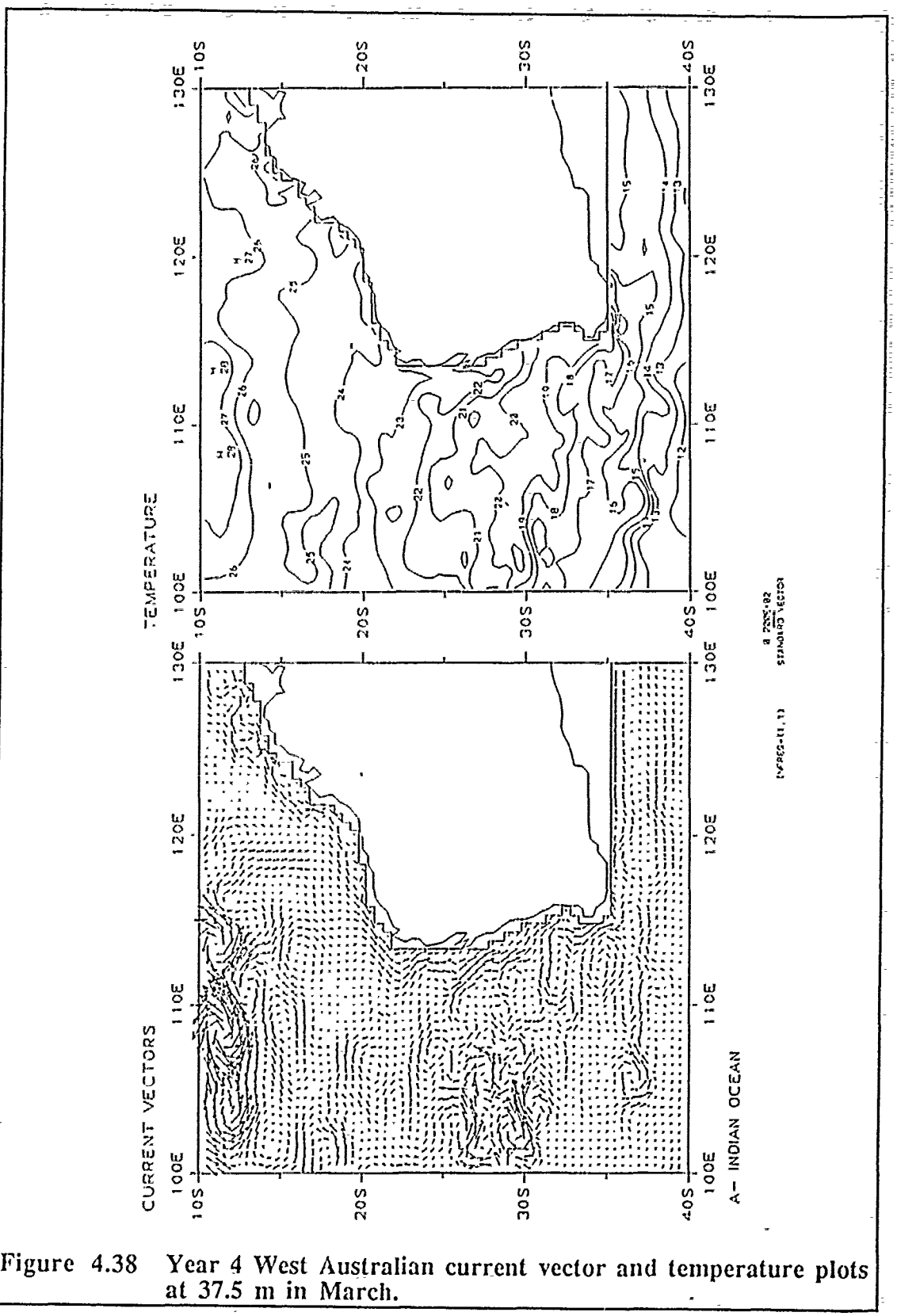

Figure 4.38 Year 4 West Australian current vector and temperature plots at 37.5 m in March.

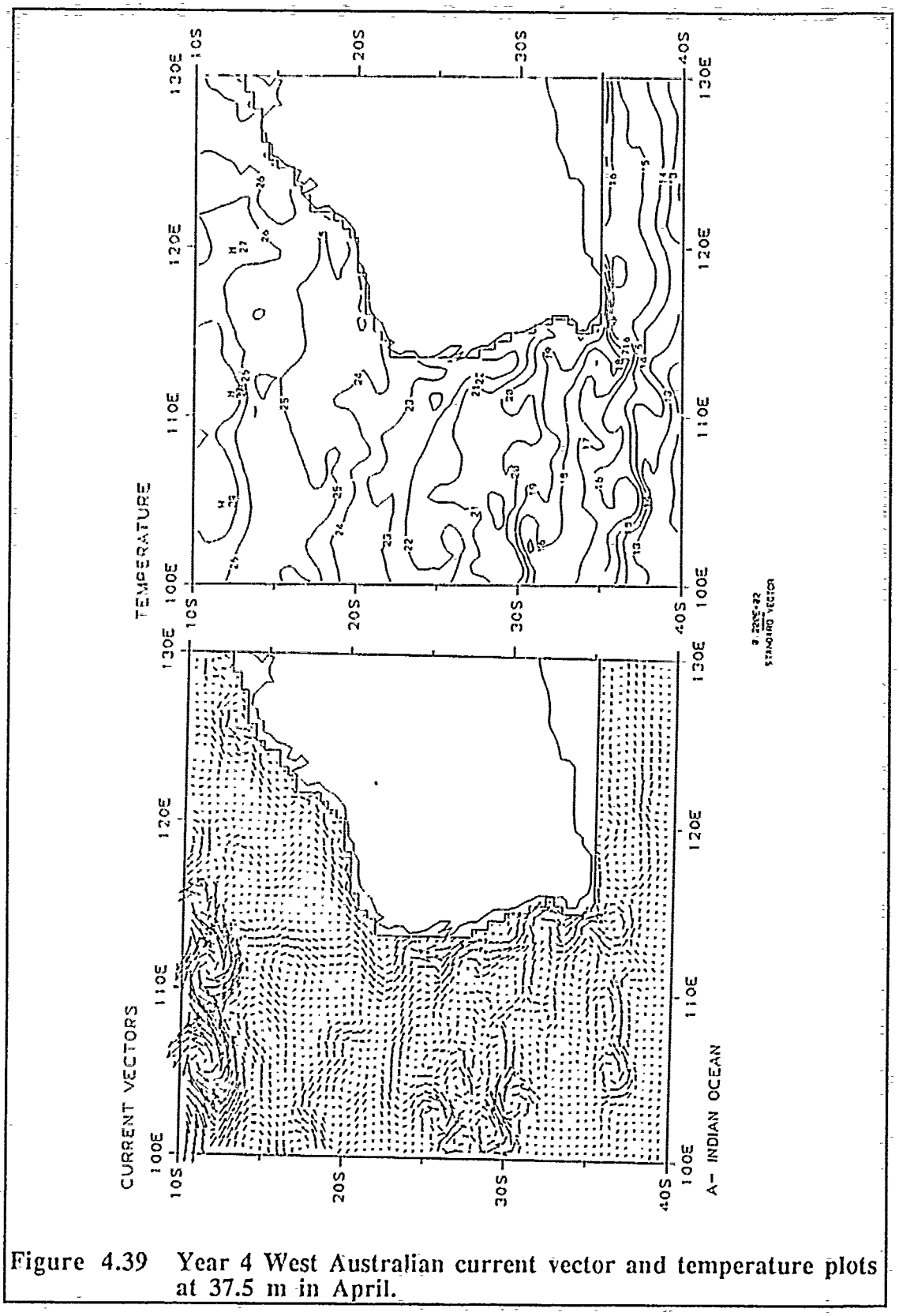

Figure 4.39 Year 4 West Australian current vector and temperature plots at 37.5 m in April.

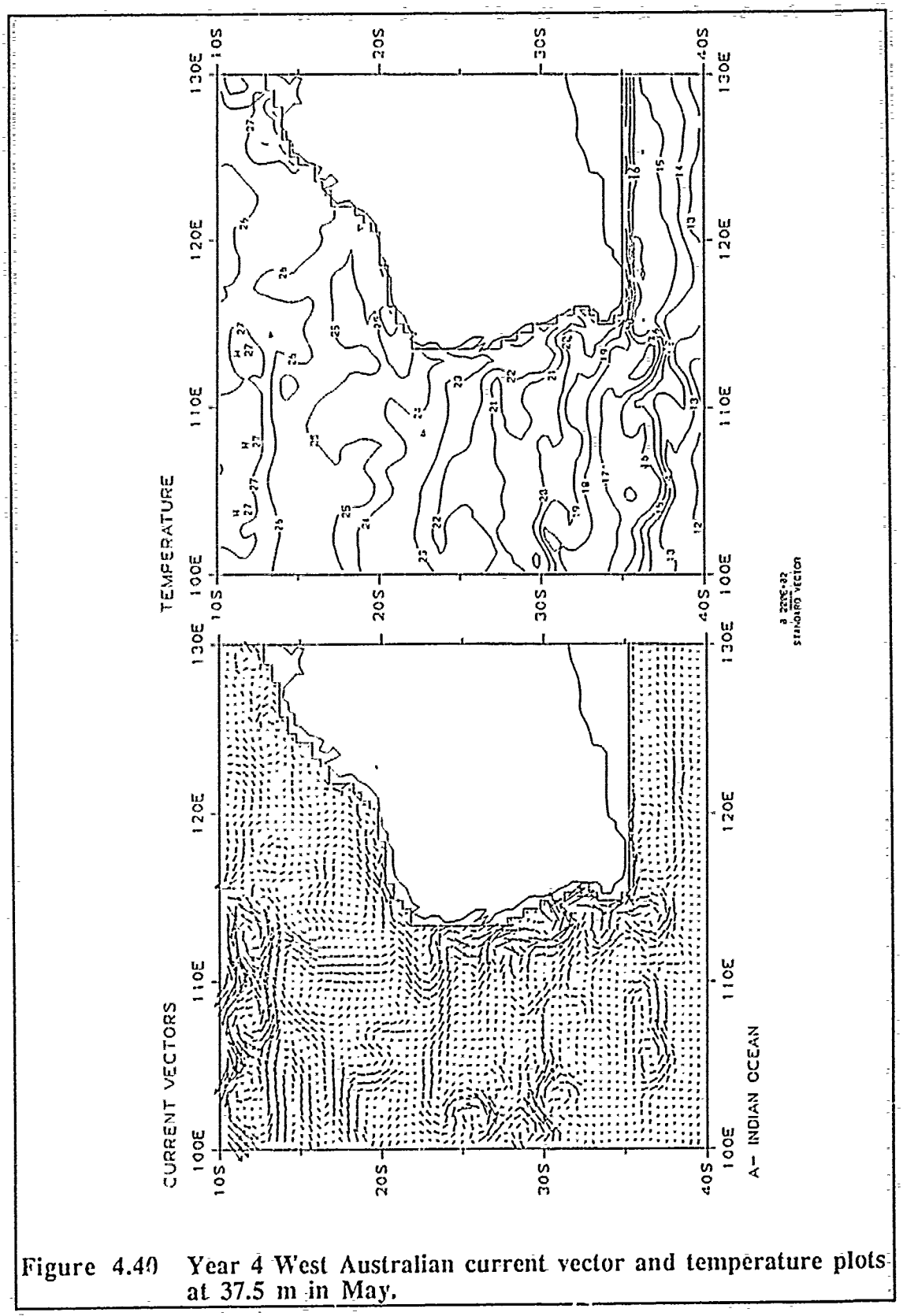

Figure 4.40 Year 4 West Australian current vector and temperature plots at 37.5 m in May.

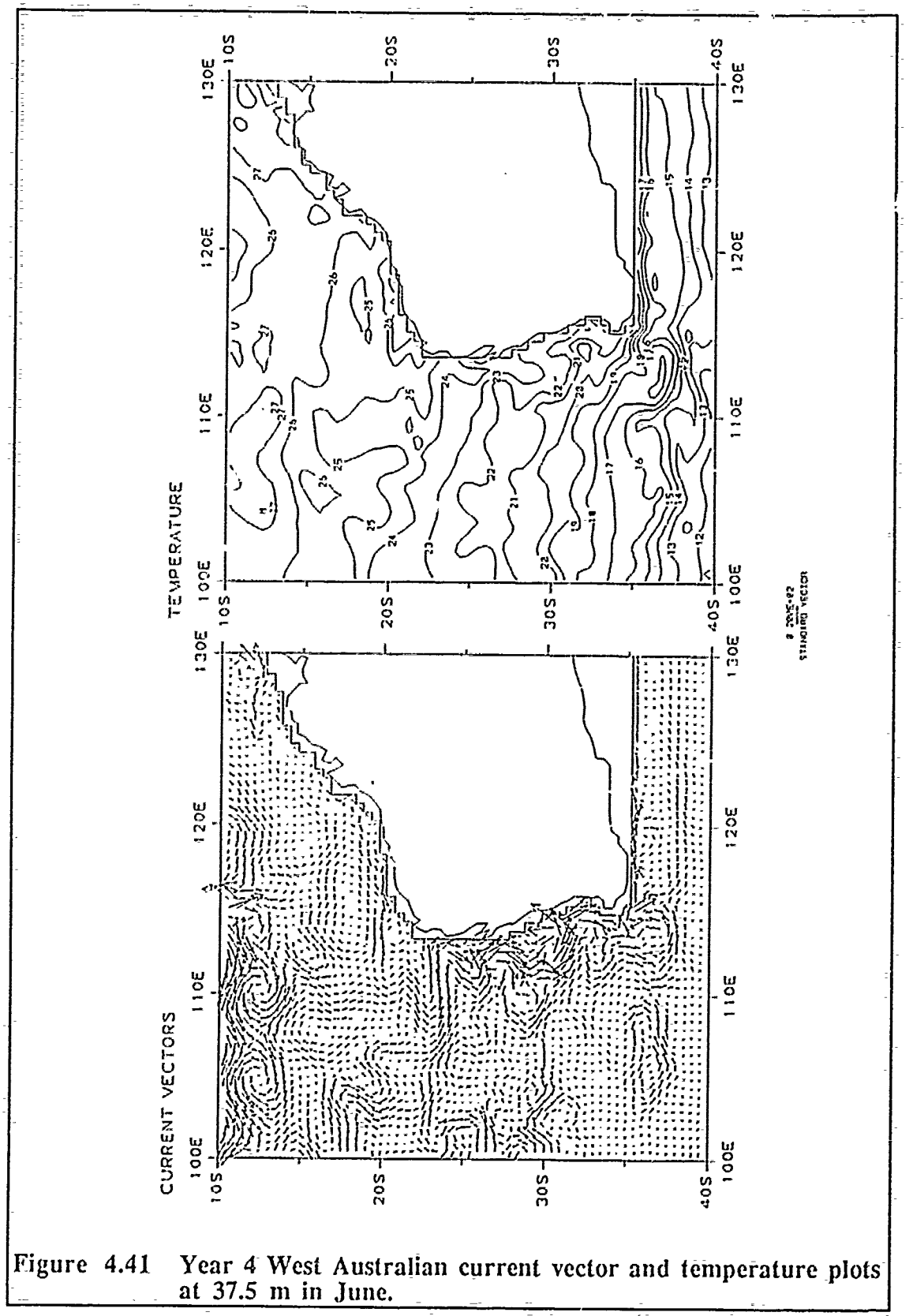

Figure 4.41 Year 4 West Australian current vector and temperature plots at 37.5 m in June.

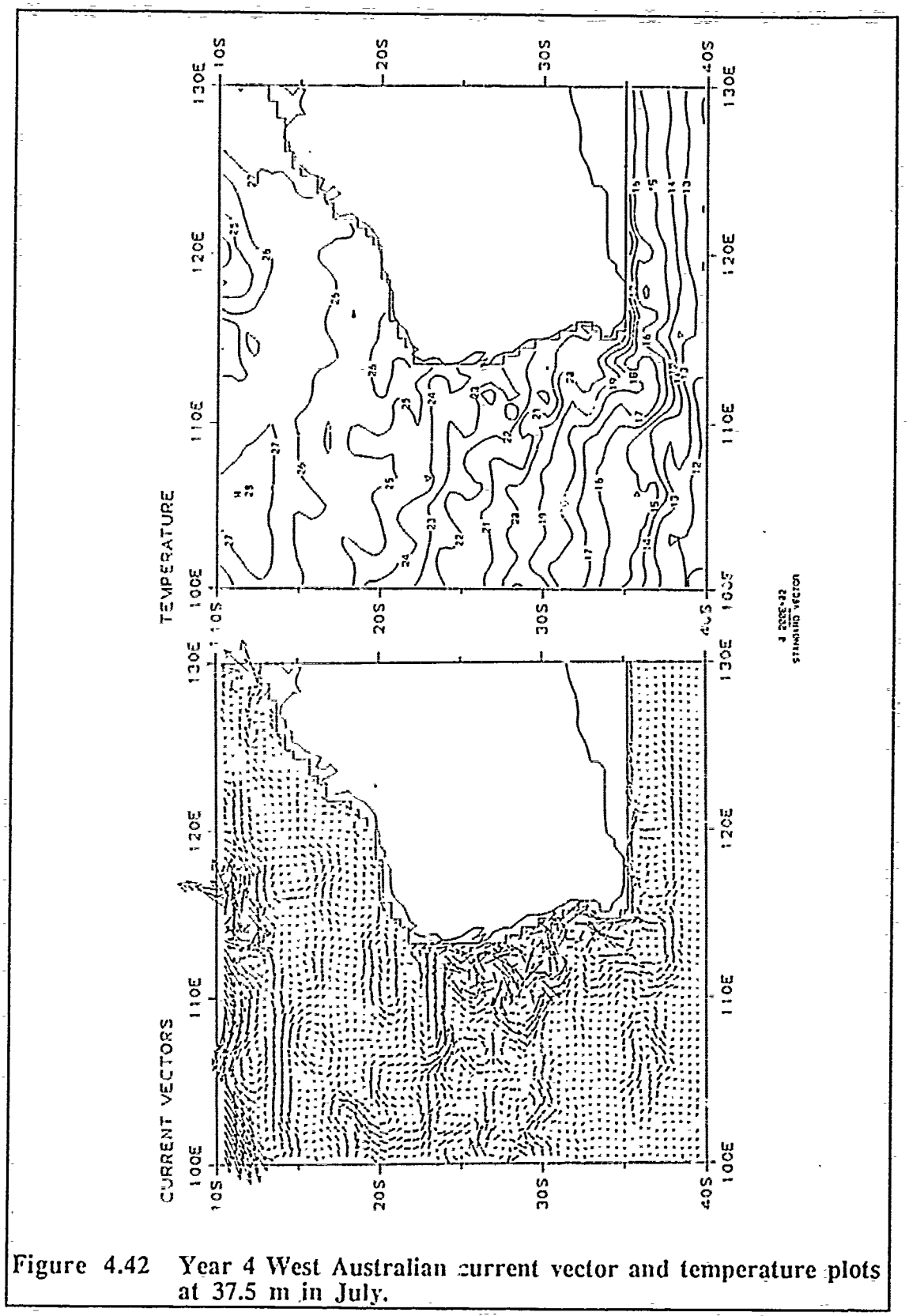

Figure 4.42 Year 4 West Australian current vector and temperature plots at 37.5 m in July.

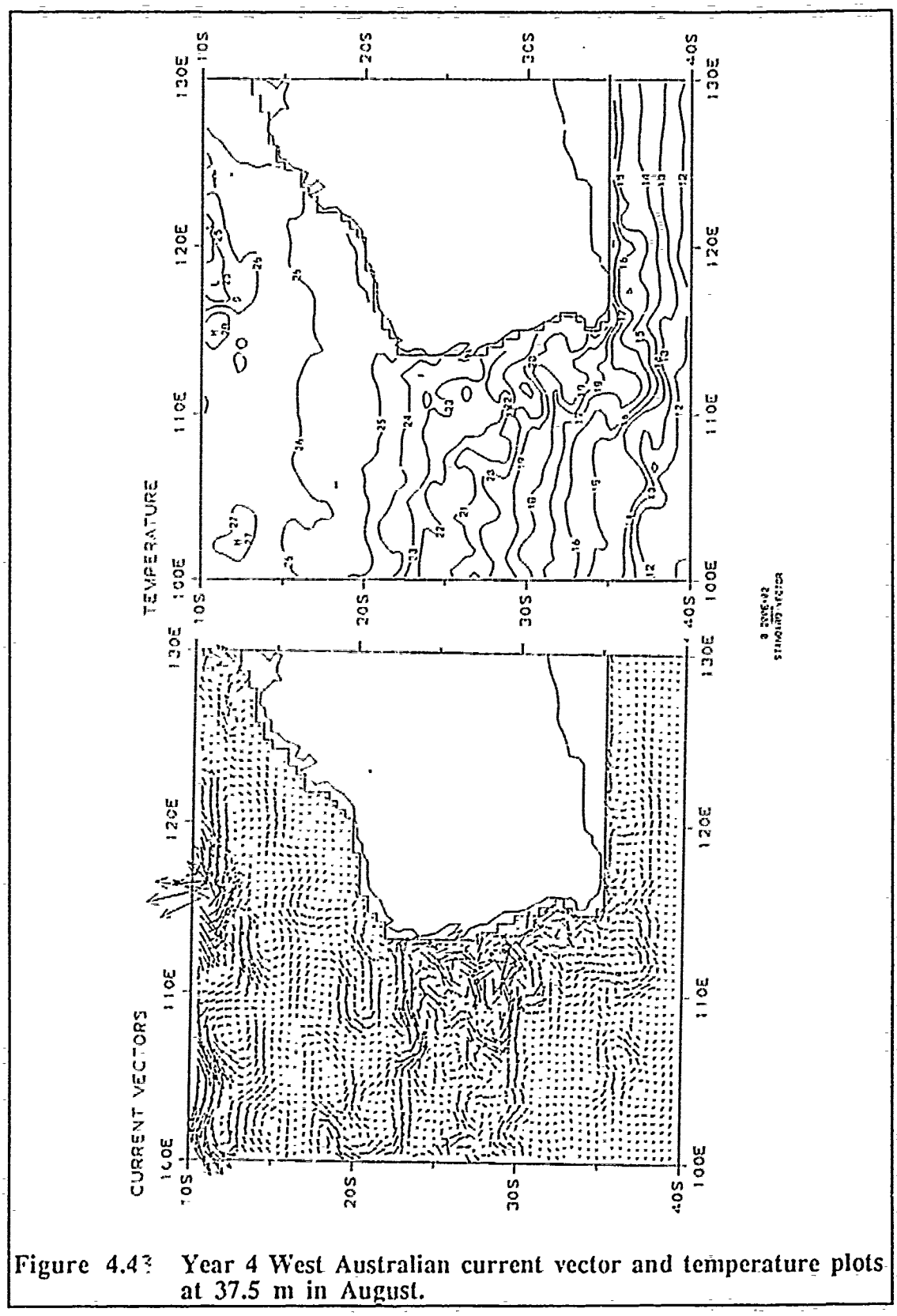

Figure 4.43 Year 4 West Australian current vector and temperature plots at 37.5 m in August.

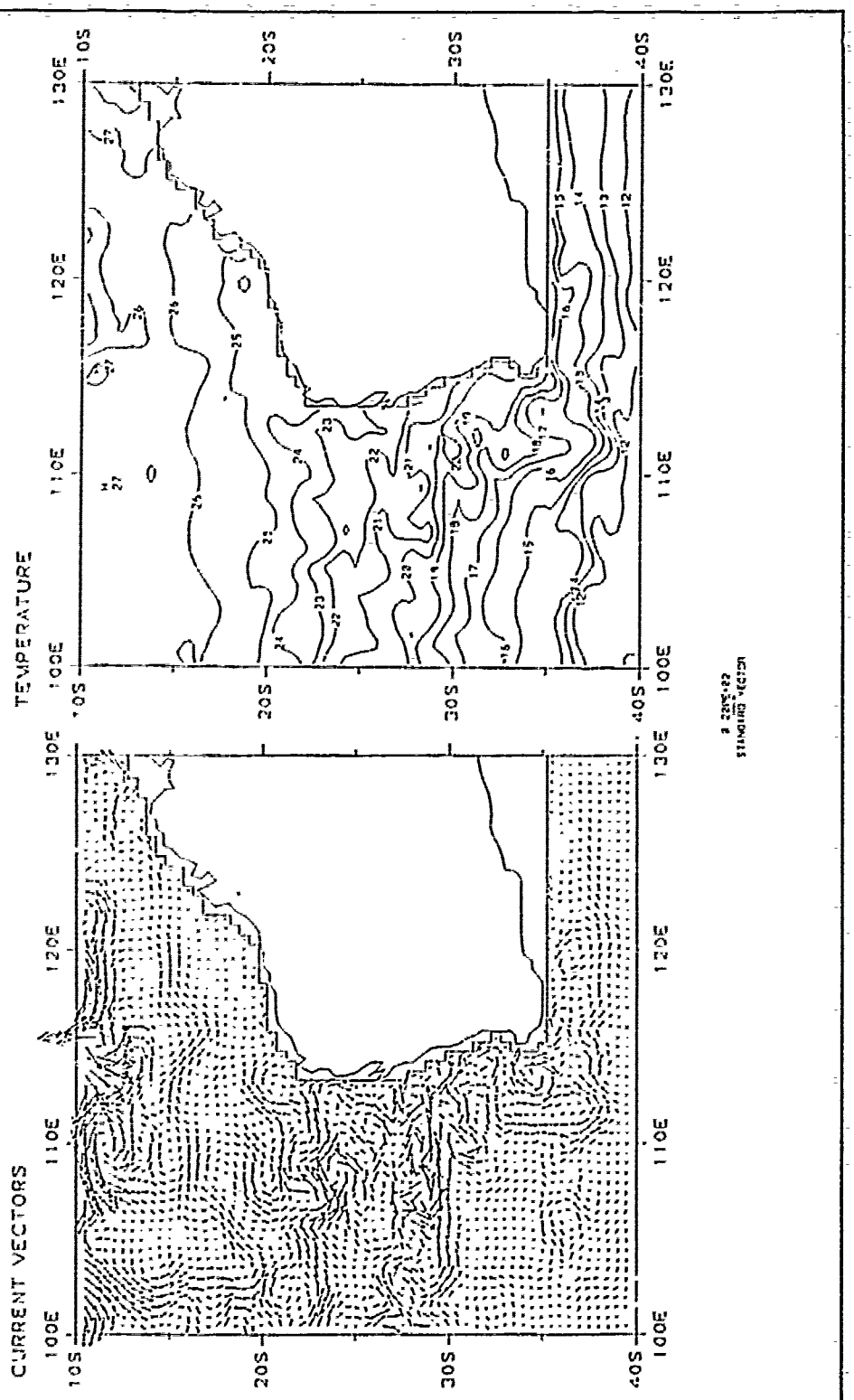

Figure 4.44 Year 4 West Australian current vector and temperature plots at 37.5 m in September.

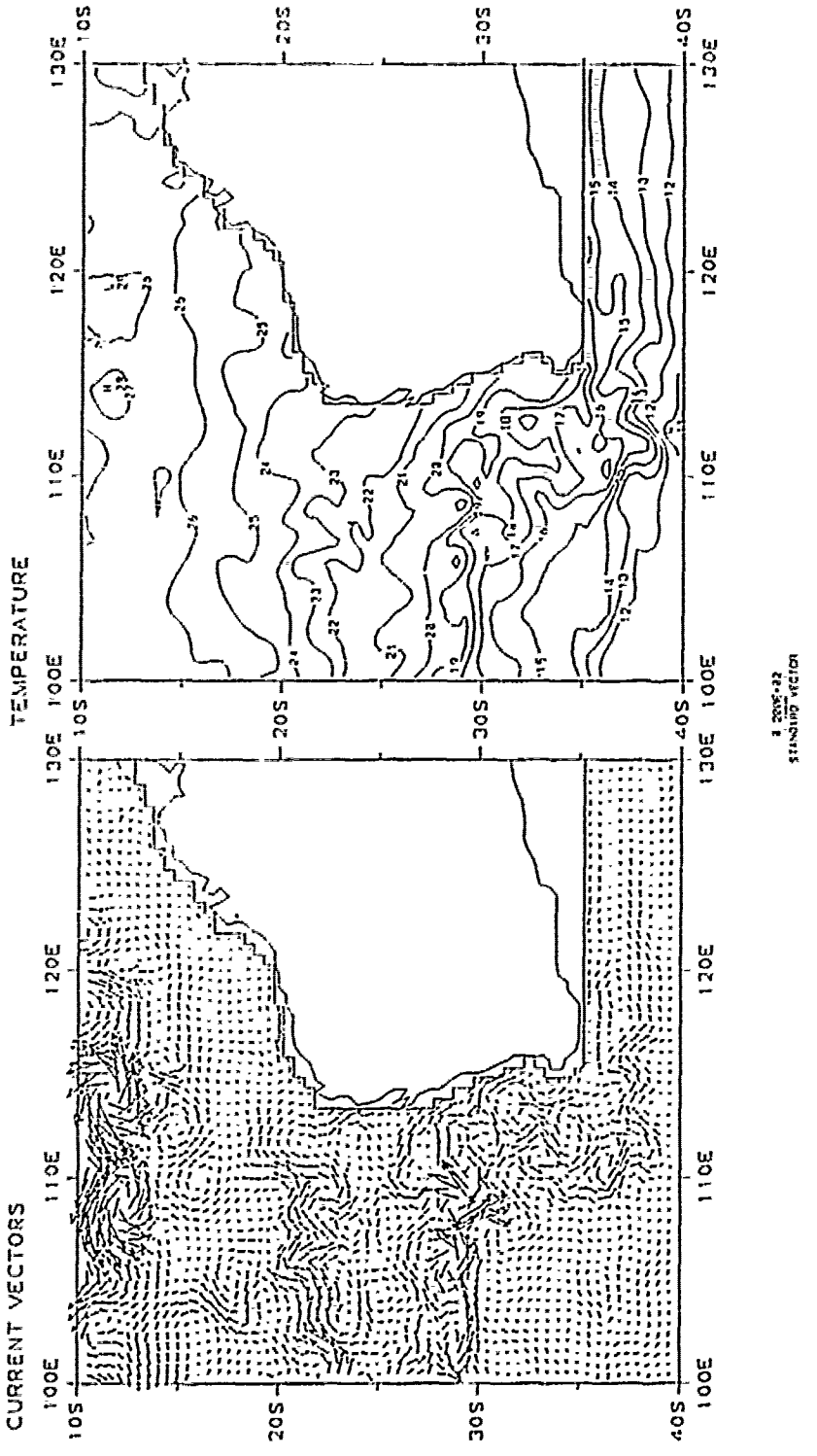

Figure 4.45 Year 4 West Australian current vector and temperature plots at 37.5 m in October.

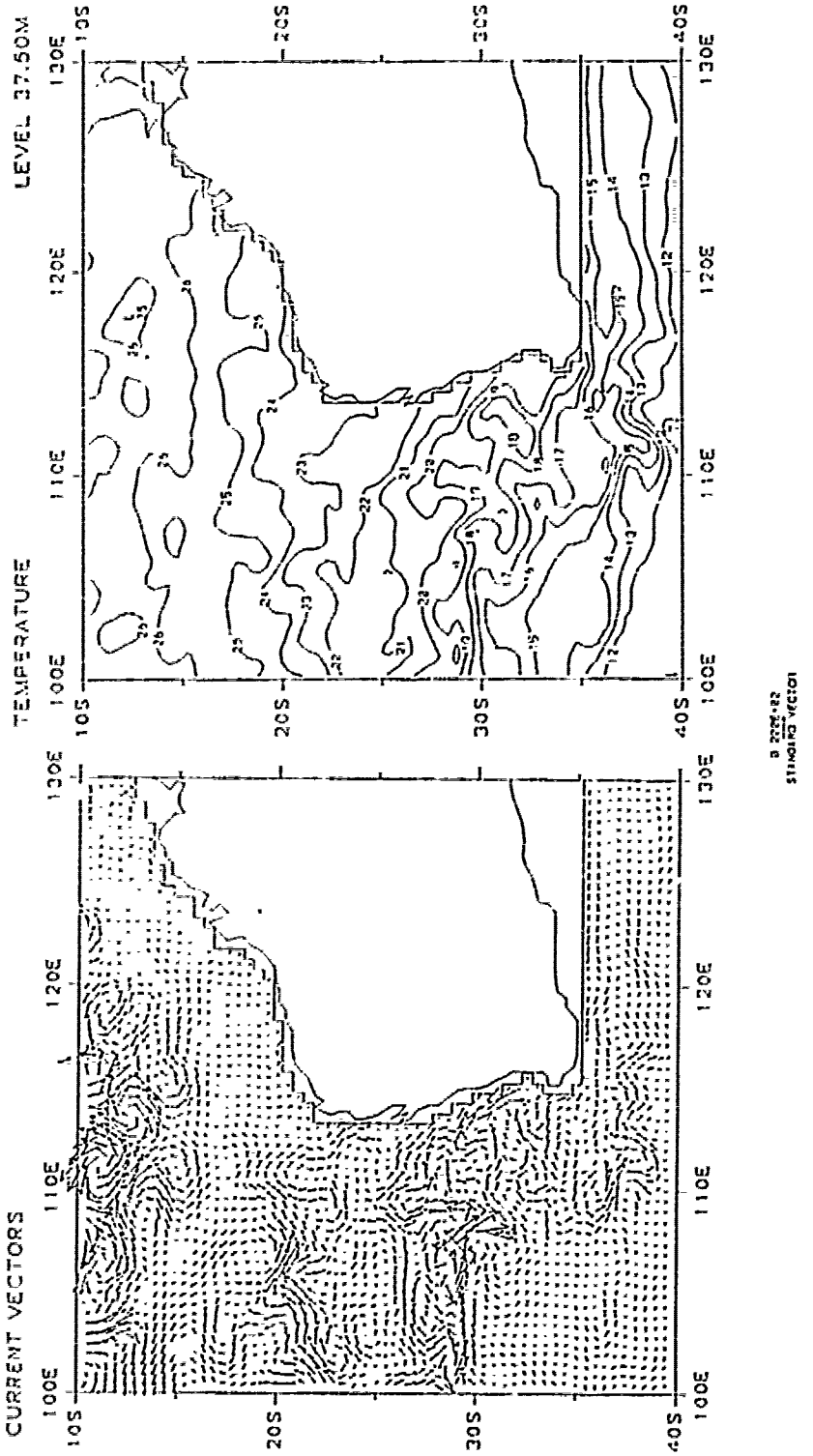

Figure 4.46 Year 4 West Australian current vector and temperature plots at 37.5 m in November.

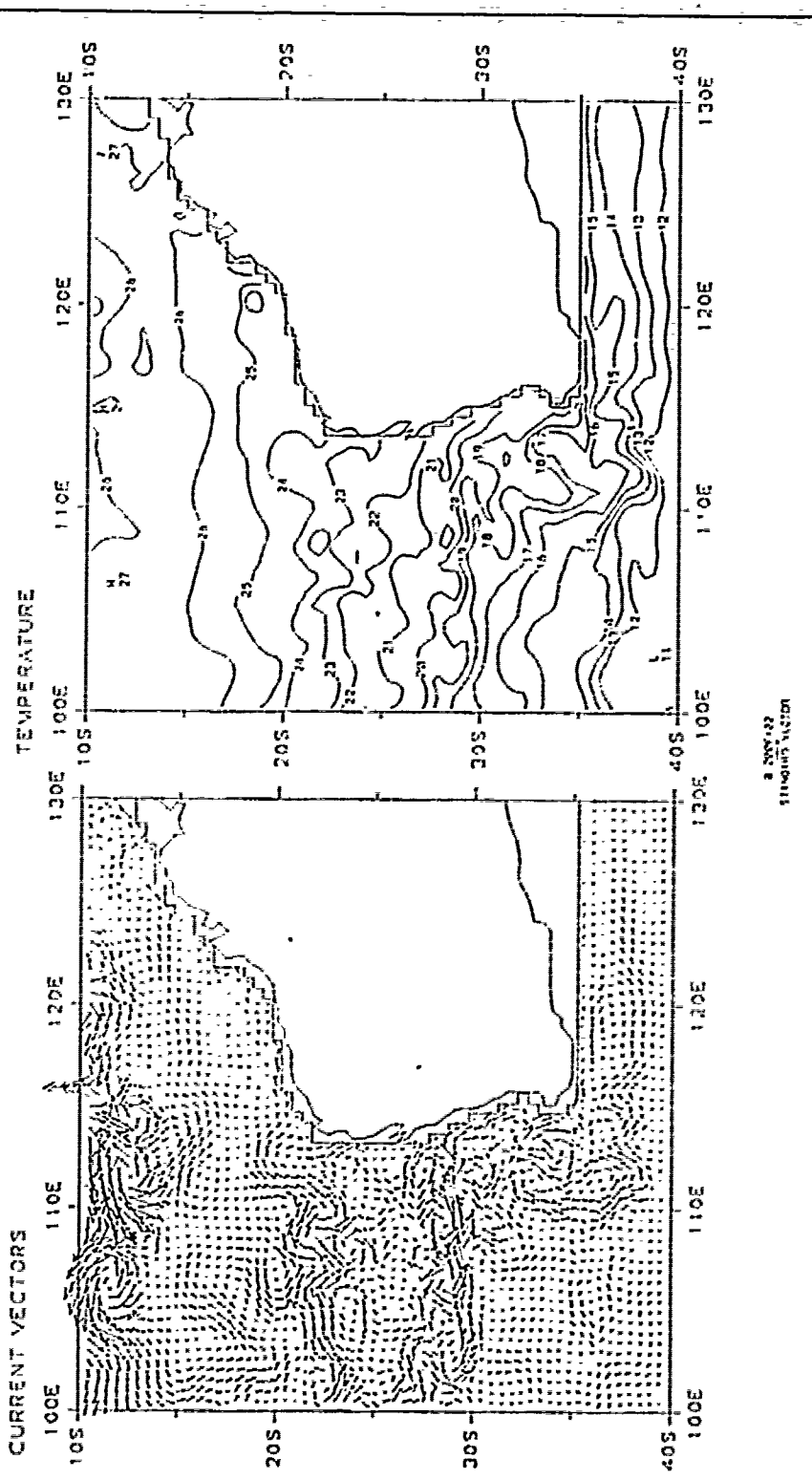

Figure 4.47 Year 4 West Australian current vector and temperature plots at 37.5 m in December.

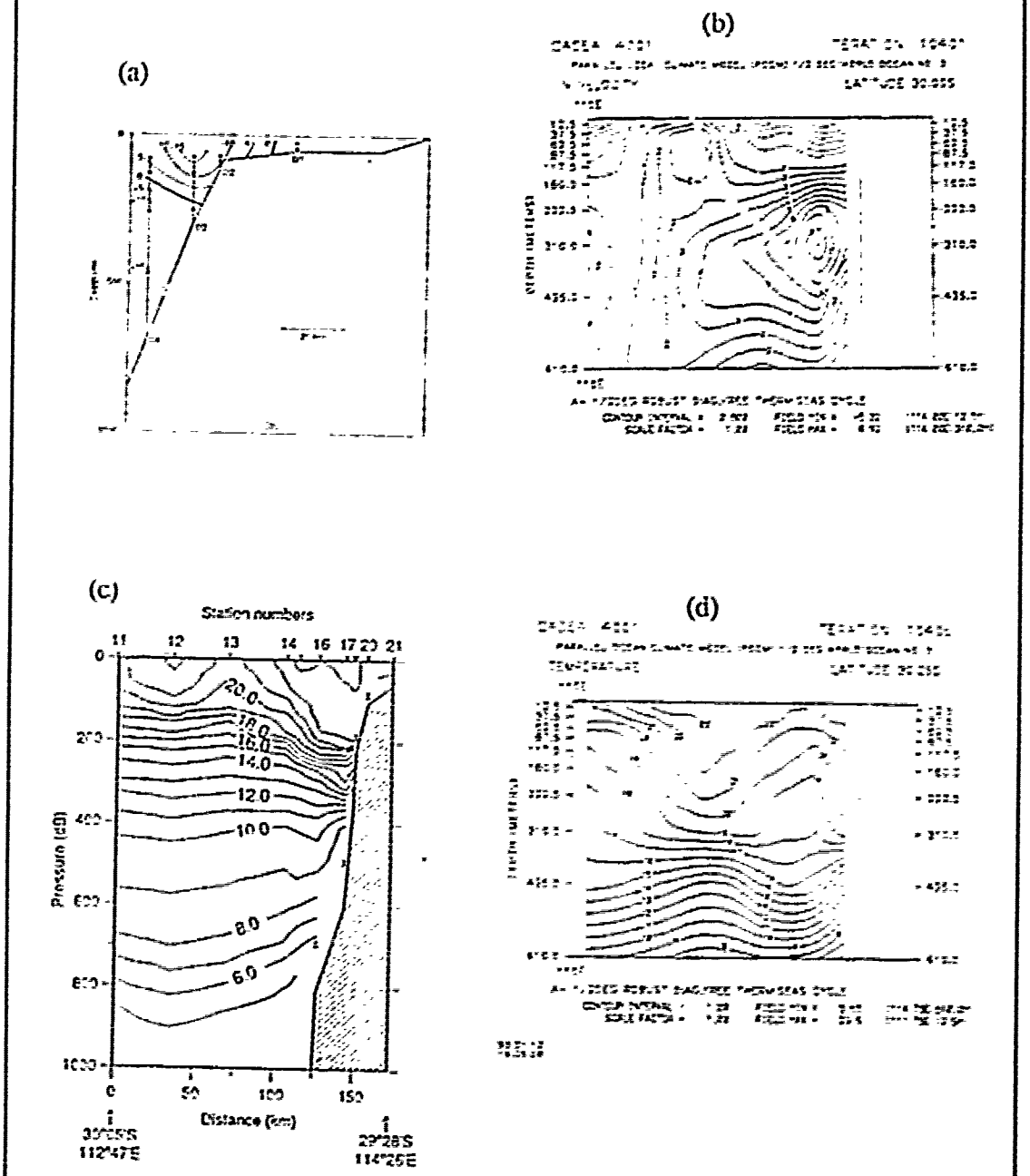

Figure 4.48 Comparison of model output in the Leeuwin Current region with LUCIE data, as reported by Church *et al.*, 1989. (a) September 1986-February 1987 mean alongshore currents at Dongora, (b) Model mean velocity in January. Year 4, (c) Potential temperature at Dongara during 7-9 June 1987, and (d) Model mean temperature during June of Year 4.

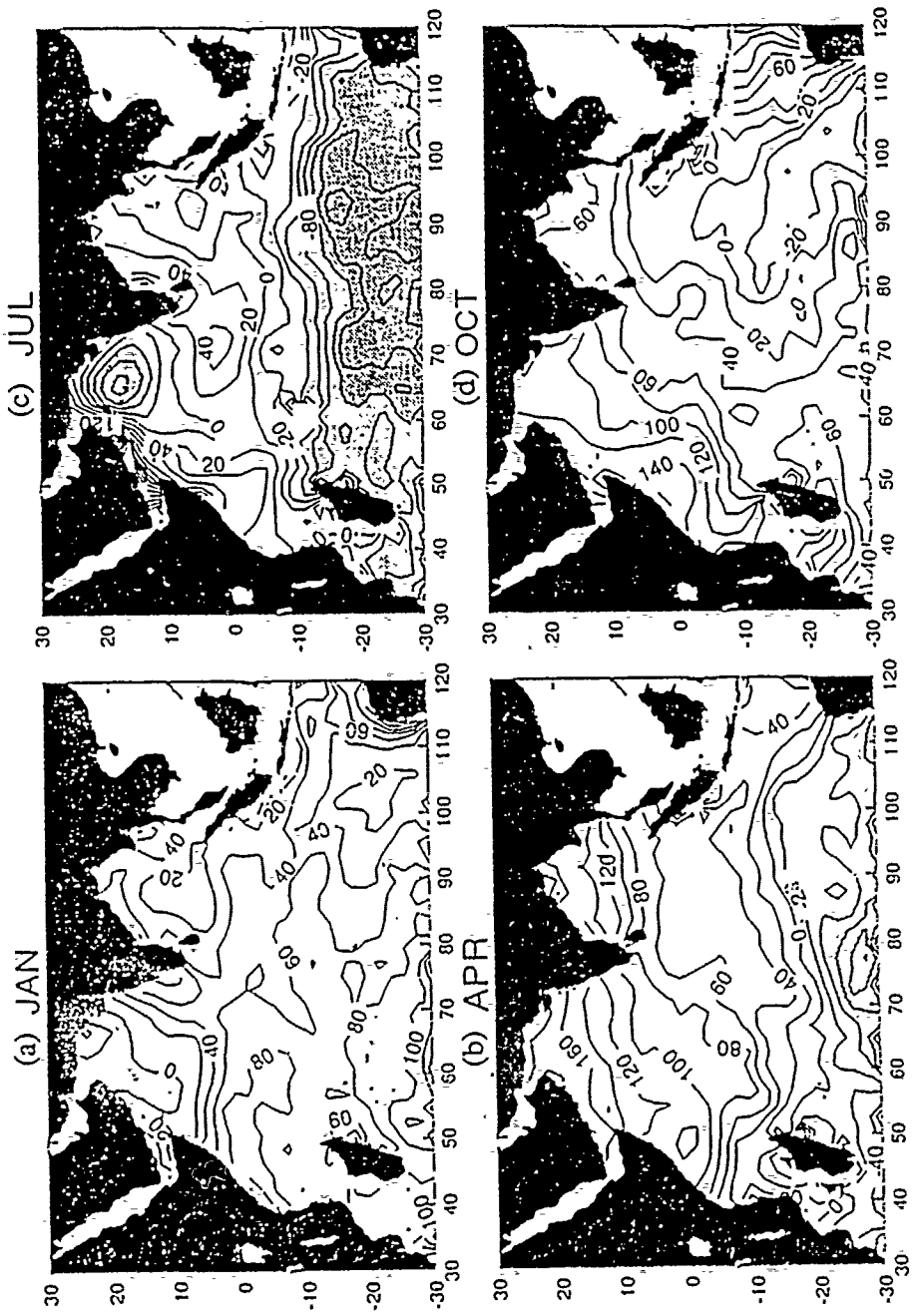

Figure 4.49 Indian Ocean surface heat fluxes (W m^{-2}) from Rao *et al.*(1989). (a) January, (b) April, (c) July, and (d) October.

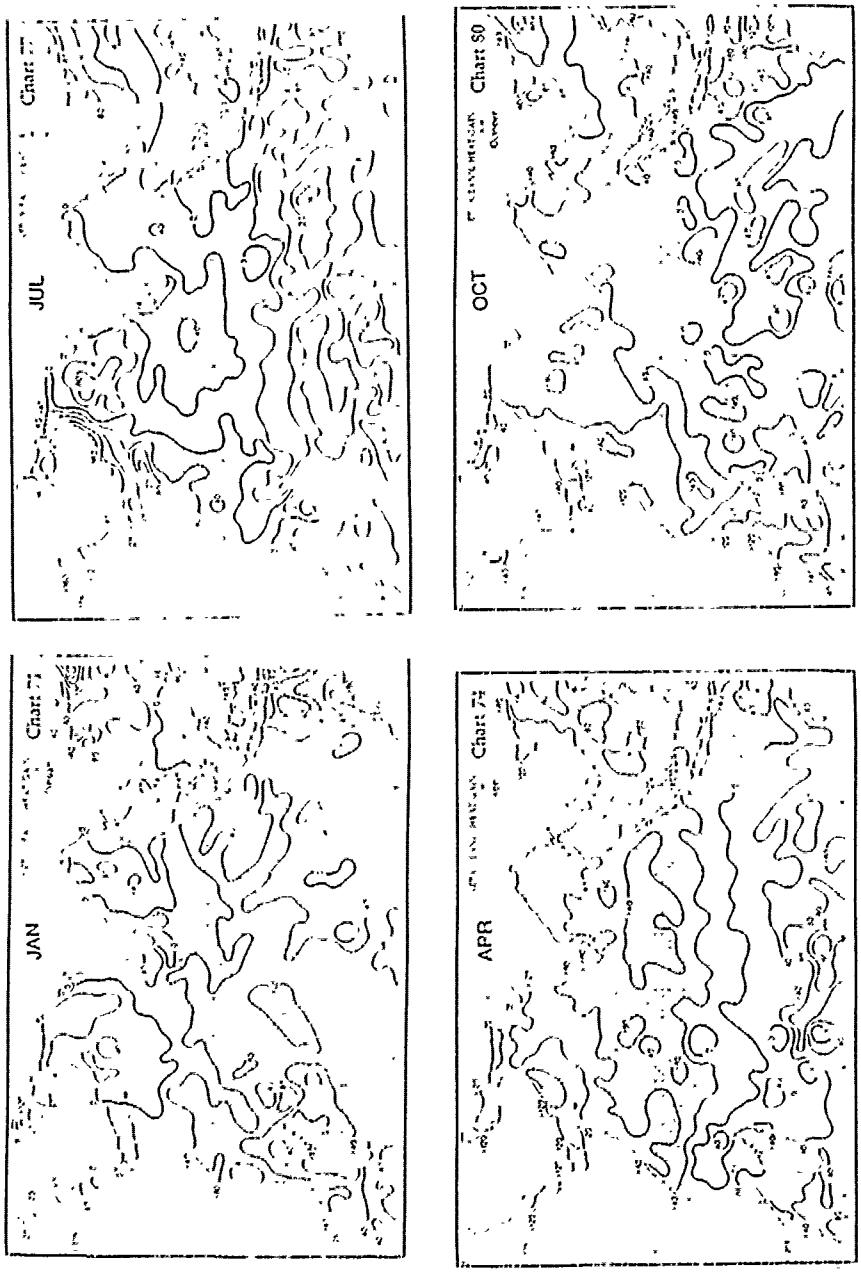

Figure 4.50 Indian Ocean surface heat fluxes (W m^{-2}) from Hastenrath and Lamb (1979). (a) January, (b) April, (c) July, and (d) October.

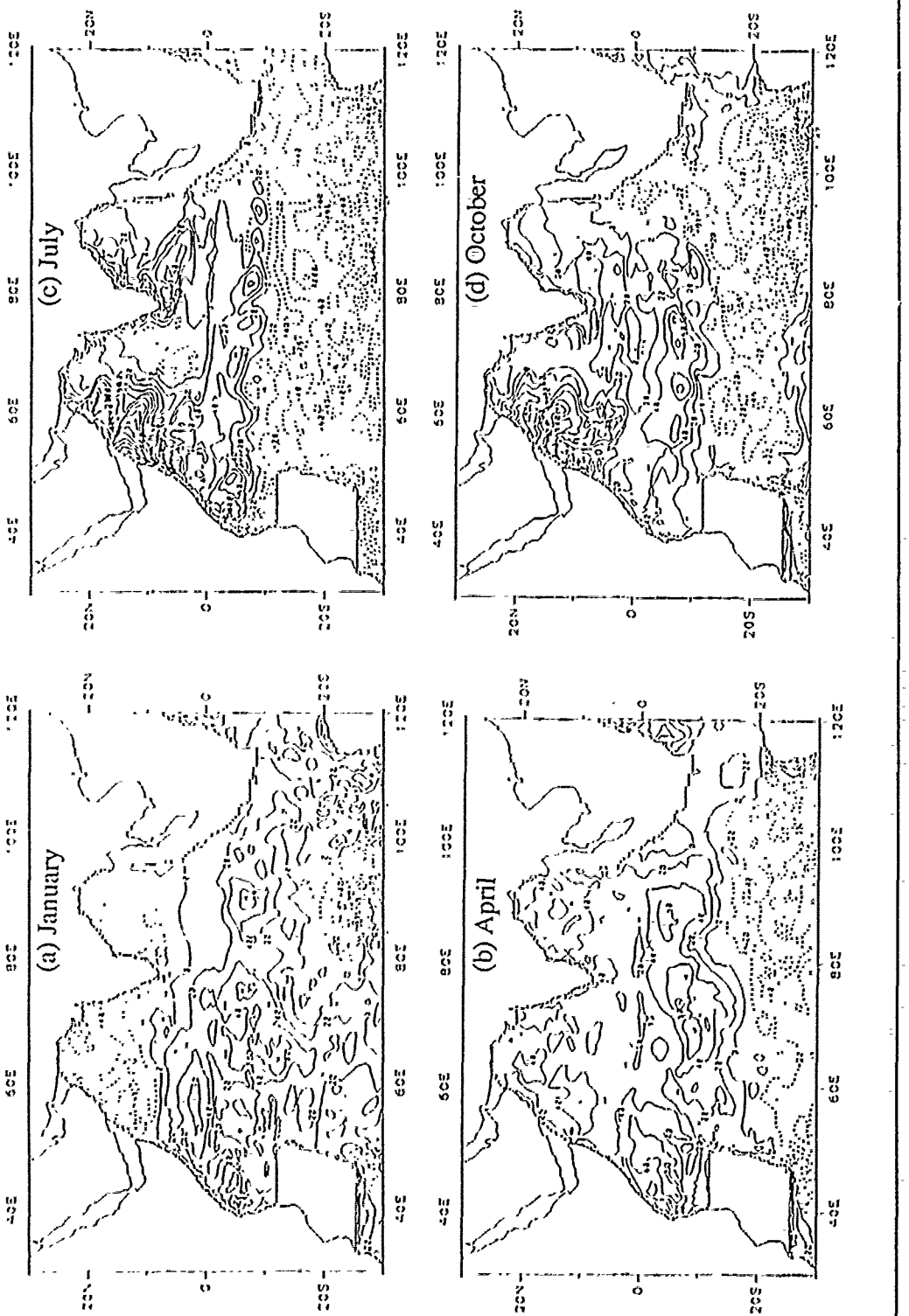

Figure 4.51 Indian Ocean Levitus (1982) surface forcing during Year 7 (W m^{-2}). (a) January, (b) April, (c) July, and (d) October.

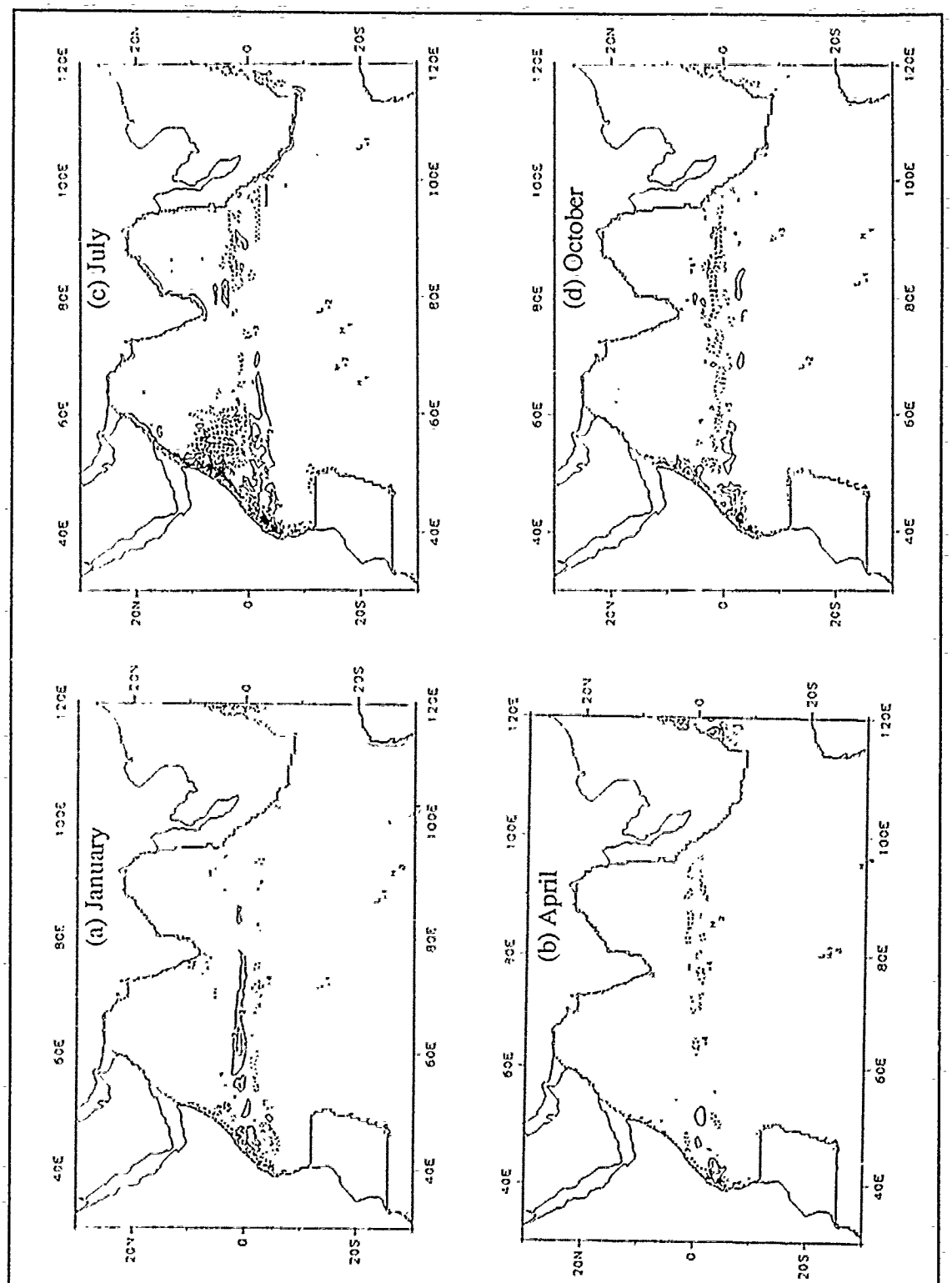

Figure 4.52 Vertical velocity at 25 m during Year 4. Solid lines indicate upwelling, dashed lines downwelling, in (a) January, (b) April, (c) July, and (d) October.

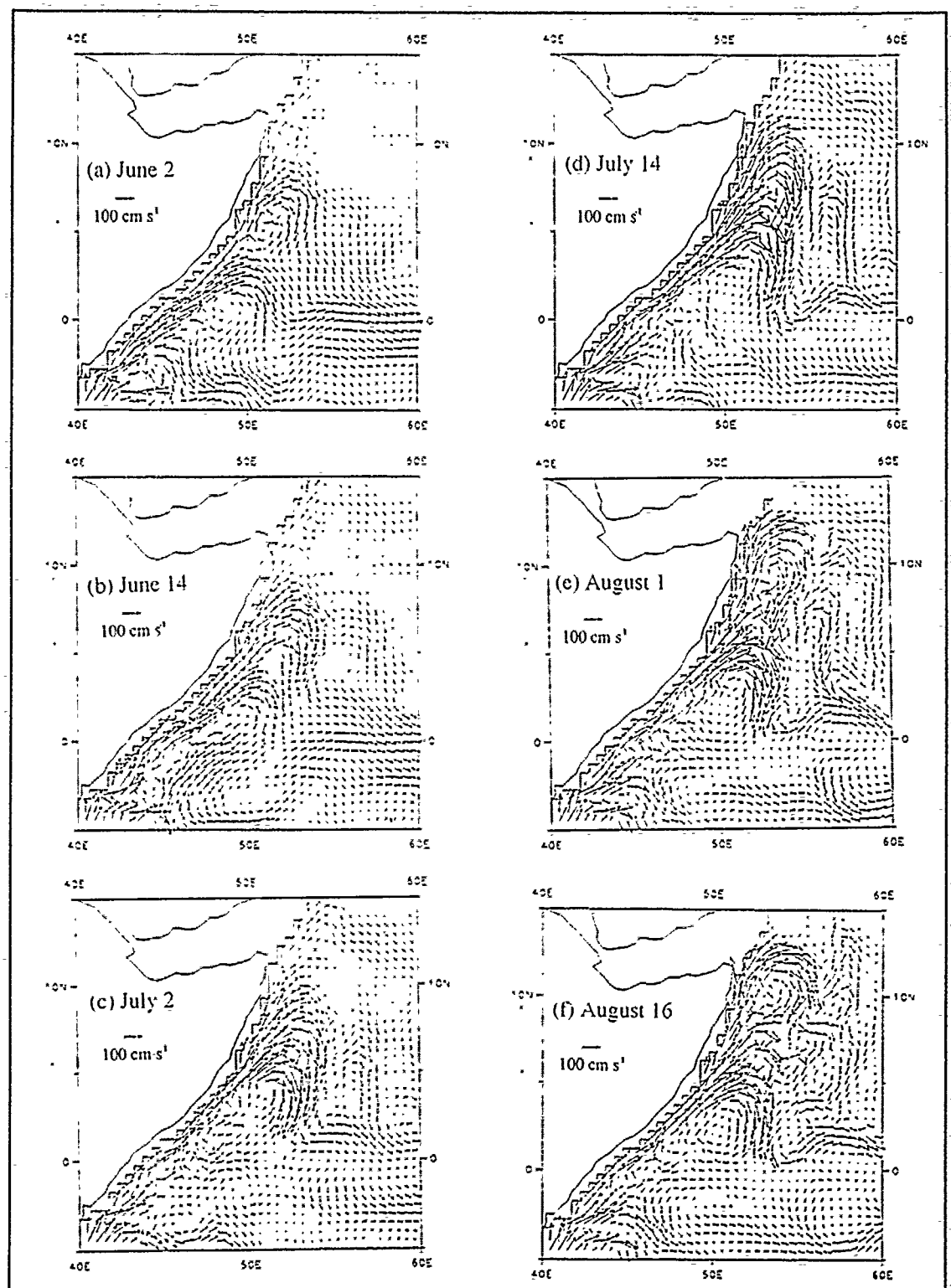

Figure 4.53 Development of the Somali Current at 37 m during Year 4. (a) June 2, (b) June 14, (c) July 2, (d) July 14, (e) August 1, (f) August 16.

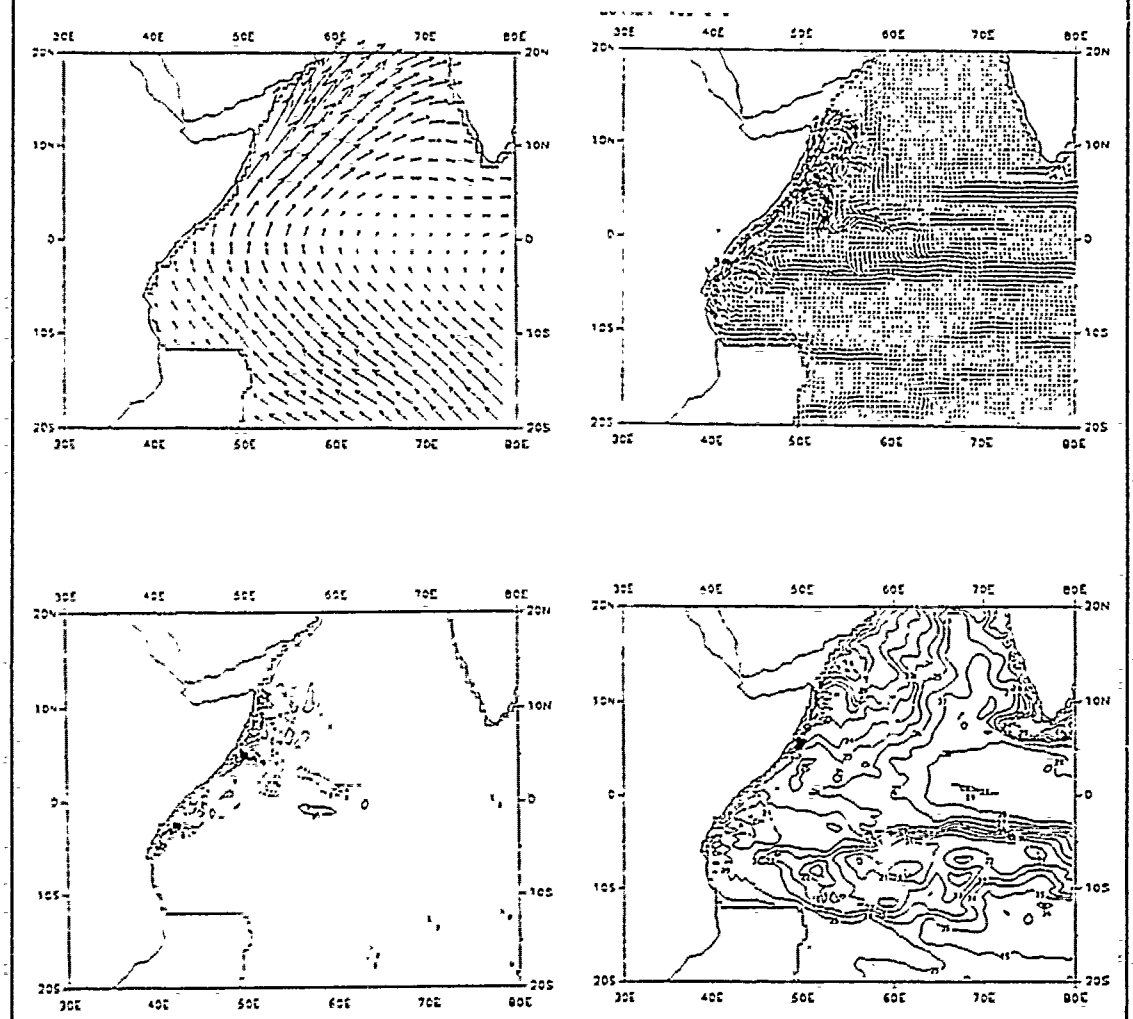

Figure 4.54 Upwelling along the Somali Current during August, Year 4. (a) Wind Stress, (b) Current vectors at 37.5 m, (c) Upwelling at 25 m, (d) T at 37.5 m.

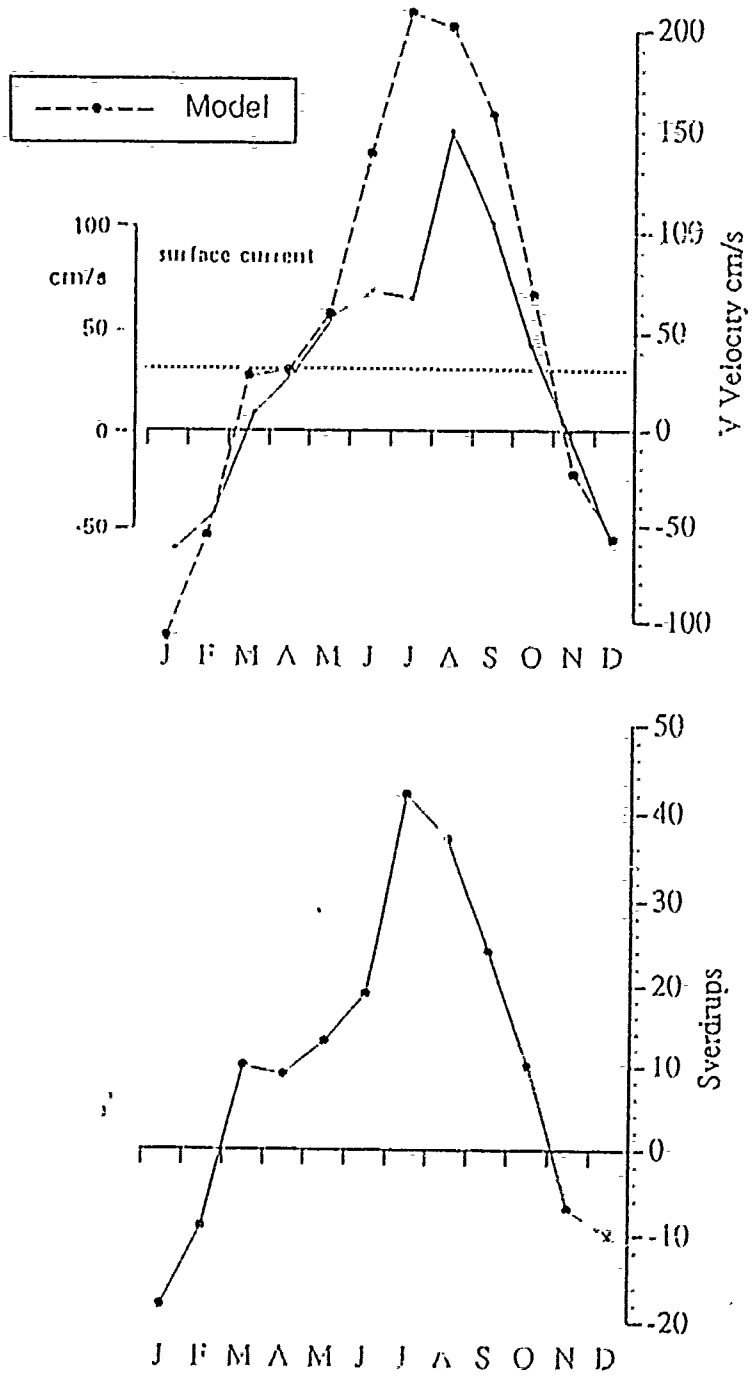

Figure 4.55 Seasonal cycle of Somali Current surface flow at 5°N. (a) Historical alongshore flow (solid line,after Quadfasel and Schott, 1983), and maximum velocity (dashed line) of the top level (12.5 m) v velocity during Year 4, from sections at 48°E-52°E. (b). Mass transport of the prevailing flow in the 5°N, 48-52°E, 0-610 m plots.

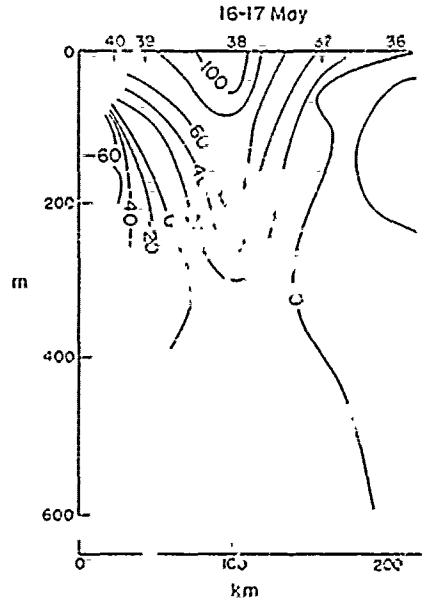

FIG. 11. Alongshore speed in depth range 0–600 m., measured along a section normal to the coast at 5°N (section 0 in Fig. 2) during 16–17 May 1979 (from LEETMAA *et al.*, 1982).

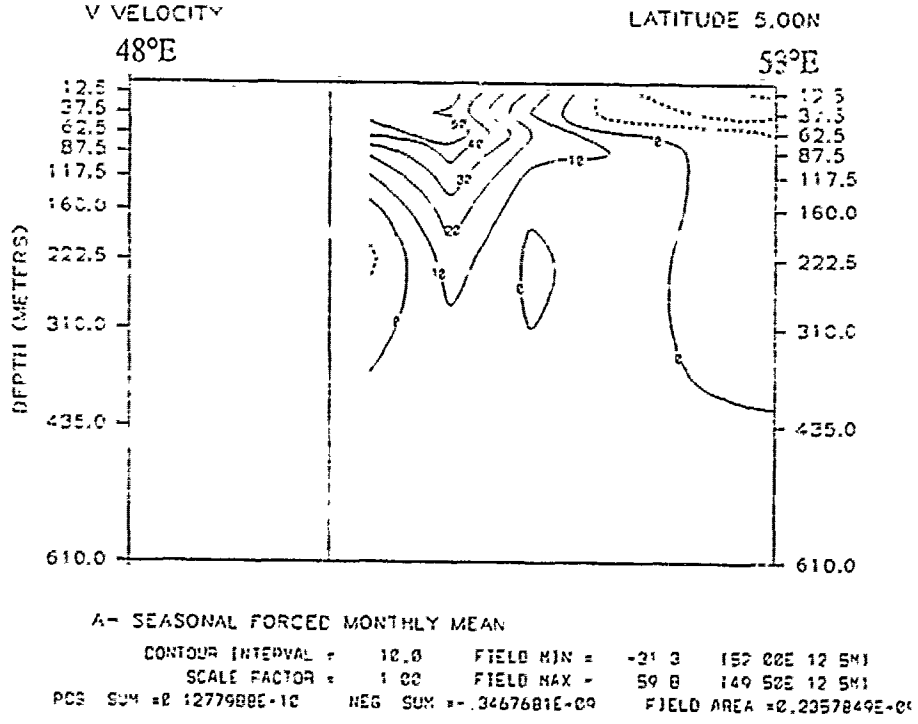

Figure 4.56 Somali Current cross sections at 5°N. (a) Alongshore speed during 16-17 May 1979 (Schott ,1983), and (b) mean v velocity in the Semtner and Chervin model during March of Year 4.

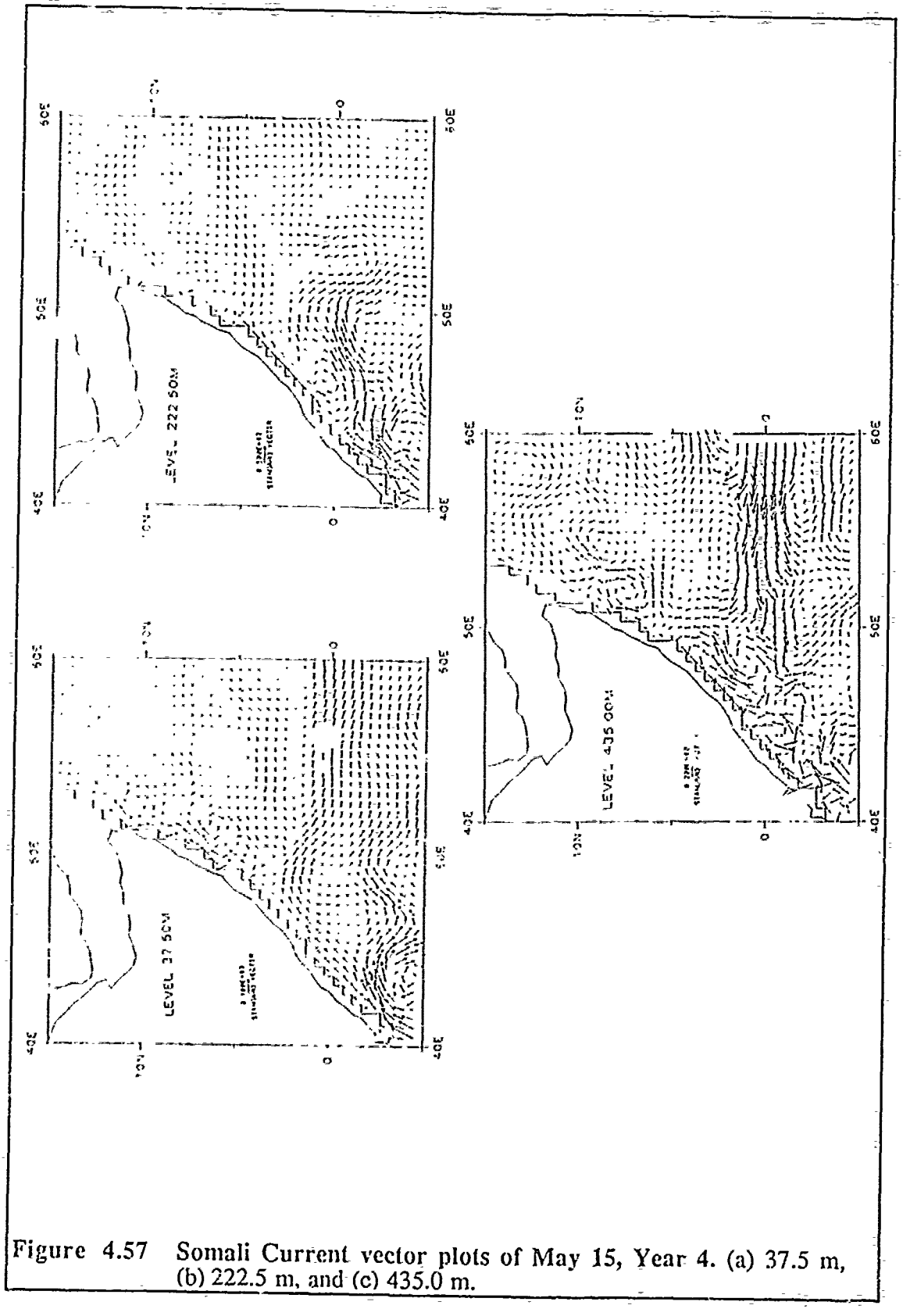

Figure 4.57 Somali Current vector plots of May 15, Year 4. (a) 37.5 m, (b) 222.5 m, and (c) 435.0 m.

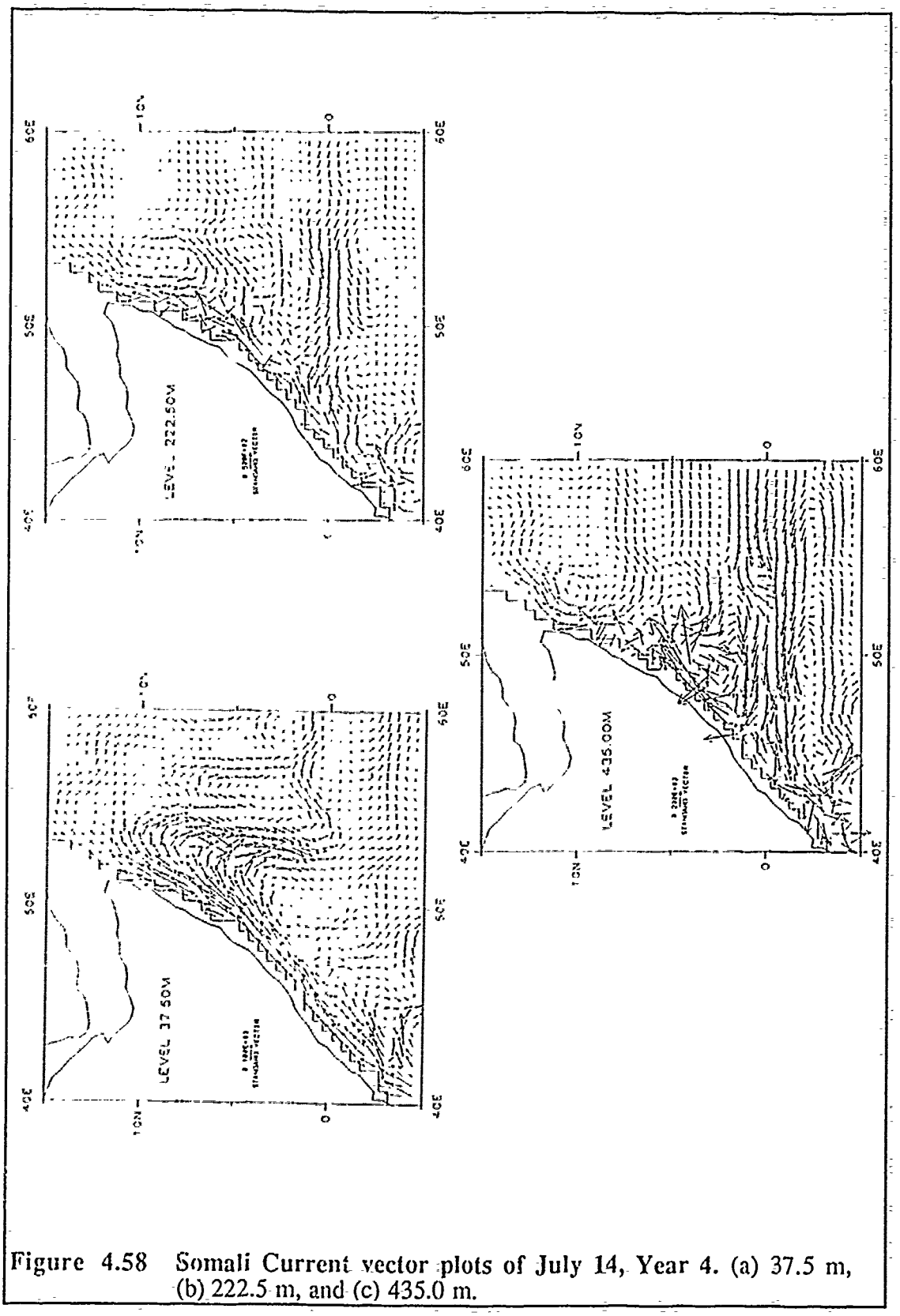

Figure 4.58 Somali Current vector plots of July 14, Year 4. (a) 37.5 m, (b) 222.5 m, and (c) 435.0 m.

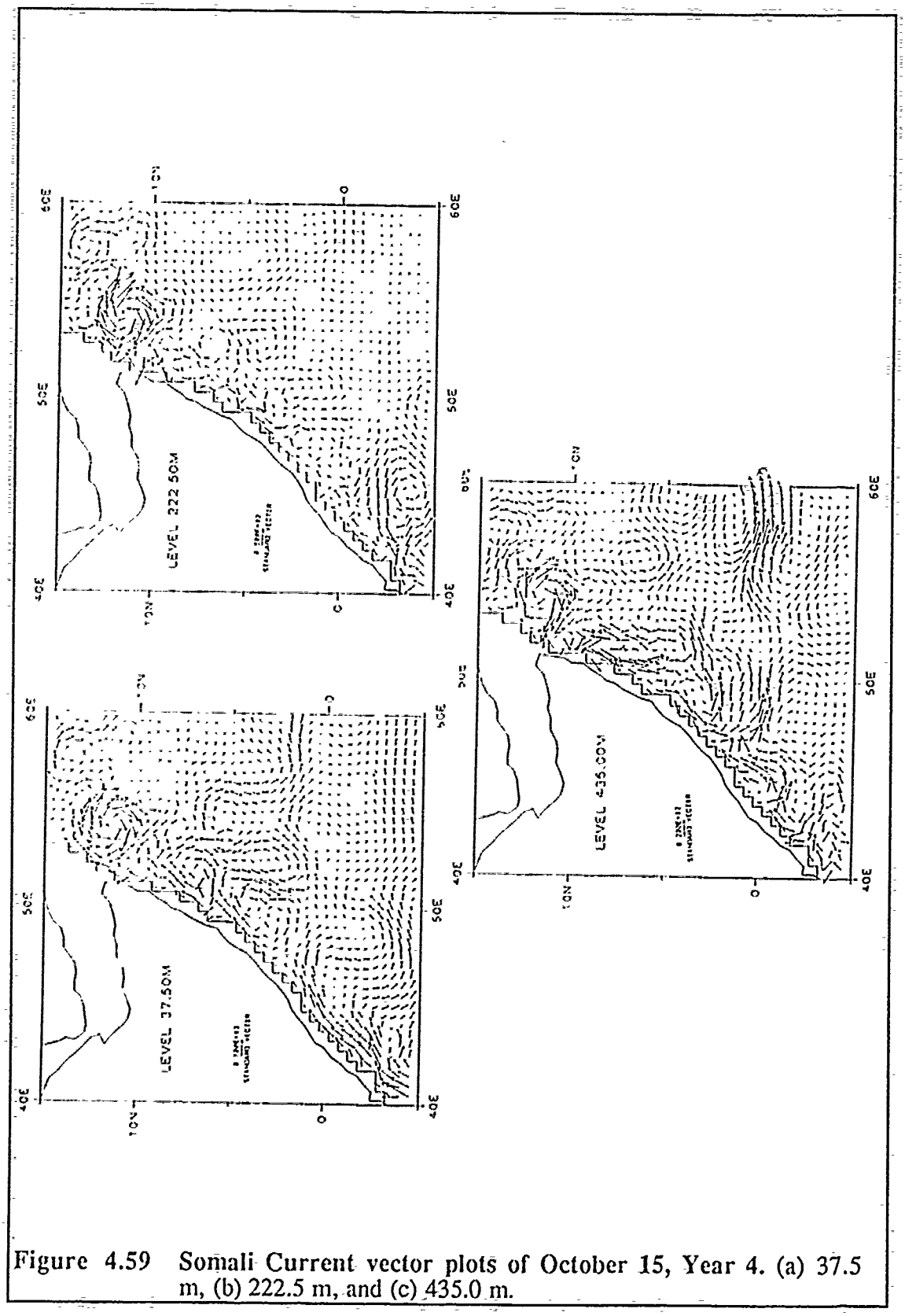

Figure 4.59 Somali Current vector plots of October 15, Year 4. (a) 37.5 m, (b) 222.5 m, and (c) 435.0 m.

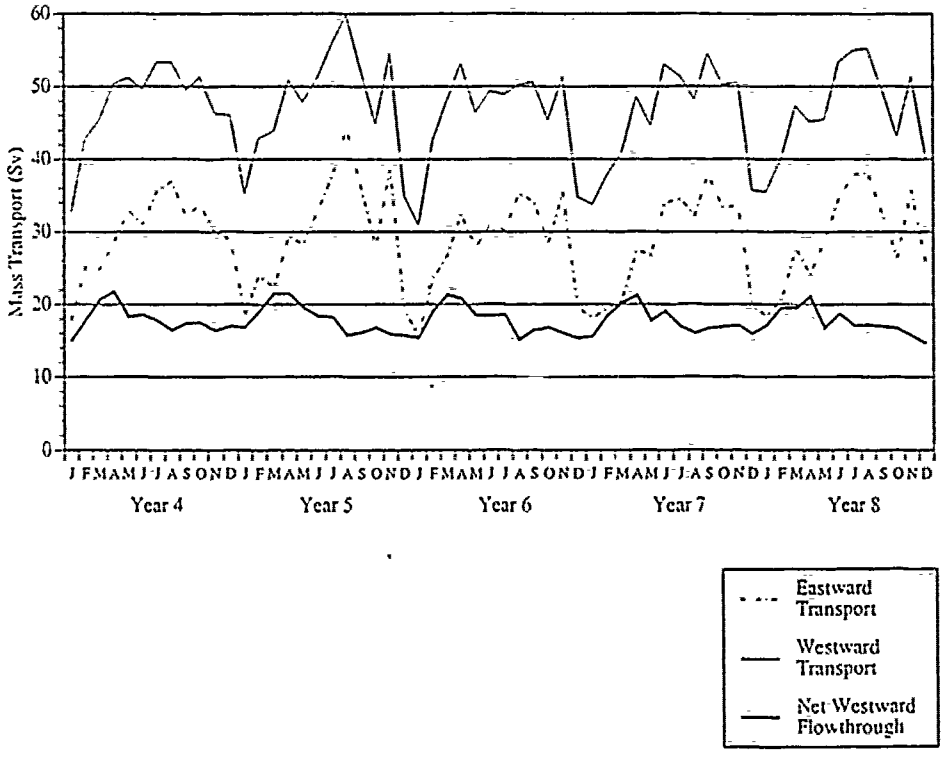

Figure 4.60 Mass transport in the Indonesian Archipelago. Compiled from monthly mean tapes in Years 4-8, at 117.5°E.

Figure 4.61 Seasonal cycle and interannual variability of Pacific-Indian Ocean throughflow at 117.5°E. Years 4-8 are superimposed on the mean.

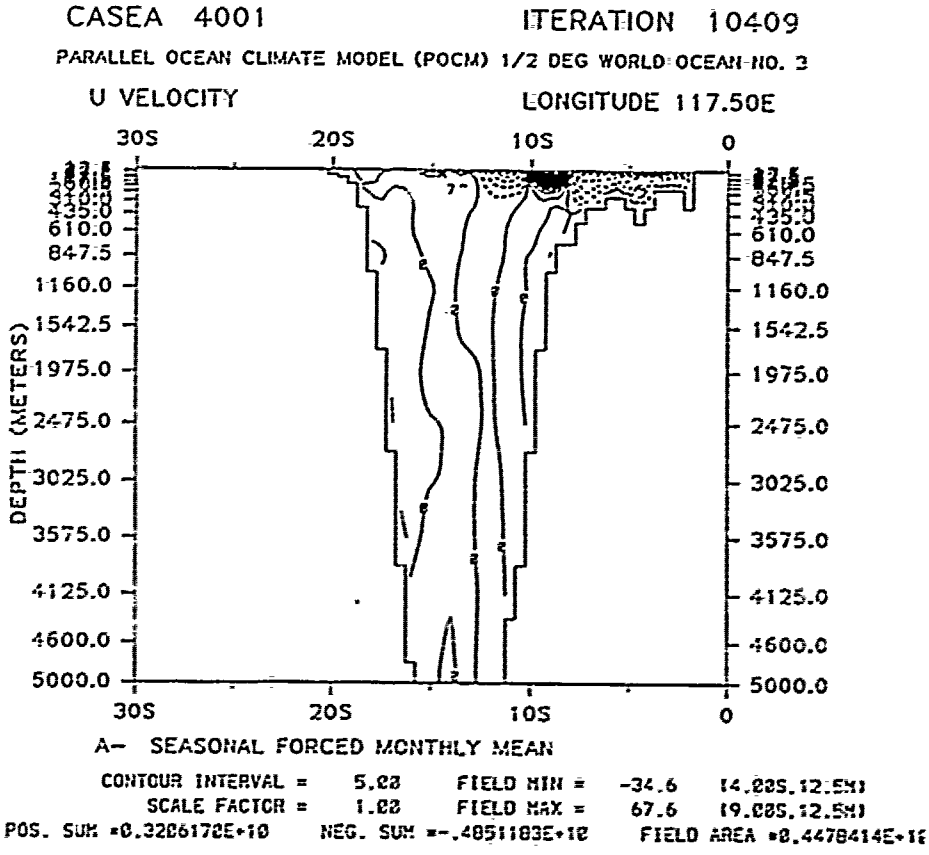

Figure 4.62 Zonal section at 117.5°E, used to calculate throughflow. The figure illustrates u velocity in August, Year 4. Although there are significant flows in each direction, the net westward mass transport is 16.4 Sv.

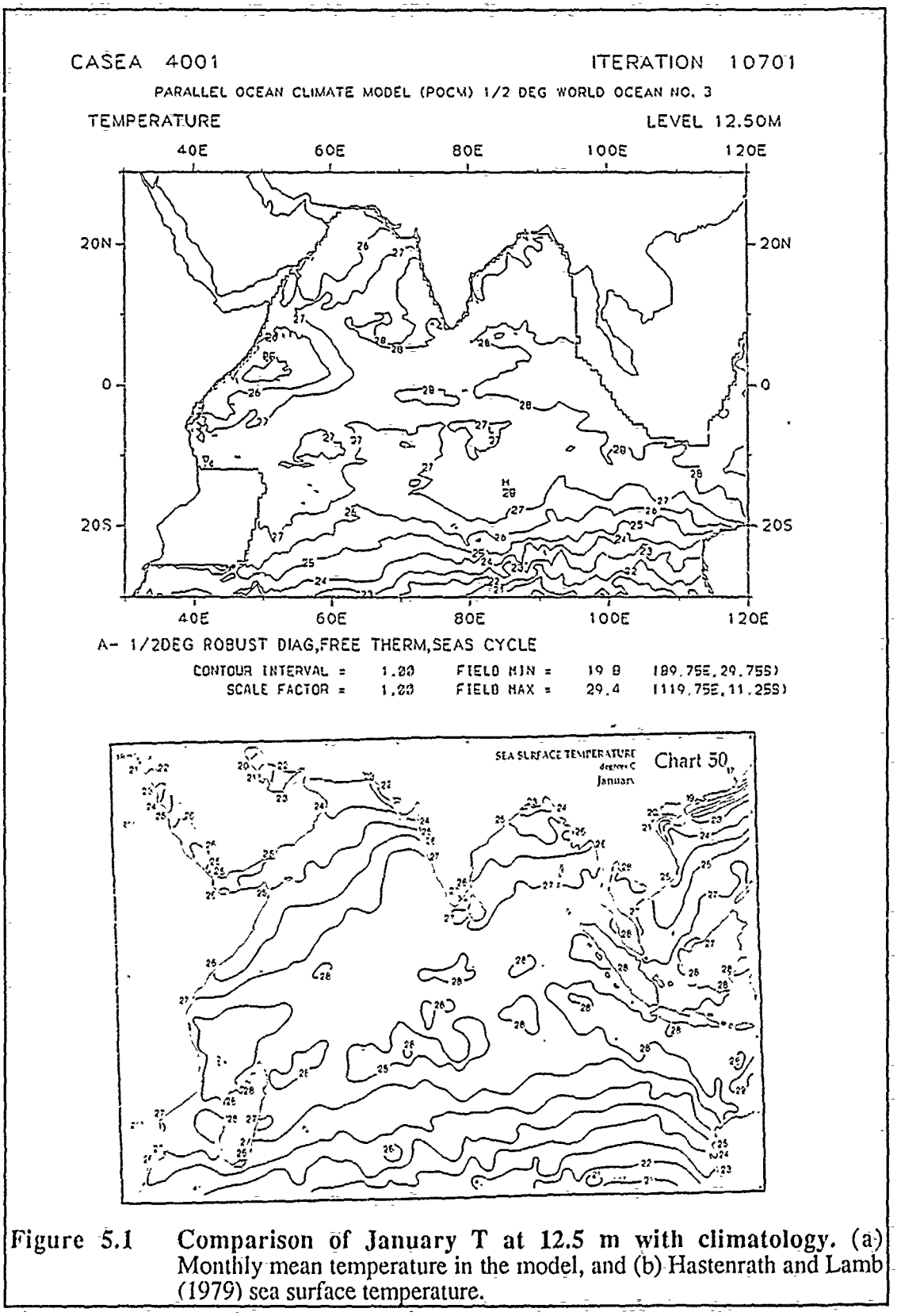

Figure 5.1 **Comparison of January T at 12.5 m with climatology.** (a) Monthly mean temperature in the model, and (b) Hastenrath and Lamb (1979) sea surface temperature.

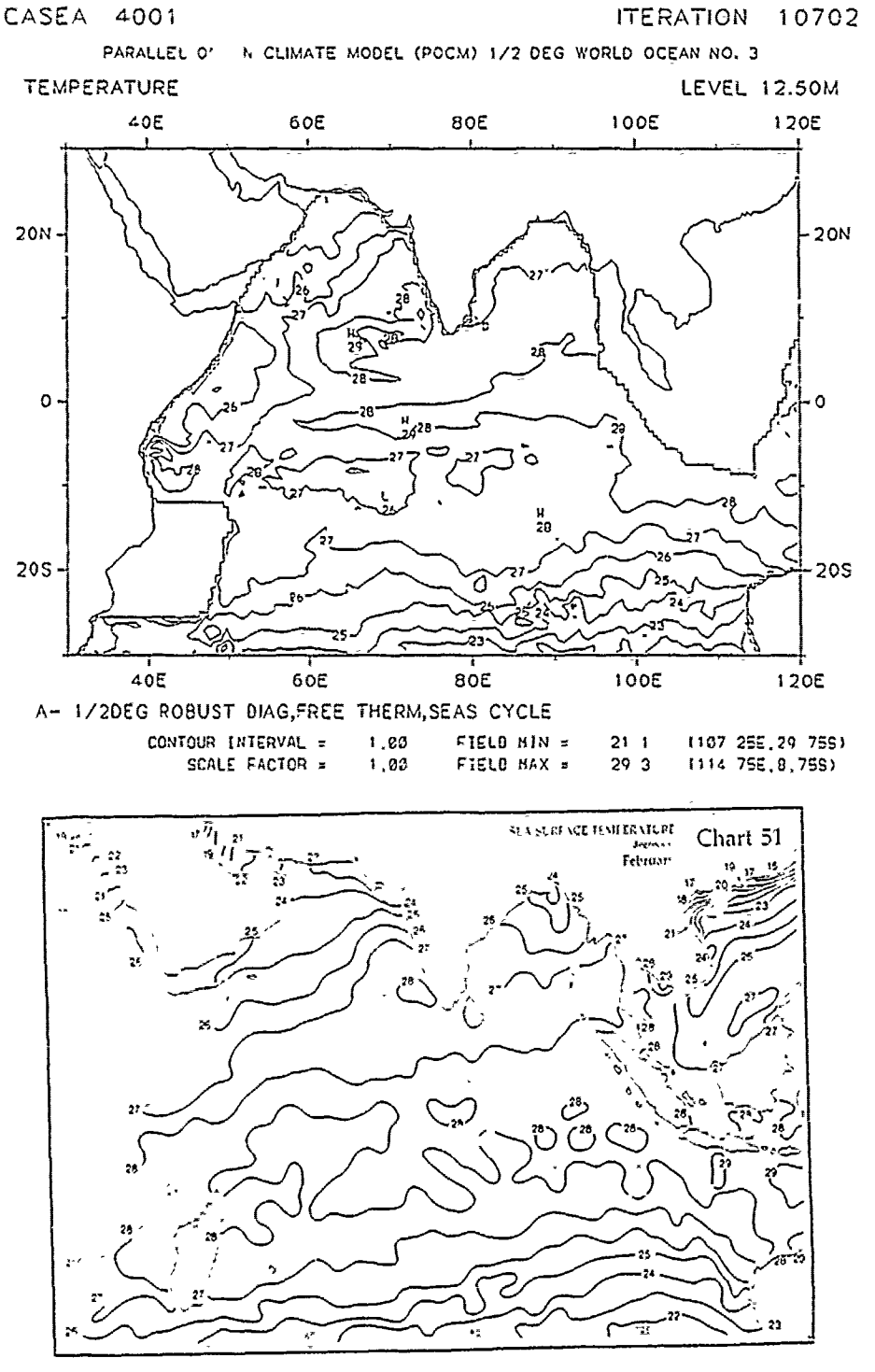

Figure 5.2 **Comparison of February T at 12.5 m with climatology.** (a) Monthly mean temperature in the model, and (b) Hastenrath and Lamb (1979) sea surface temperature.

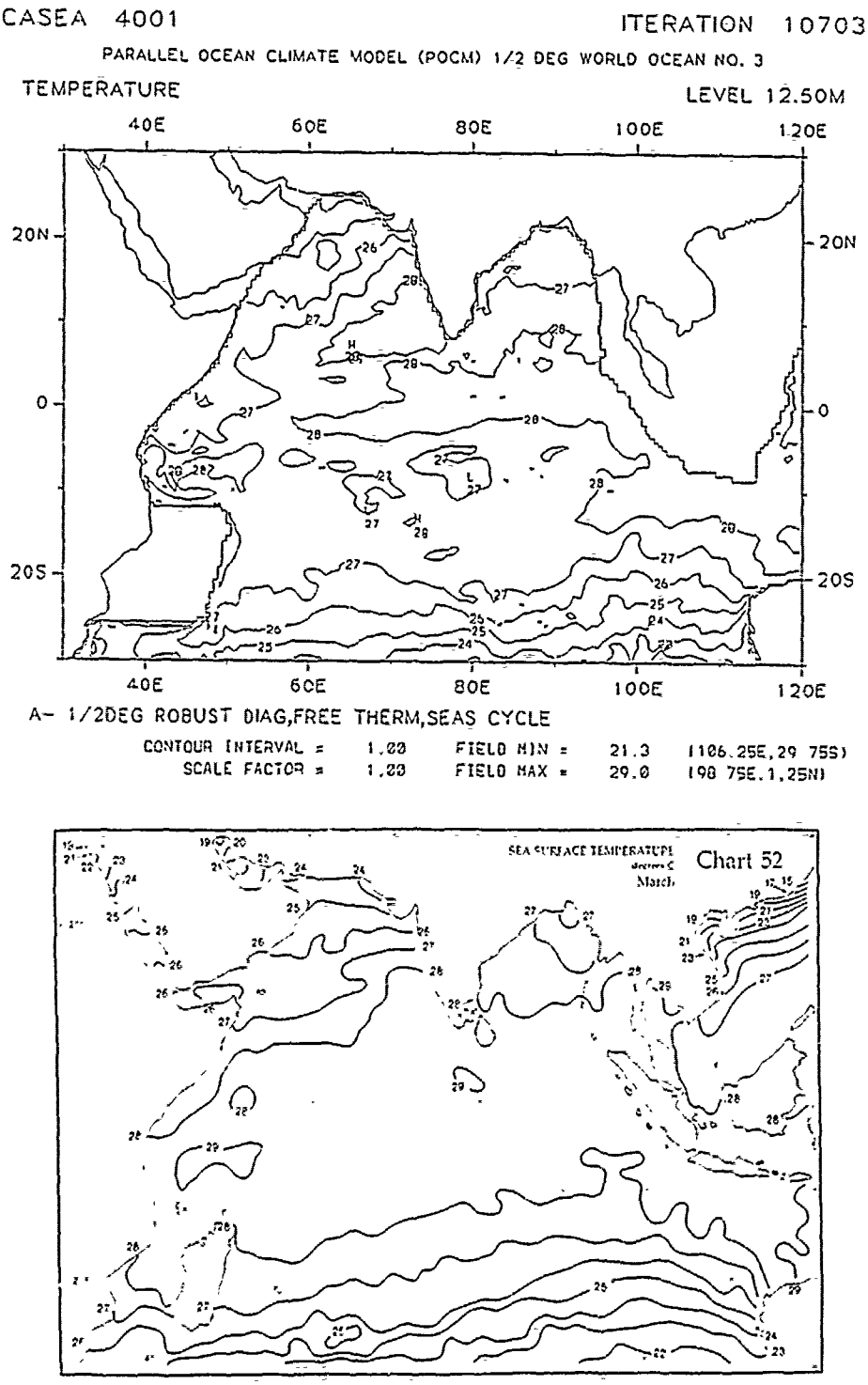

Figure 5.3 **Comparison of March T at 12.5 m with climatology.** (a) Monthly mean temperature in the model, and (b) Hastenrath and Lamb (1979) sea surface temperature.

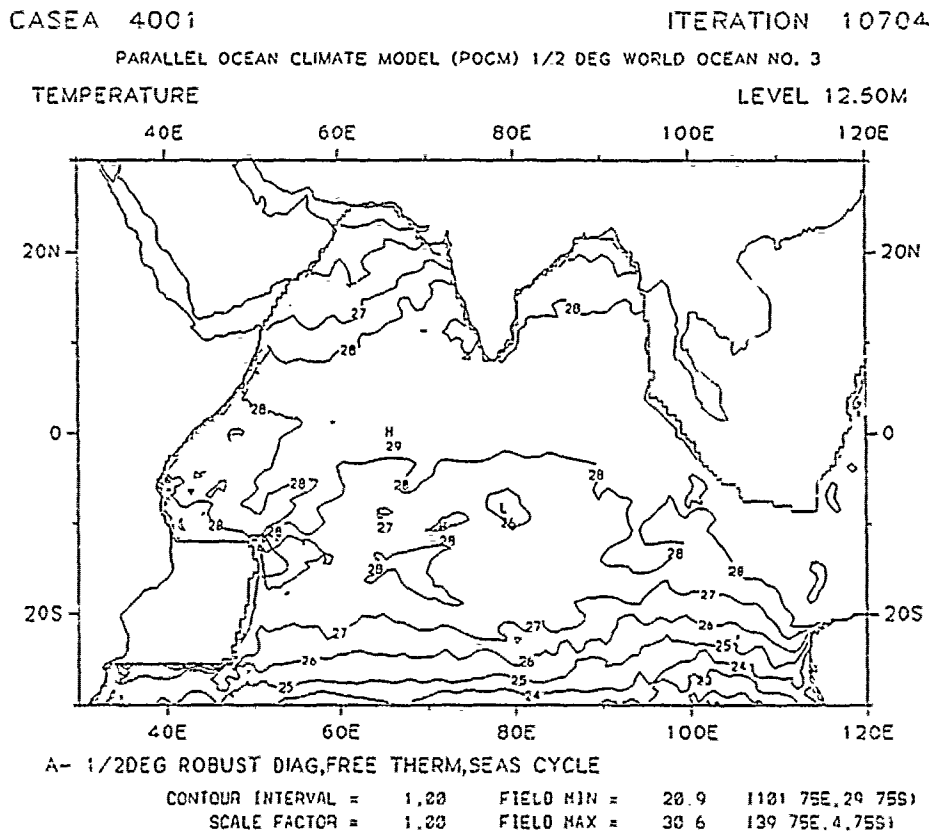

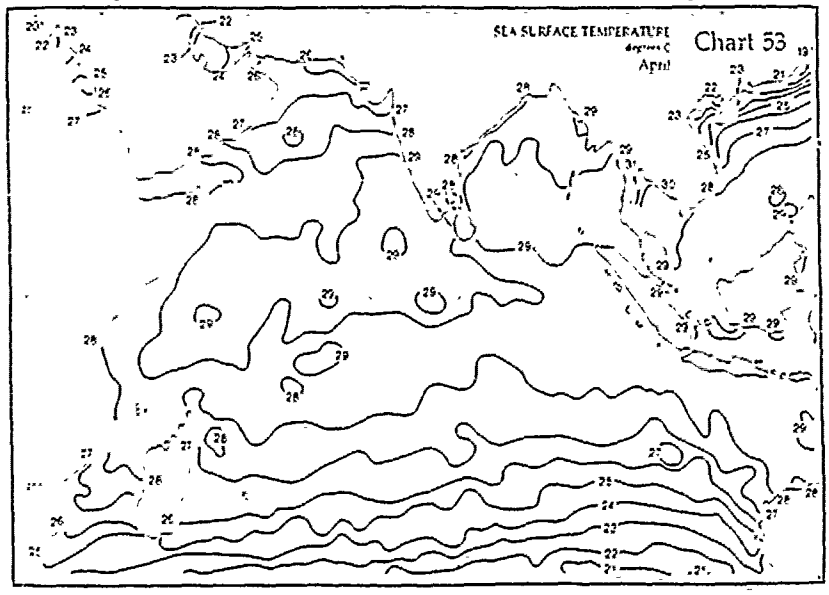

Figure 5.4 **Comparison of April T at 12.5 m with climatology.** (a) Monthly mean temperature in the model, and (b) Hastenrath and Lamb (1979) sea surface temperature.

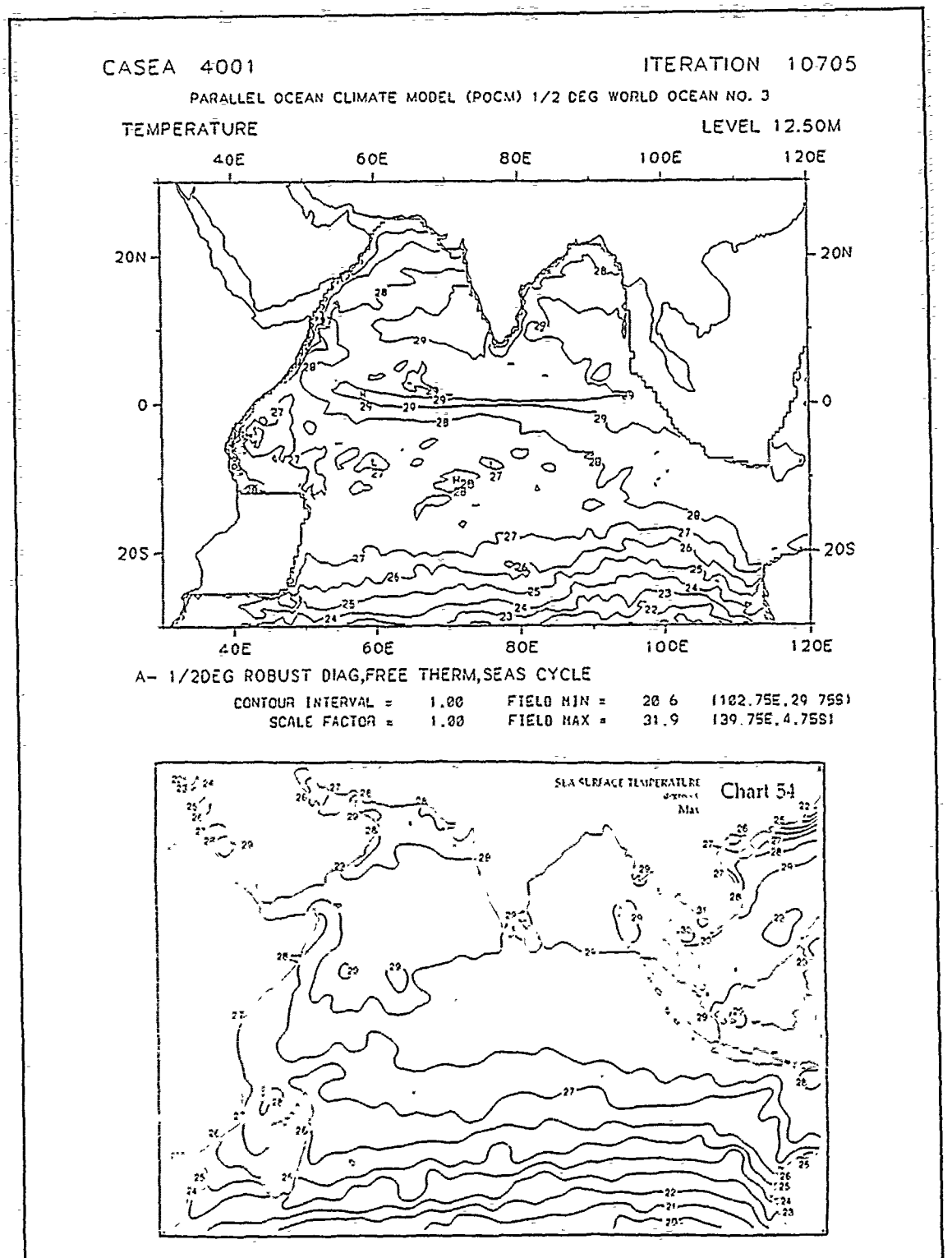

Figure 5.5 **Comparison of May T at 12.5 m with climatology.** (a) Monthly mean temperature in the model, and (b) Hastenrath and Lamb (1979) sea surface temperature.

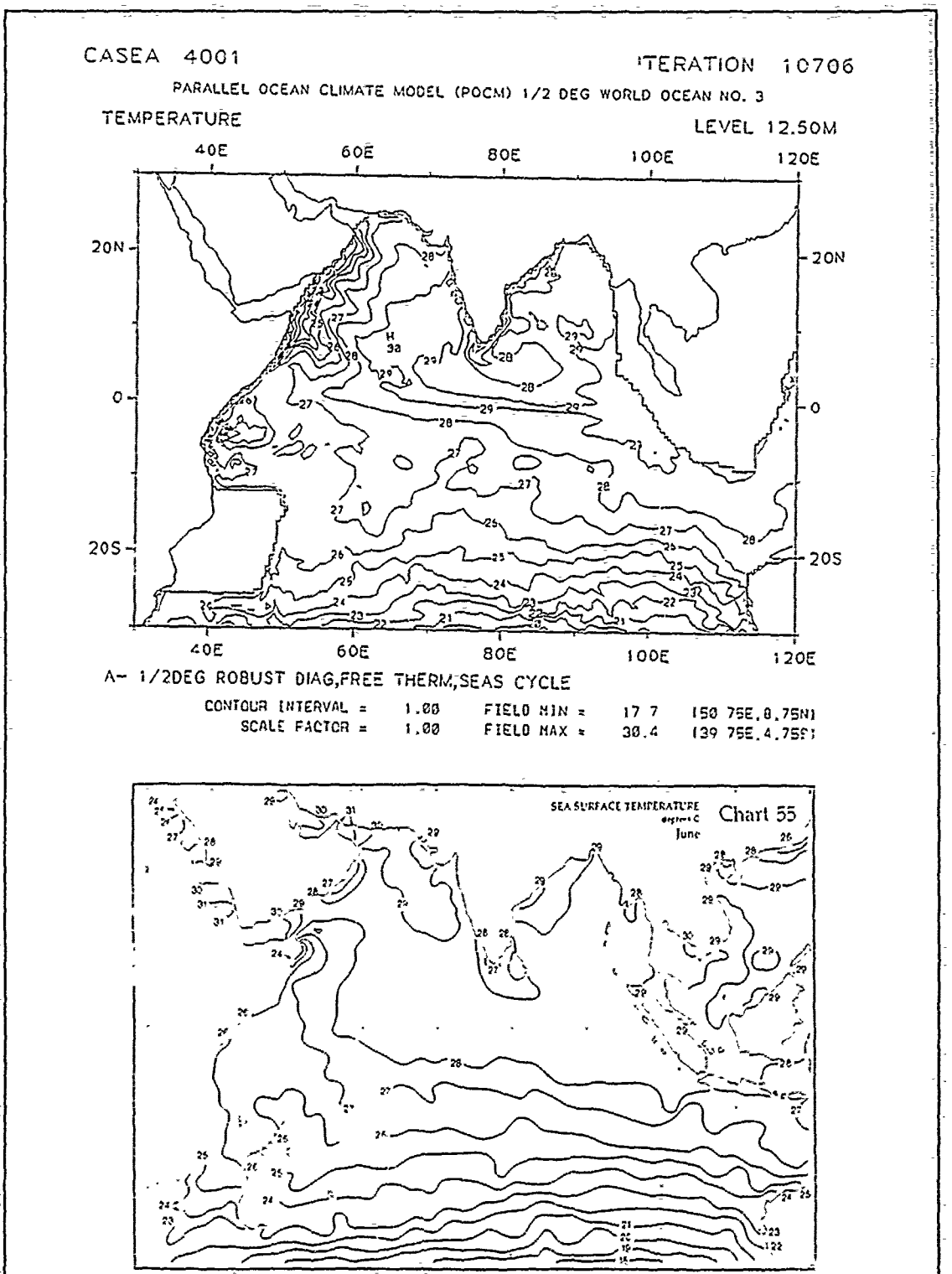

Figure 5.6 **Comparison of June T at 12.5 m with climatology.** (a) Monthly mean temperature in the model, and (b) Hastenrath and Lamb (1979) sea surface temperature.

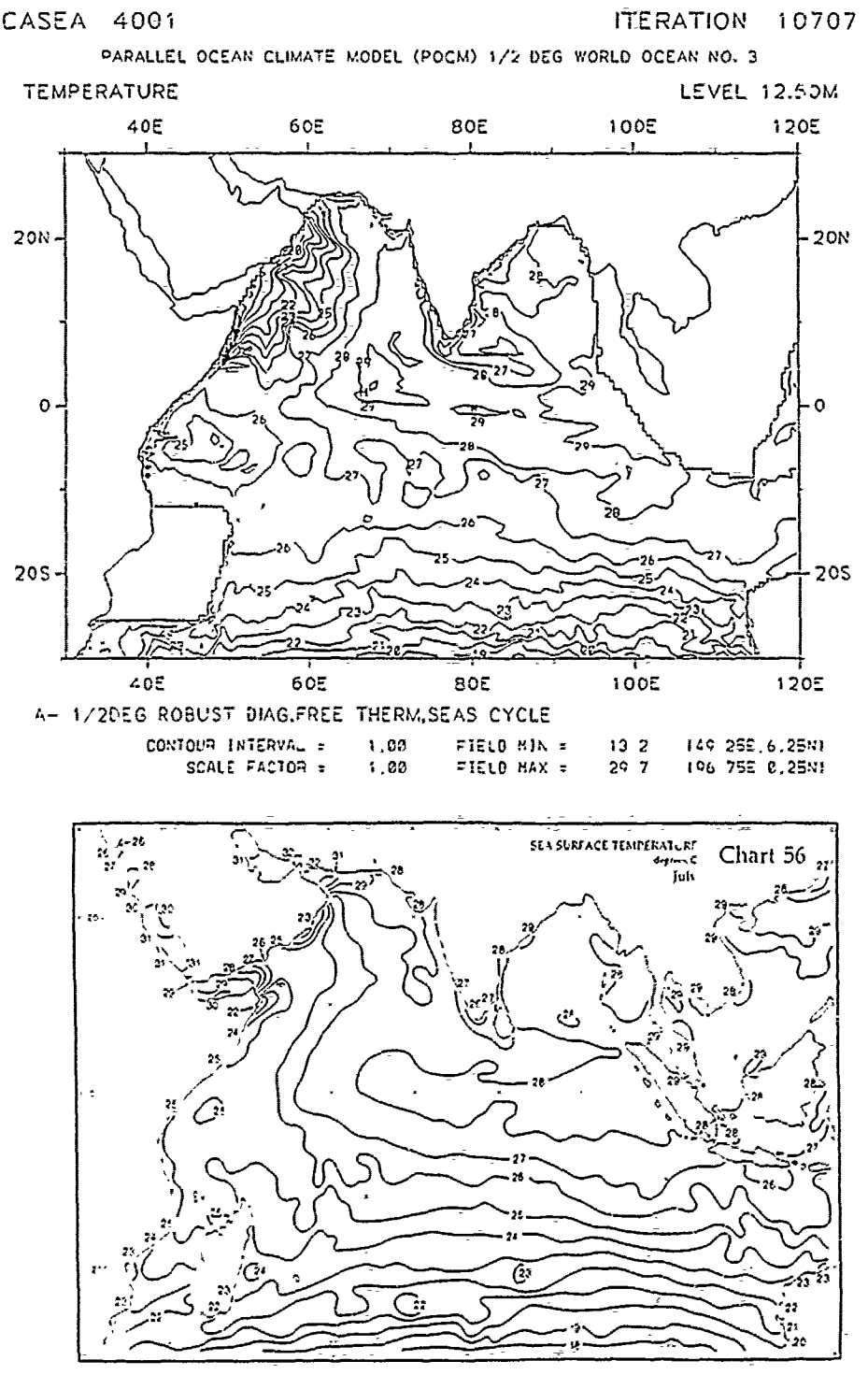

Figure 5.7 **Comparison of July T at 12.5 m with climatology.** (a) Monthly mean temperature in the model, and (b) Hastenrath and Lamb (1979) sea surface temperature.

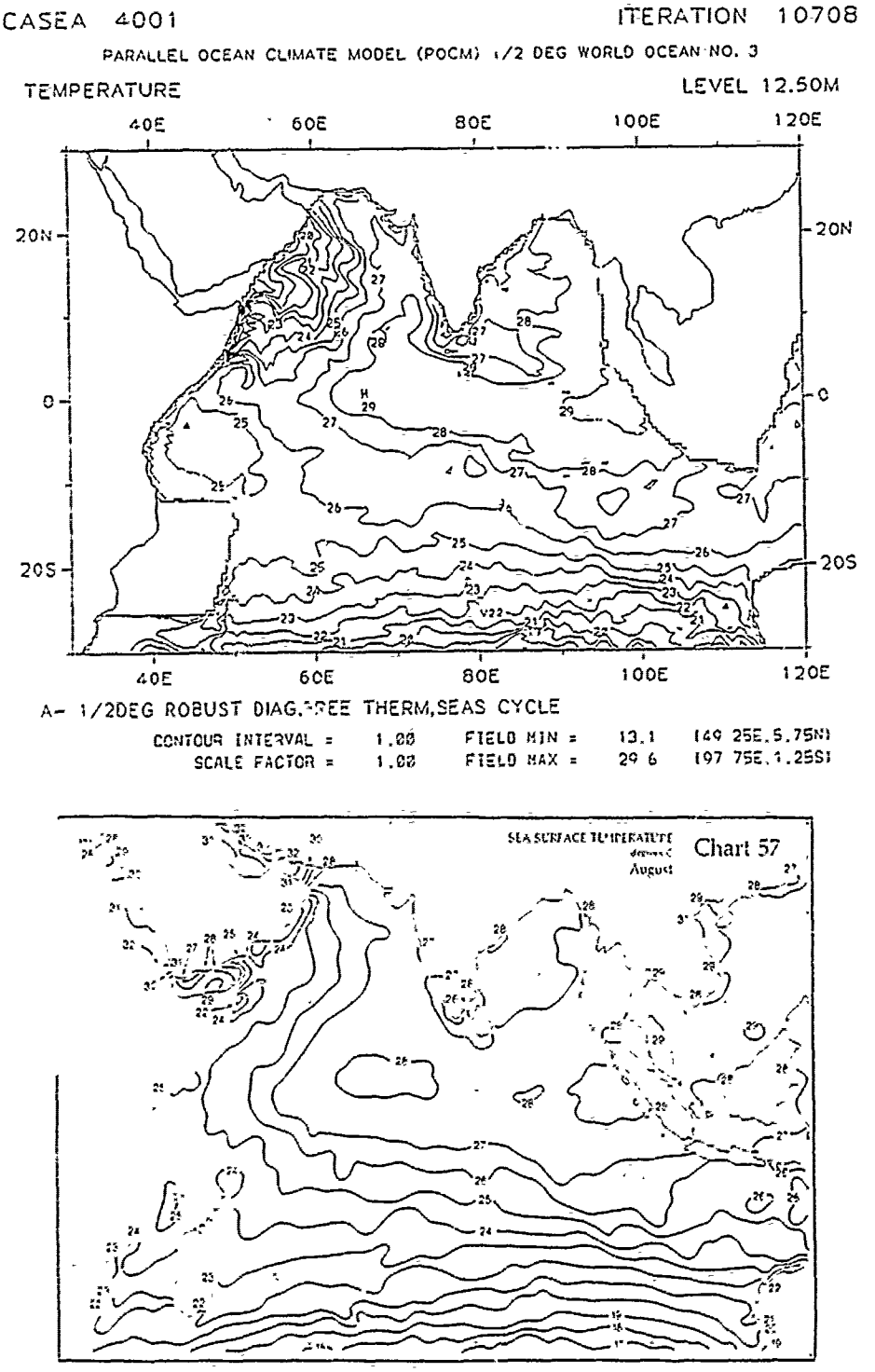

Figure 5.8 Comparison of August T at 12.5 m with climatology. (a) Monthly mean temperature in the model, and (b) Hastenrath and Lamb (1979) sea surface temperature.

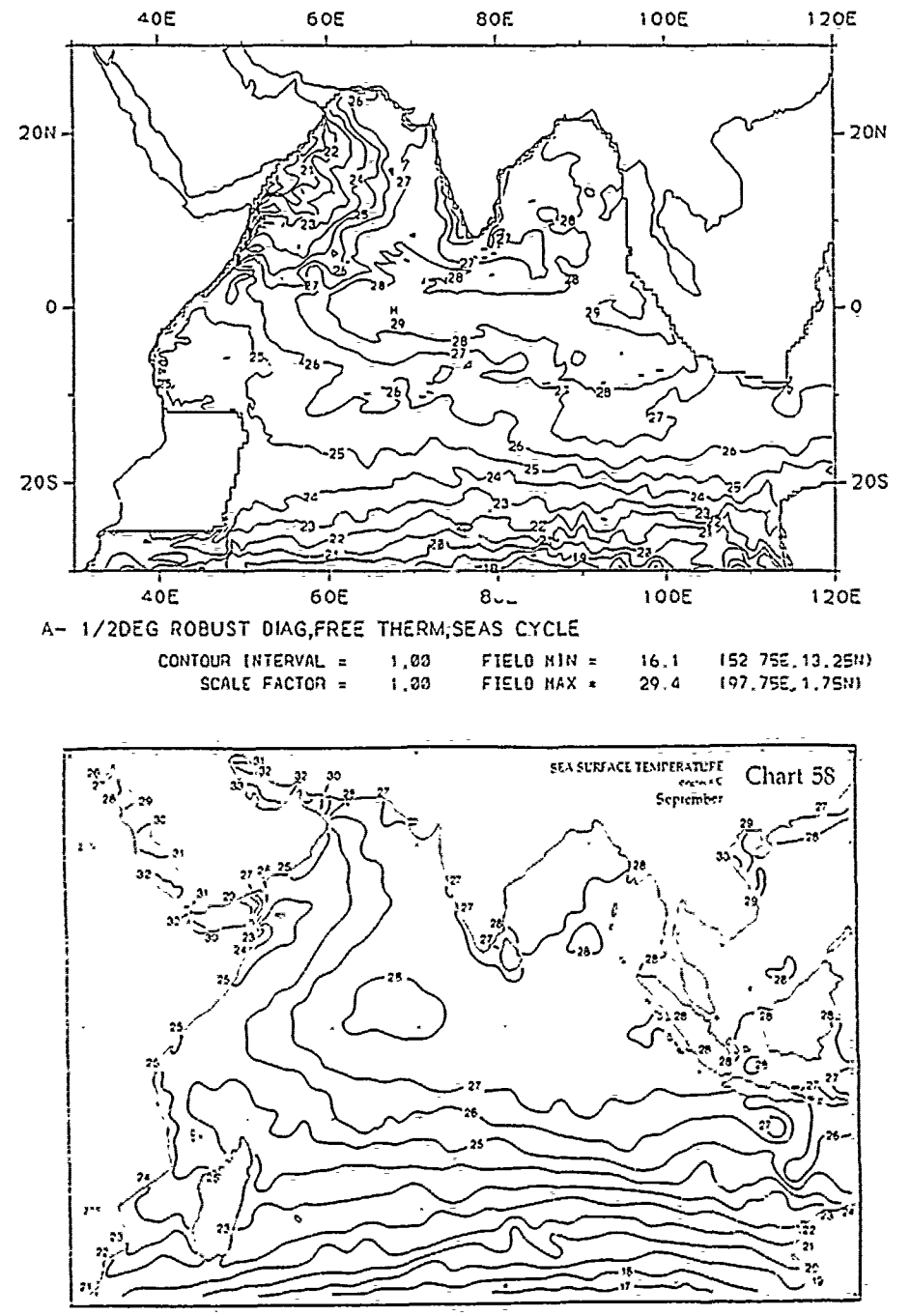

Figure 5.9 **Comparison of September T at 12.5 m with climatology.** (a) Monthly mean temperature in the model, and (b) Hastenrath and Lamb (1979) sea surface temperature.

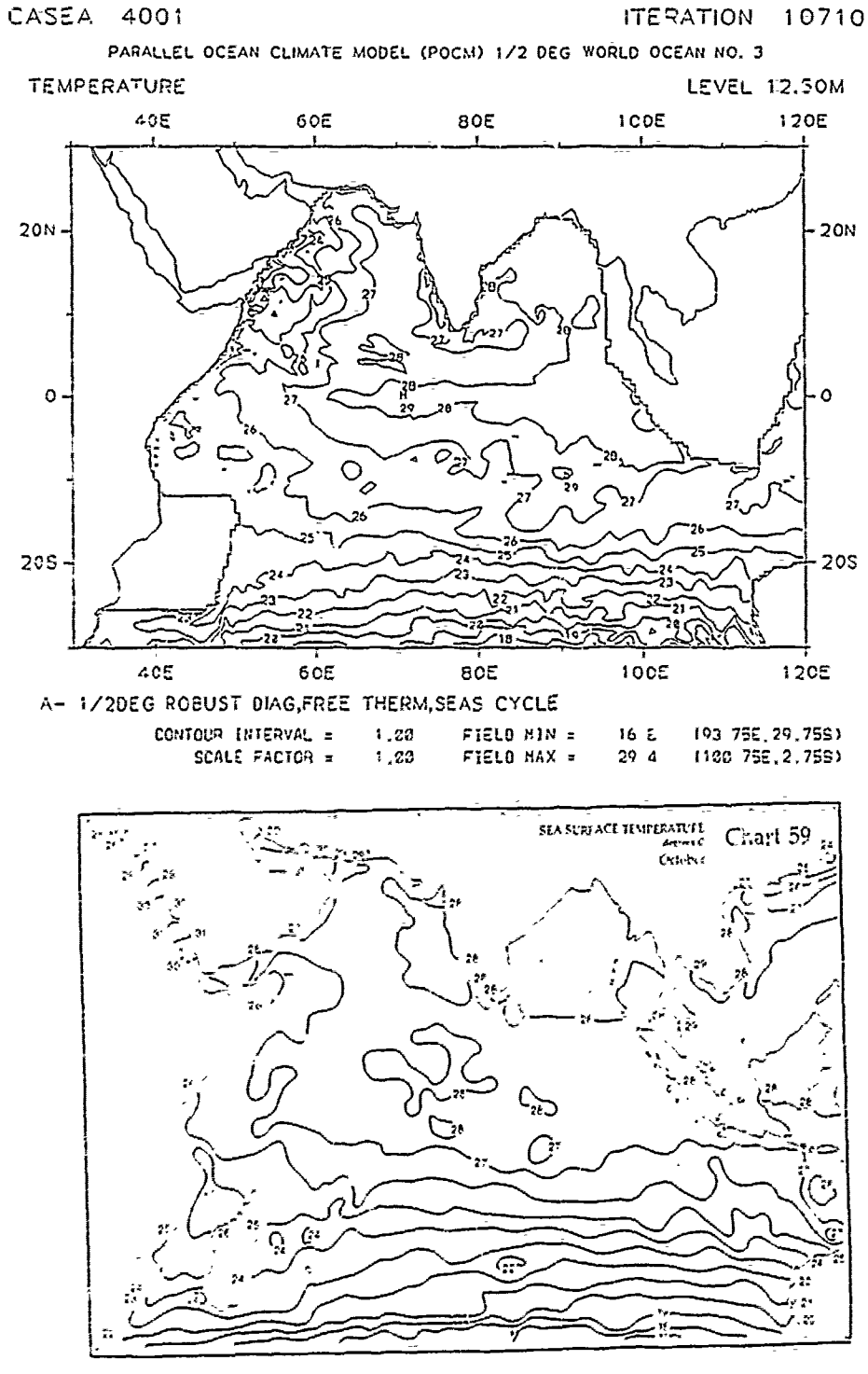

Figure 5.10 **Comparison of October T at 12.5 m with climatology.** (a) Monthly mean temperature in the model, and (b) Hastenrath and Lamb (1979) sea surface temperature.

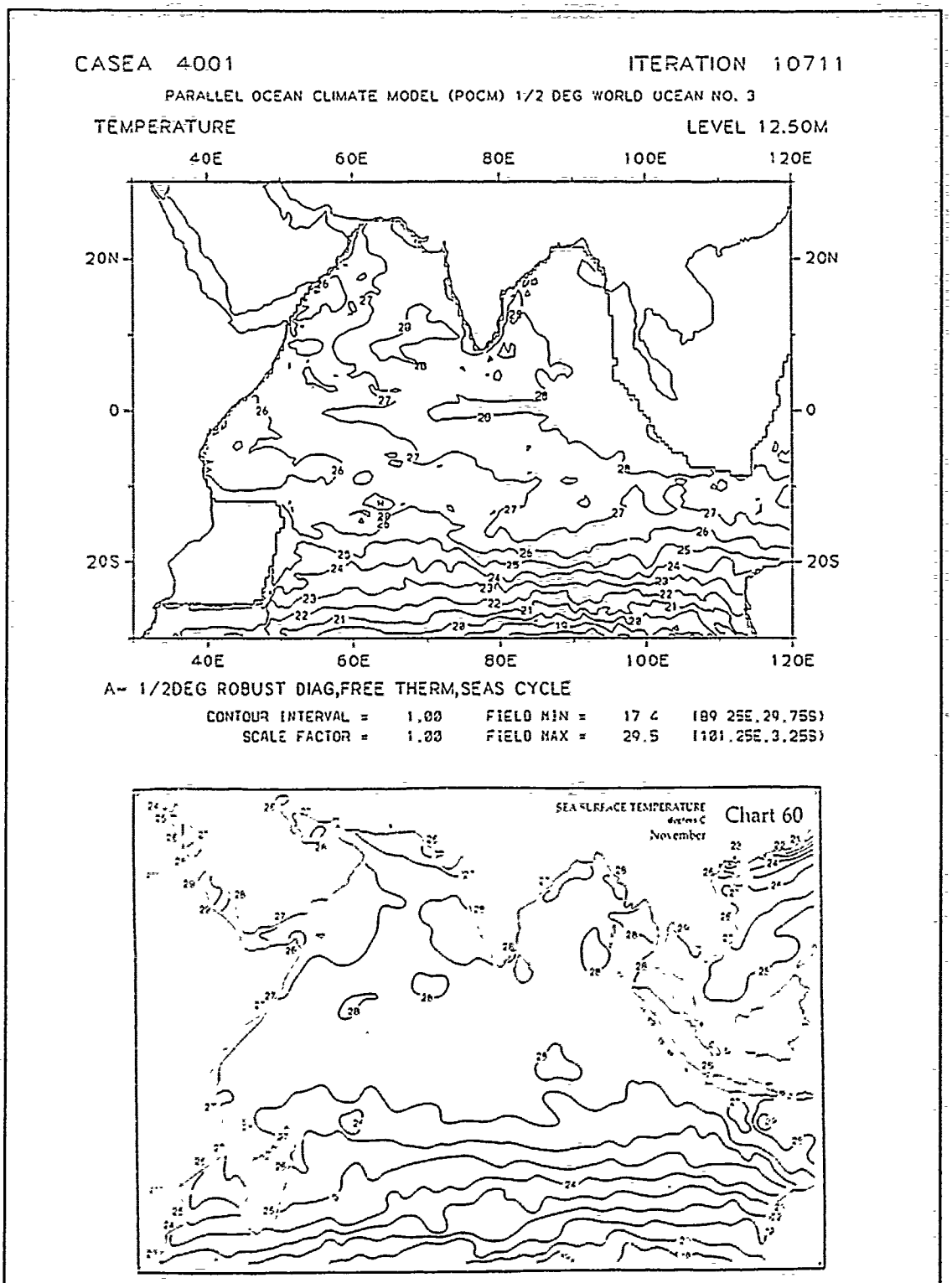

Figure 5.11 **Comparison of November T at 12.5 m with climatology.** (a) Monthly mean temperature in the model, and (b) Hastenrath and Lamb (1979) sea surface temperature.

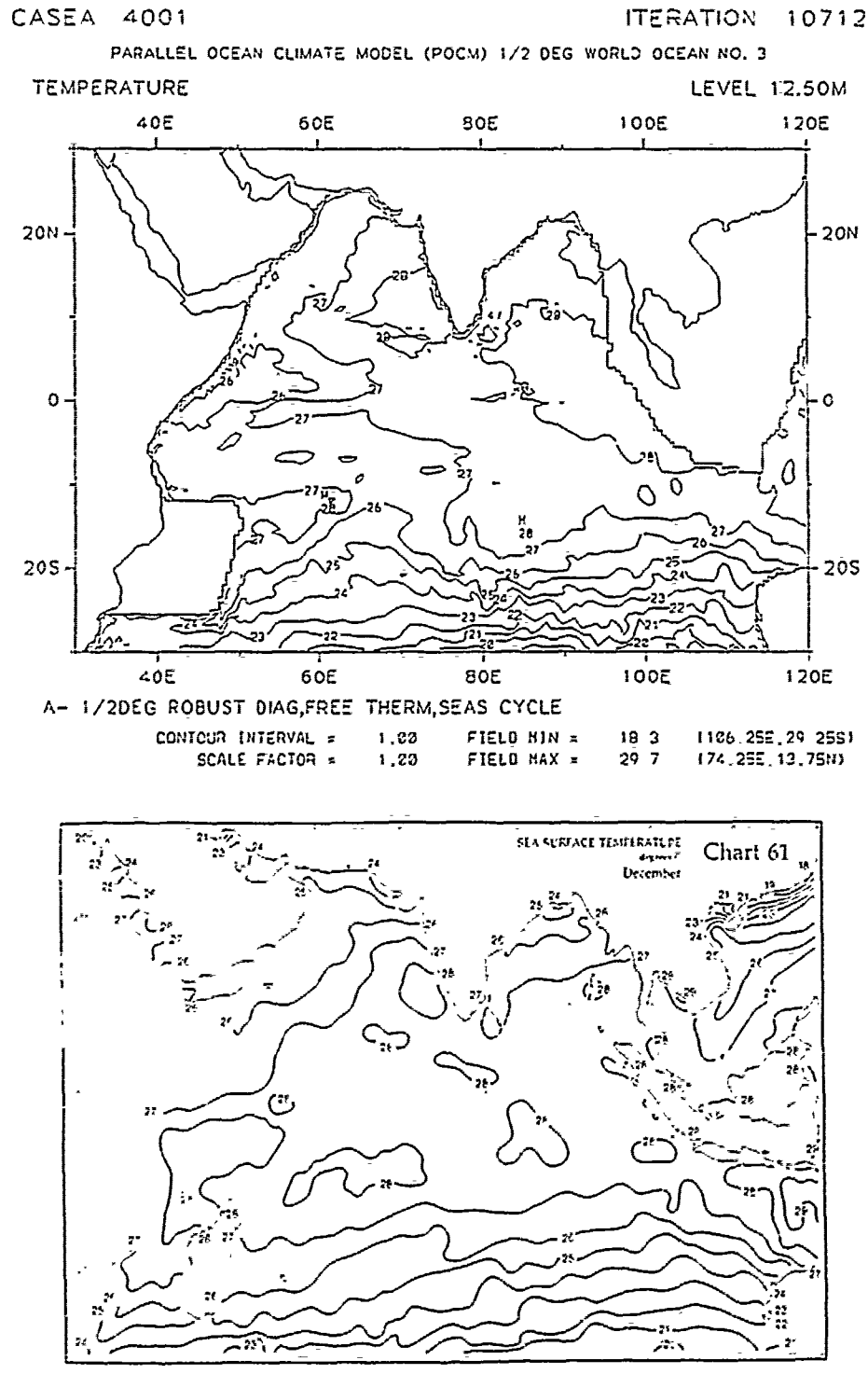

Figure 5.12 **Comparison of December T at 12.5 m with climatology.** (a) Monthly mean temperature in the model, and (b) Hastenrath and Lamb (1979) sea surface temperature.

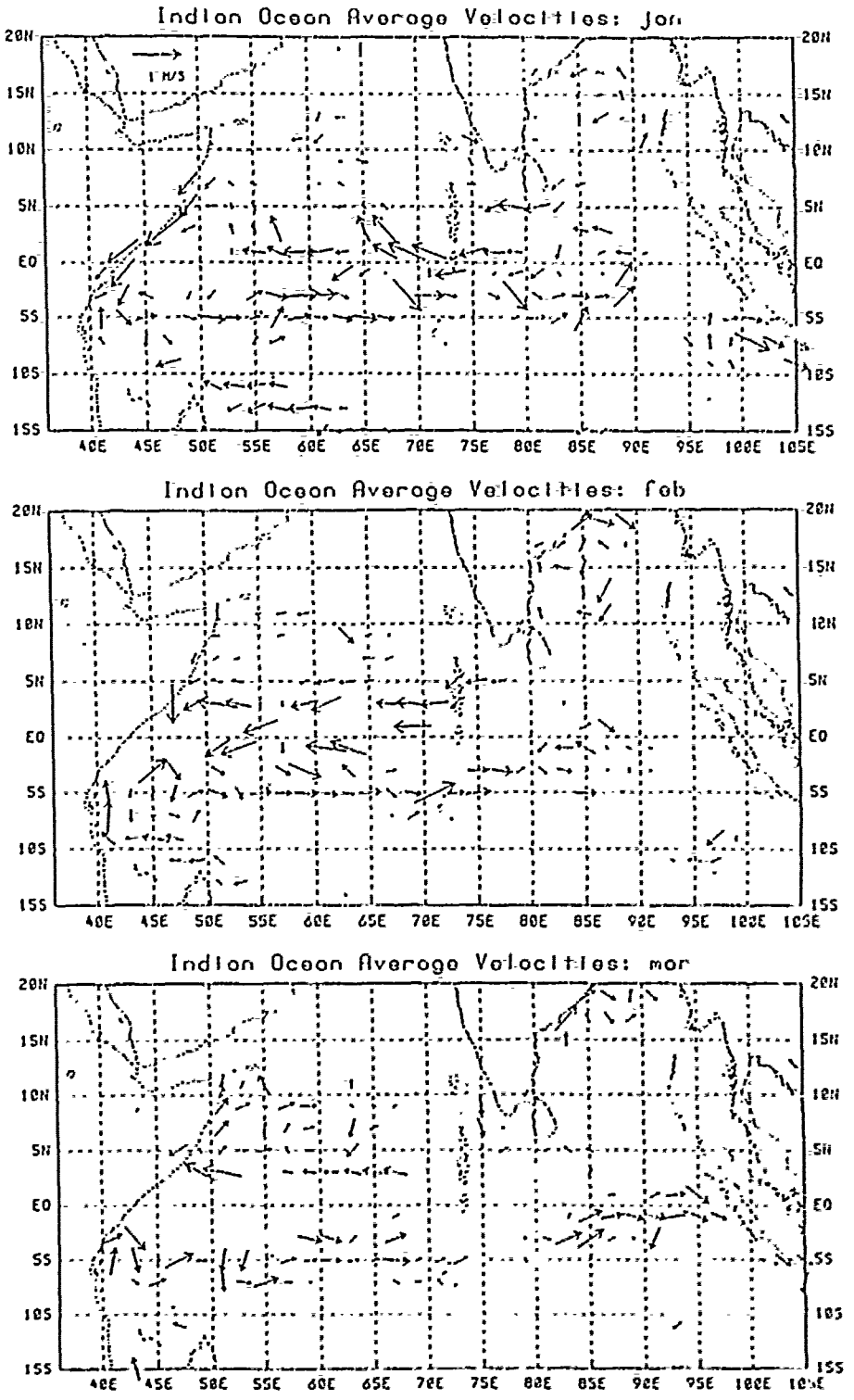

Figure 5.13 Drifting buoy-derived near-surface currents in the Indian Ocean during January, February, and March. (Molinari *et al.*, 1990).

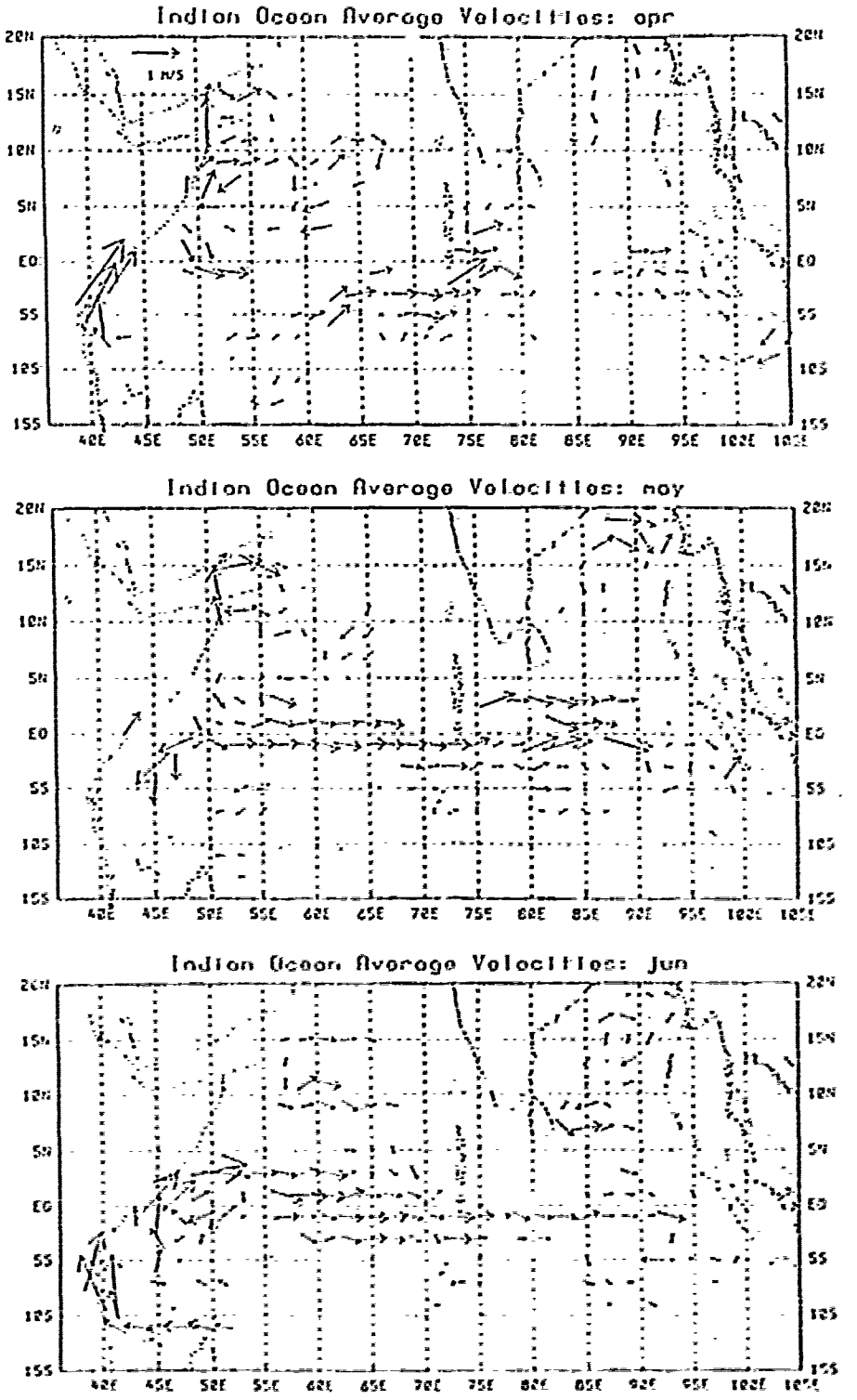

Figure 5.14 Drifting buoy-derived near-surface currents in the Indian Ocean during April, May, and June. (Molinari *et al.*, 1990).

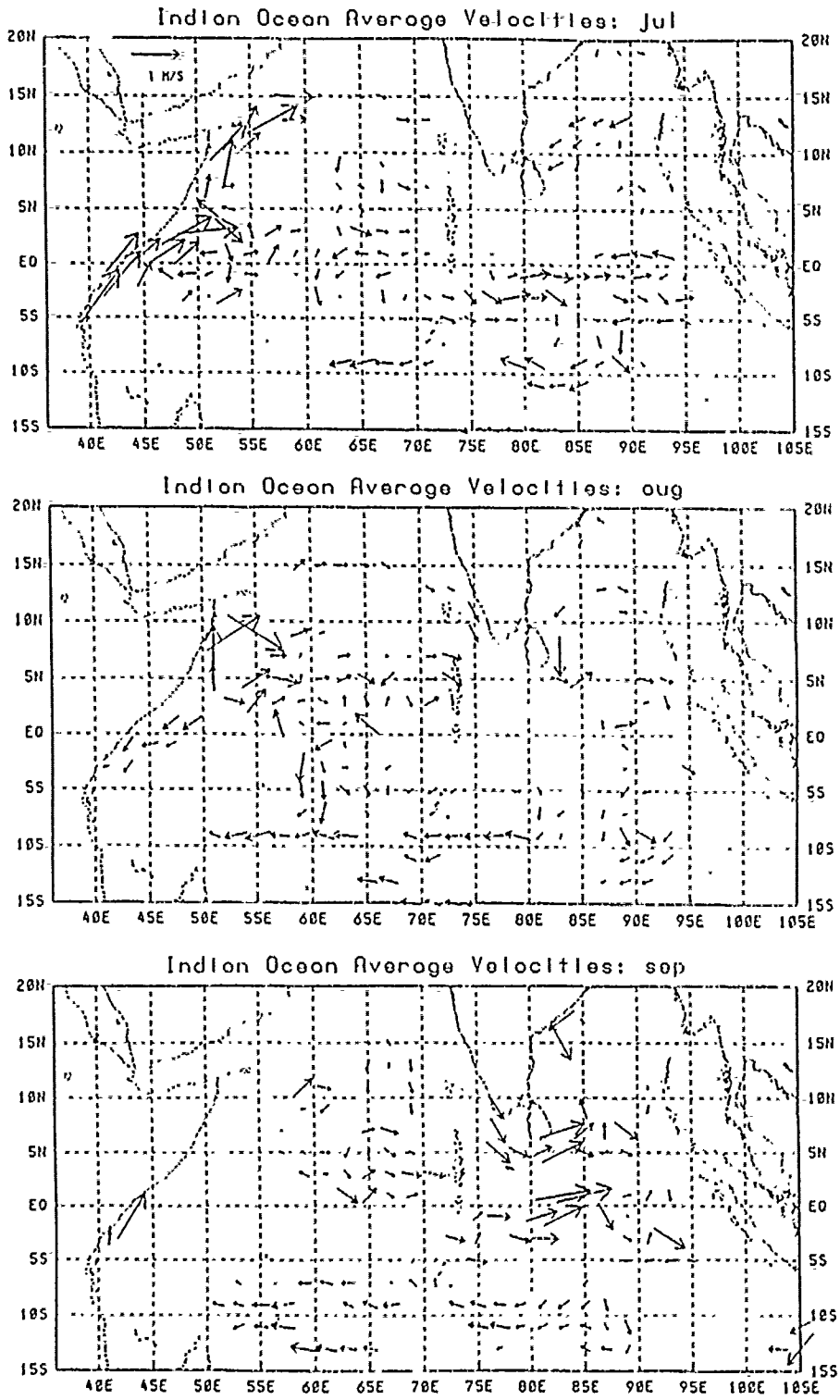

Figure 5.15 Drifting buoy-derived near-surface currents in the Indian Ocean during July, August, and September. (Molinari *et al.*, 1990).

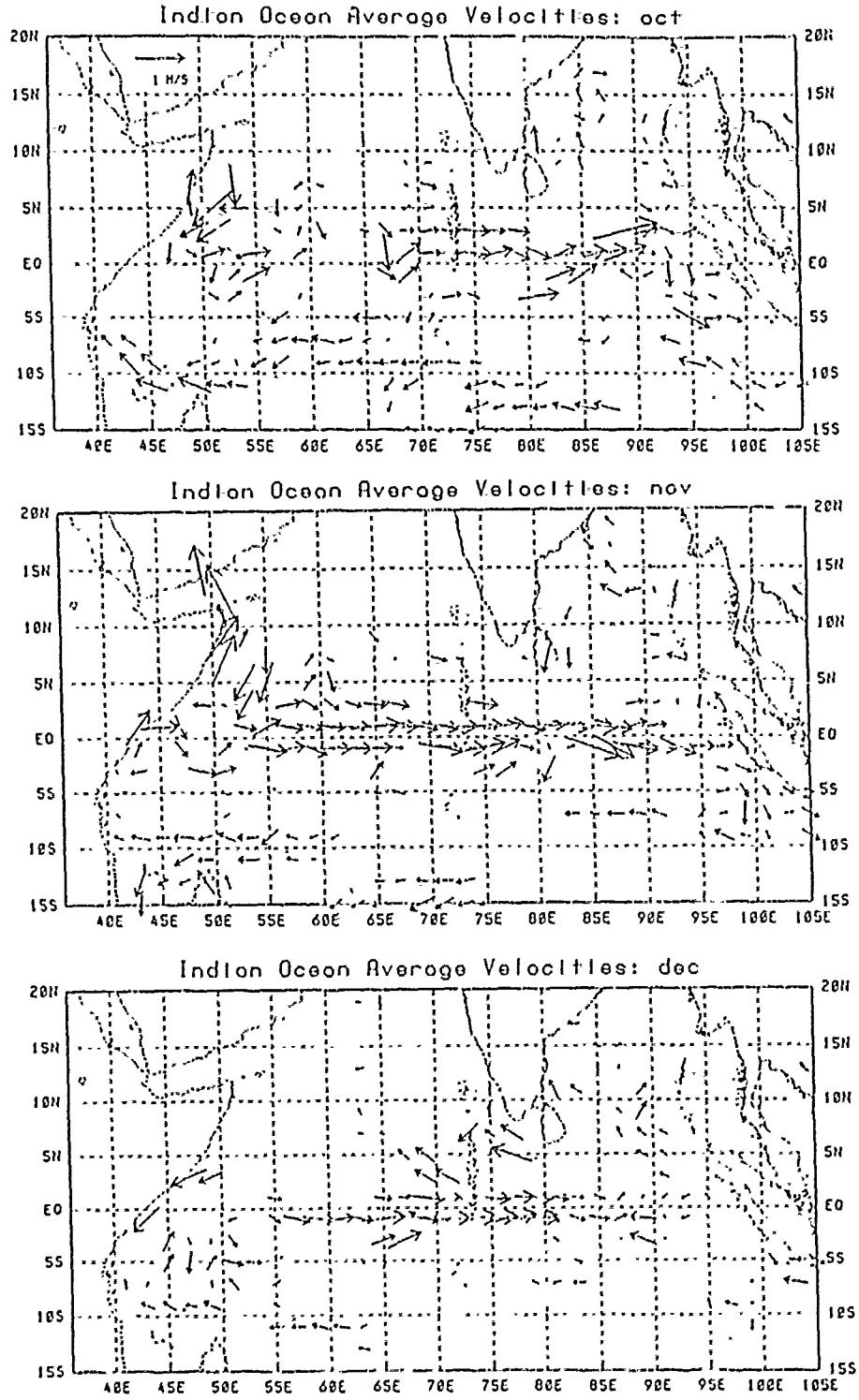

Figure 5.16 Drifting buoy-derived near-surface currents in the Indian Ocean during October, November, and December. (Molinari *et al.*, 1990).

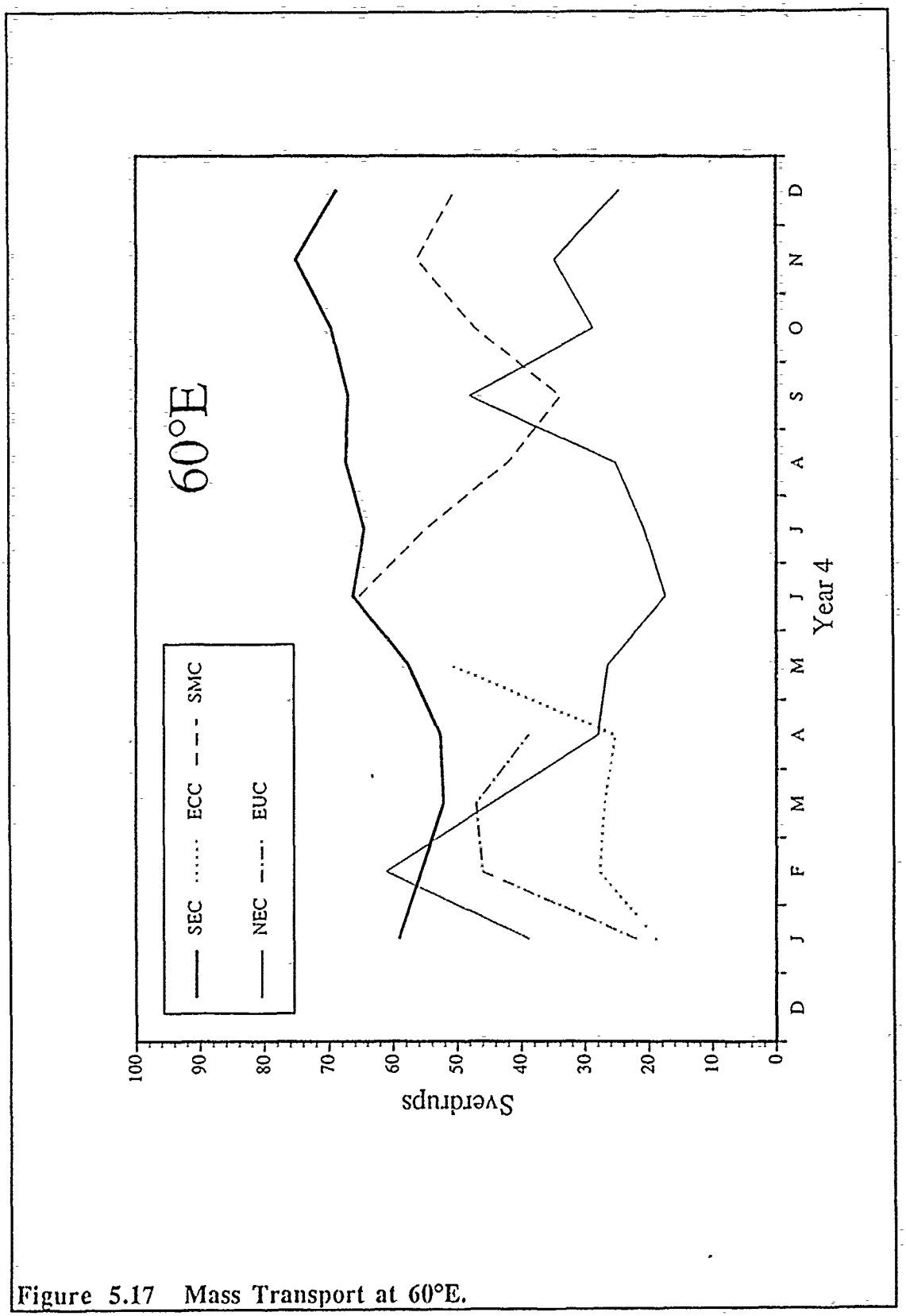

Figure 5.17 Mass Transport at 60°E.

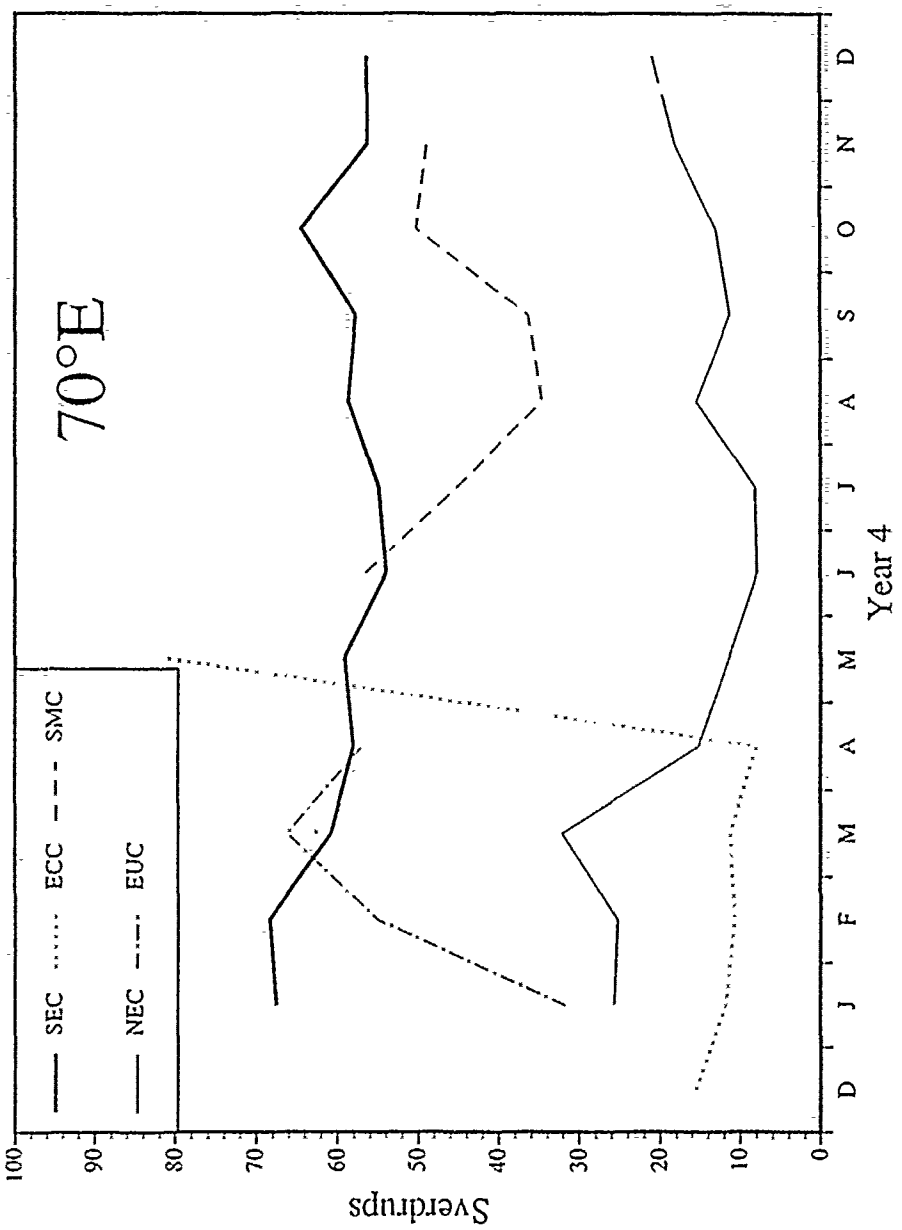

Figure 5.18 Mass transport at 70°E.

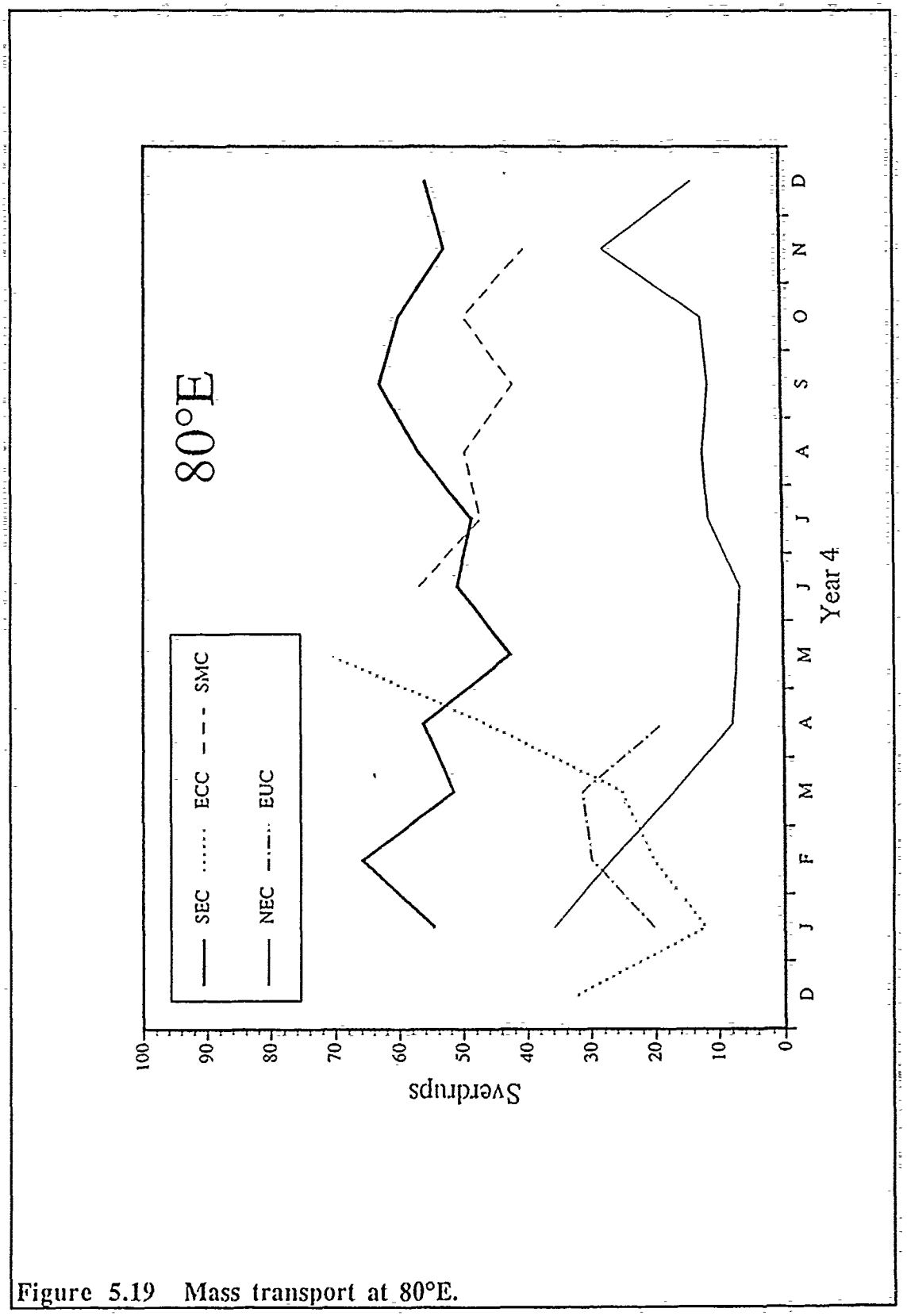

Figure 5.19 Mass transport at 80°E.

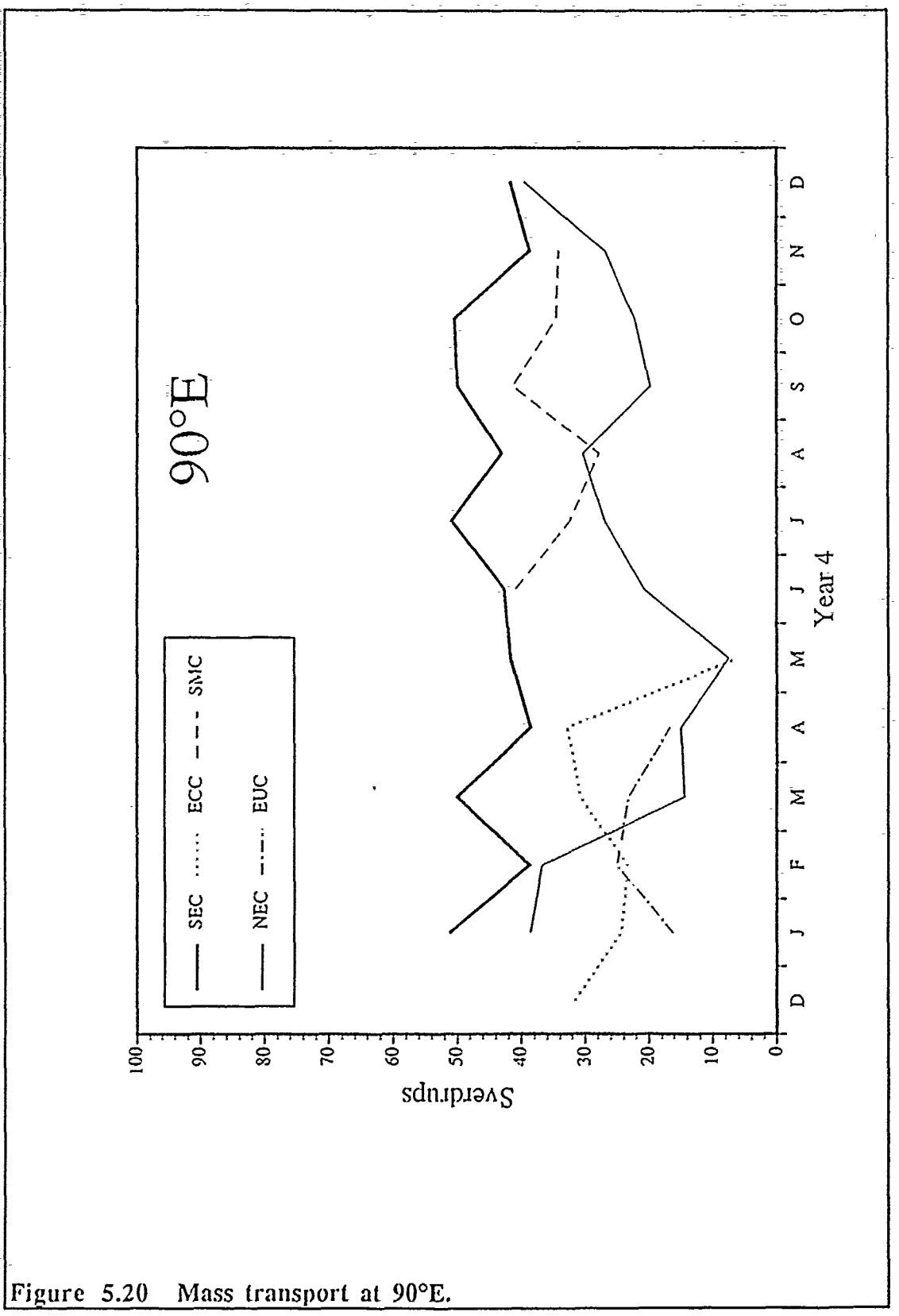

Figure 5.20 Mass transport at 90°E.

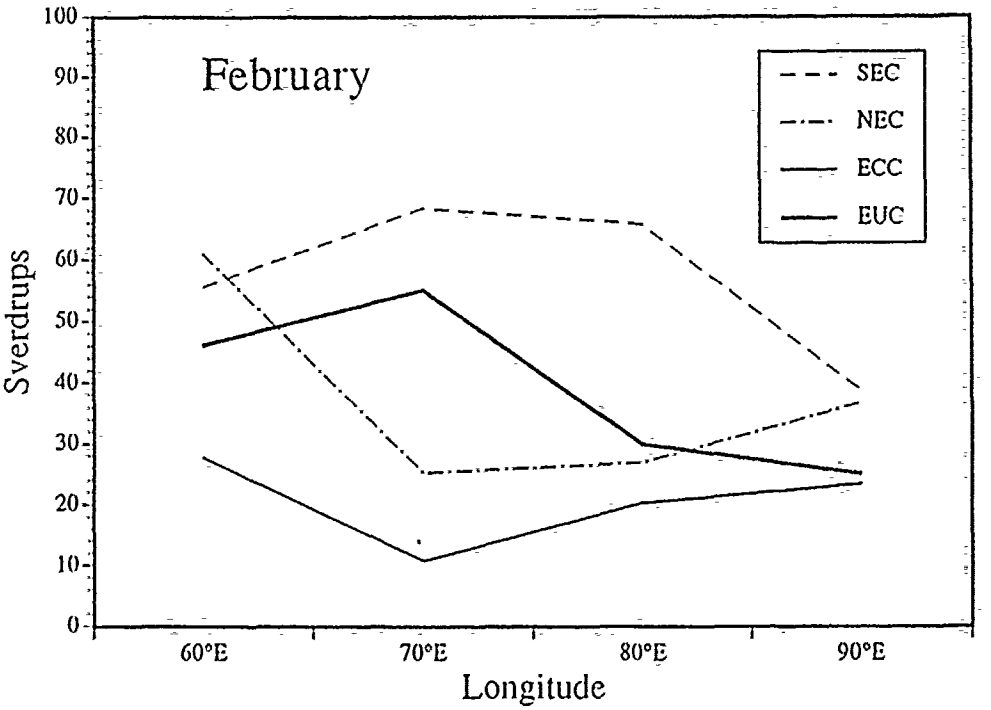

Figure 5.21 Variation of mass transport with longitude in February of Year 4.

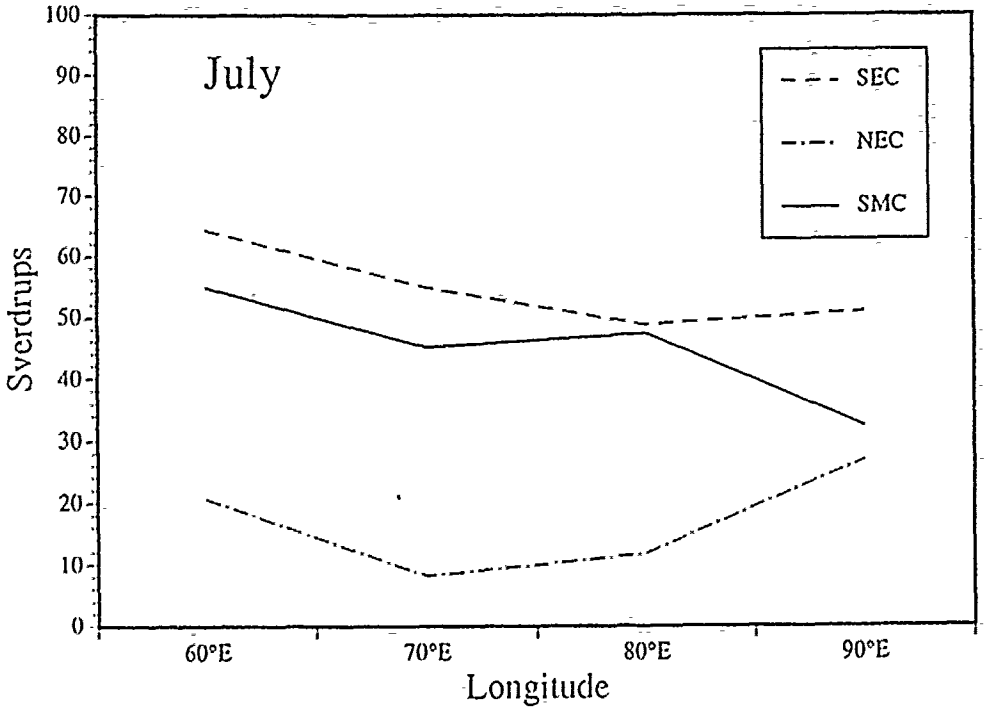

Figure 5.22 Variation of mass transport with longitude in July of Year 4.

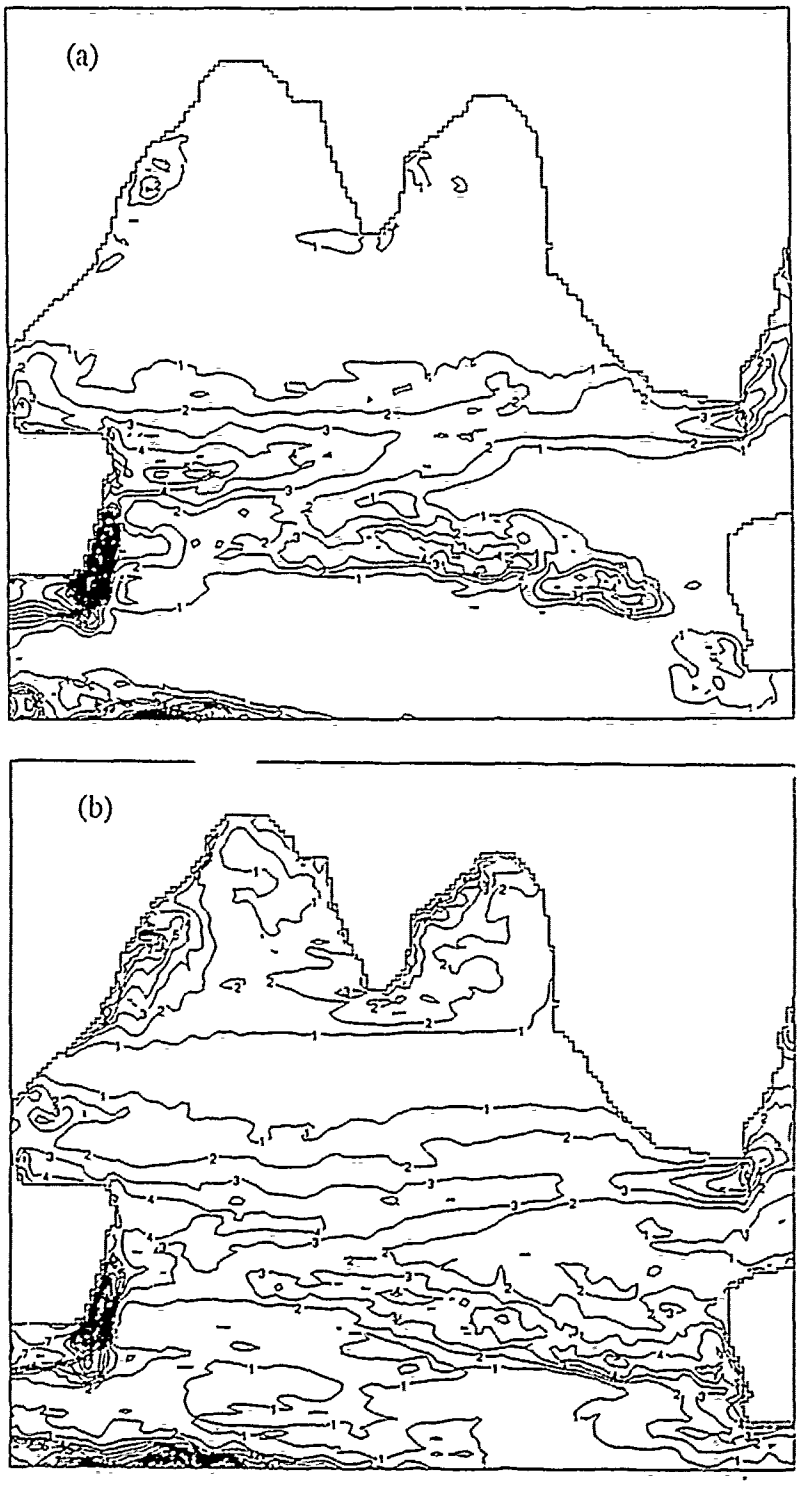

Figure 5.23 **Standard deviation of sea slope (cm/10 km) of the model.** (a) 300 day calculation during annual mean forcing phase, and (b) three-year calculation (Years 5-7) of the seasonal forcing phase.

REFERENCES

Barton, W. A., An analysis of results of a high-resolution world ocean circulation model, M. S. thesis, Naval Postgraduate School, Monterey, California, 143 pp.

Batteen, M. L., and M. J. Rutherford, 1990: Modeling studies of eddies in the Leeuwin Current: the role of thermal forcing. *J. Phys. Oceanogr.*, **20,** 1484-1520.

Brekhovskikh, A. L., Y. L. Demin, I. G. Usychenko, and A. D. Shcherbinin, 1986: New schematic patterns for the seasonal climatic circulation of the Indian Ocean. *Oceanology,* **26,** 416-422.

Brown, O. B., J. G. Bruce, and R. H. Evans, 1980: Evolution of sea surface temperature in the Somali basin during the southwest monsoon of 1979. *Science,* **209,** 595-597.

Bryan, K., 1963: A numerical investigation of a nonlinear model of a wind-driven ocean. *J. Atmos. Sci.*, **20,** 594-606.

Bryan, K., and M. D. Cox, 1968: A nonlinear model of an ocean driven by wind and differential heating: Parts I and II. *J. Atmos. Sci.*, **25,** 945-978.

Bryan, K., 1969: A numerical model for the study of the world ocean. *J. Comput. Phys.*, **4,** 347-376.

Cadet, D. L., and B. C. Diehl, 1984: Inter-annual variability of surface fields over the Indian Ocean in recent decades. *Mon. Wea Rev.*, **112,** 1921-1935.

Cox, M. D., 1975: A baroclinic numerical model of the world ocean: preliminary results. In: *Numerical Models of Ocean Circulation*, Nat. Acad. of Sciences, Washington, D. C., 107-120.

Cox, M. D., 1976: Equatorially trapped waves and the generation of the Somali Current. *Deep-Sea Res.*, **23,** 1139-1152.

Cox, M. D., 1979: A numerical study of Somali Current eddies. *J. Phys. Oceanogr.*, **9,** 311-326.

Cox, M. D., 1984: A primitive equation three-dimensional model of the ocean. *GFDL Ocean Group Tech. Rept. No. 1*, GFDL/NOAA, Princeton Univeristy, Princeton, New Jersey, 250 pp.

Chervin, R. M., and A. J. Semtner, 1988: An ocean modeling system for supercomputer architectures of the 1990's. In: *Proceedings of the NATO Advanced Research Workshop on Climate-Ocean Interaction,* Ed. M. Schlesinger, Kluwer, Dordrecht, Netherlands.

Church, J. A., G. R. Cresswell, and J. S. Godfrey, 1989: The Leeuwin Current. In: *Poleward Flows along Eastern Ocean Boundaries*, Eds. S. Neshyba, Ch. N. K. Mooers, R. I. Smith, and R. T. Barber, Springer-Verlag Lecture Notes, 230-252.

Cutler, A., and J. Swallow, 1984: Surface currents of the Indian Ocean (to 25°S, 100°E): compiled from historical data archived by the meteorological office, Bracknell, UK. *Institute of Oceanographic Sciences*, Rep. No. 187, 8pp & 36 charts.

Düing, W., 1970: *The Monsoon Regime of the Currents in the Indian Ocean.* East-West Center Press, Honolulu, Hawaii, 68 pp.

Düing, W., R. L. Molinari, and J. C. Swallow, 1980. Somali Current: evolution of surface flow. *Science*, **209**, 588-590.

Eriksen, C. C., 1979: An equatorial transect of the Indian Ocean. *J. Mar. Res.*, **37**, 215-232.

Evans, R. H., and O. B. Brown, 1981: Propagation of thermal fronts in the Somali Current system. *Deep-Sea Res.*, **28**, 521-527.

Finlater, J., 1971: Mean monthly airflow at low levels over the western Indian Ocean. *Geophys. Mem.*, **115**, H. M. S. O., London, 53pp.

Godfrey, J. S., 1989: A Sverdrup model of the depth-integrated flow for the World Ocean allowing for island circulations. *Geophys. Astrophys. Fluid Dyn.* **45**, 89-112.

Godfrey, J. S., and T. J. Golding, 1981: The Sverdrup relation in the Indian Ocean and the effect of Pacific-Indian Ocean throughflow on Indian Ocean circulation and on the East Australian Current. *J. Phys. Oceanogr.*, **11**, 771-779.

Godfrey, J. S., and K. R. Ridgway, 1985: The large-scale environment of the poleward-flowing Leeuwin Current, western Australia: longshore steric height gradients, wind stresses, and geostrophic flow. *J. Phys. Oceanogr.*, **15**, 481-495.

Gordon, A., 1986: Interocean exchange of thermocline water. *J. Geophys. Res.*, **91**, 5037-5046.

Haney, R. L., 1971: Surface thermal boundary condition for ocean circulation models. *J. Phys. Oceanogr.*, **1**, 241-248.

Hastenrath, S. L., and P. Lamb, 1979a: Climatic atlas of the Indian Ocean, Part I: Surface climate and atmospheric circulation. University of Wisconsin Press, Madison, Wisconsin, 117 pp.

Hastenrath, S. L., and P. Lamb–, 1979b: Climatic atlas of the Indian Ocean, Part II: The oceanic heat budget. University of Wisconsin Press, Madison, Wisconsin, 93 pp.

Hellerman, S., and M. Rosenstein, 1983: Normal monthly wind stress over the world ocean with error estimates. *J. Phys. Oceanogr.*, **13**, 1093-1104.

Jensen, T. G., 1989: A numerical study of the seasonal variability of the Somali Current. Mesoscale Air-Sea Interaction Group Technical Report, Geophysical Fluid Dynamics Institute, Florida State University, Tallahassee, Florida, 118 pp.

Khanaichenko, N. K., 1974:*The System of Equatorial Countercurrents in the Ocean*. Ed. A. D. Dobrovol'skii. Gidrometeoizdat, Leningrad. Translation, Amerind, New Delhi, 1980, 158pp.

Killworth, P. D., D. Stainforth, D. J. Webb, and S. M. Paterson, 1990: The development of a free-surface Bryan-Cox-Sentner ocean model. *J. Phys. Oceanogr.*,accepted for publication.

Kindle, J. C., G. W. Heburn, and R. C. Rhodes, 1987: An estimate of the Pacific to Indian Ocean throughflow from a global numerical model. In: *Further Progress in Equatorial Oceanography*. Eds. E. J. Katz and J. M. Witte, Nova University Press, Fort Lauderdale, Florida, pp. 317-321.

Knauss, J. A., and B. A. Taft, 1964: Equatorial Undercurrent of the Indian Ocean. *Science*, **143**, 354-356.

Knox, R. A., 1976: On a long series of measurements of Indian Ocean equatorial currents near Addu Atoll. *Deep-Sea Res.*, **23**, 211-221.

Kort, V. G., 1977: Equatorial currents in the Indian Ocean during the northeast monsoon. *Oceanology*, **17**, 115-120.

Kundu, P. J., and J. P. McCreary, 1986: On the dynamics of the throughflow from the Pacific into the Indian Ocean. *J. Phys. Oceanogr.*, **16**, 2191-2198.

Leetmaa, A., and H. Stommel, 1980: Equatorial current observations in the western Indian Ocean in 1975 and 1976. *J. Phys. Oceanogr.*, **10**, 258-269.

Leetmaa, A., D. R. Quadfasel, and D. Wilson, 1982: Development of the flow field during the onset of the Somali Current, 1979. *J. Phys. Oceanogr.*, **12**, 1325-1342.

Leetmaa, A., H. T. Rossby, P. M. Saunders, and P. Wilson, 1980: Subsurface circulation in the Somali Current. *Science*, **209**, 590-592.

Legler, D. M., I. M. Navon, and J. J. O'Brien, 1989: Objective analysis of pseudostress over the Indian Ocean using a direct-minimization approach. *Mon. Wea. Rev.*, **117**, 709-720.

Levitus, S., 1982: Climatological atlas of the world oceans. NOAA Prof. Pap. 13, U. S. Government Printing Office, Washington, D. C.

Levitus,1984: Annual cycle of temperature and heat storage in the world ocean. *J. Phys. Oceanogr.*, **14**, 727-746.

Levitus, 1986: Annual cycle of salinity and salt storage in the world ocean. *J. Phys. Oceanogr.*, **16** , 322-343.

Luther, M. E., 1987: Indian Ocean modelling. In: *Further Progress in Equatorial Oceanography*. Eds. E. J. Katz and M. J. White, Nova University Press, Fort Lauderdale, Florida, 303-316.

Luther, M. E., and J. J. O'Brien, 1985: A model of the seasonal circulation in the Arabian Sea forced by observed winds. *Prog. Oceanogr.*, **14**, 353-385.

Luther, M. E., and J. J. O'Brien, 1989: Modelling the variability in the Somali Current. In: *Mesoscale/Synoptic Coherent Structures in Geophysical Turbulence*. Ed. J. C. J. Nihoul, Elsevier Science Publishers B. V., Amsterdam, Netherlands, 373-386.

Luther, M. E.,J. J. O'Brien, and A. H. Meng, 1985: Morphology of the Somali Current system durng the southwest monsoon. In: *Coupled Ocean-Atmosphere Models*. Ed. J. C. J. Nihoul, Elsevier Science Publishers B. V., Amsterdam, Netherlands, 405-437.

Luyten, J. R., 1981: Recent observations in the equatorial Indian Ocean. In: *Monsoon Dynamics*. Eds.M. J. Lighthill and R. P. Pearce, Cambridge University Press, Cambridge, pp 465-480.

Luyten, J. R., 1982: Equatorial current measurements, I. Moored observations. *J. Mar. Res.*, **40**, 19-41.

Luyten, J. R., J. R., M. Fieux, and J. Gonella, 1980: Equatorial currents in the western Indian Ocean. *Science*, **209**, 600-603.

Luyten, J. R., and D. H. Roemmich, 1982: Equatorial currents at semi-annual period in the Indian Ocean. *J. Phys. Oceanogr.*, **12**, 406-413.

Luyten, J. R., and J. C. Swallow, 1976: Equatorial Undercurrents. *Deep-Sea Res.*, 23, 999-1001.

McCreary, J. P., 1987: A model of deep equatorial jets. In: *Further Progress in Equatorial Oceanography*. Eds. E. J. Katz and M. J. White, Nova University Press, Fort Lauderdale, Florida, 385-395.

Mesinger, F., and A. Arakawa, 1976: Numerical methods used in atmospheric models. *GARP Publ. Ser. 17*. WMO, 64pp.

Molinari, R. L., D. Olson, and G. Reverdin, 1990: Surface current distributions in the tropical Indian Ocean derived from compilations of surface buoy trajectories. *J. Geophys. Res.*, **95**, 7217-7238.

Moore, D. W., and S. G. H. Philander, 1977: Modeling of the Tropical Oceanic Circulation. In: *The Sea*, Vol. 6, Eds. E Goldberg, I. McCave, J. O'Brien, and J. Steele, Wiley-Interscience, New York, 319-361.

Moore, D. W., and J. P. McCreary, 1990: Excitation of intermediate-frequency equatorial waves at a western ocean boundary: with application to observations from the Indian Ocean. *J. Geophys. Res.*, **95**, 5219-5231.

Nicholls, N., 1984: The Southern Oscillation and Indonesian sea-surface temperature. *Mon. Wea. Rev.*, **112**, 424-432.

O'Brien, J. J., and H. E. Hurlburt, 1974: Equatorial jet in the Indian Ocean: Theory. *Science*, **184**, 1075-1077.

O'Neill K., and J. R. Luyten, 1984: Equatorial velocity profiles. Part II: Zonal component. *J. Phys. Oceanogr.*, **14**, 1842-1852.

Pacanowski, R. C., and S. G. H. Philander, 1981: Parameterization of vertical mixing in numerical models of tropical oceans. *J. Phys. Oceanogr.*, **11**, 1443-1451.

Pickard, G. L., and W. J. Emery, 1982: *Descriptinve Physical Oceanography*., Pergamon Press, Oxford, 249 pp.

Polonskiy, A. B., and N. B. Shapiro, 1983: Variability of hydrophysical fields in the western equatorial zone of the Indian Ocean. *Oceanology*, **23**, 172-175.

Ponte, R. M., and J. R. Luyten, 1990: Deep velocity measurements in the western equatorial Indian Ocean. *J. Phys. Oceanogr.*, **20**, 44-52.

Quadfasel, D. and F. Schott, 1983: Southward subsurface flow below the Somali Current. *J. Geophys. Res.*, **88**, 5973-5979.

Rao, L. V. G., V. R. Babu, and V. V. R. Varadachari, 1981: Structure of currents and hydrographic conditions in the western equatorial Indian Ocean during the summer monsoon. In: *Monsoon Dynamics*. Eds.M. J. Lighthill and R. P. Pearce, Cambridge University Press, Cambridge, pp 453-463.

Rao, R. R., R. L. Molinari, and J. F. Festa, 1989: Evolution of the climatological near-surface thermal structure of the tropical Indian Ocean, 1, Description of mean monthly mixed layer depth, and sea surface temperature, surface current, and surface meteorological fields. *J. Geophys. Res.*, **94**, 10801-10816.

Reverdin, G., 1987: The upper equatorial Indian Ocean: the climatological seasonal cycle. *J. Phys. Oceanogr.*, **17**, 903-927.

Reverdin, G., and J. R. Luyten, 1986: Near-surface meanders in the equatorial Indian Ocean. *J. Phys. Oceanogr.*, **16**, 1088-1100.

Sarmiento, J. L., and K. Bryan, 1982: An ocean transport model for the North Atlantic. *J. Geophys. Res.*, **87**, 394-408.

Schott, F., 1983: Monsoon response of the Somali Current and associated upwelling. *Prog. Oceanogr.*, **12**, 357-382.

Schott, F., 1987. Recent studies of western Indian Ocean circulation. In: *Further Progress in Equatorial Oceanography*. Eds. E. J. Katz and M. J. White, Nova University Press, Fort Lauderdale, Florida, 287-302.

Schott, F., and D. R. Quadfasel, 1980: Development of the subsurface currents of the northern Somali Current gyre from March to July 1979. *Science*, **209**, 593-595.

Schott, F., and D. R. Quadfasel, 1982: Variability of the Somali Current during the onset of the southwest monsoon. *J. Phys. Oceanogr.*, **12**, 1343-1357.

Schott, F., M. Fieux, J. Kindle, J. Swallow, and R. Zantopp, 1988: The boundary currents east and north of Madagascar 2. Direct measurements and model comparisons. *J. Geophys. Res.*, **93**, 4963-4974.

Simmons, R. C., M. E. Luther, J. J. O'Brien, and D. M. Legler, 1988: Verification of a numerical ocean model of the Arabian Sea. *J. Geophys. Res.*, **93**, 15437-15453.

Semtner, A. J., 1974: An oceanic general circulation model with bottom topography. Technical Report 9, Dept. of Meterorology, UCLA, Los Angeles, California, 99 pp.

Semtner, A. J., 1986a: History and methodology of modelling the circulation of the world ocean. In: *Advanced Physical Oceanographic Numerical Modelling*. Ed. J. J. O'Brien, D. Reidel, Norwell, Massachusetts, 23-32.

Semtner, A. J., 1986b: Finite-difference formulation of a world ocean model. In: *Advanced Physical Oceanographic Numerical Modelling*. Ed. J. J. O'Brien, D. Reidel, Norwell, Massachusetts, 187-202.

Semtner, A. J., and R. M. Chervin, 1988: A simulation of the global ocean circulation with resolved eddies. *J. Geophys. Res.*, **93**, 15502-15522.

Swallow, J. C., 1964: Equatorial Undercurrent in the western Indian Ocean. *Nature*, **204**, 436-437.

Swallow, J. C., 1981: Observations of the Somali Current and its relationship to the monsoon winds. In: *Monsoon Dynamics*. Eds. M. J. Lighthill and R. P. Pearce, Cambridge University Press, Cambridge, pp 445-452.

Swallow, J. C., 1983: Eddies in the Indian Ocean. In: *Eddies in Marine Science*. Ed. A. R. Robinson, Springer-Verlag, Berlin, pp 200-218.

Taft, B. A., 1967a. Equatorial Undercurrent of the Indian Ocean, 1963. *Contributions (Scripps Inst. of Oceanog.)*, **37**, 1397-1408.

Taft, B. A., 1967b. Equatorial currents. *Contributions (Scripps Inst. of Oceanog.)*, **37**, 1461-1463.

Tchernia, P., 1980. *Descriptive Regional Oceanography*. Pergamon Press, Oxford, 253 pp., 19 plates.

Thompson, R. O. R. Y., 1984: Observations of the Leeuwin Current off Western Australia. *J. Phys. Oceanogr.*, **14**, 623-628.

Weaver, A. J., and J. H. Middleton, 1989: On the dynamics of the Leeuwin Current. *J. Phys. Oceanogr.*, **19**, 626-648.

Woodberry, K. E., M. E. Luther, and J. J. O'Brien, 1989: The wind-driven seasonal circulation in the southern tropical Indian Ocean. *J. Geophys. Res.*, **94**, 17985-18002.

Wyrtki, K., 1971: *Oceanographic Atlas of the International Indian Ocean Expedition.* National Science Foundation, Washington, DC, 531 pp.

Wyrtki, K., 1973: An equatorial jet in the Indian Ocean. *Science*, **181**, 262-264.

INITIAL DISTRIBUTION LIST

		No. Copies
1.	Defense Technical Information Center Cameron Station Alexandria, Virginia 22314	2
2.	Library, Code 52 Naval Postgraduate School Monterey, California 93943-5000	2
3.	Chairman (Code OC/Co) Department of Oceanography Naval Postgraduate School Monterey, CA 93943-5000	1
4.	Chairman (Code MR/Hy) Department of Meteorology Naval Postgraduate School Monterey, CA 93943-5000	1
5.	Professor A. J. Semtner (Code OC/Se) Department of Oceanography Naval Postgraduate School Monterey, CA 93943-5000	2
6.	Professor M. L. Batteen (Code OC/Bv) Department of Oceanography Naval Postgraduate School Monterey, CA 93943-5000	1
7.	Lieutenant Commander Erik Long Submarine Development Squadron TWELVE (N206) Bldg. 3 Submarine Base New London Groton, CT 06349-5200	1
8.	Director Naval Oceanography Division Naval Observatory 34th and Massachusetts Avenue NW Washington, DC 20390	1
9.	Commander Naval Oceanography Command Stennis Space Center MS 39529-5000	1

10. Commanding Officer — 1
Naval Oceanographic Office
Stennis Space Center
MS 39522-5001

11. Commanding Officer — 1
Fleet Numerical Oceanography Center
Monterey, CA 93943-5005

12. Commanding Officer — 1
Naval Oceanographic and Atmospheric
Research Laboratory
Stennis Space Center
MS 39522-5004

13. Director — 1
Naval Oceanographic and Atmospheric
Research Laboratory
Monterey, CA 93943-5006

14. Chairman — 1
Oceanography Department
U. S. Naval Academy
Annapolis, MD 21402

15. Chief of Naval Research — 1
800 N. Quincy Street
Arlington, VA 22217

16. Office of Naval Research (Code 420) — 1
Naval Ocean Research and Development Activity
800 N. Quincy Street
Arlington, VA 22217

17. Scientific Liason Office — 1
Office of Naval Research
Scripps Institution of Oceanography
La Jolla, CA 92037

18. Library — 1
Scripps Institution of Oceanography
P.O. Box 2367
La Jolla, CA 92037

19. Library — 1
Department of Oceanography
University of Washington
Seattle, WA 98105

20. Library 1
CICESE
P.O. Box 4803
San Ysidro, CA 92073

21. Commander 1
Oceanographic Systems Pacific
Box 1390
Pearl Harbor, HI 96860

22. Commander (AIR-370) 1
Naval Air Systems Command
Washington, DC 20360

23. Chief, Ocean Services Division 1
National Oceanic and Atmospheric Administration
8060 Thirteenth Street
Silver Springs, MD 20910

24. Dr. B. Buzbee, Director 1
Scientific Computing Division
National Center for Atmospheric Research
Boulder, CO 80307-3000

25. Dr. W. Washington, Director 1
Climate and Global Dynamics Division
National Center for Atmospheric Research
Boulder, CO 80307-3000

26. Dr. R. M. Chervin 1
Climate and Global Dynamics Division
National Center for Atmospheric Research
Boulder, CO 80307-3000

27. Dr. T. Spence, Director 1
Physical Oceanography Program
National Science Foundation
Washington, DC 20550

28. Dr. M. R. Riches 1
U. S. Department of Energy, ER-12
Carbon Dioxide Research Division
Washington, DC 20545

29. Dr. Jay Fein 1
Climate Dynamics
National Science Foundation
Washington, DC 20550

30. Dr. Ari Patrinos — 1
Office of Health and Environmental Research
Department of Energy
Washington, DC 20585

31. Prof. W. L. Gates — 1
Department of Atmospheric Sciences
Oregon State University
Corvallis, OR 97330

32. Prof. A. R. Robinson — 1
Division of Applied Sciences
Pierce Hall, Room 100D
Harvard University
29 Oxford Street
Cambridge, MA 02138

33 Prof. J. J. O'Brien — 1
Department of Meteorology
Florida State University
B-174, Love 070
930 Wildwood Drive
Tallahassee, FL 32306

34. Dr. K. Bryan — 1
Geophysical Fluid Dynamics Program
Princeton University GF04
Princeton University
P. O. Box 308
Princeton, NJ 08540

35. Mr. T. Bettge — 1
Climate and Global Dynamics Division
National Center for Atmospheric Research
Boulder, CO 80307-3000

36. Prof. Friedrich Schott — 1
Institut für Meereskunde der Universitat Kiel
Dusternbrooker Weg 20
D-2300 KIEL 1, FRG

37. Dr. J. Stuart Godfrey — 1
Div. Of Oceanography
CSIRO
P. O. Box 1538
Hobart Tasmania 7001
Australia

38. Dr. D. Panakala Rao — 1
Phsical Oceanography Division
National Institution of Oceanography
Dona Paula, Goa 403 004
India

39. Dr. Carsten Frederiksen — 1
BRMC
GPO Box 1289K
Melbourne, Victoria 3001
Australia

40. Mr. Michael Mutua — 1
Kenya Marine & Fisheries Research Inst.
P. O. Box 81651
Mombasa
Kenya

41. Dr. B. N. Goswami — 1
Centre for Atmospheric Sciences
Indian Institution of Sciences
Bangalore 560012
India

42. Dr. C. H. Sui — 1
Goddard Space Flight Center/ NASA
Mail Code 913
Greenbelt, MD 20771

43. Ms. C. M. Kirby — 1
U. S. Naval Oceanographic Office
Code OC
Stennis Space Center, MS 39522-5001

44. Mr. Michael McCann (Code OC/Mc) — 1
Department of Oceanography
Naval Postgraduate School
Monterey, CA 93943-5000